



University
of Glasgow

Peloni, Alessandro (2018) *Solar-sail mission design for multiple near-Earth asteroid rendezvous*. PhD thesis.

<https://theses.gla.ac.uk/8901/>

Copyright and moral rights for this work are retained by the author

A copy can be downloaded for personal non-commercial research or study, without prior permission or charge

This work cannot be reproduced or quoted extensively from without first obtaining permission in writing from the author

The content must not be changed in any way or sold commercially in any format or medium without the formal permission of the author

When referring to this work, full bibliographic details including the author, title, awarding institution and date of the thesis must be given

SOLAR-SAIL MISSION DESIGN FOR MULTIPLE NEAR-EARTH ASTEROID RENDEZVOUS

ALESSANDRO PELONI

Submitted in fulfilment of the requirements for the
Degree of Doctor of Philosophy

School of Engineering
College of Science and Engineering
University of Glasgow



**University
of Glasgow**

© 2018 Alessandro Peloni

Alessandro Peloni: *Solar-sail mission design for multiple near-Earth asteroid rendezvous*
Submitted in fulfilment of the requirements for the Degree of Doctor of Philosophy
School of Engineering, College of Science and Engineering
University of Glasgow
© 2018 Alessandro Peloni

ADVISOR:
Dr Matteo Ceriotti

EXAMINERS:
Dr Roberto Armellin
Surrey Space Centre, University of Surrey
Guilford, United Kingdom

Dr Patrick Harkness
School of Engineering, University of Glasgow
Glasgow, United Kingdom

Glasgow, Scotland, United Kingdom
06 March 2018

ABSTRACT

Solar sailing is the use of a thin and lightweight membrane to reflect sunlight and obtain a thrust force on the spacecraft. That is, a sailcraft has a potentially-infinite specific impulse and, therefore, it is an attractive solution to reach mission goals otherwise not achievable, or very expensive in terms of propellant consumption. The recent scientific interest in near-Earth asteroids (NEAs) and the classification of some of those as potentially hazardous asteroids (PHAs) for the Earth stimulated the interest in their exploration. Specifically, a multiple NEA rendezvous mission is attractive for solar-sail technology demonstration as well as for improving our knowledge about NEAs. A preliminary result in a recent study showed the possibility to rendezvous three NEAs in less than ten years. According to the NASA's NEA database, more than 12,000 asteroids are orbiting around the Earth and more than 1,000 of them are classified as PHA. Therefore, the selection of the candidates for a multiple-rendezvous mission is firstly a combinatorial problem, with more than a trillion of possible combinations with permutations of only three objects. Moreover, for each sequence, an optimal control problem should be solved to find a feasible solar-sail trajectory. This is a mixed combinatorial/optimisation problem, notoriously complex to tackle all at once.

Considering the technology constraints of the DLR/ESA Gossamer roadmap, this thesis focuses on developing a methodology for the preliminary design of a mission to visit a number of NEAs through solar sailing. This is divided into three sequential steps. First, two methods to obtain a fast and reliable trajectory model for solar sailing are studied. In particular, a shape-based approach is developed which is specific to solar-sail trajectories. As such, the shape of the trajectory that connects two points in space is designed and the control needed by the sailcraft

to follow it is analytically retrieved. The second method exploits the homotopy and continuation theory to find solar-sail trajectories starting from classical low-thrust ones. Subsequently, an algorithm to search through the possible sequences of asteroids is developed. Because of the combinatorial characteristic of the problem and the tree nature of the search space, two criteria are used to reduce the computational effort needed: (a) a reduced database of asteroids is used which contains objects interesting for planetary defence and human spaceflight; and (b) a local pruning is carried out at each branch of the tree search to discard those target asteroids that are less likely to be reached by the sailcraft considered. To reduce further the computational effort needed in this step, the shape-based approach for solar sailing is used to generate preliminary trajectories within the tree search. Lastly, two algorithms are developed which numerically optimise the resulting trajectories with a refined model and ephemerides. These are designed to work with minimum input required by the user. The shape-based approach developed in the first stage is used as an initial-guess solution for the optimisation.

This study provides a set of feasible mission scenarios for informing the stakeholders on future mission options. In fact, it is shown that a large number of five-NEA rendezvous missions are feasible in a ten-year launch window, if a solar sail is used. Moreover, this study shows that the mission-related technology readiness level for the available solar-sail technology is larger than it was previously thought and that such a mission can be performed with current or at least near-term solar sail technology. Numerical examples are presented which show the ability of a solar sail both to perform challenging multiple NEA rendezvous and to change the mission en-route.

TABLE OF CONTENTS

ABSTRACT	III
TABLE OF CONTENTS	V
LIST OF FIGURES	VIII
LIST OF TABLES	XI
LIST OF ALGORITHMS	XIII
ACKNOWLEDGEMENTS	XIV
PUBLICATIONS AND CONFERENCES	XVII
AUTHOR'S DECLARATION	XX
NOMENCLATURE	XXI
CHAPTER 1. INTRODUCTION.....	1
1.1. Solar-Sail Mission Design for Multiple NEA Rendezvous: An Overview.....	1
1.2. Objectives	4
1.3. Outline	6
CHAPTER 2. SURVEY OF THEORY AND METHODS	8
2.1. Solar Sailing from the Ground Up	8
2.1.1. Solar Radiation Pressure: From Maxwell to Einstein	8
2.1.2. Acceleration Model	12
2.1.3. Solar Sailing from the 1970s to the Present Day	16
2.2. Techniques for Space Trajectory Optimisation	18
2.2.1. Indirect Methods	20
2.2.2. Direct Methods	23
2.2.3. Metaheuristic Optimisation Methods	32
2.2.4. Shape-Based Approaches	34
2.2.5. Solar-Sailing Trajectory Design	39

2.2.6.	Target Selection	40
2.3.	Near-Earth Asteroids.....	44
CHAPTER 3. PRELIMINARY SOLAR-SAIL TRAJECTORY DESIGN		47
3.1.	Shape-Based Approach for Solar Sailing	48
3.1.1.	Pseudo Modified Equinoctial Elements	48
3.1.2.	Choice of the Shaping Functions.....	51
3.1.3.	Study of the Gauge Freedom.....	59
3.1.4.	Boundary-Constraint Satisfaction.....	60
3.1.5.	Shaped Trajectory and Control History Generation.....	61
3.1.6.	Practical Use of the Shape-Based Approach for Solar Sailing.....	63
3.1.7.	Assessing the Performances of the Shape-Based Approach for Solar Sailing	67
3.2.	From Low Thrust to Solar Sailing: A Homotopic Approach	72
3.2.1.	Mathematical Model	72
3.2.2.	Homotopy-Continuation Approach	76
3.2.3.	Numerical Test Cases.....	81
3.3.	Discussion.....	91
CHAPTER 4. ASTEROID SEQUENCE SEARCH.....		92
4.1.	Asteroid Database Selection	93
4.2.	Local Pruning on the Database	99
4.3.	Simplified Trajectory Model	103
4.4.	Sequence Search Algorithm.....	104
4.5.	Application to Gossamer Mission	107
4.6.	Numerical Test Cases	108
4.6.1.	PHA-NHATS Database.....	108
4.6.2.	PHA-LCDB Database	119
4.7.	Discussion.....	120
CHAPTER 5. SEQUENCE OPTIMISATION		123
5.1.	Problem Formulation	124
5.2.	STO: Sequential Trajectory Optimiser	127
5.3.	ATOSS: Automated Trajectory Optimiser for Solar Sailing	129

5.3.1.	Initial-Guess Generator	131
5.3.2.	Optimisation Strategy	131
5.4.	Numerical Test Cases	136
5.4.1.	Circular-to-Circular Orbit Transfers: A Comparison with the Literature	136
5.4.2.	Three-NEA Rendezvous Mission: A Comparison with the Literature	138
5.4.3.	Multiple NEA Rendezvous Missions.....	141
5.4.4.	Multiple NEA Sample Return Mission	151
5.4.5.	Online Change of the Mission: Two Test Cases for the Planetary Defence	152
5.4.6.	Automated Optimisation Campaign	159
5.5.	Discussion.....	161
CHAPTER 6. CONCLUSIONS.....		163
6.1.	Summary of the Work.....	163
6.2.	Summary of the Findings	166
6.3.	Current Limitations and Future Research	168
6.3.1.	Current Limitations.....	168
6.3.2.	Proposed Future Research	169
APPENDIX A METAHEURISTIC OPTIMISATION METHODS: A CLOSER LOOK		171
A.1.	Genetic Algorithm.....	171
A.2.	Particle Swarm Optimisation	173
A.3.	InTrance	175
APPENDIX B IMPLEMENTATION DETAILS		177
B.1.	MATLAB and C: A Performances Study	177
B.2.	PPSO: Peloni Particle Swarm Optimiser.....	179
B.2.1.	Test Case 1: Rastrigin's Function.....	179
B.2.2.	Test Case 2: Simple Function of Two Variables	180
B.2.3.	Test Case 3: CEC 2005.....	181
B.2.4.	Test Case 4: Optimal Two-Impulsive Transfer between Two Circular Orbits.....	182
B.2.5.	Test Case 5: Bi-Impulsive Earth-Apophis Transfer	183
REFERENCES.....		185

LIST OF FIGURES

Fig. 2.1. Montage of the Halley's Comet approaching the Sun in 1910.	9
Fig. 2.2. Sketch of a perfectly-reflecting flat solar sail.	13
Fig. 2.3. Graphical view of the normal unit vector in the orbital reference frame and the sail cone and clock angles.	14
Fig. 2.4. Sketch (not to scale) of classical low-thrust vs solar-sail achievable accelerations. It is evident that the thrust given by the two propulsion systems is equal only if the sail is facing the Sun.	16
Fig. 2.5. Schematic of the trajectory structure with a direct shooting method [75] (Reproduced with permission of AIAA).	26
Fig. 2.6. Lagrange polynomial approximation of the function $1/(1+25\tau^4)$ using (a) 25 equidistant points and (b) 25 LGR points.	27
Fig. 2.7. Schematic of the tree search implementations [171] (Reproduced with permission of Springer). Dotted lines and circles indicate branches yet to be explored. Crossed circles refer to pruned branches. (a) Breadth-first search. (b) Depth-first search. (c) Beam search.	43
Fig. 2.8. NEA discovery statistics.	46
Fig. 3.1. Representation of the trajectory (bold line) as a succession of points on instantaneous ellipses. The generic case for which the gauge term is non-zero is shown.	50
Fig. 3.2. Evolution of the in-plane pMEE F (a) and G (b) over true longitude under the effect of a constant sail angle.	52
Fig. 3.3. In-plane pMEE F and G over true longitude.	53
Fig. 3.4. Semilatus rectum over true longitude.	55
Fig. 3.5. Earth-Mars coplanar orbit transfer. (a) Semilatus rectum and (b) in-plane elements F and G over true longitude.	57
Fig. 3.6. Earth-Mars coplanar orbit transfer. Sail cone angle over true longitude.	58
Fig. 3.7. Shape-based approach (Case study 9). Control history found with (a) shape-based approach - shaped trajectory, and (b) GPOPS-II with NLP solver WORHP.	71
Fig. 3.8. Polar inertial reference frame in the ecliptic plane.	73
Fig. 3.9. Homotopic approach (Test case 1). Control history for coplanar circular-to-circular Earth-Mars orbit transfer ($a_c = 1 \text{ mm/s}^2$). (a) Cone angle evolution during first continuation. (b) Low-thrust and solar-sail cone angle evolution.	85

Fig. 3.10. Homotopic approach (Test case 1). Ecliptic plane view of the transfer trajectories for coplanar circular-to-circular Earth-Mars orbit transfer ($a_c = 1 \text{ mm/s}^2$). (a) Low thrust. (b) Solar sail.	85
Fig. 3.11. Homotopic approach (Test case 1). (a) Zero-path. (b) Evolution of ε	85
Fig. 3.12. Homotopic approach (Test case 2). Coplanar circular-to-circular Earth-Mars orbit transfer ($a_c = 0.1 \text{ mm/s}^2$). (a) Cone angle evolution. (b) Solar-sail transfer trajectory (ecliptic plane view).	87
Fig. 3.13. Homotopic approach (Test case 2). (a) Zero-path. (b) Evolution of ε	87
Fig. 3.14. Homotopic approach (Test cases 3 and 4). Ecliptic plane view of the solar-sail transfer trajectories for rendezvous from Earth to (99942) Apophis. (a) $a_c = 0.6 \text{ mm/s}^2$. (b) $a_c = 0.12 \text{ mm/s}^2$	89
Fig. 3.15. Homotopic approach (Test case 4). Cone angle evolution during the second continuation.	89
Fig. 3.16. Minimum time of flight as a function of the characteristic acceleration for the coplanar Earth-Apophis case.	90
Fig. 4.1. Heliocentric view of the positions of all known NEAs (small blue dots) and PHAs (large red dots) on 24 March 2017. (a) Complete database. (b) PHA-NHATS database. Bodies not to scale.	95
Fig. 4.2. Distribution of all NEAs in the $(Y^2, -r_\oplus/a)$ space. The two curves represent the circular limit and the Earth tangency condition.	97
Fig. 4.3. Schematic of the tree search.	99
Fig. 4.4. Heliocentric view of the transfer trajectory. (a) Test case 1. (b) Test case 2.	102
Fig. 4.5. Graphical view (not to scale) of pruning on longitude of pericentre: ranges of possible variation of longitude of pericentre for two objects (a) overlap; (b) do not overlap.	102
Fig. 4.6. Sequence search flowchart.	105
Fig. 4.7. Number of unique sequences with at least one PHA and four encounters as a function of the launch date. PHA-NHATS database with $a_c = 0.2 \text{ mm/s}^2$ (Test case 1).	110
Fig. 4.8. Tree graph of first three legs of all timed sequences with five encounters found for launch date $t_0 = 30$ April 2025 (Test case 1).	112
Fig. 4.9. Number of unique sequences with at least one PHA and three encounters as a function of the launch date. PHA-NHATS database with $a_c = 0.15 \text{ mm/s}^2$ (Test case 2).	114

Fig. 4.10. Number of unique sequences with at least one PHA and three encounters as a function of the launch date. PHA-NHATS database with $a_c = 0.1 \text{ mm/s}^2$ (Test case 3).	114
Fig. 4.11. Number of unique sequences with at least one PHA and five encounters as a function of the launch date. PHA-NHATS database with $a_c = 0.3 \text{ mm/s}^2$ (Test case 4).	116
Fig. 4.12. Tree graph of the first three legs of all sequences with five encounters found for launch date $t_0 = 26 \text{ May 2020}$ (Test case 4). The number of sequences that share the same branch is shown above each of them.	117
Fig. 4.13. Number of unique sequences with at least one PHA and five encounters for six runs on the sequence search for launch date $t_0 = 28 \text{ May 2020}$ (Test case 4).....	119
Fig. 4.14. Number of unique sequences with at least one PHA and three encounters as a function of the launch date. PHA-LCDB database with $a_c = 0.2 \text{ mm/s}^2$	120
Fig. 5.1. Schematic of the multi-phase problem under consideration.	124
Fig. 5.2. Sequential trajectory optimiser algorithm.....	129
Fig. 5.3. Flowchart of single-phase ATOSS' optimisation strategy for the first stage.	132
Fig. 5.4. Flowchart of both single- and multi-phase ATOSS' optimisation strategy for the second stage.	134
Fig. 5.5. Flowchart of multi-phase ATOSS' optimisation strategy for the first stage.	135
Fig. 5.6. Optimal orbit transfers in the heliocentric ecliptic reference frame. (a) Earth-Venus. (b) Earth-Mars.	137
Fig. 5.7. Trajectory of the first leg from Earth to 2004 GU ₉ . Heliocentric ecliptic reference frame. (a) Ref. [16] (Reproduced with permission of Springer). (b) ATOSS with timed sequence as an input.	140
Fig. 5.8. Heliocentric view of the 3D trajectory of optimised sequence 1: (a) ecliptic plane view; (b) 3D view.	144
Fig. 5.9. Acceleration components history on each transfer leg of optimised sequence 1.	145
Fig. 5.10. Sail slew rate (a) and sail angular acceleration (b) over time on the last leg of optimised sequence 1.	146
Fig. 5.11. Evolution of the total mission duration within ATOSS for optimised sequence 1.	148
Fig. 5.12. Heliocentric view of the complete three-dimensional trajectory of optimised sequence 2 (ecliptic plane view).	150
Fig. 5.13. Heliocentric view of the 3D return leg to the Earth.	151
Fig. 5.14. Heliocentric view of the 3D transfer leg between 2008 EV ₅ and 2011 AG ₅	154
Fig. 5.15. Heliocentric view of the coplanar transfer between 2015 JF ₁₁ and 2017 PDC ($a_c = 0.73 \text{ mm/s}^2$).	157

Fig. 5.16. Heliocentric view of the 3D transfer trajectory to flyby 2017 PDC.	159
Fig. A.1. Schematic of the GA's evolution process.	172
Fig. A.2. Schematic of position and velocity evolution implemented within PSO. The next position of each particle is influenced by the current velocity, the location of its current personal best solution p_{best} , and the location of the current best solution of the swarm g_{best} [235].	174
Fig. A.3. Schematic of trajectory optimisation using the evolutionary neurocontroller implemented within InTrance [117].....	176
Fig. B.1. Computational times needed for the computation of the first leg of the asteroid sequence search considering four different implementations of the shape-based approach.	178

LIST OF TABLES

Table 2.1. Compendium of shape-based approaches proposed in the literature.....	38
Table 3.1. Statistical values of the fits for the pMEE P , F , and G	56
Table 3.2. Earth-Mars coplanar orbit transfer. Statistical values of the fits for the pMEE P , F , and G	58
Table 3.3. Properties of the objects considered for the single-leg rendezvous missions.	69
Table 3.4. Case studies for the single-leg rendezvous missions.	69
Table 3.5. Number of successful cases for each initial guess.	70
Table 3.6. Number of successful cases for each initial guess and NLP solver.	70
Table 3.7. Homotopic approach: numerical test cases.	82
Table 3.8. Homotopic approach: Keplerian elements of the target objects on 14 Feb 2016. The inclination of both objects is assumed equal to zero.	82
Table 3.9. Homotopic approach: homotopy and GA results comparison (Test case 1).....	84
Table 3.10. Homotopic approach: homotopy and GA results comparison (Test case 2).	86
Table 3.11. Optimal solar-sail rendezvous from Earth to (99942) Apophis (in brackets the values from [211]).....	88

Table 4.1. Characteristics of the two reduced databases considered.	95
Table 4.2. Number of Q -permutations of N objects within the complete database and the reduced ones.	98
Table 4.3. PHA-NHATS database: test cases for the sequence search algorithm.....	109
Table 5.1. Properties of all the encounters of the sequence presented in [16].	138
Table 5.2. Mission parameters for the optimal 3-NEA rendezvous (values in brackets are those presented in [16] and used as timed sequence for ATOSS).	140
Table 5.3. Mission parameters for the optimal 3-NEA rendezvous, longer mission (values in brackets are those presented in [16] and used as timed sequence for ATOSS).....	140
Table 5.4. Mission parameters for the optimal 3-NEA rendezvous in the case of a non-timed sequence as an input (values in brackets are those self-generated by ATOSS).	141
Table 5.5. Properties of the encounters of sequence 1.....	142
Table 5.6. Mission parameters for optimised sequence 1 (values in brackets are those found through the sequence search algorithm and used as a first guess for ATOSS).....	143
Table 5.7. Properties of the encounters of sequence 2.....	149
Table 5.8. Mission parameters for optimised sequence 2 (values in brackets are the ones found through the sequence search algorithm and used as an initial guess for STO).	149
Table 5.9. Mission parameters for the optimised sequence 1 with the last leg to the Earth.	152
Table 5.10. Properties of 2011 AG ₅	153
Table 5.11. Mission parameters for optimised sequence 1 with the last leg to 2011 AG ₅	155
Table 5.12. Properties of 2017 PDC.....	156
Table 5.13. Mission parameters for the baseline mission for the 2017 PDC test case.....	156
Table 5.14. Mission parameters for the baseline mission for the 2017 PDC test case with the last leg to 2017 PDC.....	158
Table 5.15. Automated optimisation campaign results.	161
Table B.1. PPSO Test Case 1: Non-default settings.....	180
Table B.2. PPSO Test Case 1: Results.....	180
Table B.3. PPSO Test Case 2: Non-default settings.....	181
Table B.4. PPSO Test Case 2: Results.....	181
Table B.5. PPSO Test Case 3: Results.....	182
Table B.6. PPSO Test Case 4: Non-default settings.....	183
Table B.7. PPSO Test Case 4: Results.....	183
Table B.8. PPSO Test Case 5: Non-default settings.....	184
Table B.9. PPSO Test Case 5: Results.....	184

LIST OF ALGORITHMS

Algorithm 3.1. Shape-based approach for solar sailing. Procedure to generate the shaped trajectory and the control history.....	63
Algorithm 3.2. Shape-based approach for solar sailing. Procedure to generate the shaped trajectory and the control history in the case of an orbit transfer.	67
Algorithm 3.3. Homotopy-continuation approach.	79
Algorithm 4.1. Sequence search algorithm.	106

ACKNOWLEDGEMENTS

This thesis is the result of my four-year work at the University of Glasgow, beyond the Wall. Several people helped and guided me throughout this wonderful experience and I am grateful to all of them.

Firstly, I would like to give my heartfelt thanks to Dr Matteo Ceriotti, my PhD advisor and mentor. He has always been supportive and helpful both inside and outside the academic environment. He is always ready and happy to help and he has been my guide during this whole experience. Even though not officially recognised, he is definitely THE research supervisor of the year 2016.

I would like to acknowledge the Engineering and Physical Sciences Research Council (EPSRC) for funding my PhD study under the James Watt Program and the School of Engineering at the University of Glasgow for hosting me. Specifically, Mrs Elaine McNamara and Ms Heather Lambie have always been kind and willing to help me in all circumstances here at the university.

I would like to thank Prof Bernd Dachwald for the support he gave during my research. His insights were of great help towards the achievement of my research goal and the publication of several journal papers.

I am thankful to Prof Anil Rao, who has been keen to help me since the very first day I decided to use GPOPS-II. Moreover, he kindly hosted me for four months at the Vehicle Dynamics and Optimization Laboratory at the University of Florida as part of his group. Speaking with him is always a pleasure and productive.

I would like to acknowledge the Royal Society of Edinburgh and the University of Glasgow for supporting my period in Florida and giving me such a fantastic opportunity.

Special thanks go to Mr Jan Thimo Grundmann. Since we met in Frascati, he surrounded me with his enthusiasm about solar sailing. He saw the relevance of my work and helped me spreading it among the scientific community. I hope that this thesis will help you advance a little in the solar-sail project you guys are carrying out in the background at DLR.

Thanks to Prof Christian Circi, who introduced me to the solar-sailing world. Without his initial advice, this entire PhD would not have existed.

I feel grateful to the several anonymous reviewers and journal editors who spent their time reviewing my papers. Their feedback and suggestions helped to improve the overall quality of my research.

I would like to thank all my friends from the Space Glasgow group here at the University of Glasgow; Leonel (and Luz), Kim, Abdul, Spencer, Alisha, Chen, Yohei, Callum, Federica, and all the people who have been part of the group even for a few months only. Of course, Prof Colin McInnes, who welcomed me within his group and shared with me several interesting and useful insights. His knowledge and interest in everything related to physics, engineering and, naturally, solar sailing inspire me.

Among all the people I met here, special thanks go to Nicola, colleague, friend, and flatmate. He listens to all my monologues about everything, from my research to my life. Without him, my life here and my research would have definitely been different.

Thanks to my first crew here at the university; Sotos (and Athina), David, Fernando, and Juan. They helped me to start my new life here and, definitely, improve my communication skills in English! Likewise, thanks to my following officemates, with whom I shared the joys (and sufferings) of our PhD life; Aaron, Anggoro, Daniel, Helen, Sean, and Lin Wei.

Thanks to their daily support and patience to my life friends Fabrizio, Stefano and Daniele. I owe you a dram!

Nilay. The love of my life. This thesis is also the result of her love and support. She always believes in me even when I do not and she led me towards this point. I cannot be happier to have her in my life.

Lastly, I am truly grateful to my family for supporting me in all my choices. Especially my mum and dad, who accepted, encouraged and helped this very decision of mine to pursue this PhD here in Glasgow. Thanks to them, I became who I am today.

To my mum and dad,
For their constant love and support.

PUBLICATIONS AND CONFERENCES

The content of this thesis has previously appeared, or will appear, in the following publications and conferences.

JOURNAL ARTICLES

Peloni, A., Ceriotti, M. and Dachwald, B., “Solar-Sail Trajectory Design for a Multiple Near-Earth-Asteroid Rendezvous Mission”, *Journal of Guidance, Control, and Dynamics*, Vol. 39, No. 12, 2016, pp. 2712-2724. DOI: 10.2514/1.G000470.

Sullo, N., **Peloni, A.** and Ceriotti, M., “Low-Thrust to Solar-Sail Trajectories: A Homotopic Approach”, *Journal of Guidance, Control, and Dynamics*, Vol. 40, No. 11, 2017, pp. 2796-2806. DOI: 10.2514/1.G002552.

Peloni, A., Dachwald, B. and Ceriotti, M., “Multiple Near-Earth Asteroid Rendezvous Mission: Solar-Sailing Options”, accepted for publication in *Advances in Space Research*. DOI: 10.1016/j.asr.2017.10.017.

Peloni, A., Rao, A. V. and Ceriotti, M., “Automated Trajectory Optimizer for Solar Sailing (ATOSS)”, *Aerospace Science and Technology*, Vol. 72, 2018, pp. 465-475. DOI: 10.1016/j.ast.2017.11.025.

Grundmann, J. T., Bauer, W., Biele, J., Boden, R. C., Ceriotti, M., Cordero, F., Dachwald, B., Dumont, E., Grimm, C. D., Herčík, D., Ho, T. M., Jahnke, R., Koch, A. D., Koncz, A., Krause, C., Lange, C., Lichtenheldt, R., Maiwald, V., Mikschl, T., Mikulz, E., Montenegro, S., Pelivan, I., **Peloni, A.**, Quantius, D., Reershemius, S., Renger, T., Riemann, J., Ruffer, M., Sasaki, K., Schmitz, N., Seboldt, W., Seefeldt, P., Spietz, P., Spröwitz, T., Sznajder, M., Tardivel, S., Tóth, N., Wejmo, E., Wolff, F., Ziach, C., “Capabilities of GOSSAMER-1 derived Small Spacecraft Solar Sails carrying MASCOT-derived Nanlanders for In-Situ Surveying of NEAs”, accepted for publication in *Acta Astronautica*. DOI: 10.1016/j.actaastro.2018.03.019.

CONFERENCE PROCEEDINGS

Peloni, A., Ceriotti, M. and Dachwald, B., “Preliminary Trajectory Design of a Multiple NEO Rendezvous Mission Through Solar Sailing”, *65th International Astronautical Congress*, IAF Paper IAC-14-C1.9.7, Toronto, Canada, 2014.

Peloni, A., Ceriotti, M. and Dachwald, B., “Solar-Sailing Trajectory Design for Close-up NEA Observations Mission”, *4th IAA Planetary Defense Conference - PDC 2015*, IAA Paper IAA-PDC-15-P-19, Frascati, Italy, 2015.

Sullo, N., **Peloni, A.** and Ceriotti, M., “From Low Thrust to Solar Sailing: A Homotopic Approach”, *26th AAS/AIAA Space Flight Mechanics Meeting*, AAS Paper 16-426, Napa, CA, USA, 2016.

Peloni, A., Wolz, D., Ceriotti, M. and Althöfer, I., “Construction and Verification of a Solution of the 8th Global Trajectory Optimization Competition Problem. Team 13: GlasgowJena+”, *26th AAS/AIAA Space Flight Mechanics Meeting*, AAS Paper 16-425, Napa, CA, USA, 2016.

Grundmann, J. T., Boden, R. C., Ceriotti, M., Dachwald, B., Dumont, E., Grimm, C. D., Lange, C., Lichtenheldt, R., Pelivan, I., **Peloni, A.**, Riemann, J., Spröwitz, T. and Tardivel, S., “Soil to Sail - Asteroid Landers on Near-Term Sailcraft as an Evolution of the GOSSAMER Small Spacecraft Solar Sail Concept for In-Situ Characterization”, *5th IAA Planetary Defense Conference - PDC 2017*, IAA Paper IAA-PDC-17-05-19, Tokyo, Japan, 2017.

Peloni, A., Dachwald, B. and Ceriotti, M., “Multiple NEA Rendezvous Mission: Solar Sailing Options”, *The Fourth International Symposium on Solar Sailing 2017*, Paper 17017, Kyoto, Japan, 2017.

Grundmann, J. T., Bauer, W., Biele, J., Boden, R. C., Ceriotti, M., Cordero, F., Dachwald, B., Dumont, E., Grimm, C. D., Herčík, D., Ho, T. M., Jahnke, R., Koch, A. D., Koncz, A., Lichtenheldt, R., Maiwald, V., Mikschl, T., Mikulz, E., Montenegro, S., Pelivan, I., **Peloni, A.**, Quantius, D., Reershemius, S., Renger, T., Riemann, J., Ruffer, M., Schmitz, N., Seboldt, W., Seefeldt, P., Spietz, P., Spröwitz, T., Sznajder, M., Tardivel, S., Tóth, N., Wejmo, E., Wolff, F., Ziach, C., “Small Spacecraft Solar Sailing for Small Solar System Body Multiple Rendezvous and Landing”, accepted for 2018 IEEE Aerospace Conference, IEEE Paper 2360, Big Sky, MT, USA, 2018.

CONFERENCE AND WORKSHOP PRESENTATIONS

Peloni, A. and Ceriotti, M., “Solar Sailing Multiple NEO Rendezvous Mission: Preliminary Results”, *First Stardust Global Virtual Workshop (SGVW-1) on Asteroids and Space Debris*, Glasgow, Scotland, UK, 2014. Presentation available online at <https://www.youtube.com/watch?v=j-uxCvo09Hc> [retrieved 06 June 2017].

Peloni, A., “Solar Sailing: How to Travel on a Light Beam”, *1st Space Glasgow Research Conference*, Glasgow, Scotland, UK, 2014. Presentation available online at https://www.gla.ac.uk/media/media_375002_en.pptx [retrieved 10 October 2017].

Peloni, A., Rao, A. V. and Ceriotti, M., “ATOSS: Automated Trajectory Optimiser for Solar Sailing”, *Fourth European Optimisation in Space Engineering (OSE) Workshop*, Bremen, Germany, 2017.

AUTHOR'S DECLARATION

I hereby declare that this submission is my own work and that, to the best of my knowledge and belief, it contains no material previously published or written by another person nor material which to a substantial extent has been accepted for the award of any other degree or diploma of the university or other institute of higher learning, except where due acknowledgment has been made in the text.

Glasgow, Scotland, United Kingdom

06 March 2018

A handwritten signature in blue ink, appearing to read "Alessandro Peloni", is written over a horizontal line.

Alessandro Peloni

NOMENCLATURE

The author attempted to use standard symbols and acronyms in use in Astrodynamics and Optimisation, giving alternatives wherever appropriate, and tried to be consistent throughout the document. Some symbols have duplicate meanings but the appropriate one should be clear from the context. The following notation will be used throughout the document. All scalar quantities will be represented by non-bold italic symbols. All vectors will be treated as column vectors and represented by bold italic symbols. Lastly, all matrices will be denoted by uppercase non-italic bold symbols.

Acronyms

3D	= Three Dimensional
ACO	= Ant Colony Optimisation
AMR	= Area-to-Mass Ratio
ANN	= Artificial Neural Network
ARRM	= Asteroid Redirect Robotic Mission
ARS	= Adjusted R-Square
ATOSS	= Automated Trajectory Optimiser for Solar Sailing
AU	= Astronomical Unit, 149,597,870.691 km
BFS	= Breadth-First Search
BS	= Beam Search
CNEOS	= Center for Near Earth Object Studies
CR3BP	= Circular Restricted Three-Body Problem
DFS	= Depth-First Search
DLR	= Deutsches zentrum für Luft und Raumfahrt e.V. (German Aerospace Centre)
EMOID	= Earth Minimum Orbit Intersection Distance, AU
ESA	= European Space Agency

EXP-TRIG	= Exponential Trigonometric
FB	= Flyby
FFS	= Finite Fourier Series
GA	= Genetic Algorithm
GO	= Global Optimisation
GTOC	= Global Trajectory Optimisation Competition
IAA	= International Academy of Astronautics
JPL	= Jet Propulsion Laboratory
KEP	= Keplerian elements
KKT	= Karush-Kuhn-Tucker
LCDB	= Lightcurve Database
LG	= Legendre-Gauss
LGL	= Legendre-Gauss-Lobatto
LGR	= Legendre-Gauss-Radau
LIN-TRIG	= Linear Trigonometric
LO	= Local Optimisation
LT	= Low Thrust
MEE	= Modified Equinoctial Elements
MTSP	= Motorised Travel Salesman Problem
NASA	= National Aeronautics and Space Administration
NC	= Neurocontroller
NEA	= Near-Earth Asteroid
NHATS	= Near-Earth object Human space flight Accessible Target Study
NLP	= Nonlinear Programming
OCC	= Orbit Condition Code
OCP	= Optimal Control Problem
ODE	= Ordinary Differential Equation
OT	= Orbit Transfer
PHA	= Potentially-Hazardous Asteroid
pMEE	= Pseudo Modified Equinoctial Elements
PDC	= Planetary Defense Conference
PSO	= Particle Swarm Optimisation
RV	= Rendezvous
SB	= Shape-Based
SI	= International System of Units

SRP	= Solar Radiation Pressure
SSE	= Sum of Squares due to Error
STO	= Sequential Trajectory Optimiser
TPBVP	= Two-Point Boundary Value Problem
TRL	= Technology Readiness Level
TSP	= Travel Salesman Problem

Symbols

$\mathbf{A}(\mathbf{x})$	= Matrix of the dynamics
A	= Sail area, m^2
$\tilde{A}, \tilde{B}, \tilde{C}, \tilde{D}$	= Multiplication factors of the Hamiltonian expansion
\mathbf{a}	= Acceleration vector, mm/s^2
a_r	= Radial component of the acceleration, mm/s^2
a_t	= Transversal component of the acceleration, mm/s^2
a	= Semimajor axis, AU
a_c	= Solar-sail characteristic acceleration, mm/s^2
a_h	= Out-of-plane magnitude of the acceleration, mm/s^2
a_{max}	= Maximum low-thrust acceleration, mm/s^2
a_{0P}, b_0	= Out-of-plane shaping parameters for the exponential sinusoid approach
$\tilde{a}, \tilde{b}, \tilde{c}, \tilde{d}, \tilde{e}, \tilde{f}, \tilde{g}$	= Shaping parameters for the inverse polynomial shape
\mathbf{B}	= Magnetic field vector, T
$\mathbf{b}(\mathbf{x})$	= Vector of the dynamics
b	= Identifier of a body
\mathbf{c}	= Vector of the path constraints
c	= Speed of light in vacuum, $2.99792 \times 10^8 \text{ m/s}$
c_i, c_c, c_s	= Inertial, cognitive and social weights
D_{ij}	= Differentiation matrix
\mathbf{E}	= Electric field vector, N/C
e	= Eccentricity

F, G	= Pseudo modified equinoctial elements corresponding to f and g
f	= Equations of the dynamics
\mathbf{f}_{SRP}	= Force acting on the sail due to the SRP, N
$\mathbf{f}_{SRP,i}$	= Force acting on the sail due to the incident radiation, N
$\mathbf{f}_{SRP,r}$	= Force acting on the sail due to the reflected radiation, N
f	= Generic continuous function
f, g	= In-plane modified equinoctial elements
\mathbf{G}	= Momentum vector ($\mathbf{G} \triangleq \ \mathbf{G}\ $), kgm/s
$\mathbf{g}(\mathbf{x})$	= Algebraic constraints
$\mathbf{g}_{best}^{(k)}$	= Best position vector of the entire swarm of iteration step k
g	= Integral cost function
g_0	= Standard sea level acceleration due to gravity, 9.80665 m/s ²
\mathcal{H}	= Hamiltonian
$\tilde{\mathcal{H}}$	= Reduced Hamiltonian
H, K	= Pseudo modified equinoctial elements corresponding to h and k
\hat{h}	= Orbital angular momentum unit vector
h, k	= Out-of-plane modified equinoctial elements
\hbar	= Reduced Planck's constant, 1.05457×10^{-34} Js
K	= Number of mesh intervals
K_{max}	= Maximum number of iteration steps
k_0, k_1, k_2, φ	= In-plane shaping parameters for the exponential sinusoid approach
I	= Poynting vector, W/m ²
I_{sp}	= Specific impulse, s
i	= Inclination, deg
J	= Objective (cost) function
j	= Phase number
\mathcal{L}	= Luminosity, W
\mathcal{L}_\odot	= Luminosity of the Sun, 3.8×10^{26} W
L	= True longitude, rad
L_b	= List of available bodies in the database

$L_{b,i}$	= List of bodies already encountered
L_{compl}	= List of complete sequences
L_{part}	= List of partial sequences
L_{tmp}	= List of temporary sequences
\hat{L}_f	= Lower boundary on L_f , rad
ℓ_j	= Lagrange interpolating polynomial at j-th collocation point
m	= Number of nonlinear equations of the shooting function
m_0	= Total spacecraft mass, kg
m_1	= Number of inequality constraints
m_{dry}	= Spacecraft dry mass, kg
m_{rest}	= Mass at rest, kg
$\hat{\mathbf{N}}$	= Acceleration unit vector, $[N_r \ N_g \ N_h]^T$
N	= Number of objects in the database
N	= Number of collocation points (CHAPTER 2)
N_k	= Number of collocation points at k-th mesh interval
N_{\max}^{seq}	= Maximum number of partial sequences to be used in the following leg within the sequence search algorithm
n	= Number of optimisation variables
n_{rev}	= Number of complete revolutions
n_r, n_g	= Number of Fourier terms in the FFS approach
\mathcal{P}	= Value of the Palermo scale
P	= Pseudo modified equinoctial element corresponding to p
P	= Solar radiation pressure, $\mu\text{N}/\text{m}^2$ (CHAPTER 2)
$P_N(\tau)$	= N -th degree Legendre polynomial
P_Q^N	= Number of Q -permutations of N elements
P_\oplus	= Solar radiation pressure at Earth distance, $4.56 \ \mu\text{N}/\text{m}^2$
\mathbf{p}	= Vector of static parameters
$\mathbf{p}_{best}^{(k)}(i)$	= Best position vector of particle i at iteration step k
p	= Semilatus rectum, AU

Q	= Number of distinct elements to be considered for the computation of the permutation
q, s^2, γ	= Auxiliary variables
r	= Cartesian position vector ($r \triangleq \ r\ $), AU
\hat{r}	= Position unit vector
$r^{(k)}(i)$	= Position vector of particle i at iteration step k
r_{\oplus}	= Mean Sun-Earth distance, 1 AU
r_a	= Radius of the apocentre, AU
r_p	= Radius of the pericentre, AU
$r(0,1)$	= Random number between 0 and 1
s_i	= Partial sequence
T	= Pseudo element corresponding to t
T	= Effective temperature, K (CHAPTER 2)
T_{0f}	= Time of flight, s
T_{\oplus}	= Tisserand parameter related to Earth
t	= Time, s
t_0	= Launch date
\tilde{t}_0	= Selected launch date
t_{stay}	= Stay time at the object, s
U_i	= Discretised control vector at i-th collocation point
\mathcal{U}	= Set of feasible controls
U	= Quality code
u	= Control vector
\hat{u}_i	= Direction of the incident radiation
\hat{u}_r	= Direction of the reflected radiation
u	= Radial velocity, km/s
\bar{u}	= Low-thrust non-dimensional control
v	= Velocity vector
$v^{(k)}(i)$	= Velocity vector of particle i at iteration step k
v	= Transversal velocity, km/s

W	= Energy flux emitted by a star, W/m^2
W_{\odot}	= Energy flux emitted by the Sun, $1,368 \text{ W/m}^2$
W_1, W_2	= Weighting factors
w_i	= Gauss quadrature weight
X	= Discretised state
x	= State vector
\boldsymbol{x}	= Vector of optimisation parameters
\mathbf{y}	= Set of free parameters, $\{\lambda_p, \lambda_{fg}, \varphi_p, \varphi_{fg}\}$
\mathbf{z}	= Vector of the optimisation variables in the homotopic approach
α	= Sail cone angle, deg
$\tilde{\alpha}$	= Desired sail cone angle, deg
$\tilde{\alpha}^*$	= Desired optimal sail cone angle, deg
β	= Sail lightness number
Γ	= Shooting function
γ	= Direction of vernal equinox (first point of Aries)
Δa	= Semimajor axis variation, AU
ΔE	= Quantity of energy transferred, J
Δp	= Momentum transported by a flux of photons, kgm/s
Δt	= Time interval, s
Δt_f	= Value used to decrease the lower boundary on the final time, days
Δv	= Velocity increment, km/s
δ	= Sail clock angle, deg
δr	= Position error of the spacecraft with respect to the target
δv	= Velocity error of the spacecraft with respect to the target
$\delta \epsilon$	= Step size for the numerical continuation
$\delta \omega$	= Longitude of pericentre variation, rad
\mathcal{E}	= Energy, J
ε	= Homotopic parameter
ζ	= Angle between two consecutive sail attitudes, deg
η	= Efficiency coefficient
$\hat{\mathbf{g}}$	= In-plane transversal unit vector
ϑ	= Spacecraft angular position in polar coordinates, deg

θ	= Angle between angular momenta of two orbits, deg
κ	= Sail loading, g/m^2
$\tilde{\kappa}$	= Critical sail loading, $1.53 \text{ g}/\text{m}^2$
λ	= Costate vector
$\lambda_1, \lambda_2, \lambda_3$	= Shaping parameters for the linear-trigonometric and exponential shapes
λ_{fg}	= Shaping parameter related to the in-plane modified equinoctial elements
λ_{max}	= Wavelength of peak emission, μm
λ_p	= Shaping parameter related to the semilatus rectum, AU
μ	= Vector of the Lagrange multipliers associated with the path constraints
μ	= Gravitational parameter of the Sun, $1.3271 \times 10^{11} \text{ km}^3/\text{s}^2$
$\tilde{\mu}$	= Permeability of the medium, N/A^2
ν	= Vector of the Lagrange multipliers associated with the boundary constraints
ν	= True anomaly, rad
σ	= Stefan-Boltzmann constant, $5.670373 \times 10^{-8} \text{ W}/\text{m}^2\text{K}^4$
τ	= Transformed time
τ_{max}	= Maximum allowed torque, Nm
Υ	= Parameter related to the unperturbed relative velocity of an object with respect to the Earth
Φ	= Scaled value of the gauge term of the velocity
φ_{fg}	= Phasing parameter related to the in-plane modified equinoctial elements, rad
φ_p	= Phasing parameter related to the semilatus rectum, rad
ϕ	= Terminal cost function
χ	= Parameter dependent on the cone angle
ψ	= Vector of boundary conditions
Ω	= Right ascension of the ascending node, rad
ω	= Argument of pericentre, rad

ω	= Photon angular frequency, rad/s (CHAPTER 2)
ϖ	= Longitude of pericentre, rad

Subscripts

0	= Initial value
1	= First homotopic transformation
2	= Second homotopic transformation
b_0	= Departing body
b_f	= Arriving body
F	= Value dependent on the boundary conditions at the final time
f	= Final value
$gauge$	= Gauge term of the velocity
I	= Value dependent on the boundary conditions at the initial time
LT	= Low thrust
$LTSS$	= Low-thrust to solar-sail homotopic transformation
\max	= Maximum
\min	= Minimum
osc	= Osculating term of the velocity
pSS	= Pseudo solar sail
SS	= Solar sail
tmp	= Temporary value

Superscripts

(\square)	= Mesh number
FB	= Flyby
j	= Phase
kep	= Keplerian elements
mee	= Modified equinoctial elements
m	= Number of constraints
n	= Number of optimisation parameters
OT	= Orbit transfer
pol	= Polar coordinates

RV	= Rendezvous
T	= Transpose
$*$	= Optimal value

Operators and other Notations

$[\square]$	= Matrix
$\{\square\}$	= List of elements
$\ \square\ $	= Euclidean L^2 norm
$\dot{\square}$	= First derivative with respect to time
$\ddot{\square}$	= Second derivative with respect to time
\square'	= First derivative with respect to true longitude
$\bar{\square}$	= Value related to the target object
$\hat{\square}$	= Unit vector
$d\square$	= Total derivative
$\partial\square$	= Partial derivative
$\nabla\square$	= Gradient
$\text{argmin}(\square)$	= Point within the domain in which the function is minimised
$\ln(\square)$	= Natural logarithm
$\text{mod}(\square, \square)$	= Remainder after division (modulo operator)
$\mathcal{O}(\square)$	= Order of magnitude
\times	= Cross product
\cdot	= Scalar product
\triangleq	= Equal by definition
\emptyset	= Empty set
\mathbb{R}	= Set of Real numbers

CHAPTER 1.

INTRODUCTION

1.1. Solar-Sail Mission Design for Multiple NEA Rendezvous: An Overview

The definition of an interplanetary trajectory is a core element of a space mission design, such as a multiple near-Earth asteroid (NEA) rendezvous mission. This shall take into consideration the mission goals, the propulsion system of the spacecraft, the amount of time available for the overall mission, the cost of the mission itself. From a flight dynamics point of view, the cost of a trajectory can be estimated through the total amount of Δv needed, i.e. the amount of impulse that is needed to perform all the necessary manoeuvres. Due to the long journey and the usually high Δv required, interplanetary missions are well suited to be carried out by means of electric propulsion. This system, in fact, enables the spacecraft to have a small, but continuous and highly efficient thrust for a long time [1]. Nonetheless, the total Δv is limited by the maximum amount of propellant that can be carried on. Because of the amount of thrust generated, electric propulsion is commonly referred to as a low-thrust propulsion system.

As opposite to the aforementioned low-thrust system (which will be referred to as *classical low-thrust*, in the remainder of this thesis), a solar sail is a large, lightweight and highly reflective membrane, deployed from the spacecraft, which propels it by reflecting the solar photons [2]. Therefore, a solar sail is an attractive solution for high- Δv missions, because it does not need any propellant and the thrust is theoretically provided for an extended amount of time. Due to the small acceleration produced, solar sailing also falls into the low-thrust category.

Nevertheless, intrinsic differences in the available thrust distinguish a solar sail from a classical low-thrust system, as it will be shown in detail in Section 2.1. To date, several studies have been carried out to demonstrate the potential of solar-sailing propulsion. However, the technology readiness level (TRL) of this kind of propulsion system still needs to be increased. For this reason, the purpose of the DLR/ESA Gossamer roadmap to solar sailing was to bring the solar-sail TRL to a “flight qualified” level¹ [3].

Great effort has been dedicated to the study of NEAs because of their importance for scientific, technological, and planetary-defence reasons. Regarding the last, several NEAs pose a potential threat to our planet and are indeed classified as potentially hazardous asteroids (PHAs). A multiple NEA rendezvous with close-up observations of several objects can help the scientific community to improve the knowledge about the diversity of these objects and to support any future mitigation act. In fact, most of the information available to date are retrieved by means of Earth-based observations. Furthermore, a multiple-target mission is preferable to a single-rendezvous mission because of the reduced cost of each observation and the intrinsic lack of knowledge that makes the choice of a single asteroid difficult. Planning of such a mission, however, is challenging because of the large number of asteroids and the huge number of different ordered sequences of NEAs that can be chosen to visit. This is a combinatorial problem first, with more than a trillion of possible sequences with only three consecutive encounters, considering a database with more than 12,000 objects². Moreover, for both solar sail and classical low-thrust propulsion, space trajectories shall be optimised according to one or more objectives, such as mission time or Δv , and constraints, such as initial/final state or thrust constraints [4]. Because no closed-form solutions exist for the low-thrust optimisation problem, an optimal control problem (OCP) must be solved numerically for each leg of the multiple rendezvous to test the feasibility of the proposed sequence with the propulsion system used. Specifically, minimum-time solar-sail transfers are sought in this study.

¹ Data available online at <http://sci.esa.int/sci-ft/50124-technology-readiness-level/> [retrieved 11 September 2017].

² Data available online at <https://cneos.jpl.nasa.gov/orbits/elements.html> [retrieved 08 August 2015].

Currently, there are several optimisation techniques available and these can be grouped into three main categories [5, 6]: direct, indirect, and metaheuristic methods. A direct method involves the transcription of the OCP into a discrete nonlinear programming (NLP) problem, which can be solved by a parametric optimisation, once an initial-guess solution is given [7]. Usually, direct methods have a large radius of convergence, i.e. they are robust to inaccurate initial-guess solutions. On the other hand, indirect methods are usually more precise than direct methods, but their radius of convergence is generally smaller, so that it is harder to find an optimal solution if the initial guess is not good enough. Lastly, metaheuristic optimisation methods do not usually need any initial guess. In fact, they usually start with an initial random population that evolves towards the optimum by following a defined set of heuristic rules, which are generally inspired by the nature. The random initialisation of the population gives a statistical confidence about the optimality of the solution found. However, there is no mathematical guarantee of the optimality of a single solution. In addition to the three aforementioned categories, semi-analytical methods, specific to the trajectory optimisation problem, produce sub-optimal solutions and thus are commonly used in the preliminary trajectory design. These are based on designing the shape of the trajectory and retrieving the control needed *a posteriori*, without any optimisation needed [8]. These methods are very fast, although there is no proof of optimality and the shape of the trajectory shall be changed until the control needed is the one that can be achieved with the available propulsion system. Due to the advantage of providing results quickly, these can be used to generate an initial guess for a more precise optimisation technique, which can guarantee the optimality of the solution, if any [9].

To date, solar-sail trajectory optimisation has been mostly carried out through indirect optimisation techniques [10-12]. However, a direct approach can be helpful in a preliminary mission design phase, because of its larger radius of convergence with respect to an indirect method. Moreover, multi-body missions (such as multiple NEA rendezvous) require the problem to be divided into several phases, each one of which is characterised by different boundaries (i.e. a multi-phase problem). In general, in a multi-phase problem, each phase can also be described by different dynamics (e.g. for interplanetary and close-approach phases) or control (e.g. hybrid propulsion system). This can be set up with little effort if a direct optimisation technique is used. On the contrary, a different

mathematical model shall be studied for each phase of the problem in the indirect method case. As previously stated, the drawback of the direct approach is the need of an initial guess. For this reason, a quick and reliable approximation of the trajectory, which can be used as an initial-guess solution for a direct optimisation method, can be obtained by means of a semi-analytical shape-based approach.

Several shape-based approaches have been developed to date but all of them deal with classical low-thrust propelled spacecraft [8, 9, 13, 14]. A solar-sail trajectory is different from a classical low-thrust one because the magnitude and direction of the thrust given by a solar sail are strongly related. As an example, a solar sail in a Sun-centred trajectory cannot give a thrust only along the tangential direction, as this would imply that no part of the sail is actually facing the Sun (see Section 2.1.2 for a more detailed explanation). Nevertheless, most of the studies on the shape-based approach assume a full-tangential thrust. For this reason, a novel shape-based approach shall be developed, considering the constraints on the available solar-sail thrust [15].

1.2. Objectives

As discussed in Section 1.1, the worldwide scientific community is currently investing resources in NEA studies. In fact, a number of missions to NEAs have been already designed. Nevertheless, a multiple NEA rendezvous mission can help the scientific community improving knowledge about these objects. A multiple-target mission is more desirable than a single-rendezvous mission is, because of the reduced cost of the single observation and the more extensive science return. Moreover, within a multiple-target mission, it might be possible to change the targets in due course, if there is enough Δv available. This can be useful if new interesting objects are discovered after launch. However, the large amount of possible sequences of objects that can be chosen to visit makes the optimal planning of such a mission very challenging. Moreover, a trajectory-optimisation problem must be numerically solved to obtain feasible trajectories with the chosen propulsion system. Regarding the propulsion system, a solar sail is more desirable than a classical low-thrust spacecraft because it does not need any propellant. In fact, a multiple rendezvous mission is, in principle, characterised by higher Δv requirements than a single-target mission is. Moreover, a change in

the targets after launch can be, in principle, unfeasible by a classical low thrust because of the limited amount of propellant available.

For the reasons above, the principal objective of this thesis is to develop a tool for the preliminary trajectory design of multiple NEA rendezvous missions through solar sailing. This will guarantee a step further in the DLR/ESA Gossamer roadmap to solar sailing [16]. In fact, such tool will give an estimate of the potential missions feasible with the chosen solar-sail technology. Among those missions, the most promising ones (in terms of mission duration, solar-sail performance, launch date, etc.) can be chosen to be further studied.

In order to pursue the main goal of this thesis, a number of secondary objectives are set. These are:

- 1) An algorithm must be developed to find potential sequences of objects to visit. Such algorithm shall produce a number of preliminary sequences to be further studied.
- 2) The optimisation of all single NEA-to-NEA transfer trajectory would require an impractical amount of computational time. Therefore, a model should be developed to have a reliable and fast approximation of the trajectory produced by a solar sail. The shape-based approach is a good candidate to achieve this goal. However, all the SB approaches proposed in the literature have been derived for classical low-thrust propulsion systems and most of them are developed in a tangential-thrust approximation (Section 2.2.4). For this reason, a novel shape-based approach should be studied specifically for the solar-sail case.
- 3) An optimisation strategy should be developed to test the feasibility (within the approximations considered) of the sequences found. Because this thesis deals with preliminary trajectory design, it is expected that many potential sequences of NEA encounters will be found. Therefore, an optimiser that can deal with several OCPs in an automatic way is preferable.
- 4) Considering the current DLR/ESA technology for solar sailing as a reference [16], a solar sail with lower performances shall be considered. As it will be shown in detail in Section 2.1, a lower performance is obtained for either a smaller sail or a heavier spacecraft. Obtaining a large area-to-mass ratio (AMR) is one of the key challenges towards the development of solar-sailing technology [17, 18]. That is, finding multiple

NEA rendezvous missions feasible by a solar sail with lower performances does indeed increase the TRL related to solar sailing.

1.3. Outline

The structure of this thesis follows the secondary objectives 1) - 3) outlined in Section 1.2. Each one of those is discussed and analysed in a different chapter, thus building the solar-sail mission design for multiple NEA rendezvous from the ground up.

CHAPTER 2 gives an overview of the building blocks needed for the mission design of multiple NEA rendezvous. A literature review on solar sailing, space-trajectory optimisation techniques and near-Earth asteroids is provided. Specifically, the methods that will be used throughout this thesis to solve the low-thrust OCP are described starting from their mathematical foundations.

CHAPTER 3 deals with the preliminary design of solar-sail trajectories, which is of crucial importance for both the search for sequences of target objects and the subsequent optimisation phase. Two different methods are developed for having a fast and reliable description of solar-sail trajectories. The first method is a shape-based approach, which has been developed specifically for solar sailing. The second method investigates the homotopy theory for generating solar-sail trajectories starting from classical low-thrust ones. Advantages and drawbacks of both methods are discussed which make the two methods complementary depending on the purpose.

CHAPTER 4 shows the algorithm implemented for the asteroid sequence search. First, the database of asteroids used is described and classifications are discussed which allow considering a reduced number of objects. The algorithm, which exploits the tree-like nature of the search space, is described in each of its building blocks. A local pruning of all the possible objects to visit, based on astrodynamics, is firstly performed to reduce the search space and thus decrease the computational effort needed by the algorithm. Subsequently, the shape-based approach for solar sailing is used to test the feasibility of the trajectory. Numerical test cases show that a significant number of sequences of NEAs exists for a wide range of launch dates, considering near-term solar-sail technology.

CHAPTER 5 describes the last step in the mission design, i.e. the optimisation. A direct-optimisation method is considered, which has been mainly chosen to guarantee versatility and robustness. Moreover, the preliminary trajectories found by means of the methods described in CHAPTER 3 are used as initial-guess solutions to initialise the direct-optimisation method. Several numerical test cases assess the performances of the developed approach. Moreover, an automated optimisation campaign demonstrates both the ability of the optimisation approach to find solutions in an automated way and the reliability of the sequences found by means of the asteroid sequence search.

Lastly, CHAPTER 6 concludes this thesis and provides a summary of the findings. Furthermore, the current limitations of the presented work are discussed and proposed directions for future research are examined.

A detailed description of the metaheuristic optimisation methods and some implementation details are provided in the appendix.

CHAPTER 2.

SURVEY OF THEORY AND METHODS

This chapter provides a review of the literature needed to study the problem of preliminary trajectory design for multiple near-Earth asteroid rendezvous missions. The chapter starts with a brief introduction to the physics behind solar sailing and the challenges and advantages of this propulsion system. A survey about space trajectory optimisation follows which gives an overview of the main analytical and numerical optimisation tools used in the literature. Afterwards, the importance of near-Earth asteroids is outlined.

2.1. Solar Sailing from the Ground Up

2.1.1. Solar Radiation Pressure: From Maxwell to Einstein

The Sun radiates energy in the entire electromagnetic spectrum, with a peak of emission in the visible spectrum at a wavelength $\lambda_{max} = 0.5 \mu\text{m}$ [19, 20]. The possibility to exploit such radiation to propel an object was theorised by German astronomer Friedrich Johannes Kepler (1571-1630) by simply observing the position of a comet's tail [2]. “Kepler observed in 1619 that a comet's tail faces away from the Sun, and concluded that the cause was outward pressure due to sunlight - a force that might be harnessed with appropriately designed sails” [21]. Figure 2.1 shows the montage of the Halley's Comet approaching the Sun in 1910. It is worth noting the comet's tail facing always away from the Sun.

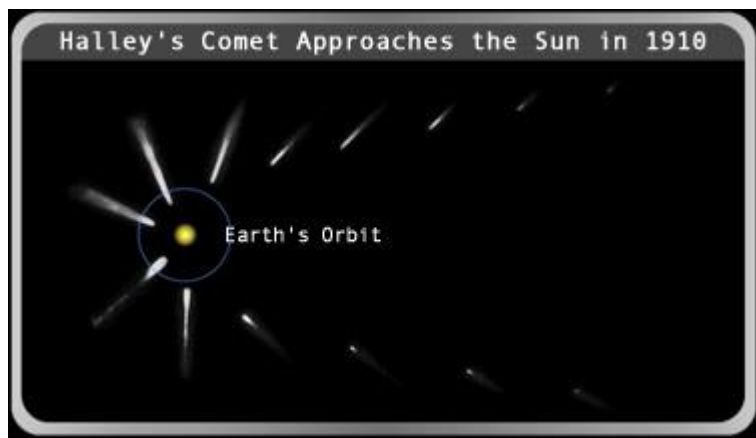


Fig. 2.1. Montage of the Halley's Comet approaching the Sun in 1910¹.

A long time after Kepler, the idea of using the solar radiation as a propulsive force was recovered by Soviet scientists Konstantin Tsiolkowsky (1857-1935) and Friedrich Tsander (1887-1933), who hypothesised a possible exploitation of the solar radiation pressure (SRP) to propel a spacecraft, other than to generate energy [2]. It is important to clarify that the solar propulsion, as intended throughout this document, is referred exclusively to the propulsion due to the solar radiation pressure. Other spacecraft concepts have been proposed in the literature which exploit the solar wind [22, 23], which is a stream of charged particles that move away from the solar corona [19, 20]. However, the dynamic pressure at Earth distance from the Sun due to the solar wind is $\sim 10^3$ times smaller than the SRP [24]. Therefore, the effect of the solar wind can be neglected if compared to that of the SRP.

Either a quantum or an electromagnetic approach can be used to study the physics of the solar radiation [2]. In the following subsections, a brief description of both approaches is given to demonstrate that the light from the Sun exerts pressure on a body in space. As such, the value of the solar radiation pressure P at the Earth distance from the Sun is analytically retrieved.

¹ Image credits: Science Education Gateway (SEGway) at UC Berkley. Image available online at http://cse.ssl.berkeley.edu/SegwayEd/lessons/cometstale/images/halleys_montage.jpg [retrieved 07 July 2017].

Quantum approach. According to quantum and relativistic mechanics, the solar electromagnetic radiation can be considered as a flux of energetic elementary particles, called photons. The energy \mathcal{E} of a photon with angular frequency ω is given by the Planck formula [25]

$$\mathcal{E} = \hbar\omega \quad (2.1)$$

in which $\hbar = 1.05457 \times 10^{-34} \text{ Js}$ is the reduced Planck's constant. Moreover, from the mass-energy equivalence given by the special relativity, the energy of a moving body is given by

$$\mathcal{E}^2 = m_{\text{rest}}^2 c^2 + G^2 c^2 \quad (2.2)$$

in which m_{rest} is the mass at rest of the body, G is its momentum and c is the speed of light in vacuum. Since a photon is massless, Eq. (2.2) can be rewritten as

$$\mathcal{E} = Gc \quad (2.3)$$

From Eqs. (2.1) and (2.3), the expression for the characteristic momentum of a photon is obtained as

$$G = \frac{\hbar\omega}{c} \quad (2.4)$$

In order to compute the SRP, however, the momentum of a flux of photons must be considered. The Stefan law correlates the luminosity \mathcal{L} of a star at the distance r from the observer with its effective temperature T and, therefore, with the energy flux W emitted by the star, as [19, 20]

$$\mathcal{L} = 4\pi r^2 \sigma T^4 = 4\pi r^2 W \quad (2.5)$$

in which $\sigma = 5.670373 \times 10^{-8} \text{ W/m}^2\text{K}^4$ is the Stefan-Boltzmann constant. In the case of the Sun, Eq. (2.5) gives the value of the energy flux W_{\oplus} that reaches the Earth, as

$$W_{\oplus} = \frac{\mathcal{L}_{\odot}}{4\pi r_{\oplus}^2} = 1,368 \text{ W/m}^2 \quad (2.6)$$

in which $\mathcal{L}_\odot = 3.8 \times 10^{26} \text{ W}$ is the luminosity of the Sun [19, 20] and $r_\oplus = 1 \text{ AU}$ is the mean Sun-Earth distance. Therefore, the energy flux at the distance r from the Sun is

$$W = W_\oplus \left(\frac{r_\oplus}{r} \right)^2 \quad (2.7)$$

By definition, the energy flux is the quantity of energy $\Delta\mathcal{E}$ transferred through a surface A in the time interval Δt :

$$W = \frac{\Delta\mathcal{E}}{A\Delta t} \quad (2.8)$$

From Eqs. (2.3) and (2.8), the momentum ΔG transported by a flux of photons is

$$\Delta G = \frac{\Delta\mathcal{E}}{c} = \frac{WA\Delta t}{c} \quad (2.9)$$

Dividing Eq. (2.9) by the time interval Δt and computing the limit, the Newton equation is retrieved, as

$$\lim_{\Delta t \rightarrow 0} \frac{\Delta G}{\Delta t} = \frac{dG}{dt} = \frac{WA}{c} \quad (2.10)$$

From Eqs. (2.6) and (2.10), the SRP that an object at 1 AU from the Sun experiences is then retrieved as

$$P_\oplus = \frac{W_\oplus}{c} = 4.56 \mu\text{N/m}^2 \quad (2.11)$$

From Eqs. (2.7) and (2.11), the pressure P due to the solar radiation that an object at the distance r from the Sun experiences is

$$P = P_\oplus \left(\frac{r_\oplus}{r} \right)^2 \quad (2.12)$$

Electromagnetic approach. An electromagnetic wave is characterised by its velocity \mathbf{v} and its directional energy flux. The latter is represented by the

Poynting vector $I = \frac{\mathbf{E} \times \mathbf{B}}{\tilde{\mu}}$, in which $\tilde{\mu}$ is the permeability of the medium the wave

is propagating into, whereas \mathbf{E} and \mathbf{B} are the electric and magnetic field vectors, respectively [26, 27]. The pressure P exerted by an electromagnetic wave is

$$P = \frac{I}{v} \quad (2.13)$$

In the case of the solar radiation, the magnitude of the Poynting vector at Earth's distance from the Sun is $I_{\oplus} = W_{\oplus}$. Moreover, the absolute value of the velocity of light in space is c . Therefore, the absolute value of the momentum vector has the same expression shown in Eq. (2.9). The value of the SRP is therefore retrieved following the same procedure described in the previous subsection for the quantum approach. "Hence in a medium in which waves are propagated there is a pressure in the direction normal to the waves, and numerically equal to the energy in unit of volume" [28]. Note that the direction normal to the waves is the direction along which the waves are propagated.

2.1.2. Acceleration Model

Section 2.1.1 demonstrated the existence of a solar radiation pressure that can be used to propel a spacecraft. Because of the small pressure due to sunlight [Eq. (2.11)], such spacecraft must have a large reflecting surface, relative to its mass, which will be referred to as sail throughout this thesis, to generate a large thrusting force. However, in order to have the expression of the propulsive acceleration that can be achieved by such sailcraft, some approximations shall be considered which are related to the geometrical and the optical properties of the sail. First, the sail is considered perfectly flat. That is, no wrinkles and deformations due, for instance, to the tensioning of the membrane are considered. Furthermore, a perfectly-reflecting sail membrane is considered, as shown in Fig. 2.2. Other acceleration models are considered in the literature, such as the optical acceleration model, in which the non-perfect reflectivity of the sail membrane is explicitly modelled [2, 10, 29].

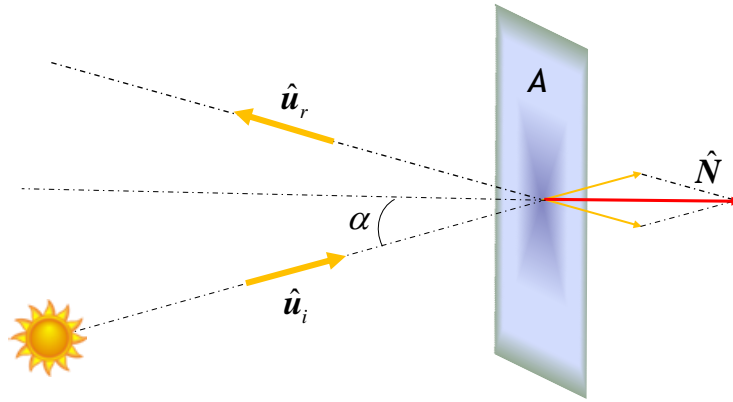


Fig. 2.2. Sketch of a perfectly-reflecting flat solar sail.

Considering the directions of the incident and reflected radiation \hat{u}_i and \hat{u}_r , the incident and reflected force $f_{SRP,i}$ and $f_{SRP,r}$ acting on the sail is given as

$$\begin{cases} f_{SRP,i} = PA(\hat{u}_i \cdot \hat{N})\hat{u}_i \\ f_{SRP,r} = PA(\hat{u}_r \cdot \hat{N})\hat{u}_r \end{cases} \quad (2.14)$$

in which $A(\hat{u} \cdot \hat{N})$ is the projected sail area along the direction \hat{u} , whereas \hat{N} is the unit vector perpendicular to the sail plane. Because of the hypothesis of complete reflection of the incident radiation, it is $\hat{u}_i - \hat{u}_r = 2(\hat{u}_i \cdot \hat{N})\hat{N}$ and the total force f_{SRP} acting on the sail is

$$f_{SRP} = 2PA(\hat{u}_i \cdot \hat{N})^2 \hat{N} \quad (2.15)$$

Define the orbital reference frame as $\{\hat{r}, \hat{\theta}, \hat{h}\}$, in which \hat{r} is the Sun-spacecraft unit vector, \hat{h} is the direction of the orbital momentum and $\hat{\theta}$ is the in-plane transversal direction, completing the right-handed reference frame. In such frame of reference, the attitude of the sailcraft can be described by either the normal unit vector \hat{N} or by the two angles α and δ , which are referred to as cone and clock angle, respectively. The cone angle α is the angle between the incident radiation and the sail normal unit vector (Fig. 2.2), such that $\cos\alpha = \hat{u}_i \cdot \hat{N}$. The

clock angle δ is defined as the angle between the projection of \hat{N} on the $\{\hat{g}, \hat{h}\}$ plane and the \hat{g} axis. Therefore, the normal unit vector \hat{N} can be expressed, by means of the cone and clock angles, as

$$\hat{N} = \begin{bmatrix} N_r \\ N_g \\ N_h \end{bmatrix} = \begin{bmatrix} \cos \alpha \\ \sin \alpha \cos \delta \\ \sin \alpha \sin \delta \end{bmatrix} \quad (2.16)$$

Figure 2.3 gives a graphical view of the sail cone and clock angles defined, in the orbital reference frame, by Eq. (2.16).

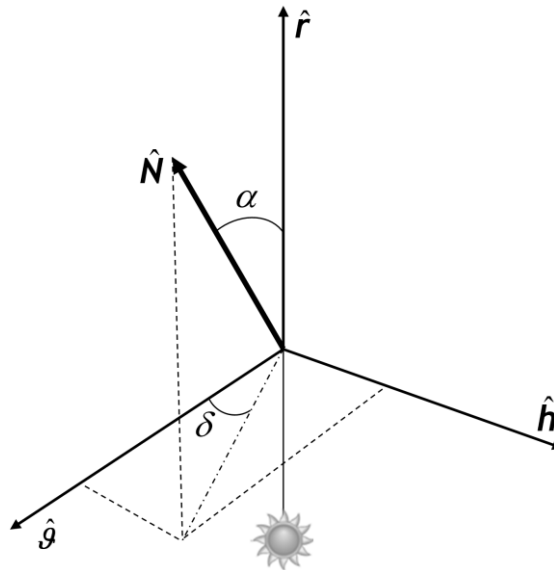


Fig. 2.3. Graphical view of the normal unit vector in the orbital reference frame and the sail cone and clock angles.

Considering the definition of the sail cone angle given by Eq. (2.16), Eq. (2.15) can be rewritten as

$$\mathbf{f}_{SRP} = 2PA\cos^2 \alpha \hat{N} \quad (2.17)$$

From Eqs. (2.11), (2.12) and (2.17), and defining the sail loading κ as the ratio between the total mass m_0 of the sailcraft and the sail area A , the acceleration \mathbf{a} that the SRP exerts on the sailcraft is given by

$$\mathbf{a} = \frac{\mathbf{f}_{SRP}}{m_0} = \frac{2P_\oplus}{\kappa} \left(\frac{r_\oplus}{r} \right)^2 \cos^2 \alpha \hat{N} = a_c \left(\frac{r_\oplus}{r} \right)^2 \cos^2 \alpha \hat{N} \quad (2.18)$$

The term a_c in Eq. (2.18) is called characteristic acceleration and is an index of the performances of the given sailcraft. In fact, the characteristic acceleration represents the magnitude of the acceleration given by the solar sail facing the Sun at the distance $r = r_{\oplus}$ from it. Conventionally, an efficiency coefficient η is introduced in the definition of the characteristic acceleration which considers the non-perfect reflectivity of the sail membrane. This value is usually $\eta = 0.9$ [2, 16]. The expression for the characteristic acceleration is therefore given by

$$a_c = \frac{2P_{\oplus}\eta}{\kappa} \quad (2.19)$$

An alternative, yet equivalent, performance index used in the literature is the sail lightness number β . Defining the critical sail loading $\tilde{\kappa}$ as the sail loading for which the acceleration given by the SRP equals the gravitational acceleration [2], the sail lightness number is given by

$$\beta = \frac{\tilde{\kappa}}{\kappa} = a_c \frac{r_{\oplus}^2}{\mu} \quad (2.20)$$

in which μ is the Sun's gravitational parameter.

From Eqs. (2.18) - (2.19) it is clear that, to have large accelerations, a solar sail should be large and lightweight, other than without wrinkles and as more reflective as possible. With the current solar-sail technology, characteristic accelerations of the order of fractions of mm/s^2 are achievable [30, 31]. Because of the low and continuous thrust provided by the solar sail, the solar-sailing mission design involves solving an OCP, since no closed-form, analytical solutions exist for continuous low-thrust propelled spacecraft [32]. Furthermore, although solar-sail propulsion represents a particular form of low-thrust propulsion, a solar sail differs from a classical low-thrust propulsion because: (a) a solar sail cannot thrust towards the Sun, and (b) the magnitude of its acceleration is nonlinearly related to the thrust direction and it depends on the inverse of the square distance from the Sun [Eq. (2.18)]. On the other hand, classical low-thrust propulsion, at least in a preliminary design phase, does not usually have such restrictions on the thrust provided. A graphical representation of these differences is given in Fig. 2.4. Assuming the sail at $r = 1 \text{ AU}$ from the Sun, the plot in Fig. 2.4 is drawn

considering a sail with a characteristic acceleration equal to the maximum acceleration a_{max} provided by a classical low-thrust propulsion system. The thrust achievable with a solar sail lies on the blue line, whereas a classical low-thrust propulsion can usually thrust in any point inside the green circle. The plot in Fig. 2.4 shows the acceleration vector \mathbf{a} due to the solar sail attitude with respect to the Sun. The radial and transversal components, namely \mathbf{a}_r and \mathbf{a}_t , are also shown in the plot.

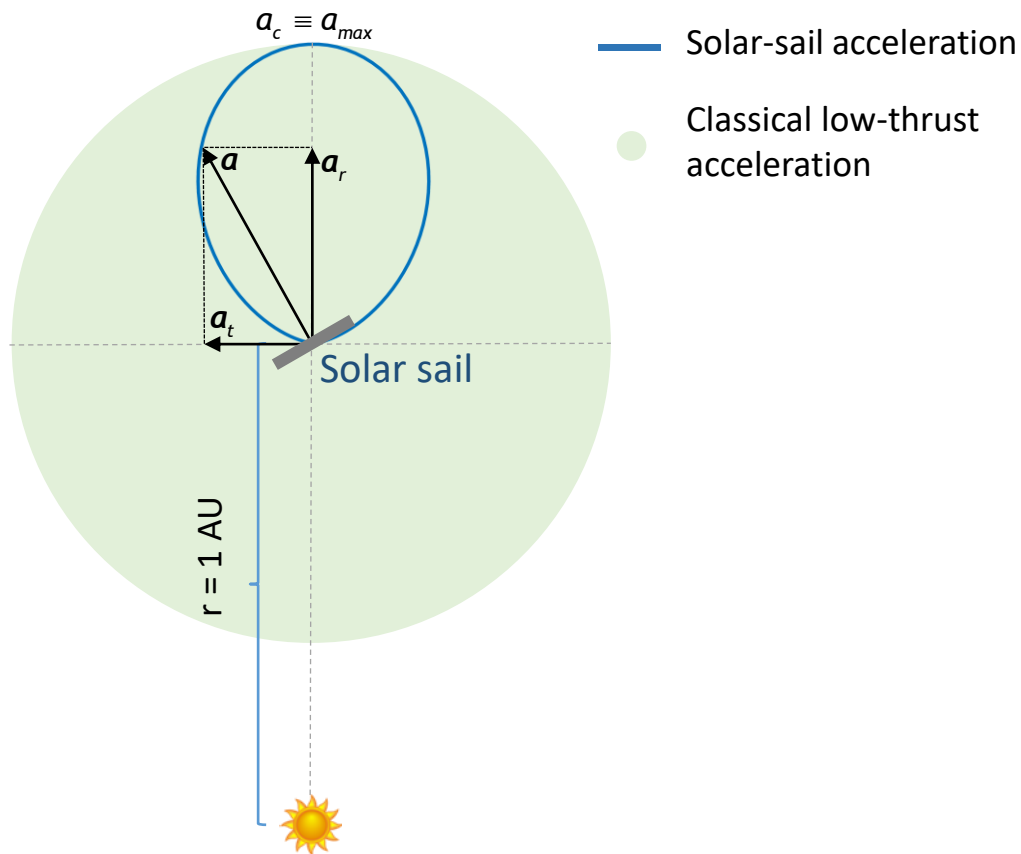


Fig. 2.4. Sketch (not to scale) of classical low-thrust vs solar-sail achievable accelerations. It is evident that the thrust given by the two propulsion systems is equal only if the sail is facing the Sun.

2.1.3. Solar Sailing from the 1970s to the Present Day

Despite the first ideas about solar sailing date as far as the 17th century, studies about this propulsion system started only recently, due to the technological advancements needed and the small immediate outcome of this technology [18]. One of the first practical demonstrations of the potential of solar propulsion was given in 1974. In that year, flying towards Mercury, NASA's Mariner 10 spacecraft showed the possibility of an attitude control by means of solar propulsion. In fact,

the mission controllers were able to control the spacecraft attitude by changing the orientation of the solar arrays with respect to the Sun¹. However, we must wait until the beginning of the 21st century for the launch of the first solar sail, Cosmos-1. Unfortunately, Cosmos-1 was never able to fly because of a rocket failure². To date, only three sailcraft have been successfully launched: IKAROS (JAXA, launched in 2010) [33, 34], NanoSail-D (NASA, launched in 2011) [35, 36], and LightSail-1 (The Planetary Society, launched in 2015) [37]. NASA's NEA Scout [38, 39] is the next solar sail to be scheduled to fly and its launch is expected in mid-2018³. Despite its predecessors, NEA Scout will be the first sailcraft to have objectives other than only demonstrate the solar-sailing physics and technology. Several studies on solar-sail missions have been carried out to date, exploiting the unique characteristic of a sailcraft to not need any propellant [40]. In fact, because of this, solar sailing is an appealing option for performing high- Δv missions [15], such as highly non-Keplerian orbits [41-43], which require continuous thrusting [30, 44]. Moreover, because of the potentially-unlimited Δv available, a solar-sail mission could cope with contingencies and enable a change in the mission targets, even after launch. This is particularly interesting for small-body missions, because dozens of new objects are discovered on a daily basis (Fig. 2.8 in Section 2.3). A classical, reaction-mass propulsion system is usually constrained by the total amount of propellant onboard and, therefore, such a change in the mission targets can be unattainable. For instance, studies have been conducted to extend the mission of JAXA's Hayabusa-2 spacecraft but, because of the limited amount of xenon propellant left aboard, it has been found that the only available extension option is an asteroid flyby [45]. Because of its advantages, several studies have been carried out on the application of solar sails for interplanetary missions, in terms of orbital dynamics [46, 47], as well as system engineering [48, 49]. The DLR/ESA Gossamer roadmap to solar sailing is one of those studies and it was divided into steps of increasing complexity [3]. Its aim was to push the boundaries of the current European solar-sailing technology by firstly testing the deployment of a small solar sail in a low-Earth orbit [50] and then performing a multiple NEA rendezvous mission [16] as well as a sub-L₁ space

¹ Data available online at https://science.nasa.gov/science-news/science-at-nasa/2008/31jul_solarsails [retrieved 10 July 2017].

² Data available online at <http://sail.planetary.org/story-part-2.html> [retrieved 10 July 2017].

³ Data available online at <https://www.nasa.gov/content/nea-scout> [retrieved 11 July 2017].

weather mission [51] and a solar polar mission [52] with a larger sail. A multiple NEA rendezvous mission, which is the focus of this thesis, is attractive for solar-sail technology demonstration as well as for improving our knowledge about NEAs (Section 2.3).

2.2. Techniques for Space Trajectory Optimisation

As discussed in Section 1.1, an optimal control problem must be solved to find a low-thrust trajectory and its control history. Solving an OCP involves finding the control history that minimises (or maximises) a given objective function, while satisfying some constraints. Without lack of generality, the problem of finding the minimum of a given objective function is considered in the remainder of this thesis.

Considering the time t as the independent variable, the dynamics can be expressed as

$$\dot{\mathbf{x}}(t) = \mathbf{f}(\mathbf{x}(t), \mathbf{u}(t), \mathbf{p}, t) \quad (2.21)$$

in which \mathbf{x} is the state vector, \mathbf{u} is the control vector and \mathbf{p} is a vector of static parameters. The boundary constraints (also referred to as endpoint constraints) at the initial and final time are defined by

$$\psi_{\min} \leq \psi(\mathbf{x}(t_0), \mathbf{x}(t_f), \mathbf{p}, t_0, t_f) \leq \psi_{\max} \quad (2.22)$$

Moreover, the solution should satisfy some path constraints of the form

$$\mathbf{c}_{\min} \leq \mathbf{c}(\mathbf{x}(t), \mathbf{u}(t), \mathbf{p}, t) \leq \mathbf{c}_{\max} \quad (2.23)$$

and bounds on the state and control variables, as

$$\begin{cases} \mathbf{x}_{\min} \leq \mathbf{x}(t) \leq \mathbf{x}_{\max} \\ \mathbf{u}_{\min} \leq \mathbf{u}(t) \leq \mathbf{u}_{\max} \end{cases} \quad (2.24)$$

The objective (or cost) function J represents the quantity to be minimised and can be written in Bolza form as [32, 53, 54]

$$J = \phi(\mathbf{x}(t_0), t_0, \mathbf{x}(t_f), t_f, \mathbf{p}) + \int_{t_0}^{t_f} g(\mathbf{x}(t), \mathbf{u}(t), \mathbf{p}, t) dt \quad (2.25)$$

in which ϕ is the terminal cost function and g is the integral one, which considers the cost during the entire time history. In general, an optimal control problem is characterised by several connected phases. In this context, a phase is defined as a part of the OCP in which the mathematical description of the problem (i.e. dynamics, path and endpoint constraints, etc.) is the same. Therefore, in a multi-phase problem, several phases are connected to each other through additional endpoint constraints (commonly referred to as linkage constraints). Nonetheless, without lack of generality, the single-phase problem will be considered in this section for the mathematical description of the OCP. For the ease of explanation, the vector of static parameters \mathbf{p} is also neglected in the remainder of this section.

In the specific case of space-trajectory optimisation, the control variables are usually the components of the thrust vector (or the acceleration vector), whereas the constraints are usually given by the mission requirements (e.g. maximum mission duration, minimum relative distance and velocity of the spacecraft with respect to the target) and the propulsion system used (e.g. maximum amount of propellant available). The objective is usually to minimise the total mission duration, the fuel consumption or a combination of the two. A trajectory optimisation problem is a complex continuous OCP due to several reasons, as: (a) the dynamics are nonlinear; (b) there can be discontinuities in the state (e.g. impulsive manoeuvres due to the use of a high-thrust engine or a planetary flyby); (c) there can be discontinuities in the control; and (d) the initial and final states depend on the initial and final times. For these reasons, several numerical methods have been developed to solve optimal control problems and, in particular, space-trajectory OCPs [5, 6, 55-57]. Based on the way they span the search space, optimisation methods can be divided into local optimisation (LO) and global optimisation (GO) methods. LO methods are characterised by finding the set of variables that minimise the chosen cost function by searching a root of a set of necessary conditions (indirect method) or by a transcription of the problem via nonlinear programming (direct method). These methods need an

initial guess to start with and usually the optimal solution found is close to the initial guess. GO methods, on the other hand, use methods inspired by nature (e.g. the biological evolution of species) to optimise an initial (often random) population. Because the aim of this work is not to develop a new optimisation method, the most common optimisation methods are investigated. This choice has also been driven by the conspicuous literature publicly available on the subject. The optimisation methods considered for this work are classified as indirect, direct, and metaheuristic optimisation methods. Moreover, shape-based (SB) approaches, although do not formally find the optimal solution to an OCP, are also discussed because they are widely used to generate sub-optimal solutions to the trajectory design OCP. Other methods, which do not formally solve any trajectory-optimisation problem, have been studied to find preliminary trajectories, by using, for instance, orbital averaging techniques [58], analytic curve-fitting functions [59], approximated dynamics [60, 61], or a decomposition of the trajectory into finite perturbative elements [62].

2.2.1. Indirect Methods

Indirect (or Hamiltonian) methods are based on the calculus of variations to find the first-order necessary conditions for optimality of the OCP defined through Eqs. (2.21) - (2.25). First, define the Hamiltonian \mathcal{H} as

$$\mathcal{H}(\mathbf{x}, \boldsymbol{\lambda}, \boldsymbol{\mu}, \mathbf{u}, \mathbf{p}, t) = \mathbf{g} + \boldsymbol{\lambda}^T \mathbf{f} - \boldsymbol{\mu}^T \mathbf{c} \quad (2.26)$$

in which $\boldsymbol{\lambda}(t)$ is the vector of the Lagrange multipliers associated with the dynamics of the system (referred to as costate or adjoint variables) and $\boldsymbol{\mu}(t)$ is the vector of the Lagrange multipliers associated with the path constraints. The term \mathbf{g} is the integral cost function defined in Eq. (2.25). Without lack of generality, consider a single-phase problem with no path constraints and no static parameters. The dynamics of the costates are

$$\dot{\boldsymbol{\lambda}} = - \left(\frac{\partial \mathcal{H}}{\partial \mathbf{x}} \right)^T \quad (2.27)$$

Defining \mathcal{U} as the set of feasible controls, the optimal control history is given by the Pontryagin's minimum principle [63]

$$\mathbf{u}^* = \underset{\mathbf{u} \in \mathcal{U}}{\operatorname{argmin}} \mathcal{H} \quad (2.28)$$

The boundary constraints on the state are so that

$$\boldsymbol{\psi}(\mathbf{x}(t_0), t_0, \mathbf{x}(t_f), t_f) = \mathbf{0} \quad (2.29)$$

The constraints on the initial and final values of the costates, which are commonly referred to as transversality conditions on the costates, are

$$\begin{cases} \lambda(t_0) = -\frac{\partial \phi}{\partial \mathbf{x}(t_0)} + \boldsymbol{\nu}^\top \frac{\partial \boldsymbol{\psi}}{\partial \mathbf{x}(t_0)} \\ \lambda(t_f) = \frac{\partial \phi}{\partial \mathbf{x}(t_f)} - \boldsymbol{\nu}^\top \frac{\partial \boldsymbol{\psi}}{\partial \mathbf{x}(t_f)} \end{cases} \quad (2.30)$$

in which $\boldsymbol{\nu}$ is the vector of costates associated with the boundary conditions $\boldsymbol{\psi}$. Lastly, the constraints on the initial and final values of the Hamiltonian, which are commonly referred to as transversality conditions on the Hamiltonian, are

$$\begin{cases} \mathcal{H}(t_0) = \frac{\partial \phi}{\partial t_0} - \boldsymbol{\nu}^\top \frac{\partial \boldsymbol{\psi}}{\partial t_0} \\ \mathcal{H}(t_f) = -\frac{\partial \phi}{\partial t_f} + \boldsymbol{\nu}^\top \frac{\partial \boldsymbol{\psi}}{\partial t_f} \end{cases} \quad (2.31)$$

Eqs. (2.27) - (2.31) represent the first-order necessary conditions for optimality of the continuous-time optimal control problem at hand. For a thorough mathematical description of the calculus of variations and the steps needed to retrieve the first-order necessary conditions, the interested reader is referred to Pontryagin et al. [63], Hull [54] and the lectures given by Dr Anil Rao for the course of Optimal Control at the University of Florida during the Spring of 2012¹.

Considering the necessary conditions for optimality, the original OCP can now be viewed as a two-point boundary value problem (TPBVP). The most common approach to solve a TPBVP is the shooting method. As such, the values of the Lagrange multipliers at one end of the time interval are guessed and the dynamics of both state [Eq. (2.21)] and costate [Eq. (2.27)] are propagated until the other

¹ Data available online at <http://www.anilvrao.com/Optimal-Control-Videos.html> [retrieved 13 July 2017].

end of the time interval. In fact, given the initial (or final) values of the state and the Lagrange multipliers, the control is analytically defined through Eq. (2.28). Hence, the reason for naming this optimisation method *indirect*. However, the values of the state and the Lagrange multipliers obtained after the propagation might not satisfy the transversality conditions defined by Eqs. (2.30) - (2.31). Therefore, the initial-guess values for the Lagrange multipliers are slightly modified and the dynamics are propagated again. This loop terminates when either the transversality conditions are satisfied within a set tolerance or some user-defined termination conditions are met (e.g. the maximum number of function evaluations is reached, the error on the transversality conditions did not change significantly during the last iterations, etc.). This method can be visualised as a cannon shooting at a target (thus the name *shooting method*). The optimal angle of the cannon, which guarantees the hit of the bull's-eye, is unknown. Therefore, a first-guess value for such angle is chosen for a test shot. The angle is subsequently adjusted based on the position the cannonball hits the target [56].

Remarks. With the indirect shooting method, the optimal control is determined analytically and, therefore, the overall method is usually computationally fast. Moreover, the level of accuracy achieved by this method is high and an optimum is guaranteed, if a solution is found. However, such optimum is only local because the solution is usually close to the initial guess used. Moreover, this method is extremely sensitive to the initial-guess values considered for the Lagrange multipliers and finding a good initial guess (i.e. an initial guess that guarantees convergence of the method) is not trivial. In fact, the Lagrange multipliers are mathematical entities with no physical meaning. To date, several techniques have been developed to overcome the issue about the small convergence radius of indirect shooting methods. An example of this is the homotopic approach, which is probably the most common approach among the studies that involve indirect methods. The homotopy is defined as a function that continuously links two continuous functions from a topological space to another [64]. That is, the (unknown) solution to the OCP at hand can be sought by studying the (known) solution to a similar OCP. A numerical continuation can be used to change the solution of the similar OCP to the one of the original problem [65]. Therefore, the combined use of the homotopy with a numerical continuation technique can ease the difficulties of the indirect shooting method due to the lack

of physical meaning of the Lagrange multipliers. A detailed (yet not exhaustive) survey of the applications of the homotopy-continuation techniques used in solving space-trajectory OCPs is available in [66]. Typical issues that arise with the use of these techniques are related to the numerical continuation that might face problems in following the path that links the initial OCP to the original one. A possible workaround is then to combine several homotopies, as proposed in [67]. An additional disadvantage of the indirect shooting method is that changes in the terminal constraints or conditions (e.g. a change in the objective function) might require a fresh derivation of the analytical optimal control laws. Lastly, the derivation of the first-order optimality conditions [Eqs. (2.26) - (2.31)] requires the computation of analytical derivatives, which is not always an easy task and sometimes can be even impossible (e.g. if tabular data are involved).

Due to the little computational effort needed, the first trajectory optimisation tools developed and used at NASA employ an indirect method to carry out preliminary mission design studies. These are VARITOP, SEPTOP, NEWSEP, and SAIL¹ [68].

2.2.2. Direct Methods

As opposed to indirect methods, direct methods discretise the continuous OCP and transcribe it into a nonlinear optimisation, or nonlinear programming (NLP) problem, which is a parameter optimisation problem. An NLP problem is defined as follows. Determine the vector of parameters $\boldsymbol{x}^* \in \mathbb{R}^n$ that minimises the objective function $J(\boldsymbol{x})$ subject to the algebraic constraints $\mathbf{g}(\boldsymbol{x}) \in \mathbb{R}^m$. The latter is composed of equality and inequality constraints, as

$$\begin{cases} \mathbf{g}_i(\boldsymbol{x}) \leq 0 & (i = 1, \dots, m_1) \\ \mathbf{g}_i(\boldsymbol{x}) = 0 & (i = m_1 + 1, \dots, m) \end{cases} \quad (2.32)$$

The first-order optimality conditions are given by the so-called Karush-Kuhn-Tucker (KKT) conditions [69]. That is, $(\boldsymbol{x}^*, \boldsymbol{\lambda}^*)$ is a local minimum if the following conditions are verified.

¹ NASA's LTTT Suite Optimization Tools. Data available online at <https://spaceflightsystems.grc.nasa.gov/SSPO/ISPTProg/LTTT/> [retrieved 13 July 2017].

$$\nabla J(\boldsymbol{x}^*) + \sum_{i=1}^m \lambda_i^* \nabla g_i(\boldsymbol{x}^*) = 0 \quad (2.33)$$

$$\begin{cases} g_i(\boldsymbol{x}^*) \leq 0 & (i = 1, \dots, m_1) \\ g_i(\boldsymbol{x}^*) = 0 & (i = m_1 + 1, \dots, m) \end{cases} \quad (2.34)$$

$$\begin{cases} \lambda_i^* g_i(\boldsymbol{x}^*) = 0 & (i = 1, \dots, m_1) \\ \lambda_i^* \geq 0 & (i = 1, \dots, m_1) \end{cases} \quad (2.35)$$

Eq. (2.33) represents the necessary condition for optimality, whereas Eqs. (2.34) and (2.35) are the so-called feasibility and complementarity conditions, respectively [70]. To date, several techniques and algorithms have been developed to solve nonlinear programming problems. For instance, some of the currently most used NLP solvers are IPOPT [71], SNOPT [72] and WORHP [73].

Direct methods can be divided into two families, whether only the control or both state and control are approximated (namely, *control parametrisation* and *state and control parametrisation*, respectively). The most common approach to the control parametrisation is the direct shooting method, whereas direct collocation is the most common approach in the family of state and control parametrisation. Because of the importance of both methods in space trajectory design, both are discussed in the following subsections.

Direct Shooting Method. In the direct shooting method, the control is discretised at the chosen discretisation points, whereas the trajectory is obtained by propagating the initial state. That is, the direct shooting method is categorised as a control parametrisation method. One of the first applications of the direct shooting in space trajectory design is attributed to Sims and Flanagan [74] (thus the name *Sims-Flanagan method*). They proposed the use of the direct shooting method to generate first-guess trajectories for low-thrust transfers. A schematic of the trajectory structure is shown in Fig. 2.5. The trajectory is divided into control nodes, which are defined as the waypoints the spacecraft must pass by. Between each couple of control nodes, the trajectory is propagated forward from the former control node and backward from the latter. The two propagated trajectories shall meet somewhere in between the two waypoints in what is called match point. The trajectory is divided into segments and, in each segment, the continuous thrust is approximated by an impulsive Δv . This method can be

therefore extended to several control nodes (each control node can be, for instance, a planet or an asteroid). The task of the NLP solver is to find the direction and magnitude of all the impulsive Δv so that the discontinuities in the state at the match points are below a set threshold (zero, ideally). A trajectory found by following this method can be used either as an initial-guess solution for a subsequent minimisation of the desired cost function or, on its own, as a trajectory for a preliminary mission design. The Sims-Flanagan method is at the base of NASA's Mission Analysis Low Thrust Optimization (MALTO) software [75]. The Sims-Flanagan method has been the object of further studies that aimed to improve the quality of the solution. For instance, Yam et al. [76] introduced an adaptive time mesh through the use of the Sundman transformation [77]. As such, the NLP is characterised by a larger number of points when the dynamics are faster (i.e. in the neighbourhood of the pericentre, in the case of elliptic orbits), thus guaranteeing a uniform spatial distribution of the points. Furthermore, to improve the reliability of the trajectory approximation within the Sims-Flanagan method, Yam et al. replaced the impulsive Δv with continuous low-thrust throughout the segment. Within each segment, both magnitude and direction of the thrust are constant [76].

The main advantage of the direct shooting method is the ease of implementation. The accuracy of the solution and the computational effort needed to find such solution might depend on the integration scheme employed for the propagation of the dynamics. For instance, Yam et al. [76] used a Taylor integration scheme [78] to contain the extra computational effort needed for considering a continuous low-thrust against an impulsive Δv manoeuvre. The main disadvantages are in that a first-guess solution is needed for the NLP solver and the continuity conditions at the match points may result in computational issues [56]. Moreover, the longer the legs are to propagate, the more sensitive the method is to the unknown initial conditions.

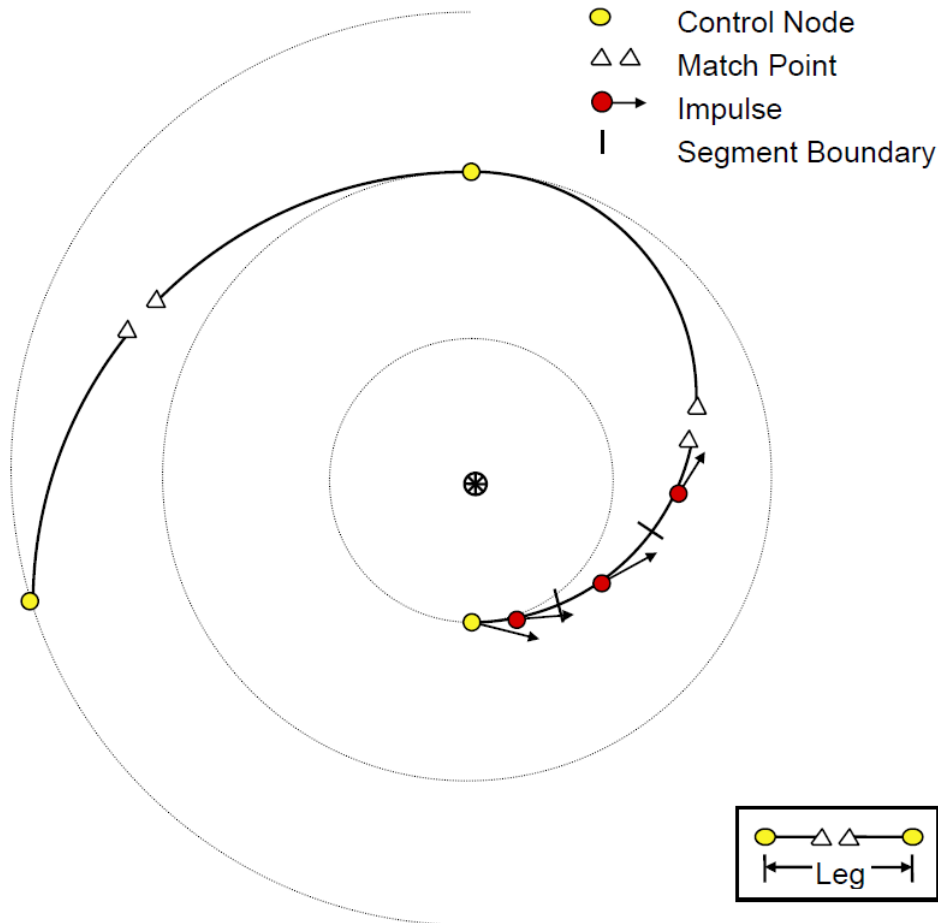


Fig. 2.5. Schematic of the trajectory structure with a direct shooting method [75] (Reproduced with permission of AIAA).

Direct Collocation Method. In the direct collocation method, both state and control are parametrised over a set of discretisation points. Usually, these points are chosen as the roots of orthogonal polynomials (or their linear combination). Three sets of collocation points are mostly used in the literature and these are the Legendre-Gauss (LG), Legendre-Gauss-Lobatto (LGL), and Legendre-Gauss-Radau (LGR) points [79]. Let us describe the LGR collocation method, since it is the one used throughout this thesis. The interested reader can find more information about the other two methods in [56, 79, 80]. The LGR points τ lie on the half-open interval $\tau \in [-1, 1]$ and are obtained as the roots of $P_{N-1}(\tau) + P_N(\tau)$, in which $P_N(\tau)$ is the N -th degree Legendre polynomial defined, by means of the Rodrigues' formula [77], as

$$P_N(\tau) = \frac{1}{2^N N!} \frac{d^N}{d\tau^N} \left((\tau^2 - 1)^N \right) \quad (2.36)$$

In Eq. (2.36), τ is obtained by means of an affine transformation from the time as [81]

$$\tau = \frac{2t}{t_f - t_0} - \frac{t_f + t_0}{t_f - t_0} \quad (2.37)$$

The collocation points are usually preferred to the more intuitive equidistant discretisation points mainly to avoid the so-called Runge phenomenon [82]. This phenomenon arises when a polynomial approximation is used to describe a real function. In fact, if the order of the polynomial is increased to describe better the real function while using equidistant points, the approximation error near the boundaries increases. This does not happen if a set of collocation points is used. A graphical example of this is shown in Fig. 2.6, in which a Lagrange polynomial is used to approximate the function $1/(1+25\tau^4)$ over 25 points. Both equidistant and LGR points are used for the discretisation. The Runge phenomenon is clearly shown in the case the equidistant points are used.

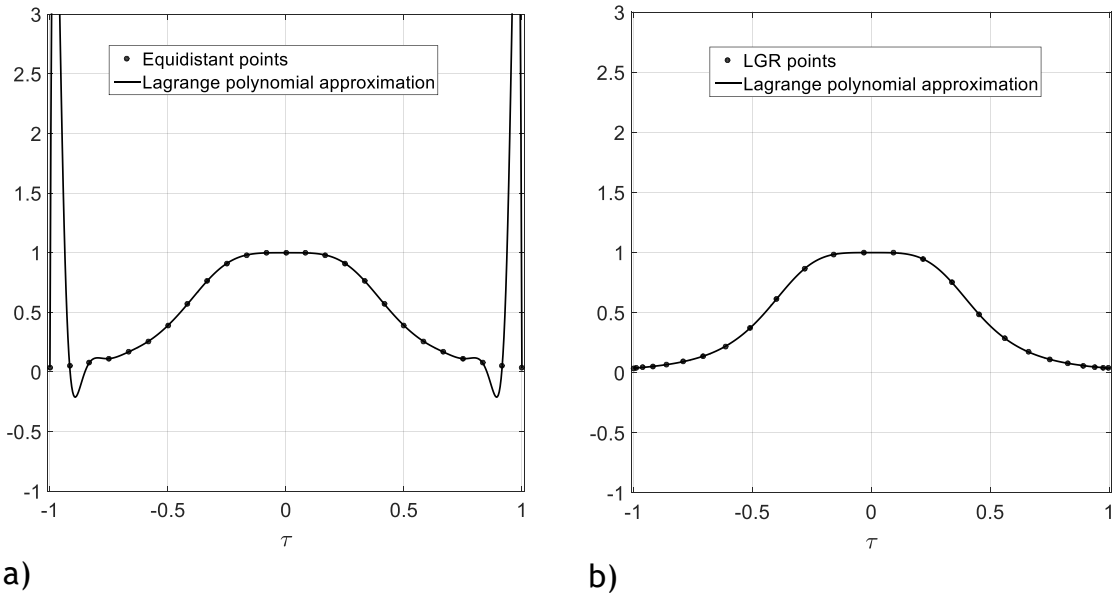


Fig. 2.6. Lagrange polynomial approximation of the function $1/(1+25\tau^4)$ using (a) 25 equidistant points and (b) 25 LGR points.

Moreover, it can be demonstrated that the use of collocation points is more likely to guarantee an accurate approximation of a continuous function f . Such function can be, for instance, the dynamics shown in Eq. (2.21) or the integral cost function

shown in Eq. (2.25). The integral of a function f can be approximated by means of the Gauss quadrature, as

$$\int_a^b f(\tau) d\tau \approx \sum_{i=1}^N w_i f(\tau_i) \quad (2.38)$$

in which w_i are suitable quadrature weights. Huntington [82] showed a spectral convergence (i.e. a convergence at an exponential rate) between the Gauss quadrature of Eq. (2.38) and the integral of f as the order of the approximating polynomial increases. Thus, a relatively small number of collocation points are needed for the approximation. This is generally valid for relatively smooth functions [83, 84].

The use of Lagrange polynomials to approximate a continuous function is common in direct collocation methods. The main reason is that the approximating N -th degree Lagrange polynomial is equal to the function at the N collocation points. Considering the LGR method, the state \mathbf{x} can be discretised, at the generic time τ_i ($i = 1, \dots, N$), as

$$\mathbf{x}(\tau_i) \approx \mathbf{X}(\tau_i) = \sum_{j=1}^{N+1} X_j \ell_j(\tau_i) \quad (2.39)$$

in which $\ell_j(\tau_i)$ is the Lagrange interpolating polynomial at the j -th LGR point, defined as

$$\ell_j(\tau_i) = \prod_{\substack{l=1 \\ l \neq j}}^{N+1} \frac{\tau_i - \tau_l}{\tau_j - \tau_l} \quad (2.40)$$

It can be demonstrated that the Lagrange interpolating polynomial is an orthogonal polynomial [82]. That is

$$\ell_j(\tau_i) = \begin{cases} 1 & \text{if } j = i \\ 0 & \text{if } j \neq i \end{cases} \quad (2.41)$$

Thus, the interpolating Lagrange polynomial has the property that, at each collocation point τ_i , Eq. (2.39) is so that $\mathbf{x}(\tau_i) \equiv \mathbf{X}(\tau_i)$.

The discretised equations of the dynamics can be obtained by differentiating the state $\mathbf{X}(\tau_i)$ in Eq. (2.39), as

$$\frac{d\mathbf{X}(\tau_i)}{d\tau_i} = \sum_{j=1}^{N+1} \mathbf{X}_j \frac{d\ell_j(\tau_i)}{d\tau_i} \quad (2.42)$$

Therefore, a set of constraints is added to the NLP so that the continuous dynamics of Eq. (2.21) are equal to the discretised dynamics shown in Eq. (2.42) [79, 85]. That is, for all LGR points τ_i ($i = 1, \dots, N$), the following dynamics constraints must be satisfied:

$$\sum_{j=1}^{N+1} D_{ij} \mathbf{X}_j - \frac{t_f - t_0}{2} \mathbf{f}(\mathbf{X}_i, \mathbf{U}_i, \tau_i) = \mathbf{0} \quad (2.43)$$

in which \mathbf{U}_i is the discretised control vector and D_{ij} is the so-called differentiation matrix, defined as

$$D_{ij} \triangleq \frac{d\ell_j(\tau_i)}{d\tau_i} \quad (2.44)$$

The boundary constraints of Eq. (2.22) are therefore discretised as

$$\psi_{\min} \leq \psi(\mathbf{X}_1, \mathbf{X}_{N+1}, t_0, t_f) \leq \psi_{\max} \quad (2.45)$$

Likewise, the path constraints of Eq. (2.23) are discretised as

$$\mathbf{c}_{\min} \leq \mathbf{c}(\mathbf{X}_i, \mathbf{U}_i, \tau_i) \leq \mathbf{c}_{\max} \quad (2.46)$$

Lastly, the objective function J of Eq. (2.25) is approximated, over the LGR points, as [85]

$$J \approx \phi(\mathbf{X}_1, t_0, \mathbf{X}_{N+1}, t_f) + \sum_{j=1}^{N+1} \frac{t_f - t_0}{2} w_j g(\mathbf{X}_j, \mathbf{U}_j, \tau_j) \quad (2.47)$$

in which w_j are the LGR quadrature weights [86].

In case the time interval $\tau \in [-1, 1]$ is divided into K subintervals (commonly referred to as meshes), the NLP formulation of Eqs. (2.39) - (2.47) must be

rewritten accordingly [85]. In particular, a further endpoint constraint is added to ensure the continuity of the state between two consecutive meshes, as

$$\mathbf{X}_{N_k+1}^{(k)} = \mathbf{X}_1^{(k+1)} \quad (k = 1, \dots, K-1) \quad (2.48)$$

in which N_k is the number of LGR points in the k -th mesh and the superscript value in brackets represents the mesh number. Moreover, the cost function of Eq. (2.47) is rewritten as

$$J \approx \phi(\mathbf{X}_1^{(1)}, t_0, \mathbf{X}_{N_k+1}^{(K)}, t_f) + \sum_{k=1}^K \sum_{j=1}^{N_k+1} \frac{t_f - t_0}{2} w_j^{(k)} g(\mathbf{X}_j^{(k)}, \mathbf{U}_j^{(k)}, \tau_j^{(k)}) \quad (2.49)$$

The transcription of the continuous OCP into an NLP problem described so far is called p collocation method [85]. It is usually also referred to as a global orthogonal collocation method [56] because it uses only one function to approximate the entire time span (thus, the definition of global) over a set of collocation points that are derived from the roots of orthogonal polynomials or their combinations [87]. The main advantage of the p methods is the exponential convergence of the Lagrange interpolating polynomials that allows a reduced-degree polynomial (thus, a reduced number of collocation points) to achieve the required accuracy. Because of their spectral convergence, these methods are also referred to as *pseudospectral methods* [56]. A different approach is the so-called h method (usually referred to as a local method) [85]. It consists of dividing the time interval τ into several consecutive meshes. The order of the interpolating Lagrange polynomial (and, thus, the number of collocation points) is fixed among all meshes and decided *a priori*. Convergence is reached by increasing the number of meshes [7]. This method does not exploit the exponential convergence of the Lagrange polynomials and, therefore, needs more collocation points to achieve the same desired accuracy as the p method. However, this is true if the real function is smooth enough. If the real function changes abruptly, a single global polynomial may incur into issues in modelling the entire spectrum of such function. On the other hand, a local collocation method can isolate those time intervals in which the function is nonsmooth by adding more meshes and approximating the entire functions through several lower-order polynomials. Lastly, a hybrid method (namely, ph method) has been introduced which considers the advantages of both h and p methods. As described by Patterson et al. [85], a

ph method first exploits the spectral convergence of the Lagrange interpolant polynomials by increasing the order of it and then increases the number of meshes. New meshes are added in the neighbourhood of those times τ in which the real function shows a non-smooth trend. As such, different-order interpolating Lagrange polynomials can be used within each mesh. This allows a decrease in the overall number of collocation points and thus the computational effort needed to solve the NLP at hand. The general-purpose optimal control software GPOPS-II¹ is based on the hybrid *ph* collocation method and is characterised by several mesh refinement techniques that allow a better error estimation and, therefore, a smarter strategy to locate the collocation points and the meshes [88, 89]. The interested reader is referred to [85, 90-92] (and the references therein) for a more detailed explanation of the mesh refinements developed. A thorough mathematical description of the direct collocation methods and, in particular, the *ph* method developed within GPOPS-II, can be found in [79, 80, 83, 84, 88, 91, 93] (and the references therein).

Remarks. The major advantages of the direct methods are: (a) convergence is generally robust to poor initial guesses; (b) easy to pass from one problem to a similar one without the need to re-derive the equations; (c) despite an initial guess is needed, this has a physical meaning, contrary to the case of the indirect methods. Moreover, they are straightforward to code and there is no necessity of being an expert on optimal control theory. On the other hand, state and control are known only at discrete points and the solution is usually in the neighbourhood of the initial guess. Despite the fact that direct methods are usually more robust to poor initial guesses than indirect methods [56], the choice of the initial guess plays an important role in the quality of the optimised solution [55]. Although this issue is not widely discussed in the literature, few works highlight the importance of a good initial guess even for direct-collocation methods. Porsa et al. [94] showed how the performances of the optimiser, in terms of both cost function and computational load, are sensitive to the choice of initial guess. The need of a good initial guess was critical for the convergence of the NLP solver in [95]. The influence of different problem formulations on the robustness of the direct-collocation method was investigated in [96], in which it was shown that not all

¹ Data available online at <http://www.gpops2.com/> [retrieved 21 July 2017].

the choices of initial guess guaranteed convergence of the optimiser. In the same paper, it is discussed, for instance, that SNOPT never converged if a good initial guess was not available, whereas IPOPT was more likely to find a solution only if the mesh had few nodes. Moreover, Graham and Rao [97] developed an algorithm to generate the initial guess for a multi-revolution low-thrust transfer in order to help the convergence of the NLP solver. To do so, a set of optimal control sub-problems needed to be solved to create the initial-guess solution.

Even if a good initial guess is provided, issues can arise in the computation of the solution by a numerical optimiser [56]. A proper scaling of the problem [7], the differentiation algorithm used to compute the derivatives [98], and the way the continuous problem is discretised [79] are only three of the possible issues in the numerical optimisation. Moreover, different settings of the numerical optimiser can potentially lead to issues in the convergence of the NLP solver. In the adaptive mesh refinements described in [85, 92], for instance, the number of collocation points is explicitly dependent to the maximum/minimum allowed polynomial degree chosen for the discretisation. That is, different settings affect the number and location of the collocation points and this can impair the ability of the NLP solver to find a solution for the given formulation of the problem. Therefore, trajectory-optimisation problems are usually solved once at a time, allowing the user to tweak manually some settings, often in a trial-and-error fashion, in order to help the convergence of the solver or to get better results.

2.2.3. Metaheuristic Optimisation Methods

Metaheuristic optimisation methods are classified as GO methods [99] and are fundamentally different from the direct and indirect methods, which require an initial guess and generally find a solution in their neighbourhood (thus the classification of LO methods). In fact, metaheuristic optimisation methods combine a heuristic component with an “intelligent” search, which is designed to lead the method towards a solution beyond the neighbourhood of the initial guess [99]. Specifically, metaheuristic methods are often population-based methods, in which the initial population is chosen within the search space and evolved towards the optimum by following a defined set of rules. That is, there is no need of an initial guess and the optimality can be statistically assessed by running several times the same method on the same problem. Therefore, a solution found by

means of a metaheuristic optimisation method is more likely to be closer to the global optimum than a solution found by an LO method. In fact, the initial guess used for the LO method is not guaranteed, in general, to be in the neighbourhood of the global optimum. Several metaheuristic algorithms have been studied to date and the majority of them mimics the ability of nature to find an optimal solution (e.g. evolution of species, need for food, etc.) [100]. The most studied metaheuristic optimisation methods are: genetic algorithm (GA) [101], particle swarm optimisation (PSO) [102, 103], ant colony optimisation (ACO) [104-106], differential evolution [107], and simulated annealing [108]. Other algorithms have been developed, such as the Physarum solver that is inspired by the behaviour of the amoeboid organism *Physarum Polycephalum* [109]. Appendix A briefly describes GA and PSO, which are the two metaheuristic optimisation methods used to find some of the results shown in this thesis.

In space-trajectory optimisation, metaheuristic algorithms are generally used when impulsive Δv are considered, such as chemical thrusters used for launch or deep-space impulsive manoeuvres, or gravity assist at planets [110, 111]. In these cases, the dimensionality of the search space is limited by the number of optimisation variables; these can be, for instance, the launch date, the time of flight, the impulsive Δv for the manoeuvre, etc. [102, 110]. In the case of continuous OCPs, such as low-thrust trajectory optimisation, metaheuristic algorithms are generally used in combination with other methods. For instance, metaheuristic algorithms can be used together with an indirect method to find the initial values of the adjoint variables that are otherwise difficult to guess [102, 112], or can be used in combination with an orbit averaging technique to find the optimal control law for an orbit transfer [113]. Metaheuristic algorithms can be even used in combination with direct methods to find, for instance, the Δv and the times of the impulsive manoeuvres within the Sims-Flanagan approach [114-116]. In 2004, Dachwald [117, 118] developed InTrance, an algorithm that combines metaheuristic optimisation methods with artificial neural networks (ANNs) for the solution of space-trajectory OCPs. A description of InTrance is given in Appendix A.3.

Remarks. As mentioned above, the main advantage of the metaheuristic optimisation methods is the absence of an initial guess. Furthermore, it is more likely to locate a global optimum with these methods than using LO methods. On

the other hand, the solution found by a GO method is considered globally optimal because the algorithm spanned the search space globally but there is no guarantee of optimality. Because of its heuristic characteristics, a GO method should be run more than once to have a statistical confidence about the global optimality of the solution [119]. From a purely algorithmically point of view, GO methods are generally easy to code and there is no need to derive any analytical condition. However, a numerical propagation of the dynamics is usually required which, together with the random initialisation of the population, may lead to a significant computational effort needed to solve an OCP by means of a metaheuristic optimisation method. Lastly, a metaheuristic optimisation algorithm is not usually able to localise optima accurately [57, 120]. Therefore, a solution found by means of a metaheuristic optimisation method might need a refinement through a second optimisation method, such as a direct or indirect approach, to reach the required level of accuracy.

2.2.4. Shape-Based Approaches

Unlike direct and indirect optimisation methods, which can be very expensive in terms of computational effort, an analytic method can be very helpful in the initial phases of the mission design. The key point of such approach is to design the shape of the trajectory that connects the initial and final desired states in Keplerian dynamics. This is done by defining a set of shaping functions that analytically describe the evolution of the state. Once the shape of the trajectory is available in a Cartesian reference frame, the acceleration \mathbf{a} needed to follow such trajectory is analytically retrieved by simply inverting the equations of motion, as

$$\mathbf{a} = \ddot{\mathbf{r}} + \mu \frac{\mathbf{r}}{r^3} \quad (2.50)$$

The main advantage of the SB approach is in that the trajectory is described analytically as a whole, without any propagation or discretisation of the state. That is, the computation of the single trajectory is very fast. However, no explicit constraint on the thrust can be generally enforced and the thrust profile is retrieved *a posteriori*. For this reason, and because no optimisation is carried out, the output of the SB approach is a sub-optimal trajectory. Nonetheless, because

of the little computational effort needed, the trajectories found by means of this approach can be used for preliminary mission design as well as initial-guess solutions for higher fidelity optimisation methods.

Several SB approaches have been proposed to date and all of them deal with classical low-thrust propulsion systems. These approaches differ one another for the sets of shaping functions used, the sets of elements chosen to describe the state and the approximations considered. Table 2.1 shows a compendium of some of the SB approaches proposed in the literature, highlighting their differences. The number of free parameters that appear in Table 2.1 refers to those parameters that can be tuned in order to change the shape of the trajectory while satisfying the boundary constraints on the state. In fact, some parameters are univocally defined by the boundary conditions on the state and, therefore, are not considered here as free parameters. For instance, in the case of the finite Fourier series (FFS) [14], the total number of parameters is $2(n_r + n_\vartheta + 1)$, in which n_r and n_ϑ are the number of Fourier terms that can be chosen. However, Taheri and Abdelkhalik [14] showed that the first eight parameters are defined by the satisfaction of the boundary constraints on the state, leading to a number of free parameters equal to $2(n_r + n_\vartheta + 1) - 8$. Note that, in most of the cases, a tangential thrust is assumed. Moreover, even though some of the existing SB approaches allow the possibility to constrain the thrust acceleration magnitude, none of them is able to deal with a constrained acceleration vector profile. Lastly, it is worth noting that a trade-off between the number of independent variables that describe the shape of the trajectory and the accuracy of the trajectory itself is an important point in the choice of the SB approach.

For the sake of conciseness, the first three SB approaches listed in Table 2.1 are briefly described here. The interested reader is referred to the literature referenced in Table 2.1 for a more detailed description of each approach.

Exponential sinusoid. Petropoulos and Longuski [8] were the first to propose the idea of a SB approach, by introducing an exponential sinusoid shape for the in-plane motion and an additional force for the out-of-plane thrust. The in-plane motion is expressed in polar coordinates (r, ϑ) . Therefore, the radius r can be described, as a function of the angular position ϑ and with the approximation of tangential thrust, as

$$r(\vartheta) = k_0 \exp(k_1 \sin(k_2 \vartheta + \varphi)) \quad (2.51)$$

in which $\{k_0, k_1, k_2, \varphi\}$ are constant parameters that determine the shape of the in-plane trajectory. By introducing the two additional parameters $\{a_{0P}, b_0\}$, the out-of-plane acceleration a_h is expressed as

$$a_h = \frac{\mu}{r^2} \left(a_{0P} + b_0 \frac{r_p}{r} \right) \quad (2.52)$$

in which r_p is the radius at the pericentre.

Pseudo-equinoctial. De Pascale and Vasile [9] followed the idea of Petropoulos and Longuski and proposed two different sets of shaping functions, the so-called linear-trigonometric and exponential shape, respectively. In both cases, the state vector is expressed in terms of modified equinoctial elements (MEE) [121, 122]

$$\mathbf{x}^{mee} = [p \ f \ g \ h \ k \ L]^T \quad (2.53)$$

in which

$$\begin{cases} p = a(1 - e^2) \\ f = e \cos(\omega + \Omega) \\ g = e \sin(\omega + \Omega) \\ h = \tan(i/2) \cos \Omega \\ k = \tan(i/2) \sin \Omega \\ L = \nu + \omega + \Omega \end{cases} \quad (2.54)$$

and $\mathbf{x}^{kep} = [a \ e \ i \ \Omega \ \omega \ \nu]^T$ is the set of the conventional Keplerian elements. Both shapes are described as a function of the true longitude L and with the approximation of tangential thrust.

The linear-trigonometric shape is given by

$$\begin{cases} p(L) = p_I + p_F(L - L_0) + \lambda_1 \sin(L - L_0) \\ f(L) = f_I + f_F(L - L_0) + \lambda_2 \sin(L) \\ g(L) = g_I + g_F(L - L_0) + \lambda_2 \cos(L) \\ h(L) = h_I + h_F(L - L_0) + \lambda_3 \sin(L) \\ k(L) = k_I + k_F(L - L_0) + \lambda_3 \cos(L) \end{cases} \quad (2.55)$$

in which λ_1 is the shaping parameter associated to p , λ_2 is the shaping parameter associated to $\{f, g\}$, and λ_3 is the shaping parameter associated to $\{h, k\}$. The terms $\{p_I, f_I, g_I, h_I, k_I\}$ and $\{p_F, f_F, g_F, h_F, k_F\}$ depend on the boundary conditions of the problem at hand.

The exponential shape is given by

$$\begin{cases} p(L) = p_I + p_F \exp(\lambda_1(L - L_0)) \\ f(L) = f_I + f_F \exp(\lambda_2(L - L_0)) \\ g(L) = g_I + g_F \exp(\lambda_2(L - L_0)) \\ h(L) = h_I + h_F \exp(\lambda_3(L - L_0)) \\ k(L) = k_I + k_F \exp(\lambda_3(L - L_0)) \end{cases} \quad (2.56)$$

In [9], De Pascale and Vasile showed that the exponential shape is more suited to describe the trajectory produced by a constant tangential thrust. On the other hand, the linear-trigonometric shape better describes the trajectory produced by a tangential thrust whose magnitude depends on the square distance from the Sun, such as the one produced by a solar electric propulsion system.

Inverse polynomial. Wall and Conway [123] represented the in-plane shape of the trajectory through an inverse polynomial. Describing the trajectory in polar coordinates as a function of the angle ϑ , the analytical expression of the radius is given by

$$r(\vartheta) = \frac{1}{\tilde{a} + \tilde{b}\vartheta + \tilde{c}\vartheta^2 + \tilde{d}\vartheta^3 + \tilde{e}\vartheta^4 + \tilde{f}\vartheta^5 + \tilde{g}\vartheta^6} \quad (2.57)$$

in which the terms $\{\tilde{a}, \tilde{b}, \tilde{c}, \tilde{e}, \tilde{f}, \tilde{g}\}$ are the shaping parameters that depend on the boundary conditions on the state and \tilde{d} is the parameter used to satisfy the time constraint. Also in this case, a tangential thrust is considered. With this approximation, Wall and Conway demonstrated that the shape of the trajectory is univocally defined if the launch date, arrival date and number of complete revolutions are set. Therefore, the only possibility to achieve a feasible trajectory through the inverse-polynomial method is to change the characteristics of the mission, if the acceleration needed to generate the shaped trajectory is beyond the capabilities of the available propulsion system.

Table 2.1. Compendium of shape-based approaches proposed in the literature.

Method	Boundary conditions		3D	Explicit constraints on thrust	Number of free parameters	Hypotheses
	Position	Velocity				
Exponential sinusoid [8, 124]	Yes	No	Yes	No	6	Tangential thrust
Pseudo-equinoctial [9, 125]	Yes	Yes	Yes	No	3	Tangential thrust
Inverse polynomial [123, 126-128]	Yes	Yes	Yes ^(a)	No	0	Tangential thrust
Spherical [129-131]	Yes	Yes	Yes	No	0	Tangential thrust
FFS [14, 132]	Yes	Yes	No	Yes ^(b)	$2(n_r+n_\theta+1)-8$	Tangential thrust
FFS 3D [133]	Yes	Yes	Yes	Yes ^(c)	$2(n_r+n_\theta+1)-9$	---
Hodographic [134, 135]	Yes	Yes	Yes	No	Variable	---
Polynomial [136]	Yes	Yes	No	No	0	Tangential thrust
Optimised Fourier series [137]	Yes	Yes	No	Yes ^(c)	$2(n_r+n_\theta+1)$	Circular orbits
Generalised logarithmic spirals [138, 139]	Yes	No	No	Yes ^(d)	2	---

^(a)Works only for small inclinations.

^(b)Only the magnitude of the acceleration is explicitly constrained.

^(c)An NLP problem is solved to satisfy the constraints on thrust.

^(d)Only the direction of the acceleration is explicitly constrained.

2.2.5. Solar-Sailing Trajectory Design

Designing a trajectory for solar sailing is a crucial task to ensure the feasibility of the mission. Several studies have been carried out to exploit the characteristics of solar sails for interplanetary missions. To date, most of these studies focus on the use of an indirect method. Sauer [140] is one of the first to propose a study of an interplanetary trajectory by means of a sailcraft, considering an ideal solar sail model. After that work, there are several studies on trajectory optimisation through solar sailing that consider ideal [141, 142] and non-ideal sails [10, 143], missions to asteroids [12, 144] or a parametrisation of the control law [11, 145]. Using the Lagrange variational equations, Stolbunov et al. [146] investigated a locally-optimal control strategy for inclination change on a low-Earth orbit. A strategy is shown in [147] which exploits a blend of locally-optimal control laws for planet-centred solar-sail transfers and station-keeping manoeuvres. Considering a fixed sail cone angle, Tsu [148] and McInnes [2] proposed a logarithmic spiral trajectory for solar sailing. Despite being an analytical description of the trajectory, the main issue of this method is that a significant Δv is needed at both the beginning and the end of the trajectory to allow the logarithmic spiral to match with the initial and final Keplerian orbits. For this reason, such a trajectory design is more suited to describe escape trajectories, for which the initial Δv can be given by the launcher's upper stage itself and the final state is not constrained.

Since it does not need any propellant, solar sailing has been extensively studied for enabling highly non-Keplerian orbits [42], such as displaced geostationary orbits [149] or Earth pole sitters [41]. Wawrzyniak and Howell [150] presented an extensive survey of numerical techniques used for generating solar-sailing orbits in a multi-body environment. In particular, they showed that the shooting methods are the most common techniques for this kind of problems. In fact, if periodic orbits about the Earth-Moon Lagrangian points are studied, a natural orbit is easily computed and used as a reference solution for a shooting method. As such, the acceleration given by the sail is considered as a perturbation to the gravitational field and the shooting method needs to adjust slightly the reference orbit considering the added perturbation.

It has been noted that most of the literature about trajectory optimisation through solar sailing deals with simplified models (e.g. two-dimensional approach

[10, 11, 151]) or single-phase problems. Regarding the latter, three of the few works on multi-phase solar-sail trajectories are: the ENEAS+ mission studies [15], the DLR/ESA Gossamer roadmap technology reference study presented by Dachwald et al. [16], and a Main Belt asteroid exploration mission [152]. In none of the cases, a systematic assessment of all possible asteroids to be visited in a multiple rendezvous mission has been carried out. The sequences of encounters have been in fact decided *a priori* and the trajectory optimisation phase (or the sailcraft design, in the case of [152]) is mainly discussed. Bando and Yamakawa [153] describe a NEA survey mission using solar-sailing technology. However, such study is focused on flybys only and two-dimensional dynamics are considered for the solar-sail motion. In the same paper, an inverse solar-sail trajectory problem is described, generalising what presented by McInnes [154] by considering a less-performant solar sail. The method consists on deriving an analytic sail steering law that allows a solar-sail transfer between two planar circular heliocentric orbits with the same radii but different angular velocities.

2.2.6. Target Selection

The selection of targets for a multiple rendezvous mission is primarily a difficult combinatorial task. In the field of discrete and combinatorial optimisation, a typical problem of this kind is the travel salesman problem (TSP). The problem is described as follows: a salesman needs to visit a total of N cities; within one tour, he must visit all the cities only once while travelling the shortest total distance. In the original formulation of the problem, the distance between two cities (i.e. the cost of each leg) is given and the problem is a purely combinatorial optimisation problem. A modified version of it is the so-called motorised travel salesman problem (MTSP) [155], in which the salesman is using a vehicle subject to specific dynamics, and can choose the path between two cities by deciding the continuous control law for the steering angle and the acceleration force of the vehicle. This problem is commonly referred to as hybrid optimal control problem, in which the combinatorial optimisation is mixed with the optimal control problem needed to solve the continuous dynamics.

In space missions, the MTSP is further complicated by the fact that the target celestial objects (corresponding to cities) are not fixed points in space but they move on orbits and their state (position and velocity) is a function of time. The

target selection for a multiple rendezvous mission is one particular case of the more general problem of multi-phase space missions. In this case, the phases of the mission can be defined by the object encounters (e.g. space debris removal [156], planet gravity assist [157], or asteroid rendezvous/flyby [158-160]) or by the composition of the trajectory (i.e. sequences of coast/thrust arcs and impulsive manoeuvres [161]). The astrodynamics community has shown much interest in the optimisation and mission design of this kind of multi-phase space missions, such that, in 2005, the ESA's Advanced Concepts Team challenged the worldwide community with the first Global Trajectory Optimisation Competition¹ (GTOC) [162]. Since then, nine editions of the competition have been completed with a constantly increasing participation. In the fourth GTOC problem, for instance, the challenge was to visit the largest possible number of asteroids with a classical low-thrust spacecraft within a given total mission duration [163]. In the majority of the solutions proposed [164], the problem was divided into two main steps: first looking for a sequence of encounters by means of impulsive thrust manoeuvres, then converting the high-thrust solutions found into classical low-thrust trajectories.

In general, multi-phase space missions are tackled by means of two-level approaches, which can be classified as sequential and integrated approaches. In the first case, the problem is divided into two sequential sub-problems, as is the case of the solutions of the fourth GTOC mentioned above. In the second case, the two levels are integrated within two nested loops, in which the sequence of events is guessed in the outer loop and the corresponding trajectory is sought in the inner loop [165]. In the majority of the cases, both approaches use ballistic Lambert arcs to model the trajectory. Moreover, an initial reduction of the search space is commonly performed at the beginning of any approach used. Such a reduction is usually based on astrodynamics considerations (e.g. nodal flybys [166], orbital element drift due to non-Keplerian forces [167]), mission requirements (e.g. manned mission [159], monitor asteroids in the inner Solar System [168]), or characteristics of the target objects (e.g. NEAs' absolute magnitude [169], asteroid spectral type [158]). For instance, the database used in Di Carlo et al. [168] is made of 12 objects (which are Atira asteroids) and the search space is simplified by considering a planar trajectory and nodal flybys.

¹ Data available online at http://sophia.estec.esa.int/gtoc_portal/ [retrieved 25 August 2015].

To date, different methods have been proposed to deal with the selection of the sequence of events (i.e. the outer loop in the integrated approach or the first subproblem in the sequential approach). These can be classified into two main categories: tree search and heuristic search. In the following subsections, a brief overview of these two categories is given. For an extensive survey of search strategies, the interested reader is referred to [170] and the references therein.

Tree search. For what concerns the first category, the search strategy can be visualised as a tree, in which each branch corresponds to a separate event, such as a trajectory to an asteroid. Starting from each branch, further branches are investigated and thus the length (commonly referred to as depth) of each branch of the tree is increased. The tree-like structure of this search strategy is schematically shown in Fig. 2.7. Two implementations of the tree search are commonly used: breadth-first search (BFS) and depth-first search (DFS) [171]. Within the BFS, all the branches at the current depth are searched before moving to the next depth, in which a further leg is added (in the case of multiple target missions). A modified version of the BFS is the so-called beam search (BS), which allows a pruning of the less promising branches before exploring the next leg. Such pruning can be based on the overall mission objective (e.g. mission time or propellant consumed) or on other criteria, such as an estimate of the cost of the transfer based on the orbital parameters [172, 173]. On the other hand, the DFS works by looking for a whole sequence of events at a time, thus exploring the tree by increasing the depth of the current branch until a stopping criterion is met (e.g. maximum mission time). Subsequently, the next branch is explored in the same way.

The BS implementation of the tree search strategy is the most commonly used because it considers the possibility to prune the less promising branches and thus reduce the overall computational time. BS implementations have been used, for instance, by the JPL team [174] and the GlasgowJena+ team [175] for the fifth and eight GTOC, respectively.

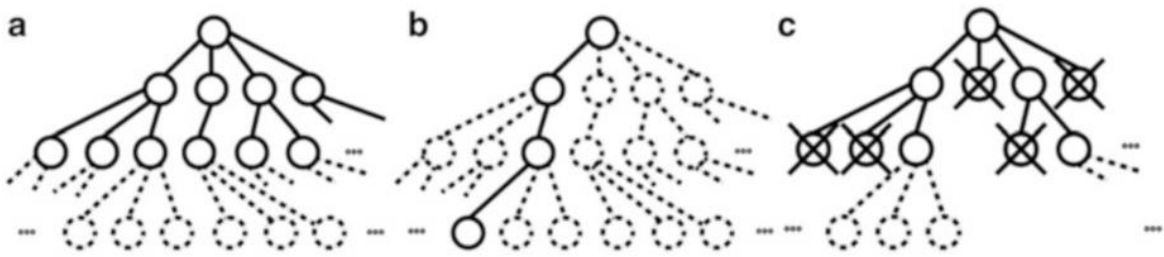


Fig. 2.7. Schematic of the tree search implementations [171] (Reproduced with permission of Springer). Dotted lines and circles indicate branches yet to be explored. Crossed circles refer to pruned branches. (a) Breadth-first search. (b) Depth-first search. (c) Beam search.

Heuristic search. For what concerns the second category, the search strategy is carried out by means of metaheuristic optimisation methods. For instance, Chilan and Conway [165] proposed an integrated approach to design multi-phase space missions which uses a genetic algorithm and an NLP transcription. The approach consists of two nested loops: the integer combinatorial problem is handled within the outer loop by the GA, whereas the continuous dynamics optimisation is tackled within the inner loop by transcribing the problem into an NLP. A binary chromosome of fixed length is used within the GA so that the mission event sequence is easily described. Such sequence is then used within the inner loop to generate an optimal trajectory. An approximate solution, which is found by means of a separate GA, is used as an initial guess for the NLP solver. This approach guarantees an optimal solution at the cost of a significant computational time needed. A similar approach was used by Englander et al. [161] for the mission design of trajectories with impulsive manoeuvres only (i.e. multiple gravity assists and deep space manoeuvres). Other studies use ACO to generate the sequences of events. For instance, Stuart et al. [156, 158] used ACO to generate missions for space debris mitigation and for visiting Trojan asteroids, respectively. In both cases, ACO's task was to find the optimal sequence by using pre-computed trajectories. Those trajectories were computed before the beginning of the search and stored in a library [176], which is a similar approach to what presented in [177] for the case of impulsive manoeuvres. ACO is also used in [106] to generate optimal multiple gravity assist trajectories in a two-dimensional space. Other studies can be found in the literature which use metaheuristic methods for the target selection, such as the Physarum solver used within the toolbox CAMELOT [166] or a blend of evolutionary programming and a tree search used within the toolbox EPIC [178].

Remarks. Both the tree and the heuristic searches have advantages and drawbacks. For instance, the tree search is easy to implement and it can easily cope with changes in the mission, such as an increase in the total mission duration. Moreover, several different solutions are available at the end of the simulation so that the mission analyst can consider a number of potential mission scenarios to investigate in the next phase of study. On the other hand, a tree search is computationally expensive and the optimality of the final solutions can be affected by the pruning criteria used. In the case of the heuristic search, no explicit pruning criteria are used because the algorithm itself is prone to explore the most promising path. Thus, it is more likely that a heuristic search finds a good solution in less time than a tree search. Nevertheless, only one solution is returned by a heuristic search if a single-objective optimisation is considered. Moreover, because of the stochastic characteristic of the metaheuristic algorithms, a single run of the heuristic search may not be enough to locate a difficult sequence of events.

In both cases, a good mathematical model for the continuous dynamics is needed to ensure the feasibility of the sequence found. If the model is not accurate enough, a subsequent optimisation with a higher-fidelity model might find the solution infeasible. For instance, the time needed to encounter the first object in a multiple rendezvous mission can be longer than the one found during the target selection and this can affect the phasing of the other objects in the sequence.

2.3. Near-Earth Asteroids

In the last decades, near-Earth asteroids received considerable attention for planetary defence, science, human spaceflight and technology demonstration. From a technological point of view, NASA considers NEAs as a bridge towards the human exploration of Mars [159]. A manned NEA mission offers similar challenges as a mission to the red planet (i.e. a relevant deep-space environment and a total mission duration similar to an Earth-Mars transit). On the other hand, the total mission duration and the required Δv (and, therefore, the launch costs) are below those needed for a full Mars return mission. As reported in [159], however, for safety considerations, the asteroid selection for such a mission shall take into

account several characteristics of the target objects (e.g. size, composition, rotation rate, etc.). Based on the observations taken from Earth, the characterisation of NEAs discovered to date often suffers from uncertainties in their physical, chemical and orbital properties. Moreover, some NEAs are defined as potentially hazardous asteroids (PHAs) and, especially for planetary defence, an accurate characterisation of their properties is needed [179]. Sugimoto et al. [180] underlined this need for deflection purposes. Even if methods exist to deal with NEA composition uncertainties (e.g. evidence theory), Sugimoto showed how some deflection methods - the ones that have a strong interaction with the target object (e.g. nuclear interceptor, solar sublimation or kinetic impactor) - are affected by uncertainties about asteroid composition (i.e. porosity, surface materials, precise shape, etc.) more than others. Furthermore, not only the chemical, physical and mineralogical composition but also the rotation of these objects can have an important role in the success of a mission, for both deflection and sample-return missions. Miller et al. [181] gave an overview of the asteroid-characterisation priorities for planetary defence, pointing out the possible issues derived by a deflection mission to badly-characterised objects. Several survey and mitigation programs have been established for the purpose of a better knowledge of NEA characteristics (NEOWISE [182], JPL/NASA Center for Near Earth Object Studies (CNEOS)¹, and NEOShield [183] are just three examples) but most of them deal with ground-based observations. Thanks to these survey programs, more than 15,000 NEAs have been discovered to date and this number is constantly increasing, as shown in Fig. 2.8. Specifically regarding Europe, Koschny and Drolshagen [184] showed the ongoing activities to mitigate the potential threat posed by NEAs.

To date, few missions to small bodies have been successfully completed (e.g. NEAR [185], Deep Impact [186], Hayabusa [187, 188], and Rosetta [189, 190]) and two spacecraft (OSIRIS-REx [191] and Hayabusa-2 [192]) are currently on their way to rendezvous two different NEAs (Bennu and 1999 JU₃, respectively). The Asteroid Impact and Deflection Assessment (AIDA) mission aims to demonstrate the kinetic-impact technique for asteroid deflection and consists of two spacecraft, the first of which is scheduled to be launched in late 2020 [193]. A further mission, the Asteroid Redirect Mission (ARM), was under study and was planned to capture and

¹ Data available online at <https://cneos.jpl.nasa.gov/> [retrieved 11 July 2017].

redirect a small NEA into an orbit accessible to a human crew [194]. Even private companies recently began to direct their interest towards asteroid exploration. For instance, the American company Deep Space Industries aims to reach asteroids with the purpose of mining them and, ultimately, market in-space resources¹ [195].

Despite the number of surveys and mitigation programs, our knowledge about NEAs is still far from a robust and stable scheme of classification. As Grundmann et al. [196] state, “The current level of understanding is occasionally simplified into the phrase ‘If you’ve seen one asteroid, you’ve seen one asteroid’”. That is, more studies about these objects, possibly considering close-up observations and sample-return missions, are still needed.

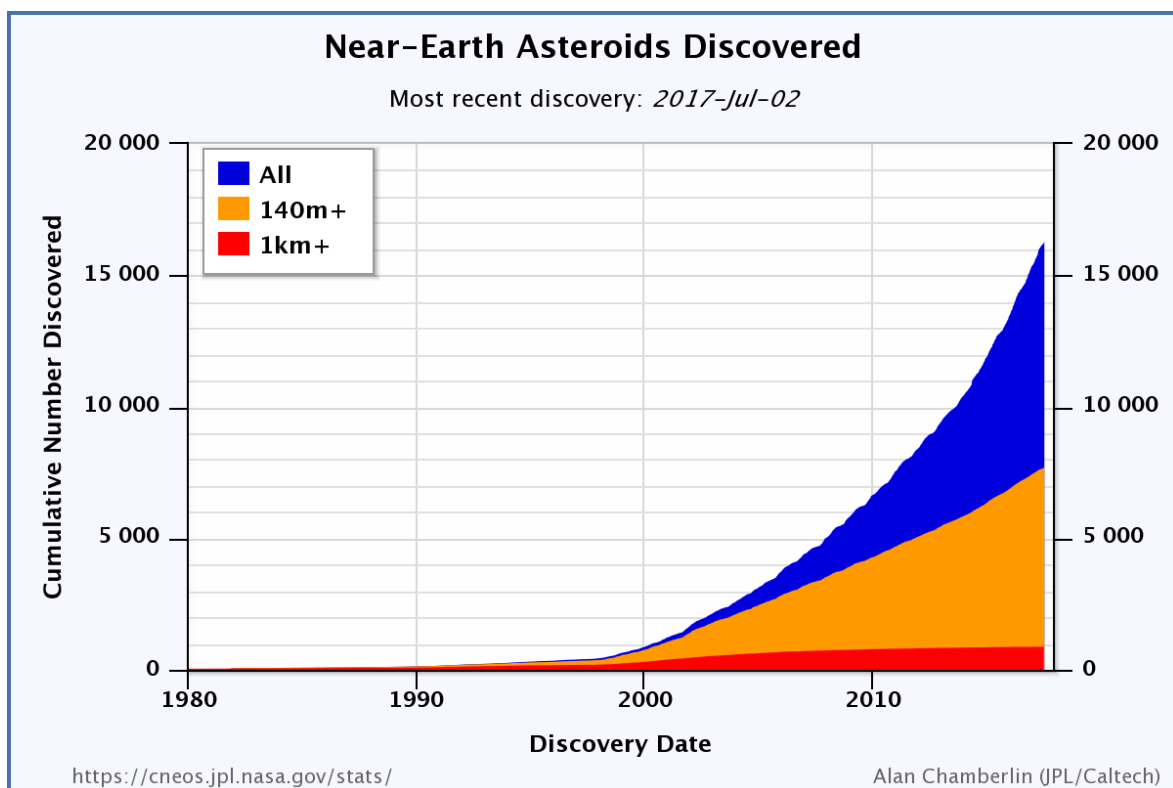


Fig. 2.8. NEA discovery statistics².

¹ Data available online at <http://deepspaceindustries.com/> [retrieved 09 August 2017].

² Chart generated online at <https://cneos.jpl.nasa.gov/stats/totals.html> [retrieved 11 July 2017].

CHAPTER 3.

PRELIMINARY SOLAR-SAIL TRAJECTORY DESIGN

This chapter introduces two methods developed to generate solar-sail trajectories quickly and reliably. The former is a shape-based approach, whereas the latter exploits a homotopy to link a low-thrust trajectory with a solar-sail one. For both methods, a mathematical formulation is given followed by the specific methodology. The performances of the shape-based approach for solar sailing as an initial-guess solution for GPOPS-II are assessed against a simpler thrust law. Regarding the second method, a number of case studies are shown to assess its performances against other established approaches. Both methods will be used to find initial-guess solutions for a local optimiser such as GPOPS-II.

The content of this chapter was published in [197-200], for what concerns the shape-based approach, and in [66, 201], for what concerns the homotopic approach.

3.1. Shape-Based Approach for Solar Sailing

The first method developed to find preliminary solar-sail trajectories is based on finding the functions that well describe the shape of the desired trajectory. As discussed in Section 2.2.4, the idea behind the shape-based approaches is to have a set of shaping functions that allows a fast and reliable, but approximated, description of the trajectory. This can be used in a preliminary mission design or as an initial-guess solution for a more detailed local optimiser. This section shows a new set of shaping functions developed for solar sailing and describes their practical use. Lastly, the performances of the proposed shape-based approach as an initial guess for the local optimiser GPOPS-II are shown in a set of case studies.

3.1.1. Pseudo Modified Equinoctial Elements

Because of the different constraints on the available thrust between a solar sail and a classical low-thrust system highlighted in Section 2.1.2, a set of shaping functions for solar sailing has been investigated. Numerical issues can arise if the state vector is expressed in terms of either Cartesian position and velocity or conventional Keplerian elements (KEP). In the first case, each component of the state shows a significant change in time that can undermine the stability of a numerical optimiser. On the other hand, if the conventional Keplerian elements are chosen to describe the state, singularities arise in the cases of circular or planar orbits, for which the line of apsides or the line of the nodes are not defined, respectively [77]. Therefore, the state vector is expressed in terms of MEE. As such, the instantaneous Cartesian position and velocity can be analytically retrieved by means of the following relations [7]:

$$\mathbf{r} = \frac{r}{s^2} \begin{bmatrix} \cos L + \gamma \cos L + 2hk \sin L \\ \sin L - \gamma \sin L + 2hk \cos L \\ 2(h \sin L - k \cos L) \end{bmatrix} \quad (3.1)$$

$$\mathbf{v} = -\frac{1}{s^2} \sqrt{\frac{\mu}{p}} \begin{bmatrix} \sin L + \gamma \sin L - 2hk \cos L + g - 2fhk + \gamma g \\ -\cos L + \gamma \cos L + 2hk \sin L - f + 2ghk + \gamma f \\ -2(h \cos L + k \sin L + fh + gk) \end{bmatrix} \quad (3.2)$$

in which

$$\begin{cases} q = 1 + f \cos L + g \sin L \\ r = p/q \\ \gamma = h^2 - k^2 \\ s^2 = 1 + h^2 + k^2 \end{cases} \quad (3.3)$$

A trajectory in space can be described by a succession of points in time, each one of which lies on an instantaneous ellipse. Three infinities of ellipses exist that share the same Cartesian position but have different instantaneous velocity. That is, a trajectory described as a succession of ellipses is characterised by three degrees of freedom. Such characterisation is referred to as gauge freedom [202]. For each point in time, the osculating ellipse, which is “the two-body orbit the satellite would follow if the perturbing forces were suddenly removed at that instant” [203], is only one among all the possible choices. In particular, the osculating ellipse is that for which the instantaneous Cartesian velocity is exactly the one shown in Eq. (3.2). For this reason, the velocity described by Eq. (3.2) will be referred to as *osculating velocity* v_{osc} throughout this document.

Consider the true longitude L , instead of the time t , as the independent variable and denote with primes the derivatives with respect to it. Therefore, the time is now the sixth element of the state, as follows.

$$\mathbf{x} = [p \ f \ g \ h \ k \ t]^T \quad (3.4)$$

Within this new representation, the instantaneous velocity \mathbf{v} at each point of the trajectory is described by

$$\mathbf{v} = \frac{d\mathbf{r}}{dL} \frac{dL}{dt} = \frac{1}{t'} \left(\frac{\partial \mathbf{r}}{\partial \mathbf{x}} \frac{d\mathbf{x}}{dL} + \frac{\partial \mathbf{r}}{\partial L} \right) \quad (3.5)$$

The velocity described in Eq. (3.5) is the sum between the osculating velocity v_{osc} and a gauge term \mathbf{v}_{gauge} , since the ellipses are, in the generic case, not osculating. Recall the equation of motion for the true longitude as [121]

$$\frac{dL}{dt} = \sqrt{\mu p} \left(\frac{q}{p} \right)^2 = \frac{1}{t'_{osc}} \quad (3.6)$$

Therefore, the osculating velocity is given by

$$\mathbf{v}_{osc} = \frac{1}{t'_{osc}} \frac{\partial \mathbf{r}}{\partial L} \quad (3.7)$$

From Eqs. (3.5) and (3.7), the gauge term of the velocity is given by

$$\mathbf{v}_{gauge} = \mathbf{v} - \mathbf{v}_{osc} = \frac{1}{t'} \left[\frac{\partial \mathbf{r}}{\partial \mathbf{x}} \frac{d\mathbf{x}}{dL} + \left(1 - \frac{t'}{t'_{osc}} \right) \frac{\partial \mathbf{r}}{\partial L} \right] = \frac{1}{t'} \boldsymbol{\Phi} \quad (3.8)$$

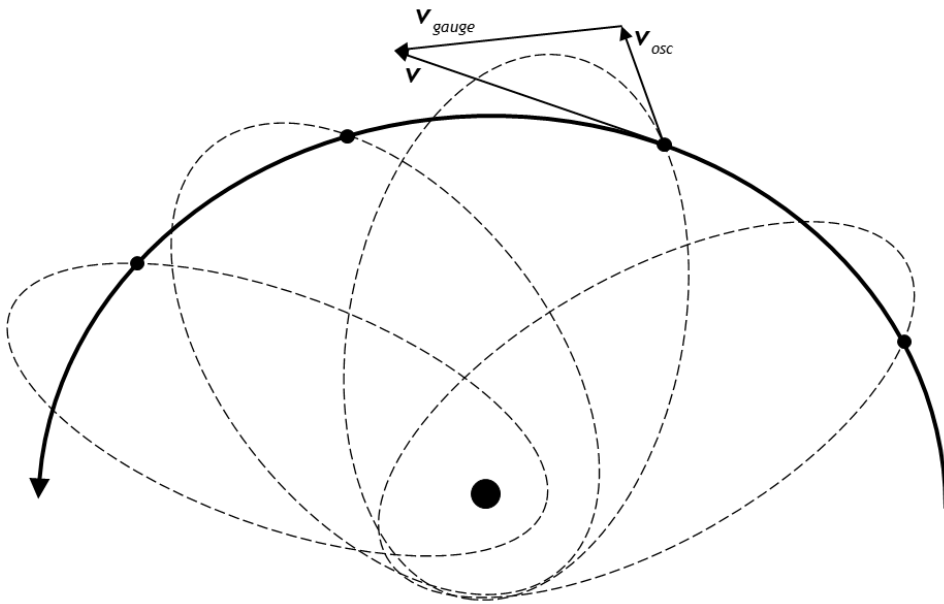


Fig. 3.1. Representation of the trajectory (bold line) as a succession of points on instantaneous ellipses. The generic case for which the gauge term is non-zero is shown.

Figure 3.1 shows a schematic representation of a trajectory described by a succession of points as part of instantaneous ellipses. In the generic case shown, the instantaneous ellipses are not osculating and the velocity is shown for a representative point as the sum of an osculating term and a gauge one.

In the case of a shape-based approach, the trajectory is represented through a set of functions that design the shape of each element of the state as a function of the true longitude. Therefore, there is no *a priori* guarantee that the instantaneous ellipses are osculating. Hence, the MEE that describe the instantaneous state through the chosen set of shaping functions are referred to as pseudo modified equinoctial elements (pMEE) and are denoted by the capital letters. These elements correspond to the classical MEE when the gauge term of the velocity is zero.

3.1.2. Choice of the Shaping Functions

To find a shape of the trajectory that can be achieved with the solar-sail thrust constraints, several shaping functions have been investigated over two test cases. The set of functions that are considered for the choice of the shaping functions to be used in the description of the solar-sail trajectory will be discussed together with the test cases. A coplanar approximation has been made, so that the out-of-plane elements H and K are neglected. Moreover, the time is shaped through its derivative in L . Because of the coplanar approximation considered, an appropriate function to describe the derivative of time is $T' = t'_{osc}$ [131]. From Eq. (3.6), the shaping function for the derivative of time can be rewritten explicitly as

$$T' = \frac{1}{\sqrt{\mu P}} \left(\frac{P}{q} \right)^2 \quad (3.9)$$

Therefore, the formulation of the time as a function of the true longitude is computed as

$$T(L) = \int_{L_0}^L T'(l) dl \quad (3.10)$$

Each one of the three in-plane pMEE $\{P, F, G\}$ is studied separately as a function of the true longitude L . The shaping functions found for these three elements are compared with the linear-trigonometric shape presented in Ref. [9] and shown in Eq. (2.55). For each element, the MATLAB Curve Fitting toolbox [204] has been used to find the function that best fits the data points. Three parameters have been considered to determine the quality of the fit:

- a) Overlapping of the fitting curve with the data
- b) Sum of squares due to error (SSE)
- c) Adjusted R-square (ARS)

To be a good fit, the value of SSE must be close to zero, whereas the value of ARS must be close to one. Therefore, the first decision about the goodness of the selected shaping function is driven by the values of both SSE and ARS given by the MATLAB Curve Fitting toolbox. Subsequently, the overlapping of the fitting curve

with the data, together with the trend given by the extrapolation of the evolution of the curve beyond the data range, is considered to assess the quality of the chosen shaping function. Obviously, this alone is not sufficient as it is not a quantitative parameter and is potentially subject to personal opinions. However, it helps providing a complete assessment as the SSE and ARS alone might be biased by fitting the data rather than the trend.

Test case 1. In the first test case, the heliocentric trajectory of a sail with a constant cone angle of $\alpha = 35$ deg is numerically propagated for seven years, starting from the initial orbit stated in Eq. (3.11).

$$\mathbf{x}_0^{kep} = [r_{\oplus} \ 0.2 \ 0 \ 0 \ 0 \ 2 \text{ rad}]^T \quad (3.11)$$

The sailcraft considered in this test case has a characteristic acceleration $a_c = 0.3 \text{ mm/s}^2$.

It has been noted that the evolution of the in-plane elements $\{P, F, G\}$, as a function of L , is characterised by a short-term periodical component and a secular variation. This is well illustrated in Fig. 3.2, which shows the evolution of $F(L)$ and $G(L)$ for a solar-sail trajectory propagated for twenty years with a constant cone angle $\alpha = 35$ deg.

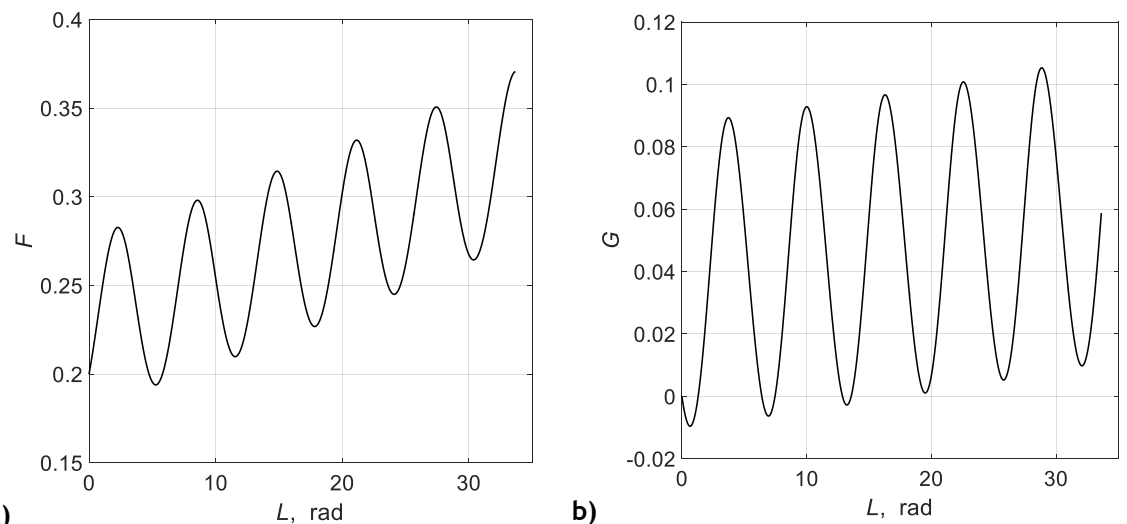


Fig. 3.2. Evolution of the in-plane pMEE F (a) and G (b) over true longitude under the effect of a constant sail angle.

Hence, a function that is the sum of a linear and a sinusoidal term well describes the evolution of the two in-plane elements F and G subject to the acceleration given by a solar sail. The linear-trigonometric shapes proposed in [9] are, therefore, good choices to describe the evolution of these elements. However, a modification of the formulation given in the reference paper has been considered to allow a better flexibility at describing the evolution of F and G , yet without introducing too many free parameters that will significantly increase the computational effort needed to find them. Therefore, the solar-sailing shape (which is a linear-trigonometric shape) is

$$\begin{aligned} F(L) &= F_i + F_F(L - L_0) + \lambda_{fg} \sin(L - L_0 + \varphi_{fg}) \\ G(L) &= G_i + G_F(L - L_0) - \lambda_{fg} \cos(L - L_0 + \varphi_{fg}) \end{aligned} \quad (3.12)$$

in which λ_{fg} and φ_{fg} are, respectively, the shaping and phasing parameters related to the in-plane elements F and G . The terms $\{F_i, F_F, G_i, G_F\}$ depend on the boundary conditions of the problem at hand.

Table 3.1 shows the statistical values used to measure the quality of the fit, whereas Fig. 3.3 shows the fits of the in-plane elements F and G through the solar-sailing shape and the ones from [9].

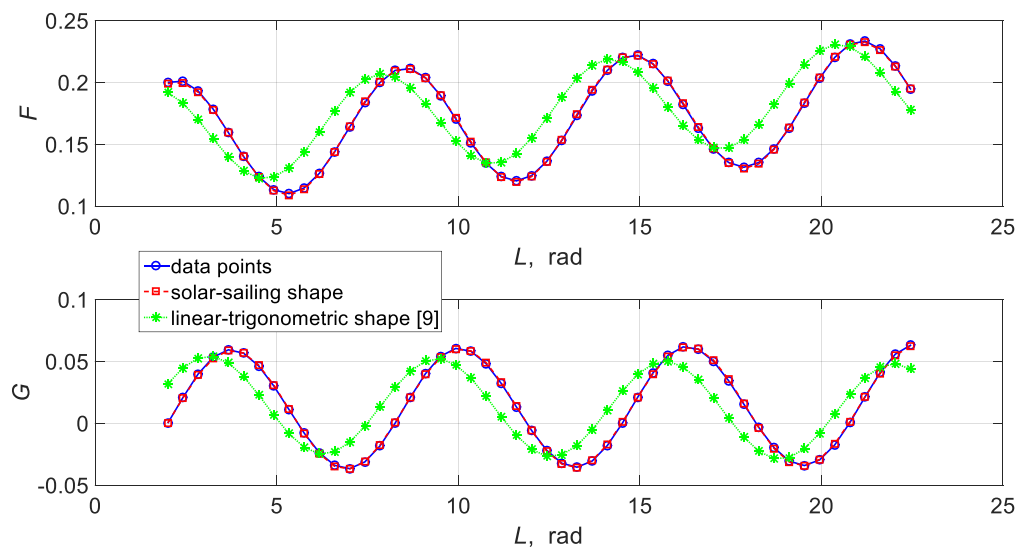


Fig. 3.3. In-plane pMEE F and G over true longitude.

In the case of the semilatus rectum, the secular term prevails over the short-term sinusoidal component. For this reason, the following set of functions have been considered as potential candidates:

1. Linear-trigonometric (LIN-TRIG) shape presented in [9].
2. Exponential-trigonometric (EXP-TRIG) shape presented in [9].
3. Third-order Fourier expansion.
4. Solar-sailing shape, which is an exponential-trigonometric shape of the form

$$P(L) = P_i \exp[P_f(L - L_0)] + \lambda_p \sin(L + \varphi_p) \quad (3.13)$$

in which P_i and P_f depend on the initial and final conditions, λ_p and φ_p are, respectively, the shaping and phasing parameters related to the semilatus rectum.

It is worth mentioning that the exponential-trigonometric shape from [9], which has been considered in both case studies, is the simplified one, which does not consider the trigonometric term. In fact, the Curve Fitting toolbox was not able to satisfy the convergence requirements for the fit computation and stopped without finding any solution, in the case of the general exponential-trigonometric shape shown in [9].

Figure 3.4 shows the fit of the semilatus rectum P against the true longitude L through both the linear-trigonometric shape presented in [9] and the solar-sailing shape of Eq. (3.13). The linear-trigonometric shape (dotted green line with asterisks) does not overlap exactly the data (solid blue line with circles). On the other hand, the solar-sailing shape (dashed red line with squares) fits well with the data points. The quantitative parameters SSE and ARS for both the shaping functions are shown in Table 3.1.

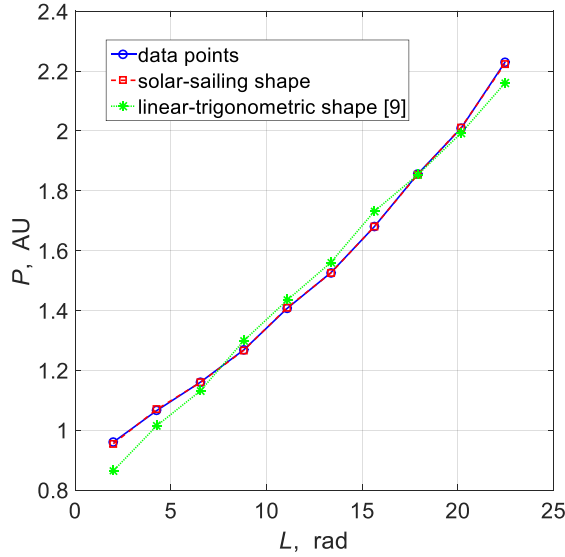


Fig. 3.4. Semilatus rectum over true longitude.

As for the in-plane elements F and G , both the statistical values of the fit and the plot of the fitting curve against the data points show how the new set of solar-sailing shaping functions better describes the solar-sail trajectory than the linear-trigonometric functions presented in [9]. For what concerns the Fourier expansion, a third-order series is characterised by eight free parameters, which reduce to six if the initial and final conditions are considered. Moreover, the statistical results show that this function is not significantly better than the exponential-trigonometric shape of Eq. (3.13). That is, the additional effort needed to find four free parameters more is not justified by better performances. Lastly, also the statistical results related to the exponential-trigonometric shape in [9] describe a fit that is worse than the one of the proposed shaping function.

Table 3.1. Statistical values of the fits for the pMEE P , F , and G .

<i>Statistical values</i>	<i>Shape-based approach</i>	P	F	G
SSE	LIN-TRIG shape in [9]	1.489	0.3972	0.3655
	EXP-TRIG shape in [9]	0.065	-	-
	3 rd order Fourier	0.049	-	-
	Solar-sailing shape	0.004	4.5×10^{-4}	3.9×10^{-4}
ARS	LIN-TRIG shape in [9]	0.9891	0.6991	0.6679
	EXP-TRIG shape in [9]	0.9995	-	-
	3 rd order Fourier	0.9996	-	-
	Solar-sailing shape	1.0000	0.9997	0.9996

Test case 2. For the second test case, an Earth-Mars coplanar orbit transfer through a solar sail with characteristic acceleration of $a_c = 1 \text{ mm/s}^2$ is considered. The reference orbit is computed via an indirect optimisation approach, as in Mengali and Quarta [11]. The statistical values of the fits are shown in Table 3.2, whereas Fig. 3.5 shows the fits of the in-plane pMEE over true longitude for the solar-sailing shape and the linear-trigonometric shape in [9]. In this case, the third order Fourier expansion does show slightly better statistical results than the solar-sailing shape. Nevertheless, such improvement still does not justify the extra effort needed to have six free parameters instead of two.

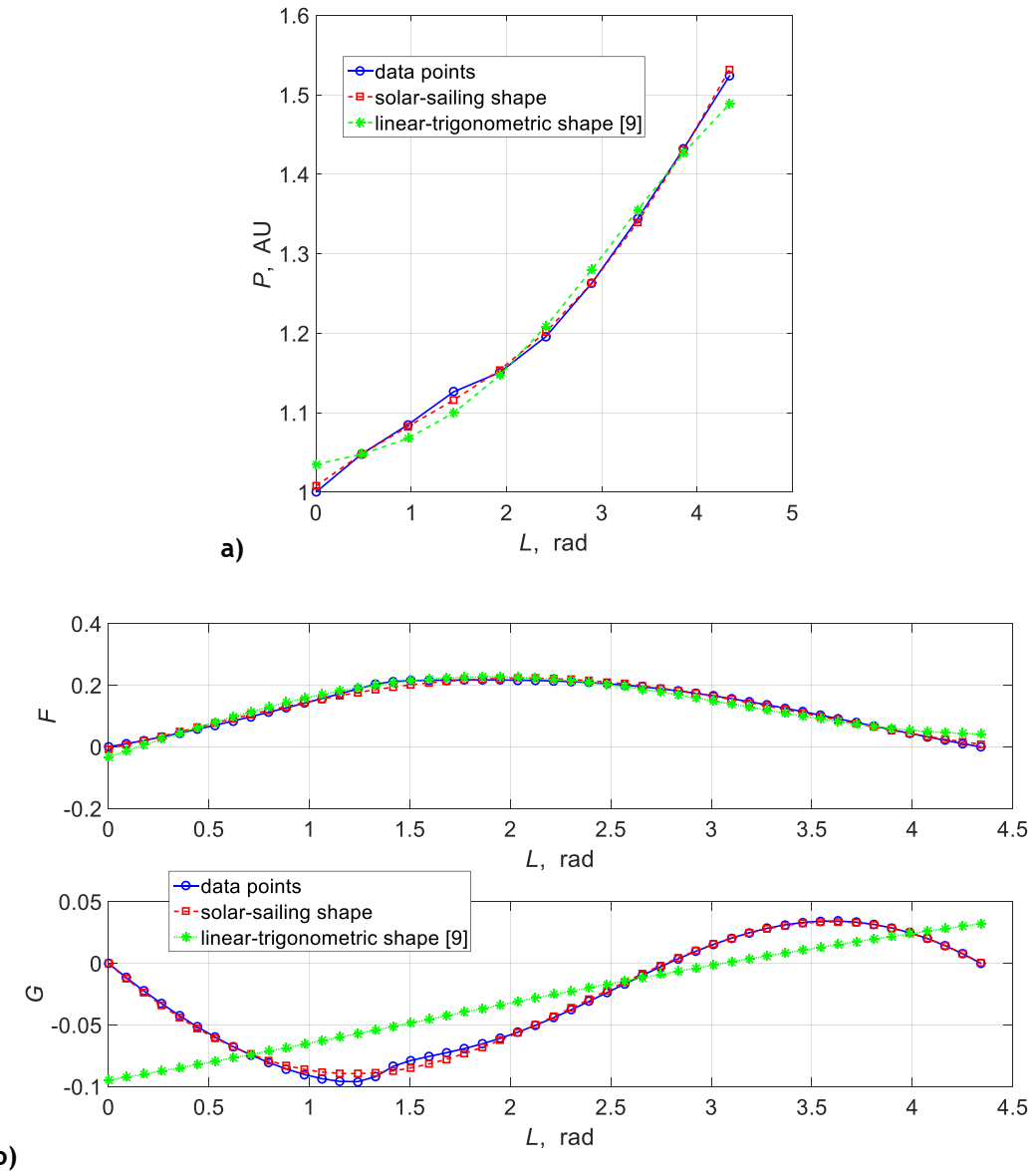


Fig. 3.5. Earth-Mars coplanar orbit transfer. (a) Semilatus rectum and (b) in-plane elements F and G over true longitude.

Table 3.2. Earth-Mars coplanar orbit transfer. Statistical values of the fits for the pMEE P , F , and G .

<i>Statistical values</i>	<i>Shape-based approach</i>	P	F	G
SSE	LIN-TRIG shape in [9]	1.2×10^{-1}	9.5×10^{-2}	3.3×10^{-1}
	EXP-TRIG shape in [9]	2.5×10^{-2}	-	-
	3 rd order Fourier	1.9×10^{-3}	-	-
ARS	Solar-sailing shape	8.9×10^{-3}	1.7×10^{-2}	2.7×10^{-3}
	LIN-TRIG shape in [9]	0.9880	0.9615	0.6512
	EXP-TRIG shape in [9]	0.9975	-	-
ARS	3 rd order Fourier	0.9998	-	-
	Solar-sailing shape	0.9991	0.9928	0.9972

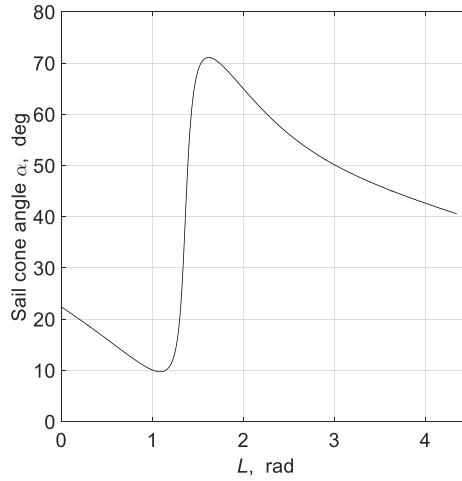


Fig. 3.6. Earth-Mars coplanar orbit transfer. Sail cone angle over true longitude.

Figure 3.5 shows that the fits are slightly worse than in the previous simple case. This happens around $L = 1.5$ rad, which is the value of the true longitude when the control shows a significant change, as shown in Fig. 3.6. Nevertheless, both the fits shown in Fig. 3.5 and the statistical values SSE and ARS shown in Table 3.2 demonstrate the overall quality of the chosen shaping functions. Therefore, from this test case, as well as from the previous one with a constant thrust, it is clear how the new set of shaping functions describes a solar-sail trajectory better than the linear-trigonometric shape used as a reference.

An extension to the three-dimensional (3D) space of the proposed shape-based approach for solar sailing has been studied by González [205].

3.1.3. Study of the Gauge Freedom

The shaping functions chosen to describe the solar-sail trajectory are defined by a succession of non-osculating ellipses. To support this statement, the gauge term of the velocity shown in Eq. (3.8) is studied in detail.

Since the derivative of the time is shaped through its osculating value, as shown in Eq. (3.9), the scaled velocity Φ introduced in Eq. (3.8) can be rewritten as

$$\Phi = \frac{\partial \mathbf{r}}{\partial \mathbf{x}} \frac{d\mathbf{x}}{dL} \quad (3.14)$$

Because of the planar approximation, the values of the out-of-plane elements are constant in L and equal to the values related to the osculating orbit at the initial time, such as

$$\begin{aligned} H(L) &= h_0 \\ K(L) &= k_0 \end{aligned} \quad (3.15)$$

Substituting Eqs. (3.13), (3.12) and (3.15) within Eq. (3.14) and after some mathematical manipulations, the formulation of the scaled velocity is

$$\Phi = \frac{qP' - PF'\cos L - PG'\sin L}{q^2 s^2} \begin{bmatrix} \cos L + \gamma \cos L + 2h_0 k_0 \sin L \\ \sin L - \gamma \sin L + 2h_0 k_0 \cos L \\ 2(h_0 \sin L - k_0 \cos L) \end{bmatrix} \quad (3.16)$$

Eq. (3.16) demonstrates that the gauge term of the velocity is not always null and, therefore, it cannot be neglected. As a consequence, the Cartesian velocity \mathbf{v} cannot be computed through Eq. (3.2) but it must be computed as the sum of the osculating and the gauge term, as shown in Eq. (3.5).

Lastly, this demonstrates that the trajectory is described by a succession of pseudo modified equinoctial elements.

3.1.4. Boundary-Constraint Satisfaction

From Eqs. (3.13), (3.12) and (3.15), recall the formulation of the shaping functions as

$$\begin{aligned} P(L) &= P_i \exp[P_F(L - L_0)] + \lambda_p \sin(L + \varphi_p) \\ F(L) &= F_i + F_F(L - L_0) + \lambda_{fg} \sin(L - L_0 + \varphi_{fg}) \\ G(L) &= G_i + G_F(L - L_0) - \lambda_{fg} \cos(L - L_0 + \varphi_{fg}) \\ H(L) &= h_0 \\ K(L) &= k_0 \end{aligned} \quad (3.17)$$

in which the values of $\{P_i, P_F, F_i, F_F, G_i, G_F\}$ depend on the desired initial and final state. The boundary conditions on initial and final Cartesian position and velocity to be satisfied are

$$\begin{cases} r(P(L_0), F(L_0), G(L_0), H(L_0), K(L_0), L_0) = \mathbf{r}_0 \\ r(P(L_f), F(L_f), G(L_f), H(L_f), K(L_f), L_f) = \mathbf{r}_f \\ \mathbf{v}(P(L_0), F(L_0), G(L_0), H(L_0), K(L_0), L_0) = \mathbf{v}_0 \\ \mathbf{v}(P(L_f), F(L_f), G(L_f), H(L_f), K(L_f), L_f) = \mathbf{v}_f \end{cases} \quad (3.18)$$

Since a planar approximation is considered, Eq. (3.18) describes a system of eight equations in the six unknowns $\{P_i, P_F, F_i, F_F, G_i, G_F\}$. Moreover, the shaping functions in Eq. (3.17) do not describe osculating MEE, as demonstrated in Section 3.1.3. To solve this system, a two-step approach can be followed.

First, the values of the pMEE at initial and final true longitude are set equal to the desired osculating ones. From Eq. (3.17), the first-guess values for $\{P_i, P_F, F_i, F_F, G_i, G_F\}$ are

$$\left\{ \begin{array}{l} P_I = p_0 - \lambda_p \sin(L_0 + \varphi_p) \\ P_F = \frac{1}{L_f - L_0} \ln \left[\frac{p_f - \lambda_p \sin(L_f + \varphi_p)}{P_I} \right] \\ F_I = f_0 - \lambda_{fg} \sin(\varphi_{fg}) \\ F_F = \frac{1}{L_f - L_0} \left[f_f - F_I - \lambda_{fg} \sin(L_f - L_0 + \varphi_{fg}) \right] \\ G_I = g_0 + \lambda_{fg} \cos(\varphi_{fg}) \\ G_F = \frac{1}{L_f - L_0} \left[g_f - G_I + \lambda_{fg} \cos(L_f - L_0 + \varphi_{fg}) \right] \end{array} \right. \quad (3.19)$$

The values found by means of Eq. (3.19) are used as a first guess to solve Eq. (3.18). The modified version of the Levenberg-Marquardt algorithm implemented within the MINPACK subroutine *lmdif*¹ is used for this purpose. Note that the values given by Eq. (3.19) are good first-guess values if the gauge term of the velocity is small enough with respect to the osculating velocity. That is, if $\|\boldsymbol{\Phi}\| \ll \|\partial r / \partial L\|$.

3.1.5. Shaped Trajectory and Control History Generation

In the previous sections, the shaping functions proposed for solar sailing have been presented and discussed. Here, the procedure for the full generation of the shaped trajectory and the control history is presented (Algorithm 3.1).

For a rendezvous problem, as the one considered in this case, the initial time t_0 , as well as the identifiers of the departing and arriving bodies b_0 and b_f , are given. That is, the initial/final desired state can be computed from the ephemerides of the target bodies, given also the time of flight T_{0f} , as

¹ Data available online at <http://www.netlib.no/netlib/minpack/lmdif.f> [retrieved 23 November 2014].

$$\begin{cases} \mathbf{x}_0^{kep} = \mathbf{x}_{b_0}^{kep}(t_0) \\ \mathbf{x}_f^{kep} = \mathbf{x}_{b_f}^{kep}(t_0 + T_{0f}) \end{cases} \quad (3.20)$$

Since a planar approximation of the transfer trajectory is considered, the orbital plane of the arriving target body b_f is projected onto the one of the departing target body b_0 , as follows.

$$\begin{cases} i_{b_f} = i_{b_0} \\ \omega_{b_f} = \omega_{b_f} + (\Omega_{b_f} - \Omega_{b_0}) \\ \Omega_{b_f} = \Omega_{b_0} \end{cases} \quad (3.21)$$

Only once the orbits of the two target bodies lie on the same plane, it is possible to compute the initial/final desired state in terms of MEE, following the definition given in Eq. (2.54).

$$\begin{cases} \mathbf{x}_0^{mee} = [p_0 \ f_0 \ g_0 \ h_0 \ k_0 \ L_0]^T \\ \mathbf{x}_f^{mee} = [p_f \ f_f \ g_f \ h_f \ k_f \ L_f]^T \end{cases} \quad (3.22)$$

in which $L_f = \text{mod}(L_f, 2\pi) + 2n_{rev}\pi$.

Therefore, the set $\{P_I, P_F, F_I, F_F, G_I, G_F\}$ can be obtained through Eq. (3.18), once their first-guess values have been computed from Eq. (3.19). Given the values of the shaping and phasing parameters $\{\lambda_p, \lambda_{fg}, \varphi_p, \varphi_{fg}\}$, the shaped trajectory and the evolution of time are obtained through Eqs. (3.17) and (3.10), respectively. After obtaining the Cartesian position and velocity through Eqs. (3.1) and (3.5), the Cartesian acceleration is obtained as

$$\ddot{\mathbf{r}} = \frac{d\mathbf{v}}{dL} \frac{dL}{dt} \quad (3.23)$$

Substituting Eq. (3.23) into Eq. (2.50), the acceleration needed to follow the shaped trajectory is retrieved in the Cartesian frame. Lastly, the evolution of the cone angle α is analytically retrieved as

$$\alpha = \arccos\left(\frac{\mathbf{a} \cdot \hat{\mathbf{r}}}{\|\mathbf{a}\|}\right) \quad (3.24)$$

Note that the control given by the shape-based approach is only expressed in terms of the cone angle. That is, there is no control over the magnitude of the sail acceleration. Nevertheless, it is worth recalling that the magnitude and direction of the acceleration given by a solar sail are strictly related. Thus, there is only one degree of freedom in the choice of the sail acceleration, in the two-dimensional case.

Algorithm 3.1. Shape-based approach for solar sailing. Procedure to generate the shaped trajectory and the control history.

- 1: Given $\{b_0, b_f, t_0, T_{0f}\}$, compute initial/final desired state in KEP [Eq. (3.20)]
- 2: Project orbital plane of b_f onto the one of b_0 [Eq. (3.21)]
- 3: Given n_{rev} , compute initial/final desired state in MEE [Eq. (3.22)]
- 4: Compute first-guess values for $\{P_i, P_F, F_i, F_F, G_i, G_F\}$ [Eq. (3.19)]
- 5: Compute exact values for $\{P_i, P_F, F_i, F_F, G_i, G_F\}$ by solving the nonlinear system of Eq. (3.18)
- 6: Given $\{\lambda_p, \lambda_{fg}, \varphi_p, \varphi_{fg}\}$, compute the shaping functions [Eq. (3.17)] and the evolution of the time [Eq. (3.10)]
- 7: Compute Cartesian position and velocity [Eqs. (3.1) and (3.5)]
- 8: Compute Cartesian acceleration [Eq. (3.23)]
- 9: Retrieve the evolution of the cone angle α [Eq. (3.24)]

3.1.6. Practical Use of the Shape-Based Approach for Solar Sailing

As shown in Eq. (3.17), given initial and final state, the trajectory is defined by the four free parameters $\mathbf{y} = \{\lambda_p, \lambda_{fg}, \varphi_p, \varphi_{fg}\}$. The acceleration \mathbf{a} needed to follow the shape of the trajectory and defined by the shaping and phasing parameters is then analytically retrieved, as detailed in Algorithm 3.1. The control history is changed by tuning these parameters such that the constraints on the achievable thrust [Eq. (2.18)] are satisfied. To do so, the set of free parameters

\mathbf{y} , together with the time of flight T_{0f} and the number of complete revolutions n_{rev} , are searched with the MATLAB built-in genetic algorithm (GA). Taking into account the heuristic nature of the genetic algorithm, a maximum of 3,000 generations is allowed, resetting the population up to three times in case of stalls.

Because the acceleration needed to follow the shaped trajectory is only retrieved *a posteriori*, a set of nonlinear constraints is implemented within the GA such that the shaped trajectory is as close as possible to a solar-sail trajectory. These are implemented as inequality constraints, since equality constraints reduce the degree of freedom of the problem and thus make it harder to solve, as discussed in [102]. The nonlinear constraints are set so that:

- a) The magnitude of the acceleration is the one that the selected sailcraft can provide.
- b) The acceleration is never directed towards the Sun.
- c) The time of flight T_{0f} is consistent with the shaped time $T(L_f)$ given by Eq. (3.10).

The latter is necessary to make the solution physical, because it is the only link between the time of flight and the shaped trajectory, as discussed in [9, 129]. In fact, the initial and final values of the true longitude depend on the absolute time, since a rendezvous problem is considered. The evolution of time given by Eq. (3.10) is not linked to the physical time evolution, unless the aforementioned nonlinear constraint c) is enforced. Note that such constraint can be solved by means of a Newton loop, as discussed in [129, 131]. However, a metaheuristic algorithm (which is the GA, in this case) needs to be used to find the values of the shaping and phasing parameters and the time of flight to know where the initial/final target objects are. Moreover, the two nonlinear constraints a) - b) must be enforced, despite what happens in the classical low-thrust case. Therefore, the explicit use of the constraint on the time of flight as nonlinear constraint for the GA has proven to be as effective as the use of the Newton loop.

The objective function of the GA can be changed according to the application. In this work, two different objective functions are considered. When used within the sequence-search phase (CHAPTER 4), the shaping functions are found by minimising the time of flight. Note that the evaluation of the objective function by the GA is very fast, since the time of flight is one of the optimisation variables. Therefore, only the evaluation of the function of the constraints requires sensible

computational time. However, because the relation between magnitude and direction of the acceleration is not explicitly constrained, the shaped trajectory can differ from the one propagated by using the control history given by the shape-based approach. In fact, recall that the acceleration needed to follow the shaped trajectory [Eq. (3.23)] is converted into the sail cone angle [Eq. (3.24)]. As such, the acceleration used to propagate the trajectory is that given by Eq. (2.18). For this reason, when the solution of the shape-based approach is used as an initial-guess solution for the local optimiser, three different approaches can be chosen, as follows.

- 1) Minimisation of the time of flight: shaped trajectory. In this case, the initial-guess trajectory is the shaped trajectory related to the minimum time of flight. This choice of initial guess has the advantage that the initial and final values of the state satisfy the end-point constraints. Moreover, the evaluation of such solution is very fast. The drawback is that state and control are not perfectly related. That is, the main task of the optimiser is to change both trajectory and control to satisfy the equations of motion (path constraint).
- 2) Minimisation of the time of flight: propagated trajectory. Also in this case, the minimisation of the time of flight is considered. The initial-guess trajectory is the trajectory found by propagating the initial state with the acceleration given by the shape-based approach. The acceleration vector is interpolated with a constant piecewise law. This choice of initial guess has the advantage that state and control are perfectly consistent with each other. Moreover, the evaluation of such solution is very fast. The drawback of this choice is that the final state can differ from the desired one. That is, the main task of the optimiser is to change both state and control histories to find a feasible solution that satisfies the end-point constraints.
- 3) Minimisation of the error on the final state. In this case, a different objective function can be used. That is, the objective function J is chosen to minimise the error between the final state due to propagation and the final desired state. This objective function is shown in Eq. (3.25), in which $W_1 = 1,000$ and $W_2 = 10$ are two dimensionless weighting factors. These factors have been found after a trial-and-error process and have been

chosen with the purpose of weighting the error in position more than the one in velocity. Despite different weights would produce different solutions, the methodology would not change, and the final choice on the weights is therefore ultimately for the mission analyst. Moreover, position and velocity are scaled so that $r_{\oplus} = 1$ and $\mu = 1$.

$$J = W_1 \| \mathbf{r}_f - \bar{\mathbf{r}}_f \| + W_2 \| \mathbf{v}_f - \bar{\mathbf{v}}_f \| \quad (3.25)$$

In Eq. (3.25), $\bar{\mathbf{r}}_f$ and $\bar{\mathbf{v}}_f$ are the Cartesian position and velocity of the target object at the final time t_f , respectively. On the other hand, the terms \mathbf{r}_f and \mathbf{v}_f are the final values of the Cartesian position and velocity of the propagated trajectory, respectively.

Note that the shape-based approach described above, as well as the majority of shape-based approaches in the literature, deal with rendezvous problems. In fact, if the problem under consideration is an orbit transfer, this approach cannot be used as it is. Therefore, a different implementation of the shape-based approach is developed for orbit transfers. Specifically, in an orbit transfer problem, the spacecraft is not required to be in any specific point on the desired target orbit. Therefore, the number of complete revolutions and the time of flight are replaced by the final true longitude L_f as the unknown of the GA. Consequently, the objective function for the GA to be minimised becomes the final value of the true longitude. Lastly, since T_{0f} is irrelevant, the third nonlinear constraint discussed above can be ignored. In conclusion, the implementation of the shape-based approach for an orbit transfer problem is characterised by one less nonlinear constraint and one less variable to be considered within the GA if compared to the rendezvous problem. The procedure for the full generation of the shaped trajectory and the control history in the case of an orbit transfer is shown in Algorithm 3.2.

Algorithm 3.2. Shape-based approach for solar sailing. Procedure to generate the shaped trajectory and the control history in the case of an orbit transfer.

- 1: Given $\{b_0, t_0\}$, compute initial desired state in KEP [Eq. (3.20)]
- 2: Given b_f , project its orbital plane onto the one of b_0 [Eq. (3.21)]
- 3: Given L_f , compute initial/final desired state in MEE [Eq. (3.22)]
- 4: Compute first-guess values for $\{P_I, P_F, F_I, F_F, G_I, G_F\}$ [Eq. (3.19)]
- 5: Compute exact values for $\{P_I, P_F, F_I, F_F, G_I, G_F\}$ by solving the nonlinear system of Eq. (3.18)
- 6: Given $\{\lambda_p, \lambda_{fg}, \varphi_p, \varphi_{fg}\}$, compute the shaping functions [Eq. (3.17)] and the evolution of the time [Eq. (3.10)]
- 7: Compute Cartesian position and velocity [Eqs. (3.1) and (3.5)]
- 8: Compute Cartesian acceleration [Eq. (3.23)]
- 9: Retrieve the evolution of the cone angle α [Eq. (3.24)]

3.1.7. Assessing the Performances of the Shape-Based Approach for Solar Sailing

The two variants of the shape-based approach with the minimisation of the time of flight (points 1) - 2) of Section 3.1.6) were used to assess the performances of the shape-based approach for solar sailing. The performances of this method, in terms of success rate, are assessed by using it as an initial-guess solution for GPOPS-II for a number of numerical case studies. That is, GPOPS-II is run, for each test case, using each one of the two variants of the shape-based approach as an initial guess. The number of optimal solutions found by GPOPS-II, among all the cases tested, gives an estimate of the goodness of the trajectory and control approximation given by the shape-based approach for solar sailing. Moreover, a third method is used as a benchmark. In this third method, the initial-guess trajectory is the one given by a pseudo solar sail with a constant transversal thrust. A pseudo solar sail is defined here as a solar sail in which magnitude and direction of the thrust are not related, as

$$\mathbf{a}_{pss} = a_c \left(\frac{r_\oplus}{r} \right)^2 \hat{\mathbf{N}} \quad (3.26)$$

The trajectory starts at the initial set time and state and it is propagated for a defined time of flight. In the orbital reference frame, the acceleration is considered being always in the transversal direction, as

$$\mathbf{a}_{pss} = \mathbf{a}_c \left(\frac{r_{\oplus}}{r} \right)^2 [0 \ \pm 1 \ 0]^T \quad (3.27)$$

The \pm sign in Eq. (3.27) represents a thrust directed either towards or opposite to the transversal unit vector $\hat{\mathbf{g}}$ and, therefore, an outward or inward spiral, respectively. Note that a perfectly-reflecting flat solar sail cannot produce the propulsive acceleration of Eq. (3.27) because the direction of such acceleration would be defined by $\alpha = \pi/2$, whereas its magnitude by $\alpha = 0$.

Regarding the numerical case studies, eleven single-leg rendezvous transfers are considered in which the chosen objects are part of the PHA-NHATS database used for the sequence-search phase (CHAPTER 4). Such database is made of PHAs and asteroids part of the Near-Earth Object Human Space Flight Accessible Target Study (NHATS) [206]. By definition, NHATS asteroids are targets possible to reach from the Earth in a short (less than two years) return mission with low total required Δv . PHAs, on the other hand, are in general characterised by higher Δv if reached from the Earth. For this reason, all the transfers considered in this study are so that the first object is either Earth or a NHATS asteroid and the second object is a PHA.

Table 3.3 shows the main properties of the selected objects, whereas Table 3.4 details the properties of the transfers for each case study. Table 3.3 shows that, among the chosen PHAs, seven are characterised by an eccentricity $e > 0.2$ and seven are characterised by an inclination $i > 2$ deg. The departing date and the time of flight for each rendezvous mission listed in Table 3.4 are taken from the results of the search for sequences described in CHAPTER 4. The time of flight is considered only if the transversal-thrust law is used as the initial guess. Both inwards and outwards spirals are considered for the transversal-thrust law, as shown in Eq. (3.27). Note that the ninth and tenth test cases study a transfer between the same couple of asteroids but with different departing times and times of flight (Table 3.4).

Table 3.3. Properties of the objects considered for the single-leg rendezvous missions.

<i>Object</i>	<i>a</i> , AU	<i>e</i>	<i>i</i> , deg	<i>PHA</i>	<i>NHATS</i>
Earth	1	0	0	no	no
2011 CG ₂	1.178	0.158	2.757	yes	yes
2005 TG ₅₀	0.923	0.135	2.402	no	yes
2015 JF ₁₁	1.073	0.111	5.400	yes	no
2012 KB ₄	1.093	0.061	6.328	no	yes
2008 EV ₅	0.958	0.084	7.437	yes	yes
2009 YF	0.936	0.121	1.523	no	yes
2002 AW	1.071	0.256	0.571	yes	no
2010 WR ₇	1.046	0.235	1.563	no	yes
1989 UQ	0.915	0.265	1.299	yes	no
2005 FG	1.122	0.213	3.882	no	yes
1999 AQ ₁₀	0.934	0.236	6.501	yes	no
2008 TX ₃	1.180	0.187	2.180	no	yes
2000 EA ₁₄	1.117	0.202	3.555	yes	no
2004 JN ₁	1.085	0.176	1.499	no	yes
2006 KV ₈₉	1.150	0.273	3.554	yes	no
2001 QE ₇₁	1.078	0.159	3.035	no	yes
2001 US ₁₆	1.356	0.253	1.905	yes	no
2015 EF ₇	1.209	0.225	3.570	no	yes
2000 QK ₁₃₀	1.181	0.262	4.722	yes	no

Table 3.4. Case studies for the single-leg rendezvous missions.

<i>Case study</i>	<i>Departing object</i>	<i>Arrival object</i>	<i>Departing date</i>	<i>Time of flight, days</i>
1	Earth	2011 CG ₂	09 Jan 2029	690
2	2005 TG ₅₀	2015 JF ₁₁	26 Jan 2035	718
3	2012 KB ₄	2008 EV ₅	22 Feb 2031	647
4	2009 YF	2002 AW	23 Aug 2035	607
5	2010 WR ₇	1989 UQ	14 Jun 2024	640
6	2005 FG	1999 AQ ₁₀	19 Nov 2027	711
7	2008 TX ₃	2000 EA ₁₄	30 Aug 2028	740
8	2004 JN ₁	2006 KV ₈₉	31 Mar 2035	896
9	2001 QE ₇₁	2001 US ₁₆	06 Dec 2027	697
10	2001 QE ₇₁	2001 US ₁₆	23 Oct 2027	728
11	2015 EF ₇	2000 QK ₁₃₀	17 Apr 2026	531

An optimal solution to all the case studies shown in Table 3.4 has been sought by using GPOPS-II with the three different initial guesses discussed above. Moreover, the three NLP solvers available in GPOPS-II are used to test them in problems like those ones discussed in this document. An optimisation is defined successful when: a) the NLP solver returns a successful exit flag, b) a further mesh refinement performed by GPOPS-II will not improve the quality of the solution, and c) all the boundaries of time, state and control are verified through a post-processing check. For the sake of conciseness, only the statistical results and the control profiles of a representative case study are shown here. Table 3.5 shows the number of successful cases for each initial guess used. On the other hand, Table 3.6 shows the number of successful cases for each initial guess and each NLP solver used. Figure 3.7a shows the control profile found by means of the shaped-trajectory variant of the shape-based approach for case study 9. The control profile of the optimised trajectory found by GPOPS-II with WORHP, for the same case study, is shown in Fig. 3.7b.

Table 3.5. Number of successful cases for each initial guess.

<i>Initial guess</i>	<i>Number of successful cases</i>
Transversal-thrust law	5/11 (45%)
Shape-based approach - propagated trajectory	10/11 (91%)
Shape-based approach - shaped trajectory	11/11 (100%)

Table 3.6. Number of successful cases for each initial guess and NLP solver.

<i>Initial guess</i>	<i>Number of successful cases</i>		
	IPOPT	SNOPT	WORHP
Transversal-thrust law	3/11 (27%)	4/11 (36%)	4/11 (36%)
Shape-based approach - propagated trajectory	9/11 (82%)	9/11 (82%)	9/11 (82%)
Shape-based approach - shaped trajectory	9/11 (82%)	11/11 (100%)	11/11 (100%)

The overall results show that the use of the shape-based approach as an initial-guess solution helps the convergence of GPOPS-II as ten optimal solutions have been found out of the total number of eleven cases tested with the shape-based

guesses. In fact, an optimal solution has been found for all eleven cases tested with the shaped-trajectory variant of the shape-based algorithm. On the contrary, only five solutions have been found by using the trajectory obtained through the transversal-thrust law as the initial guess. This validates the shape-based approach developed for solar sailing. Moreover, the better performances shown by using the shape-based approach against the transversal-thrust law endorse its use as an initial guess for a high-fidelity direct-collocation optimisation method such as GPOPS-II. The overall statistical results are very similar between the two variants of the shape-based approach used, if no distinction among the NLP solvers is made (Table 3.5). If the number of successful test cases is investigated as a function of both the initial-guess method and the NLP solver used (Table 3.6), it can be seen that, overall, the shaped-trajectory variant of the shape-based approach works better than the propagated-trajectory variant. In fact, the statistical results show a 100% success rate for both SNOPT and WORHP. Nevertheless, Table 3.6 shows that both variants of the shape-based approach, as well as all the available NLP solvers, are robust enough to be used in the early stages of solar-sail trajectory design.

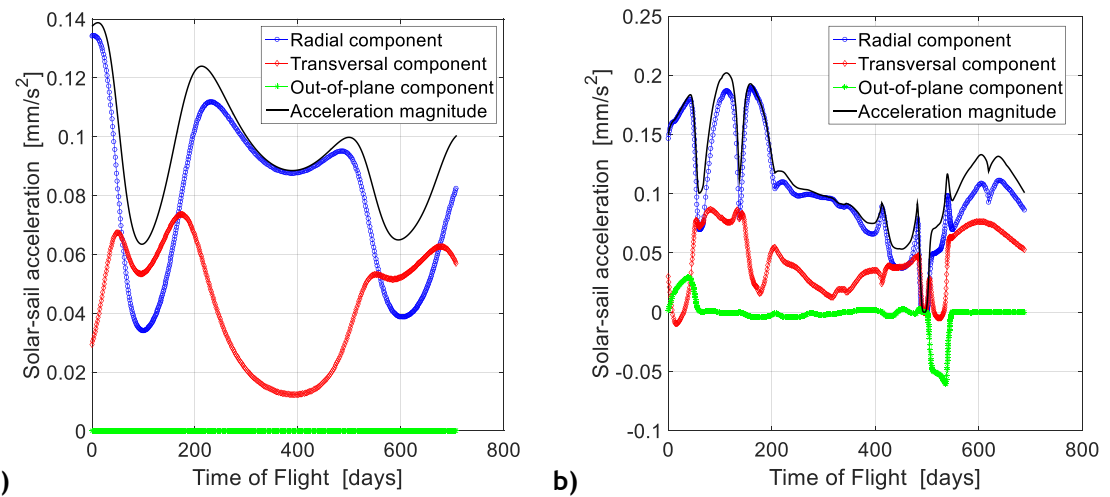


Fig. 3.7. Shape-based approach (Case study 9). Control history found with (a) shape-based approach - shaped trajectory, and (b) GPOPS-II with NLP solver WORHP.

3.2. From Low Thrust to Solar Sailing: A Homotopic Approach

An alternative method, with respect to the shape-based approach, has been developed to quickly find preliminary solar-sail trajectories. The idea behind it is to use a homotopic approach [64], together with a numerical continuation technique [65], to find the desired solar-sail trajectory starting from a classical low-thrust (LT) one. In fact, because of the differences in the control vector between a classical LT propulsion system and a solar sail (Section 2.1.2), a low-thrust OCP can be easier to solve numerically than a solar sail one.

The purpose of this section is to develop an efficient method to find a minimum-time solar-sail transfer, starting from a solution for a low-thrust minimum-time OCP, which can be easier to find or readily available. Given a constant-mass low-thrust solution of the minimum-time OCP, the homotopic transformation is introduced on the propulsive acceleration a . A constant-mass LT is considered because the optimal control law for a LT-propelled spacecraft is transformed to that of a propellantless solar sail. Moreover, finding a solution to the minimum-time LT OCP with no mass variation is even easier than a classical low-thrust OCP. As for the case of the shape-based approach for solar sailing described in Section 3.1, the approximation of planar transfers is considered here. Nevertheless, it has been demonstrated that, for small changes in the inclination, the planar transfers obtained by means of this method are good approximations of the 3D solar-sail solutions [66].

3.2.1. Mathematical Model

Consider a polar inertial reference frame $\{\hat{r}, \hat{\vartheta}\}$ in the ecliptic plane, as shown in Fig. 3.8. The state vector is

$$\mathbf{x}^{pol} = [r \ \vartheta \ u \ v]^T \quad (3.28)$$

in which r is the radial distance of the spacecraft measured from the Sun, ϑ identifies the spacecraft angular position from a fixed axis in space (inertial), u and v are the radial and transversal spacecraft velocities, respectively. In this case, the inertial axis, from which the angular position ϑ is computed, is the

direction of the vernal equinox γ (or first point of Aries) [203], as shown in Fig. 3.8. Therefore, note that ϑ can be actually related to the true longitude L . However, ϑ will be used throughout this Section 3.2 to be consistent with the common notation used for polar coordinates.

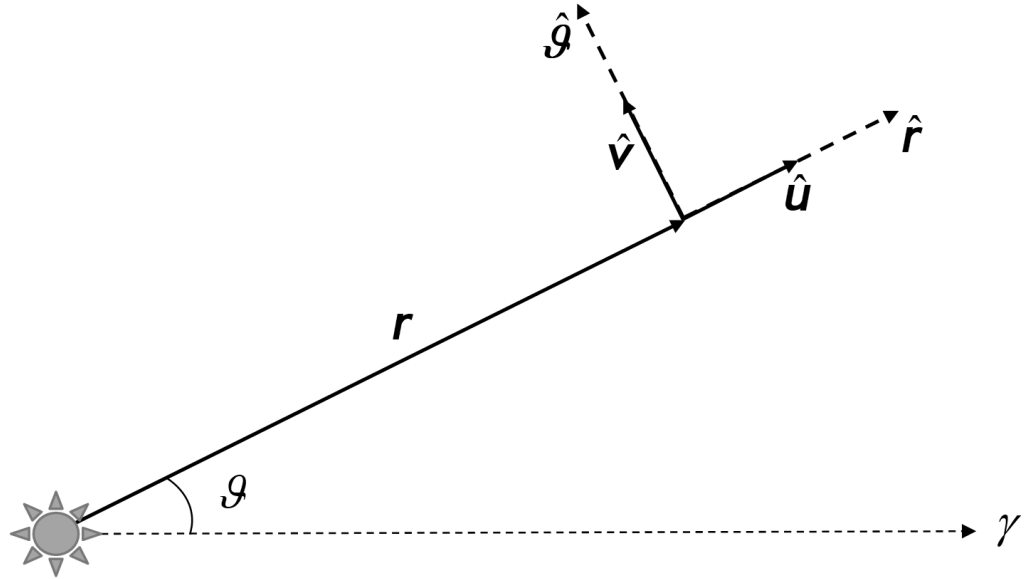


Fig. 3.8. Polar inertial reference frame in the ecliptic plane.

The equations of motion of a spacecraft under the action of gravity and a generic acceleration \mathbf{a} are [11]

$$\dot{\mathbf{x}}^{pol} = \begin{bmatrix} u \\ \frac{v}{r} \\ \frac{v^2}{r} - \frac{\mu}{r^2} + \mathbf{a} \cdot \hat{r} \\ -\frac{uv}{r} + \mathbf{a} \cdot \hat{\theta} \end{bmatrix} \quad (3.29)$$

Denoting with a_{max} the low-thrust maximum acceleration and with $\bar{u} \in [0,1]$ the non-dimensional control, the acceleration \mathbf{a}_{LT} given by a constant-mass low-thrust system is

$$\mathbf{a}_{LT} = \bar{u} a_{max} \begin{bmatrix} \cos \alpha \\ \sin \alpha \end{bmatrix}, \quad \alpha \in [-\pi, \pi] \quad (3.30)$$

The cone angle α has the same meaning as in the solar-sail case, which is the angle between the direction of the acceleration and the radial direction ($\cos\alpha = \mathbf{a}_{LT} \cdot \hat{\mathbf{r}}$). However, in the classical LT case, α can assume any value, as shown in Eq. (3.30). For the sake of clarity, recall the acceleration \mathbf{a}_{ss} given by a solar sail as

$$\mathbf{a}_{ss} = a_c \left(\frac{r_{\oplus}}{r} \right)^2 \cos^2 \alpha \begin{bmatrix} \cos \alpha \\ \sin \alpha \end{bmatrix}, \quad \alpha \in \left[-\frac{\pi}{2}, \frac{\pi}{2} \right] \quad (3.31)$$

Optimal control problem formulation. The optimal control problems are stated for both low-thrust and solar-sail cases [54]. The minimisation of the total transfer time is considered for rendezvous (RV), flyby (FB), and orbit transfer (OT) problems. Therefore, the objective function to be minimised is expressed as

$$J = T_{0f} = t_f - t_0 \quad (3.32)$$

From Eq. (3.32), it is clear that, in this case, the integral cost function is null [see Eq. (2.25)]. Moreover, no path constraints are considered. Therefore, the Hamiltonian defined in Eq. (2.26) becomes

$$\mathcal{H} = \lambda^T \dot{\mathbf{x}}^{pol} \quad (3.33)$$

in which the vector of the costates is defined as $\lambda = [\lambda_r \quad \lambda_g \quad \lambda_u \quad \lambda_v]^T$. The time evolution of the costates is given by

$$\dot{\lambda} = - \left(\frac{\partial \mathcal{H}}{\partial \mathbf{x}^{pol}} \right)^T \quad (3.34)$$

The initial and final boundary conditions are derived for an orbit transfer, a flyby and a rendezvous problem, as follows [11, 207].

$$\left\{ \begin{array}{l} \psi_0^{OT} = \mathbf{x}(t_0) - \bar{\mathbf{x}}_0 = \mathbf{0} \\ \psi_f^{OT} = \begin{bmatrix} r(t_f) - \bar{r}_f \\ \lambda_g(t_f) \\ u(t_f) - \bar{u}_f \\ v(t_f) - \bar{v}_f \\ \mathcal{H}(t_f) + 1 - \lambda^*(t_f) \cdot \frac{\partial \bar{\mathbf{x}}_f}{\partial t_f} \end{bmatrix} = \mathbf{0} \end{array} \right. \quad (3.35)$$

$$\left\{ \begin{array}{l} \psi_0^{FB} = \mathbf{x}(t_0) - \bar{\mathbf{x}}_0 = \mathbf{0} \\ \psi_f^{FB} = \begin{bmatrix} r(t_f) - \bar{r}_f \\ \vartheta(t_f) - \bar{\vartheta}_f \\ \lambda_u(t_f) \\ \lambda_v(t_f) \\ \mathcal{H}(t_f) + 1 - \lambda^*(t_f) \cdot \frac{\partial \bar{\mathbf{x}}_f}{\partial t_f} \end{bmatrix} = \mathbf{0} \end{array} \right. \quad (3.36)$$

$$\left\{ \begin{array}{l} \psi_0^{RV} = \mathbf{x}(t_0) - \bar{\mathbf{x}}_0 = \mathbf{0} \\ \psi_f^{RV} = \begin{bmatrix} \mathbf{x}(t_f) - \bar{\mathbf{x}}_f \\ \mathcal{H}(t_f) + 1 - \lambda^*(t_f) \cdot \frac{\partial \bar{\mathbf{x}}_f}{\partial t_f} \end{bmatrix} = \mathbf{0} \end{array} \right. \quad (3.37)$$

The term $\bar{\mathbf{x}}_0$ Eqs. (3.35) - (3.37) is the initial state of the departing object, whereas the terms $\{\bar{\mathbf{x}}_f, \bar{r}_f, \bar{\vartheta}_f, \bar{u}_f, \bar{v}_f\}$ are referred to the final state of the arrival object. The last scalar boundary condition in Eqs. (3.36) - (3.37) is the transversality condition on the Hamiltonian [Eq. (2.31)].

The optimal control laws for both low thrust and solar sail are derived by minimising of the Hamiltonian with respect to the control variables. Consider the first-order necessary condition for optimality and assume that no singular arcs occur. That is, $(\lambda_u, \lambda_v) \neq (0, 0)$ always. This hypothesis has been numerically verified *a posteriori* for all the cases tested. Considering the Pontryagin's minimum principle, the optimal control law, in terms of the cone angle, is

$$\alpha^* = \operatorname{argmin}_{\alpha} \mathcal{H} \quad (3.38)$$

For the case of a constant-mass low-thrust system, the optimal control law is what is usually referred to as a bang-bang thrust profile. That is, $\bar{u} = 1$ and the magnitude of the acceleration is the maximum available in all points of the trajectory. The optimal direction of the thrust can be expressed, as a function of the costates, as [102]

$$\cos \alpha^* = -\frac{\lambda_u^*}{\sqrt{(\lambda_u^*)^2 + (\lambda_v^*)^2}}, \quad \sin \alpha^* = -\frac{\lambda_v^*}{\sqrt{(\lambda_u^*)^2 + (\lambda_v^*)^2}} \quad (3.39)$$

in which $\alpha^* \in [-\pi, \pi]$. On the other hand, for the case of a solar sail, Eq. (3.38) becomes [2]

$$\tan \alpha^* = \left(\frac{-3\lambda_u^* - \sqrt{9(\lambda_u^*)^2 + 8(\lambda_v^*)^2}}{4\lambda_v^*} \right) \quad (3.40)$$

in which $\alpha^* \in \left[-\frac{\pi}{2}, \frac{\pi}{2} \right]$. It is worth noting that the optimal control law described by Eq. (3.40) is defined for any values of $(\lambda_u^*, \lambda_v^*)$. In fact, it can be demonstrated that $\lim_{\lambda_v^* \rightarrow 0} \alpha^* = 0$, if $\lambda_u^* < 0$, and $\lim_{\lambda_v^* \rightarrow 0} \alpha^* = -\frac{\pi}{2}$, if $\lambda_u^* > 0$.

3.2.2. Homotopy-Continuation Approach

In this section, the use of the homotopy to link the shooting functions relative to the low-thrust and solar-sail OCPs is described. The shooting function for a single OCP is represented by the nonlinear function $\Gamma(\mathbf{z}) : \mathbb{R}^n \rightarrow \mathbb{R}^m$, in which n represents the number of optimisation variables and m is the number of nonlinear scalar equations included in Γ [208]. The zeros of the shooting function represent the solution of the optimal control problem. For the OCPs at hand, such function is expressed as

$$\Gamma(\mathbf{z}) = \psi_f \quad (3.41)$$

in which \mathbf{z} is the vector of the optimisation variables given by the initial values of the costates $\lambda(t_0)$ and the time of flight T_{0f} , as follows.

$$\mathbf{z} = \begin{bmatrix} \lambda(t_0) \\ T_{0f} \end{bmatrix} \quad (3.42)$$

Introducing the homotopic parameter $\varepsilon \in [0,1]$ to link the solutions of the OCPs throughout the homotopy, the shooting function becomes $\Gamma(\mathbf{z}, \varepsilon) : \mathbb{R}^n \times \mathbb{R} \rightarrow \mathbb{R}^m$. When $\varepsilon = 0$, the shooting function is the one relative to the classical low-thrust problem, whereas, when $\varepsilon = 1$, the shooting function is the one relative to the solar-sail problem.

Two linear homotopic transformations on the spacecraft acceleration are considered and the related homotopic parameters are referred to as ε_1 and ε_2 , respectively. The first homotopic transformation is introduced as

$$\mathbf{a} = \mathbf{a}_{LTSS} = a_{\max} \left[(1 - \varepsilon_1) \bar{\mathbf{a}} + \left(\left(\frac{r_{\oplus}}{r} \right)^2 \cos^2 \alpha \right) \varepsilon_1 \right] \begin{bmatrix} \cos \alpha \\ \sin \alpha \end{bmatrix}, \quad \alpha \in [-\pi, \pi] \quad (3.43)$$

The corresponding shooting function is

$$\Gamma_1(\mathbf{z}, \varepsilon_1) = \mathbf{0} \quad (3.44)$$

The relation in Eq. (3.43) links the low-thrust acceleration of Eq. (3.30) to the one that can be provided by a pseudo solar sail, given by Eq. (3.31) with $a_c = a_{\max}$.

Here, the term *pseudo solar sail* is referred to the fact that no constraint on the thrust direction are enforced. That is, the pseudo-solar-sail solution of $\Gamma_1(\mathbf{z}, 1) = \mathbf{0}$ can be characterised by some points in the trajectory in which the acceleration is directed towards the Sun. Nevertheless, such solution is used as initial guess for the computation of the solar-sail OCP through a single-shooting approach. That is,

the zeros of $\Gamma_1(\mathbf{z}, 1) = \mathbf{0}$ are computed subject to the constraint $\alpha \in \left[-\frac{\pi}{2}, \frac{\pi}{2} \right]$. In

all the numerical cases tested, the pseudo-solar-sail solution was always a good initial guess for the direct computation of the solar-sail solution. Therefore, a second homotopic transformation to link the solution of Eq. (3.44) with the solar-sail OCP by continuously changing the boundaries on the cone angle, as shown in [209], was not necessary.

The second linear homotopic transformation is introduced as the desired characteristic acceleration can be different with respect to the corresponding low-thrust acceleration (i.e. $a_c \neq a_{\max}$). This second transformation allows linking the initial solar-sail solution with $a_c = a_{c,0} = a_{\max}$ to the final one, which is characterised by $a_c = a_{c,f} \neq a_{\max}$, as

$$\mathbf{a} = \left[(1 - \varepsilon_2) a_{c,0} + \varepsilon_2 a_{c,f} \right] \left(\left(\frac{r_{\oplus}}{r} \right)^2 \cos^2 \alpha \right) \begin{bmatrix} \cos \alpha \\ \sin \alpha \end{bmatrix}, \quad \alpha \in \left[-\frac{\pi}{2}, \frac{\pi}{2} \right] \quad (3.45)$$

Note that the expression of the acceleration \mathbf{a} in Eq. (3.45) is the same as the one of a solar sail shown in Eq. (3.31), considering a modified characteristic acceleration given by

$$a_c = (1 - \varepsilon_2) a_{c,0} + \varepsilon_2 a_{c,f} \quad (3.46)$$

In this case, the corresponding shooting function is

$$\Gamma_2(\mathbf{z}, \varepsilon_2) = \mathbf{0} \quad (3.47)$$

Numerical continuation. For both homotopies, which are described in terms of the shooting functions of Eqs. (3.44) and (3.47), the zeros of the solar-sail shooting function can be computed by using numerical continuation, starting from the low-thrust solution \mathbf{z}_{LT} (Algorithm 3.3). This technique allows following the so-called zero-path of the homotopy (i.e. the locus of solutions $(\mathbf{z}, \varepsilon)$ of the system $\Gamma(\mathbf{z}, \varepsilon) = \mathbf{0}$) by numerically changing the parameter ε , starting from the solution at $\varepsilon = 0$ until computing the final solution at $\varepsilon = 1$. The numerical continuation used to solve the problem at hand is implemented in the form of discrete continuation [208, 210]. That is, the value of the parameter ε is progressively increased and, at each step, the solution of an intermediate OCP is computed. Each intermediate solution is used as a starting point for the computation of the following problem until the solution of the desired problem is found. The continuation step size is determined as follows, starting by a defined initial value. If the solution of an intermediate problem is found, the algorithm doubles the step size to speed up the continuation process. On the contrary, if no solution is found

for the current intermediate problem, the step size is halved and the continuation iteration is run again with a decreased step size until convergence is reached. If the new step size is below a defined threshold $\delta\epsilon_{min}$, the algorithm terminates unsuccessfully.

Algorithm 3.3. Homotopy-continuation approach.

```

1: Given  $\{t_0, b_0\}$ , compute  $x_0^{pol}$ 
2: Given  $\mathbf{z}_{LT} = [\lambda_{LT}^T(t_0) \ T_{0f}]^T$ , initialise  $\mathbf{z} = \mathbf{z}_{LT}$ 
3: Define  $\{\epsilon, \delta\epsilon, \delta\epsilon_{min}, \delta\epsilon_{max}\}$  s.t.  $\epsilon > \delta\epsilon$ 
4: While  $\epsilon < 1$ , Do
5:   Solve  $\Gamma(\mathbf{z}, \epsilon) = \mathbf{0} \rightarrow \{\mathbf{z}_{tmp}, exitflag\}$ 
6:   If  $exitflag < 0$ , Then
7:      $\epsilon = \epsilon - \delta\epsilon$ 
8:      $\delta\epsilon = \delta\epsilon/2$ 
9:   If  $\delta\epsilon < \delta\epsilon_{min}$ , Then
10:    Termination (Unsuccessful)
11:   End If
12:    $\epsilon = \epsilon + \delta\epsilon$ 
13: Else
14:   Update  $\mathbf{z} = \mathbf{z}_{tmp}$ 
15:   If  $\epsilon < 1$ , Then
16:      $\delta\epsilon = 2\delta\epsilon$ 
17:      $\epsilon = \epsilon + \delta\epsilon$ 
18:   Else
19:     Termination (Successful)
20:   End If
21: End If
22: End Do

```

Since the first homotopic transformation shown in Eq. (3.43) introduces some complexity in the OCP formulation discussed in Section 3.2.1, a close look at the transformed OCP formulation is given in the following subsection. On the contrary, the second homotopic transformation does not affect the OCP formulation, being the homotopy related to the value of the characteristic acceleration only.

Transformed optimal control problem formulation. The equations of motion that describe the evolution in time of the state of the spacecraft during the first homotopy are

$$\dot{\mathbf{x}}_{LTSS}^{pol} = \begin{bmatrix} u \\ v \\ r \\ \frac{v^2}{r} - \frac{\mu}{r^2} \\ -\frac{uv}{r} \end{bmatrix} + a_{\max} \left[(1 - \varepsilon_1) \bar{u} + \left(\left(\frac{r_{\oplus}}{r} \right)^2 \cos^2 \alpha \right) \varepsilon_1 \right] \begin{bmatrix} 0 \\ 0 \\ \cos \alpha \\ \sin \alpha \end{bmatrix} \quad (3.48)$$

The part of the Hamiltonian that depends only on the control variables \bar{u} and α is denoted by $\tilde{\mathcal{H}}$ and expressed as

$$\tilde{\mathcal{H}} = \lambda^T \mathbf{a}_{LTSS} = \tilde{A} \sin \alpha + \tilde{B} \cos \alpha + \tilde{C} \cos^3 \alpha + \tilde{D} \sin \alpha \cos^2 \alpha \quad (3.49)$$

in which

$$\begin{aligned} \tilde{A} &= \lambda_v ((1 - \varepsilon_1) \bar{u} a_{\max}), & \tilde{B} &= \lambda_u ((1 - \varepsilon_1) \bar{u} a_{\max}) \\ \tilde{C} &= \lambda_u \left(\varepsilon_1 a_{\max} \left(\frac{r_{\oplus}}{r} \right)^2 \right), & \tilde{D} &= \lambda_v \left(\varepsilon_1 a_{\max} \left(\frac{r_{\oplus}}{r} \right)^2 \right) \end{aligned} \quad (3.50)$$

Accordingly, the time evolution of the costates, shown in Eq. (3.34), becomes

$$\begin{cases} \dot{\lambda}_r = \lambda_u \left(\frac{v^2}{r^2} - \frac{2\mu}{r^3} + \frac{2\varepsilon_1 a_c r_{\oplus}^2 \cos^3 \alpha}{r^3} \right) - \lambda_v \left(\frac{uv}{r^2} - \frac{2\varepsilon_1 a_c r_{\oplus}^2 \cos^2 \alpha \sin \alpha}{r^3} \right) + \lambda_g \left(\frac{v}{r^2} \right) \\ \dot{\lambda}_g = 0 \\ \dot{\lambda}_u = -\lambda_r + \lambda_v \left(\frac{v}{r} \right) \\ \dot{\lambda}_v = -\lambda_g \left(\frac{1}{r} \right) + \lambda_v \left(\frac{u}{r} \right) - \lambda_u \left(\frac{2v}{r} \right) \end{cases} \quad (3.51)$$

The first-order optimality condition, shown in Eq. (3.38), becomes

$$\begin{aligned} \frac{\partial \tilde{\mathcal{H}}}{\partial \alpha} = & (\tilde{A} + \tilde{D})\chi^6 + 2(\tilde{B} + 3\tilde{C})\chi^5 + (\tilde{A} - 11\tilde{D})\chi^4 + \\ & + 4(\tilde{B} - 3\tilde{C})\chi^3 - (\tilde{A} - 11\tilde{D})\chi^2 + 2(\tilde{B} + 3\tilde{C})\chi - (\tilde{A} + \tilde{D}) = 0 \end{aligned} \quad (3.52)$$

in which $\chi = \tan\left(\frac{\alpha}{2}\right)$, thus $\alpha = 2\tan^{-1}(\chi)$. On the hypothesis that no singular arcs occur, the first-order optimality condition for \bar{u} leads to

$$\bar{u} = \begin{cases} 1 & \text{if } (\lambda_u \cos \alpha + \lambda_v \sin \alpha) < 0 \\ 0 & \text{if } (\lambda_u \cos \alpha + \lambda_v \sin \alpha) > 0 \end{cases} \quad (3.53)$$

It should be noted that no analytical solution exists for the roots of the sixth-order polynomial of Eq. (3.52), in the generic case in which both $\lambda_u \neq 0$ and $\lambda_v \neq 0$. Therefore, the optimal control can be only found by means of a numerical algorithm able to compute the optimal values \bar{u}^* and α^* that minimise $\tilde{\mathcal{H}}$. That is, for each value of the non-dimensional control \bar{u} in Eq. (3.53), the real roots of the sixth-order polynomial of Eq. (3.52) are numerically computed. Therefore, the value of $\tilde{\mathcal{H}}$ is evaluated for all the sets of solutions (α, \bar{u}) , retrieving the optimal control as

$$(\alpha^*, \bar{u}^*) = \arg \min \tilde{\mathcal{H}}(\alpha, \bar{u}) \quad (3.54)$$

3.2.3. Numerical Test Cases

In this section, four numerical test cases are presented (Table 3.7). The first two test cases are considered to validate the proposed approach. As such, two planar circular-to-circular Earth-Mars orbit transfers are studied with different values of the sail characteristic acceleration. In these cases, the proposed homotopic approach is compared with both a conventional solution method, which is based on the use of a metaheuristic algorithm, and the results found in the literature. The last two test cases are considered to assess the performances of the proposed method in computing a solution to a planar rendezvous OCP. As such, two planar rendezvous transfers from Earth to asteroid (99942) Apophis are considered with different values of the sail characteristic acceleration. In these

last two test cases, the results found by means of the proposed homotopic approach are compared with those ones shown in [211].

Table 3.7. Homotopic approach: numerical test cases.

	a_c , mm/s ²	Problem
Test case 1	1	Earth-Mars orbit transfer
Test case 2	0.1	Earth-Mars orbit transfer
Test case 3	0.6	Earth-Apophis rendezvous
Test case 4	0.12	Earth-Apophis rendezvous

Table 3.8 shows the main properties, in terms of Keplerian elements, of both Mars and Apophis. Apophis orbit is considered coplanar with the ecliptic plane. This assumption is reasonable in a first approximation, being its inclination only 3.3 deg [66]. The Earth orbit is considered circular with radius $r_{\oplus} = 1$ AU.

Table 3.8. Homotopic approach: Keplerian elements of the target objects on 14 Feb 2016. The inclination of both objects is assumed equal to zero.

Object	a , AU	e	i , deg	Ω , deg	ω , deg	ν , deg
Mars ¹	1.52368	(0)	(0)	(0)	(0)	(0)
(99942) Apophis ²	0.92228	0.191	(0)	204.5	126.4	283.4

The tolerances on the errors on the final state have been set to 1,000 km, for the position, and 0.1 m/s, for both the radial and transversal velocities, as stated in [11]. These tolerances are the same for all the test cases considered in this section. It is also worth mentioning that a C++ implementation of the Bulirsch-Stoer algorithm has been used to propagate the equations of motion more efficiently, with higher accuracy and lower computational effort than the conventional ordinary differential equation (ODE) solvers [212]. The absolute and relative tolerances for the propagator have both been set to 10^{-8} [11]. All the simulations have been performed in MATLAB on a 3.4 GHz Core i7-3770 with 16 GB

¹ The orbit of Mars is assumed planar and circular. Moreover, only the semimajor axis is considered, being Mars used only for orbit-transfer problems. The value of the semimajor axis is the same as the one considered in [11].

² Data available online at <https://cneos.jpl.nasa.gov/orbits/elements.html> [retrieved 08 August 2015].

of RAM, running Linux Ubuntu 14.04. In the next subsections, the four test cases are discussed in detail.

Validation of the homotopic approach: Earth-Mars orbit transfer. The first two test cases have been considered for the purpose of (a) validating the novel method proposed for computing solar-sail OCPs and (b) comparing its performances with respect to a conventional GA method used to solve the same solar-sail OCPs. The objective function to be minimised within the GA is the Euclidean L^2 norm of the shooting function ($\|\Gamma_1(z, 1)\|$ or $\|\Gamma_2(z, 1)\|$, according to the specific test case).

Twenty different sets of settings have been considered for the GA simulations, differing in the population size ($Population = \{50, 100, 150, 200, 500\}$) and the maximum number of generations allowed ($MaxGenerations = \{500, 1000, 1500, 2000\}$). Because of the heuristic nature of the GA, each set of settings has been run 100 times and statistical values have been considered for the comparison. Moreover, the solutions from GA have been refined by means of a gradient-based method, which is implemented in the *interior-point* algorithm in the MATLAB function *fmincon*. The results for GA are expressed in terms of success rate of each set of settings, which is the percentage of runs (out of 100) that terminate with at least one feasible solution (a solution within the required tolerances). It has been noted that GA showed improved performances (in terms of both computational time and success rate) if the transversality condition (which is the last scalar boundary condition in Eqs. (3.35) - (3.37)) was not considered. From an analytical point of view, it can be demonstrated that the transversality condition is negligible, at least for what concerns the problems at hand [66, 102, 103]. For these reasons and for the sake of consistency, the transversality condition on the Hamiltonian has been excluded in all the numerical cases considered throughout this section. Nevertheless, it has been verified *a posteriori* that the transversality condition was always verified. Because of the transversality-condition avoidance, Eqs. (3.44) and (3.47) reduce to an underdetermined system of nonlinear equations. That is, a least-square numerical solver [213] is needed to find the solutions of such system within the homotopic approach. However, it has been empirically verified that this approach is both

numerically stable and faster than (or, at least, as fast as) solving a square system, at least for the cases tested.

The first test case is the planar circular-to-circular Earth-Mars orbit transfer described in [11]. The low-thrust maximum acceleration has been considered the same as the characteristic acceleration in the reference paper. That is, $a_{\max} = a_c = 1 \text{ mm/s}^2$. The results of both the homotopy approach and the GA are shown in Table 3.9. The first row of Table 3.9 shows the number of sets with a success rate above 90% (note that the homotopy can only be either successful or not successful, since it is a deterministic approach). For the GA, the computational time is the lowest average computational time among all the sets of settings with a success rate above 90%. In Table 3.9, the minimum and maximum values of the time of flight are shown for the GA. The result obtained through the homotopy approach is consistent with those obtained via the GA method. Moreover, the result found by means of the homotopic approach is in perfect agreement with what shown in [11] (i.e. $T_{0f} = 407.7$ days). Only eight sets of settings of the GA out of twenty have a success rate above 90% and the homotopy method is 42% faster than the GA.

Table 3.9. Homotopic approach: homotopy and GA results comparison (Test case 1).

	Homotopy	GA
Sets with success rate above 90%	-	8/20
Computational time, s	11	19
T_{0f} , days	407.72	407.69 (min) 407.72 (max)

Figure 3.9a shows the evolution of the cone angle over time during the first continuation, which is from low thrust (green thick dashed line) to pseudo solar sail (red thick continuous line), as shown in Eq. (3.43). All the intermediate solutions are represented by thin cyan lines. Figure 3.9b shows the comparison between the low-thrust (green dashed line) and the solar-sail (red continuous line) cone angle over time. Figures 3.10a and 3.10b show the low-thrust and solar-sail transfer trajectories, respectively. A plot of the acceleration vector along the transfer is also shown. Figure 3.11a shows the zero-path of the homotopy, as

defined in [201], whereas Fig. 3.11b shows the evolution of the continuation parameter during the first continuation.

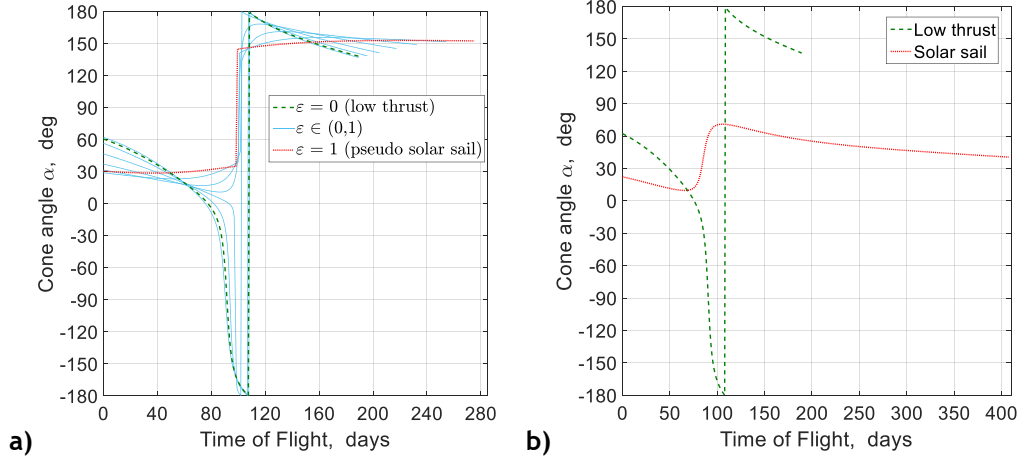


Fig. 3.9. Homotopic approach (Test case 1). Control history for coplanar circular-to-circular Earth-Mars orbit transfer ($a_c = 1 \text{ mm/s}^2$). (a) Cone angle evolution during first continuation. (b) Low-thrust and solar-sail cone angle evolution.

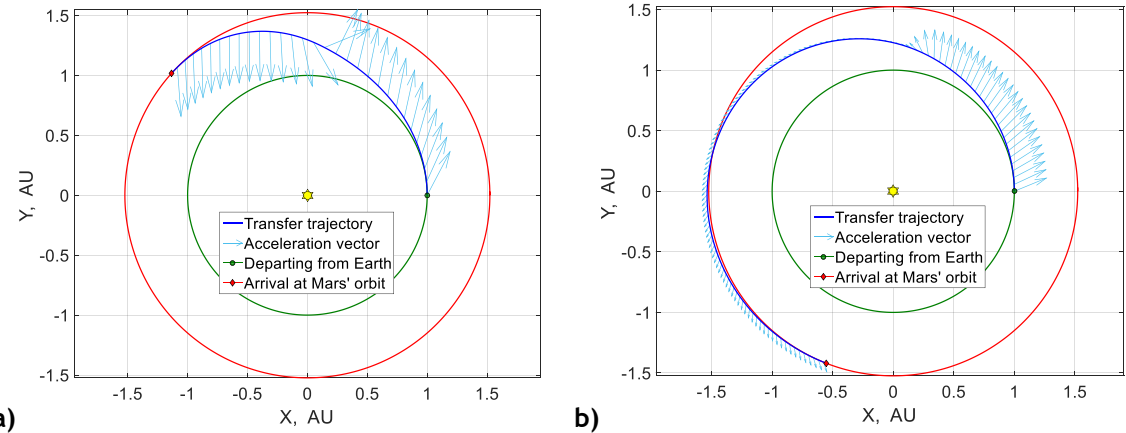


Fig. 3.10. Homotopic approach (Test case 1). Ecliptic plane view of the transfer trajectories for coplanar circular-to-circular Earth-Mars orbit transfer ($a_c = 1 \text{ mm/s}^2$). (a) Low thrust. (b) Solar sail.

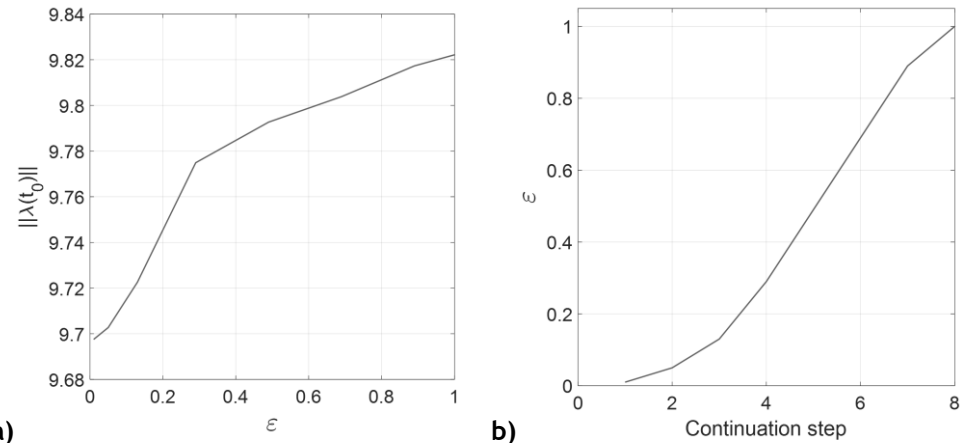


Fig. 3.11. Homotopic approach (Test case 1). (a) Zero-path. (b) Evolution of ε .

A second scenario has been tested, considering the same problem but with a smaller solar-sail characteristic acceleration (i.e. $a_c = 0.1 \text{ mm/s}^2$). That is, the second continuation, described in Eq. (3.45), can be applied to the solution of the previous test case. On the other hand, the optimisations through GA shall be repeated with the new value of the characteristic acceleration. Table 3.10 shows the comparison between the results of the homotopy approach and GA. The computational time shown for the homotopic approach is the one needed to find a solution to the second continuation only, starting from the solution of the first one found in the previous test case. Note that this scenario is purely of academic interest. In fact, it is unlikely that anybody would ever launch a seven-year solar-sail mission to Mars. Nevertheless, this scenario is a good test bed for the second continuation, given the long flight time.

Table 3.10. Homotopic approach: homotopy and GA results comparison (Test case 2).

	<i>Homotopy</i>	<i>GA</i>
Sets with success rate above 90%	-	14/20
Computational time, s	1	16
T_{0f} , days	2661.51	2661.34 (min) 2661.43 (max)

Figure 3.12a shows the evolution of the cone angle during the second continuation, in which the characteristic acceleration changes from $a_{c,0} = 1 \text{ mm/s}^2$ to $a_{c,f} = 0.1 \text{ mm/s}^2$. Figure 3.12b shows the planar circular-to-circular Earth-Mars orbit-transfer trajectory through a solar sail with $a_c = 0.1 \text{ mm/s}^2$. As for Test case 1, the plots of the zero-path of the homotopy and the evolution of the continuation parameter are shown in Fig. 3.13. In this case, the continuation parameter needs to be halved several times when the solution of the intermediate problem is not found, as described in Algorithm 3.3. Nonetheless, despite the larger number of continuation steps with respect to Test case 1, the convergence of the algorithm is very fast, as shown in Table 3.10.

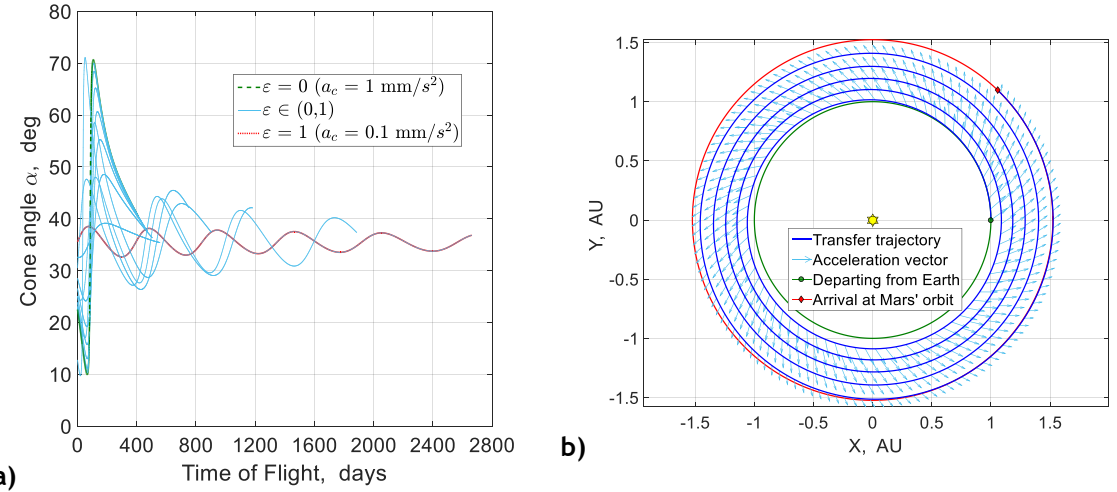


Fig. 3.12. Homotopic approach (Test case 2). Coplanar circular-to-circular Earth-Mars orbit transfer ($a_c = 0.1 \text{ mm/s}^2$). (a) Cone angle evolution. (b) Solar-sail transfer trajectory (ecliptic plane view).

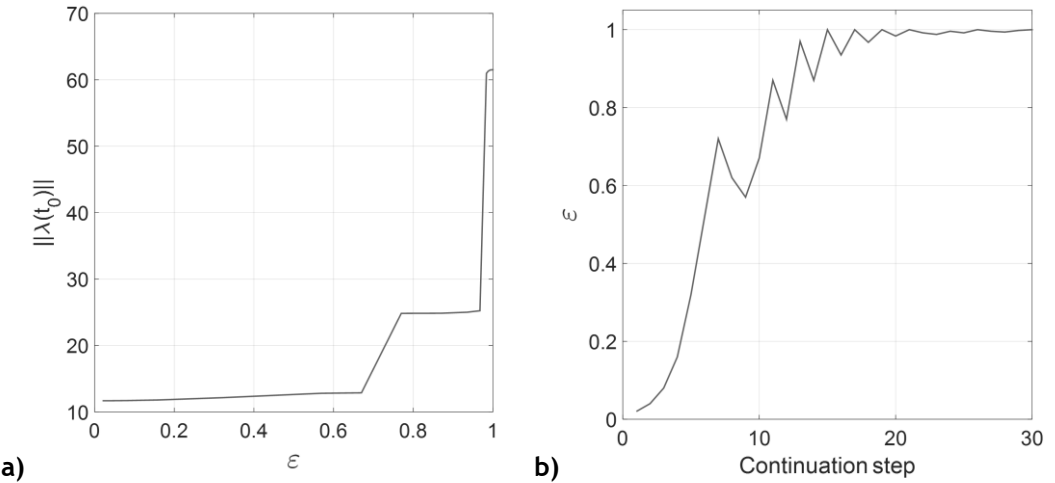


Fig. 3.13. Homotopic approach (Test case 2). (a) Zero-path. (b) Evolution of ε .

Validation of the homotopic approach: Earth-Apophis rendezvous. The last two test cases aim to validate the proposed approach for more complex transfer scenarios. While keeping the hypothesis of planar transfers, the homotopic approach is now applied to solar-sail optimal transfers to rendezvous with an object onto an elliptic orbit. As shown in Table 3.7, the mission scenario consists in a solar-sail transfer from the Earth to rendezvous with the asteroid (99942) Apophis, as described in [211].

The spacecraft is injected directly into an interplanetary trajectory at Earth, with zero hyperbolic excess energy, on 27 July 2017, as in [211]. The only difference between the two cases tested is the value of the characteristic acceleration. In Test case 3, the value of the characteristic acceleration is

$a_c = 0.6 \text{ mm/s}^2$, which corresponds to a sail lightness number $\beta = 0.1$, whereas, in Test case 4, $a_c = 0.12 \text{ mm/s}^2$, which corresponds to $\beta = 0.02$ [Eq. (2.20)]. The two values correspond to the extreme values in the range of the sail lightness numbers considered in [211], for a solar-sail-only transfer. The initial solution of the low-thrust Earth-Apophis rendezvous OCP is computed by means of the PSO algorithm described in Appendix B.2, in the Hamiltonian formulation. The maximum acceleration considered for the low-thrust solution is $a_{\max} = 0.6 \text{ mm/s}^2$. Therefore, the first homotopy is used to find a solar-sail solution with $a_c = 0.6 \text{ mm/s}^2$ (Test case 3). Such solution is subsequently used to find the solar-sail trajectory for Test case 4. The results of the two numerical cases presented in this section are summarised in Table 3.11, together with the results shown in [211]. As already discussed for Test case 2, the computational time shown in Table 3.11 and related to Test case 4 is the one needed for the second continuation only, since the solution of the solar-sail OCP with $a_c = 0.6 \text{ mm/s}^2$ was already found in Test case 3.

Table 3.11. Optimal solar-sail rendezvous from Earth to (99942) Apophis (in brackets the values from [211]).

	Test case 3	Test case 4
$a_c, \text{ mm/s}^2$	0.6	0.12
Computational time, s	28	1
$T_{0f}, \text{ days}$	457 (468)	1160 (1260)

Figure 3.14 shows the optimal solar-sail transfer trajectories for both $a_c = 0.6 \text{ mm/s}^2$ and $a_c = 0.12 \text{ mm/s}^2$. Figure 3.15 shows the evolution of the cone angle during the second continuation. As shown in Table 3.11, the results are in good agreement with the ones presented in [211], considering that those solutions are computed for 3D transfers rather than planar transfers. Nevertheless, it has been shown that the planar solutions presented here can be used as first-guess solutions for a single-shooting approach to easily compute 3D transfers [66]. Furthermore, despite an increased complexity of the OCP to be solved, both Test cases 3 and 4 require a little computational time, comparable with the ones of the previous test cases, relative to circular-to-circular orbit transfers.

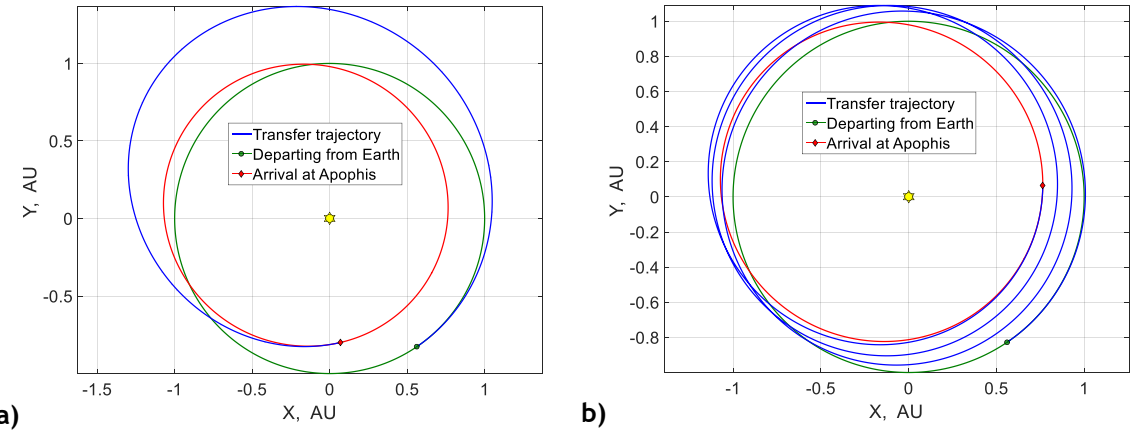


Fig. 3.14. Homotopic approach (Test cases 3 and 4). Ecliptic plane view of the solar-sail transfer trajectories for rendezvous from Earth to (99942) Apophis. (a) $a_c = 0.6 \text{ mm/s}^2$. (b) $a_c = 0.12 \text{ mm/s}^2$.

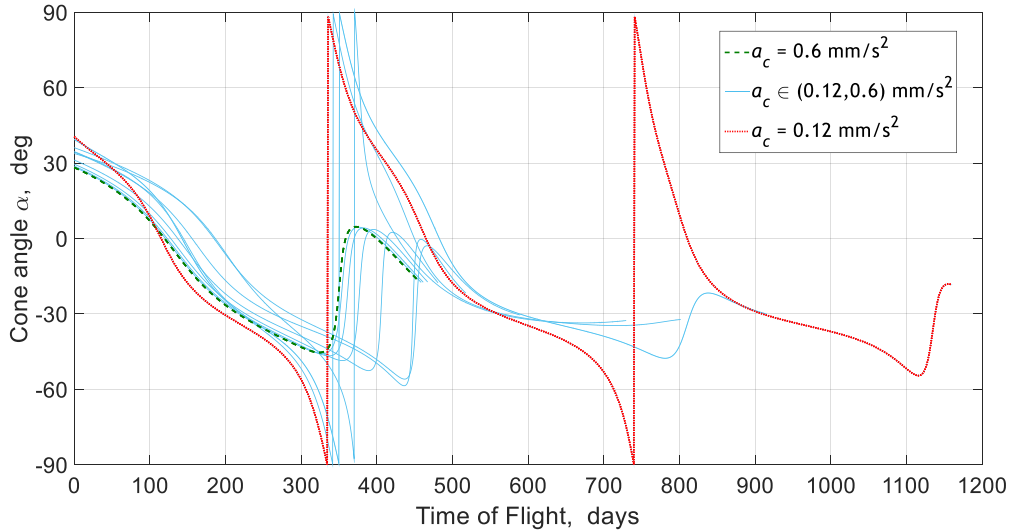


Fig. 3.15. Homotopic approach (Test case 4). Cone angle evolution during the second continuation.

The proposed homotopic approach allows computing optimal solar-sail trajectories for a wide range of characteristic accelerations, in a single and fast run. This is achieved by means of the continuation on the characteristic acceleration, in which intermediate solutions with $a_c \in [a_{c,0}, a_{c,f}]$ are computed at each successful iteration. Other approaches would usually require a single optimisation to be performed for each value of the characteristic acceleration, leading to a higher computational effort to obtain the entire family of solutions. Therefore, the homotopic approach presented here is particularly appealing for preliminary mission design. In fact, the early stages of a solar-sail mission planning are usually characterised by an uncertainty on the value of the sail characteristic

acceleration. For instance, in [16], the value of the characteristic acceleration is shown as a function of the sail size for the DLR/ESA Gossamer Roadmap. A preliminary mission is described in [16] which considers a characteristic acceleration $a_c = 0.3 \text{ mm/s}^2$ and a sail size in the range between $(54 \text{ m})^2$ and $(65 \text{ m})^2$, depending on the bus mass taken into account. One of the improvements outlined in [16] is to find a solar-sail trajectory, within the same mission criteria, with a lower value of the characteristic acceleration. For instance, Fig. 3.16 shows a plot for the minimum time of flight T_{0f} as function of a_c (computed by means of the second homotopic continuation) in the case of the Earth-Apophis planar rendezvous with characteristic acceleration bounded in $a_c \in [0.12, 0.6] \text{ mm/s}^2$. A time of flight of about 660 days is needed if a sail with a characteristic acceleration $a_c = 0.3 \text{ mm/s}^2$ is considered.

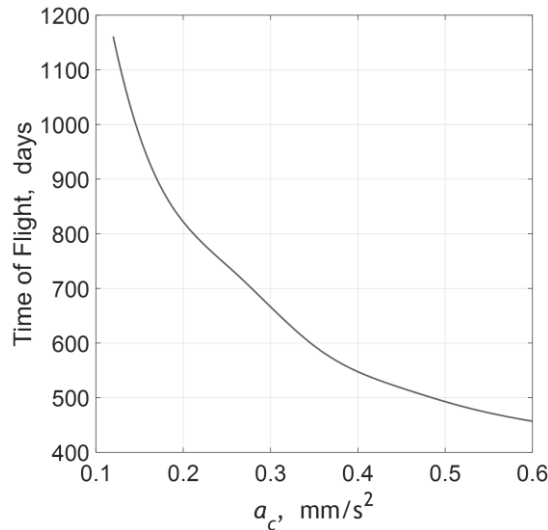


Fig. 3.16. Minimum time of flight as a function of the characteristic acceleration for the coplanar Earth-Apophis case.

3.3. Discussion

In this chapter, two different formulations for a fast solar-sail trajectory design have been presented in the coplanar approximation: the shape-based approach and the homotopic approach. The two formulations are conceptually very different. In fact, in the case of the shape-based approach, the trajectory is designed by means of predefined shaping functions and the control is analytically retrieved *a posteriori*. Since there is no explicit control on the acceleration history, a genetic algorithm is used to find the shape of the trajectory that best fits the acceleration feasible by the given spacecraft. The use of the genetic algorithm within the shape-based approach slightly slows down the overall method but allows a more automatic use of the method. In fact, the inputs required from the user are minimal. On the other hand, the homotopic approach exploits the Pontryagin's minimum principle to find the (locally) optimal solution to the given solar-sail optimal control problem. This approach has been shown to be very accurate and fast. Moreover, the output of this method is already an optimal solution to the desired coplanar transfer. The drawback of this approach lies in the sensitivity of the indirect method. In fact, even though the use of the homotopy increases the convergence radius of the indirect method, the initial values of the continuation parameter ε and its initial step size, as well as the maximum and minimum allowed step size, may still affect the convergence of the solution. Furthermore, the proposed method does not consider the computation of the low-thrust solution. That is, the effort needed to find such solution should be taken into account if an actual comparison between the computational efforts of the two presented approaches is required. On the contrary, the shape-based approach is a standalone method that does not need any pre-computed initial guess to start with.

Because of the advantages and drawbacks of both methods, each approach is used for a different purpose, as it will be shown in the next chapters. The shape-based approach is used when several preliminary solar-sail trajectories are needed, exploiting the little input needed from the user. On the contrary, the homotopic approach is used in the cases of more complex mission scenarios that do not require a large number of trajectories to be found.

CHAPTER 4.

ASTEROID SEQUENCE SEARCH

This chapter describes the developed approach to find a set of sequences of asteroids for a multiple-NEA rendezvous mission through solar sailing. Finding a sequence of NEA to be visited is primarily a combinatorial problem because of the large amount of objects and the huge number of possible permutations between them, as pointed out in Section 4.1. Furthermore, for each transfer leg, an optimisation problem must be solved to assess the existence of a trajectory feasible by a solar sail. For these reasons, two subsets of the whole NEA database are introduced to reduce the amount of objects to deal with, as explained in detail in Section 4.1. Therefore, the sequence search algorithm, described in Section 4.4, is characterised by a local pruning to reduce further the number of NEAs to test in each step of the tree-search algorithm, as detailed in Section 4.2. Lastly, the shape-based approach for solar sailing, described in Section 3.1, is used to have a reliable approximation of the solar-sail trajectory within a reasonable amount of time.

The content of this chapter was published in [198, 214-216], except for Test cases 2-4 in Section 4.6.1.

4.1. Asteroid Database Selection

The choice of target asteroids to be visited in a mission is a difficult task because it shall consider, among all, composition, scientific interest, orbital dynamics, and available launch window. NASA's Near Earth Object Program listed 12,840 NEAs on 08 August 2015¹ and this number is rapidly increasing. All those objects with an Earth minimum orbit intersection distance (EMOID) ≤ 0.05 AU and an absolute magnitude ≤ 22 (i.e. diameter $\gtrapprox 110 - 240$ m, depending on the albedo²) are classified as PHAs. The problem of finding a sequence of encounters is firstly a combinatorial problem. In fact, more than a trillion of sequences of three objects can be found, if all the possible combinations with permutations are considered. Moreover, there seem to be no clear common priorities on the selection of NEAs in the scientific community. To reduce this huge amount of possible combinations, further classifications can be considered which consider the interest from an exploration point of view. Barbee et al. [206] introduced the Near-Earth Object Human Space Flight Accessible Target Study (NHATS) in which the objects are selected as those for which a four-impulse return mission can be found within a set of design parameters such as total Δv required, total mission duration, stay time at the object, and launch date interval. Because the mission parameters for the trajectory computation can be set in several different ways, the list of NHATS asteroids is not univocally defined.

To have a more useful and interesting database, a subset containing only PHAs and NHATS asteroids is, therefore, considered in this work. This database contains 1,801 objects, 1,607 of which are PHAs. The criteria used to select the NHATS database are the following.

¹ Data available online at <https://cneos.jpl.nasa.gov/orbits/elements.html> [retrieved 08 August 2015].

² Data available online at <http://www.minorplanetcenter.net/iau/lists/Sizes.html> [retrieved 08 August 2015].

$$\text{NHATS criteria: } \left\{ \begin{array}{l} \text{total } \Delta v \text{ required} \leq 8 \text{ km/s} \\ \text{total mission duration} \leq 450 \text{ days} \\ \text{stay time at the object} \geq 8 \text{ days} \\ \text{launch : 2015 – 2040} \\ \text{absolute magnitude} \leq 26 \\ \text{OCC} \leq 7 \end{array} \right. \quad (4.1)$$

The term OCC in Eq. (4.1) is the Orbit Condition Code of a NEA's orbit, which refers to the accuracy of the orbit determination. For a complete explanation of the above criteria, the interested reader is referred to the JPL/NASA NHATS website¹. In the following, this subset will be referred to as the *PHA-NHATS database*.

Boden et al. [159] studied the target selection for manned NEA exploration and realised that the NEA accessibility to date is limited due to uncertainties in the objects' characterisation and the available technology. Nonetheless, they pointed out, “there might be more targets within the currently known NEA population” for a NEA sample return mission. “One reason is that the actual rotation rates of most NEAs are unknown”. A fast rotator, in fact, is not suitable for a sample return mission, either human or robotic. On the other hand, slow rotators can exist among those asteroids for which there currently is little knowledge about the rotation. Therefore, a second subset for a multiple NEA rendezvous mission can consider those objects with a large uncertainty on the rotation rate to improve our knowledge for better planning a future exploration mission. The asteroid lightcurve database (LCDB) is “a set of files generated from a database that includes information directly and indirectly obtained from observations made to determine the period and/or amplitude of asteroid lightcurves” [217]. The quality code U provides the assessment of the quality of the period solutions within the LCDB. For this reason, a second subset is considered in this study, which considers PHAs and those NEAs in the LCDB with $U \leq 2 -$. That is, all those objects for which the given value of the rotation rate is not reliable for a statistical analysis. Such second database contains 1,813 objects, 271 of which are NEAs in the LCDB with $U \leq 2 -$ ². Note that, as for the PHA-NHATS database, all the 1,607 known PHAs are

¹ Data available online at <https://cneos.jpl.nasa.gov/nhats/intro.html> [retrieved 08 August 2015].

² Data available online at <http://www.minorplanet.info/lightcurvedatabase.html> [retrieved 20 February 2016].

also considered as part of this second database. In the following, this subset will be referred to as the *PHA-LCDB database*.

Table 4.1 shows the characteristics of the two databases considered in this work.

Table 4.1. Characteristics of the two reduced databases considered.

Database	PHAs	NHATS	LCDB	Total
PHA-NHATS database	1,607	204	8	1,801
PHA-LCDB database	1,607	8	271	1,813

A graphical comparison between the complete database and the PHA-NHATS database is given in Fig. 4.1, in which the heliocentric positions of all objects are plotted for both databases, at a given reference time.

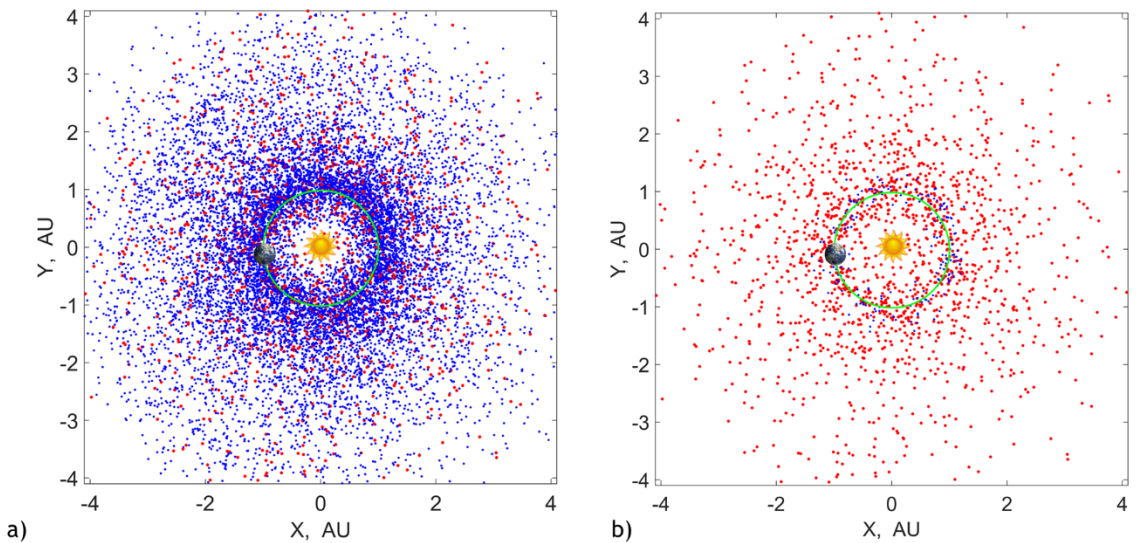


Fig. 4.1. Heliocentric view of the positions of all known NEAs (small blue dots) and PHAs (large red dots) on 24 March 2017. (a) Complete database. (b) PHA-NHATS database. Bodies not to scale.

It is worth noting that the two subsets considered in this study are very different from each other. Despite the fact of having a similar number of objects and being made mostly of PHAs, the PHA-NHATS database contains NHATS asteroids that are, by definition, easy to be reached from the Earth. Therefore, their orbital elements do not differ much from those of the Earth. In contrast, there is not such constraint on the LCDB objects considered in the PHA-LCDB

database. Such difference between the two databases can be visualised as follows. Define the Tisserand parameter related to the Earth as [218]

$$T_{\oplus} = \frac{r_{\oplus}}{a} + 2\sqrt{\frac{a(1-e^2)}{r_{\oplus}}} \cos i \quad (4.2)$$

in which the orbit of the Earth is considered circular. Perozzi et al. [169] proposed the use of the Tisserand parameter related to the Earth as an indication of the relative unperturbed velocity of an asteroid at close encounter with the Earth. To do so, the parameter Υ is defined as

$$\Upsilon \triangleq \sqrt{3 - T_{\oplus}} \quad (4.3)$$

The negative value of the inverse normalised semimajor axis $-r_{\oplus}/a$ can be plotted against Υ^2 . Figure 4.2 shows the distribution of all NEAs in the complete database in the $(\Upsilon^2, -r_{\oplus}/a)$ space. The Earth in such space is in the point $(0, -1)$. The dashed blue line has been obtained setting to zero both inclination and eccentricity in the computation of the Tisserand parameter, thus representing the circular limit of an orbit with the given value of the semimajor axis. That is, the portion of space on the left side of the circular limit represents a forbidden portion of space, being characterised by $e^2 < 0$. The Earth tangency condition is also plotted as a magenta solid line. It has been obtained setting to zero the inclination in Eq. (4.2). Such condition represents an orbit with a given semimajor axis being tangent with that of the Earth. Except for the trivial case in which the unknown orbit is exactly that of the Earth, the only other case in which the tangency condition is verified is when either the radius of pericentre r_p or the radius of the apocentre r_a is equal to the semimajor axis of the Earth. This condition univocally defines the geometry of the orbit on the ecliptic plane, as follows.

$$\begin{cases} r_a = r_{\oplus} = a(1+e) & \text{if } a < r_{\oplus} \\ r_p = r_{\oplus} = a(1-e) & \text{if } a > r_{\oplus} \end{cases} \Rightarrow \quad (4.4)$$

$$\Rightarrow \begin{cases} e = \frac{r_{\oplus}}{a} - 1 & \text{if } a < r_{\oplus} \\ e = 1 - \frac{r_{\oplus}}{a} & \text{if } a > r_{\oplus} \end{cases} \quad (4.5)$$

Substituting Eq. (4.5) into Eq. (4.2) and considering $i = 0$, the expression of Υ^2 for the tangency condition is given by

$$\Upsilon^2 \Big|_{\text{tangency condition}} = 3 - \frac{r_\oplus}{a} - 2\sqrt{2 - \frac{r_\oplus}{a}} \quad (4.6)$$

Note that all the NEAs in the complete database have $a > 0.5$ AU and, therefore, Eq. (4.6) is defined for all the objects in the database. The distance along the Υ^2 axis of a NEA from the tangency condition provides an indication of the additional velocity needed for a planar rendezvous with the selected object. Such velocity should be added to the one needed for the apocentre/pericentre manoeuvre once the tangency condition is reached. Moreover, the quantity $-r_\oplus/a$ on the y-axis is related to the asteroid orbital energy normalised with respect to that of the Earth. From Fig. 4.2, it is clear that the NHATS asteroids are easier to reach from the Earth, since their energy is close to the one of the Earth ($-r_\oplus/a \in [-1.2, -0.8]$) and $\Upsilon^2 < 0.1$. On the other hand, the NEAs from LCDB with $U \leq 2$ – are spread over the allowed $(\Upsilon^2, -r_\oplus/a)$ space. Therefore, finding feasible sequences of asteroids within the PHA-LCDB database is expected to be more difficult.

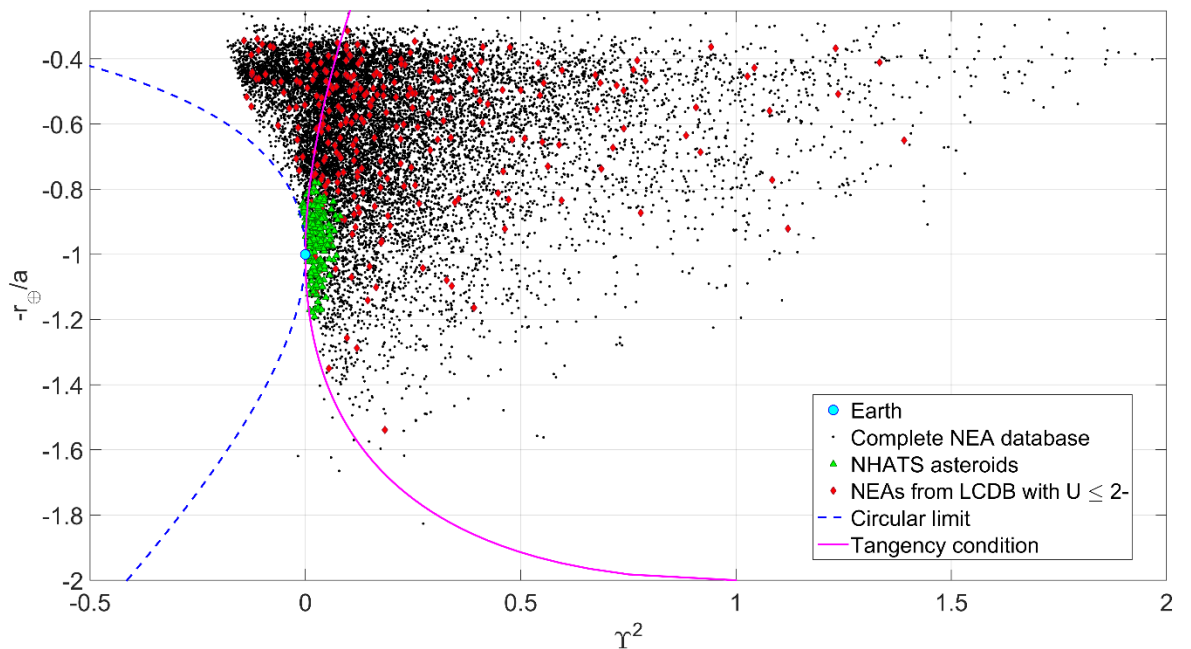


Fig. 4.2. Distribution of all NEAs in the $(\Upsilon^2, -r_\oplus/a)$ space. The two curves represent the circular limit and the Earth tangency condition.

From a purely combinatorial point of view, an order of magnitude for the complexity of the problem of finding a sequence of encounters can be given by considering the total number of possible sequences of $Q = 3, 4$ and 5 objects without repetition, both from the original and the two reduced databases. The number of these Q -permutations of N objects P_Q^N (Table 4.2) is given by

$$P_Q^N = \frac{N!}{(N-Q)!} \quad (4.7)$$

Table 4.2. Number of Q -permutations of N objects within the complete database and the reduced ones.

Database	N	$Q = 3$	$Q = 4$	$Q = 5$
Complete database	12,840	2.1×10^{12}	2.7×10^{16}	3.5×10^{20}
PHA-NHATS database	1,801	5.8×10^9	1.0×10^{13}	1.9×10^{16}
PHA-LCDB database	1,813	5.9×10^9	1.1×10^{13}	1.9×10^{16}

Such combinatorial problem can be easily visualised for the specific case of an asteroid sequence search. If all the objects in the considered database are used, the asteroid sequence search can be represented as a tree, as discussed in Section 2.2.6 and schematically shown in Fig. 4.3. The BS implementation of the tree search is considered in this work (see Section 2.2.6). The implementation of BS has been chosen against DFS because it allows considering a maximum fixed number of partial sequences as starting point for the next leg. A drawback of this method is that complete sequences are available only at the end of the tree search. On the other hand, the DFS implementation allows having complete sequences already at the early stages of the tree-search run. However, branching criteria based on the quality of the sequences found cannot be defined in the DFS implementation. Figure 4.3 shows how the computational effort needed to find all the possible branches in the tree grows as more feasible transfers are found. The dotted red lines in the figure represent branches of the tree for which no feasible solution has been found. In order to reduce further the computational cost of the asteroid sequence search, a local pruning on the database is carried out at the beginning of each leg. A detailed description of it is given in the next Section 4.2.

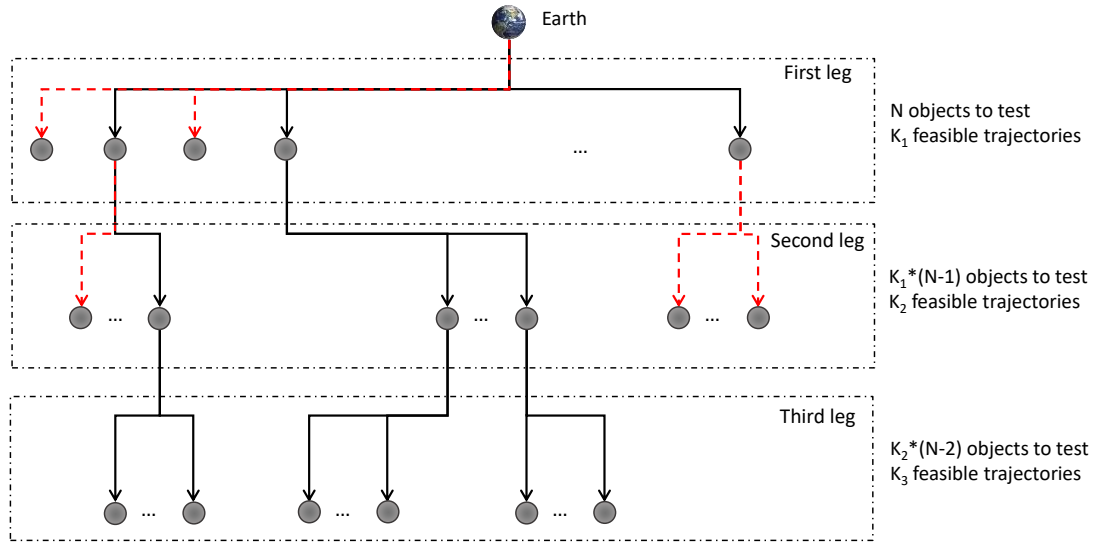


Fig. 4.3. Schematic of the tree search.

4.2. Local Pruning on the Database

A local pruning on the available NEA database is performed, based on astrodynamics. This has been carried out to work on a locally reduced database, for the reasons mentioned in Section 4.1. The local pruning is performed at the beginning of each leg of the sequence and it depends on the starting orbit of the respective leg, as it will be discussed in detail in Section 4.4.

Four conditions for the local pruning of the database are used: the first three criteria are related to the in-plane trajectory, whereas the fourth takes into account the orientation of the orbital planes:

- i. The current spacecraft state is propagated, in an outward and inward spiral, for the maximum allowed time of flight $T_{0f,\max}$ considered within the trajectory model. A control law that maximises the semimajor axis change is considered for the propagation of the spacecraft state. To obtain the maximum and minimum semimajor axes, the locally-optimal law for changing the semimajor axis through solar sailing, described in [2], is used. The optimal sail cone and clock angles can be expressed as

$$\begin{cases} \alpha^* = \begin{cases} \tilde{\alpha}^* & \text{if } \tilde{\alpha}^* \leq \tan^{-1}(1/\sqrt{2}) \\ \tan^{-1}(1/\sqrt{2}) & \text{if } \tilde{\alpha}^* > \tan^{-1}(1/\sqrt{2}) \end{cases} \\ \delta^* = 0 \end{cases} \quad (4.8)$$

in which

$$\tan \tilde{\alpha}^* = \frac{-3 + \sqrt{9 + 8 \tan^2 \tilde{\alpha}}}{4 \tan \tilde{\alpha}} \quad (4.9)$$

The angle $\tilde{\alpha}$ in Eq. (4.9) represents the cone angle relative to the ideal direction of the thrust for the maximisation of the change of the desired orbital element. For the maximisation of the semimajor axis, such angle has the following expression [2]:

$$\tan \tilde{\alpha} = \frac{1 + e \cos \nu}{e \sin \nu} \quad (4.10)$$

The maximum and minimum semimajor axes obtained are, then, the maximum and minimum semimajor axes that the solar sail can reach starting from the current state and traveling for the maximum available time of flight. All NEAs with a semimajor axis outside the available range are therefore excluded from the locally pruned database for the current leg.

- ii. Similarly to the preceding case, the trajectory is propagated by considering a control law that maximises the change of eccentricity and thus a maximum range of possible eccentricity variation is found. Only those NEAs with eccentricity inside the available range are included in the locally pruned database for the current leg. As in the preceding case, the optimal sail cone and clock angles are given by Eqs. (4.8) - (4.9). However, in this case, the angle $\tilde{\alpha}$ is given by the following relation [2]:

$$\tan \tilde{\alpha} = \frac{2 + e \cos \nu}{1 + e \cos \nu} \cot \nu + \frac{e \cosec \nu}{1 + e \cos \nu} \quad (4.11)$$

- iii. Defining the longitude of pericentre as $\varpi = \omega + \Omega$, a transfer trajectory between two orbits (subscript 1 and 2) with a large $\delta\varpi = \text{mod}(\varpi_1 - \varpi_2, \pi)$ is more difficult to achieve as the eccentricities of the two orbits increase. This can be verified with the following test cases, in which two 200-day transfers are computed by means of a zero-full-revolution ballistic Lambert arc [77, 170, 219]. Keplerian elements of departing and arrival

orbits are the same in both cases except for the eccentricity, as shown in the following.

TEST CASE 1

$$\begin{cases} \mathbf{x}_0^{kep} = [1 \text{ AU} \ 0.1 \ 0 \ 0 \ 0 \ 0]^T \\ \mathbf{x}_f^{kep} = [1 \text{ AU} \ 0.1 \ 0 \ 30 \text{ deg} \ 0 \ 180 \text{ deg}]^T \end{cases} \quad (4.12)$$

TEST CASE 2

$$\begin{cases} \mathbf{x}_0^{kep} = [1 \text{ AU} \ 0.5 \ 0 \ 0 \ 0 \ 0]^T \\ \mathbf{x}_f^{kep} = [1 \text{ AU} \ 0.5 \ 0 \ 30 \text{ deg} \ 0 \ 180 \text{ deg}]^T \end{cases} \quad (4.13)$$

Figure 4.4 shows the Lambert solution for both transfer trajectories. The difference in the required Δv is highlighted in the figure: the required Δv related to the second test case is more than three times larger than that of the first test case.

For this reason, a threshold on the maximum variation of the longitude of pericentre has been considered for each object, taking into account the value of the eccentricity as follows.

$$\delta\varpi_{\max} \triangleq \pi(1-e)^2 \quad (4.14)$$

By using this threshold, the arrival object is removed from the locally-pruned database if at least one of the following conditions is not satisfied.

$$\begin{cases} \text{mod}(\varpi_1 + \delta\varpi_{\max,1} + \pi, 2\pi) > \text{mod}(\varpi_2 - \delta\varpi_{\max,2} + \pi, 2\pi) \\ \text{mod}(\varpi_2 + \delta\varpi_{\max,2} + \pi, 2\pi) > \text{mod}(\varpi_1 - \delta\varpi_{\max,1} + \pi, 2\pi) \end{cases} \quad (4.15)$$

In Fig. 4.5, two examples (not to scale) are sketched to give a graphical view of the pruning on the longitude of pericentre given by Eq. (4.15). Figure 4.5a shows a case in which Eq. (4.15) is satisfied and, in fact, the ranges of possible variation of ϖ for the two objects overlap. On the other hand, in Fig. 4.5b, the orbit of the second object is more eccentric, so that the available range of variation of ϖ is smaller and does not overlap with the one of the first object. In this second case, the first condition in Eq. (4.15) is not satisfied and the second object is, therefore, not part of the locally pruned database for the current leg.

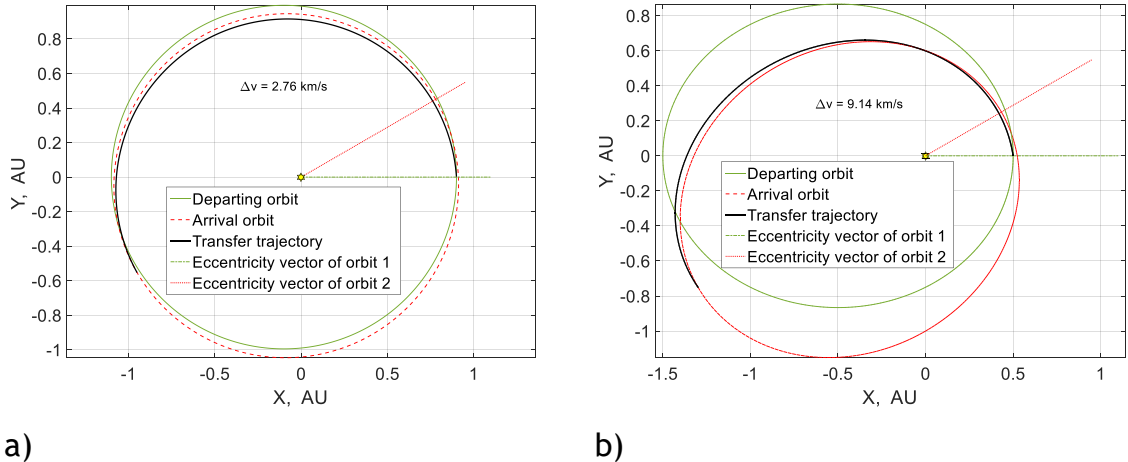


Fig. 4.4. Heliocentric view of the transfer trajectory. (a) Test case 1. (b) Test case 2.

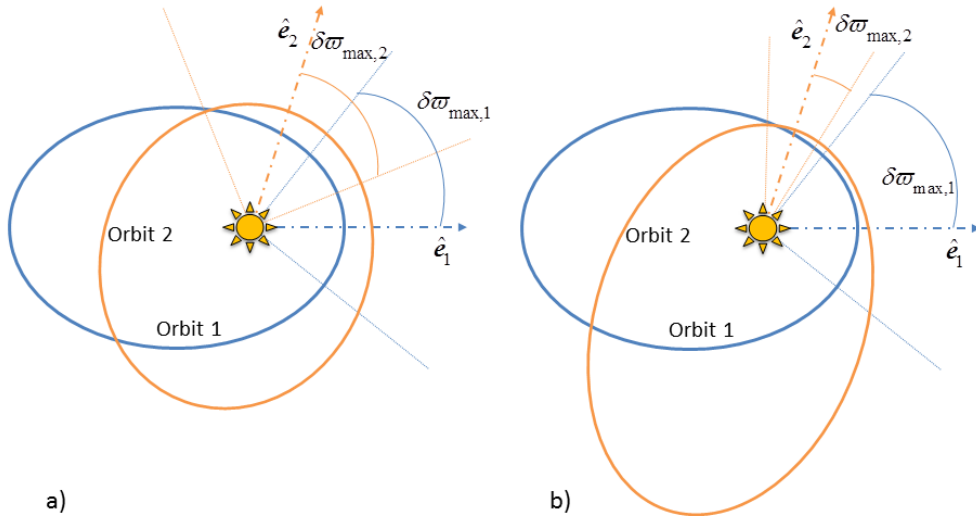


Fig. 4.5. Graphical view (not to scale) of pruning on longitude of pericentre: ranges of possible variation of longitude of pericentre for two objects (a) overlap; (b) do not overlap.

- iv. Let us define θ as the angle between the angular momenta of the two orbits, as

$$\theta \triangleq \arccos(\hat{h}_1 \cdot \hat{h}_2) \quad (4.16)$$

Because a coplanar transfer is considered for the simplified trajectory description (Section 4.3), a maximum value of θ is selected as the threshold to consider the second object to be part or not of the locally pruned database. This way, objects are not considered where a change of the inclination and/or the longitude of the ascending node would be too large in the 3D case.

4.3. Simplified Trajectory Model

A simplified trajectory model is used to check the feasibility of the trajectory transfer from each object of the current leg to all the others in the locally pruned database. One possibility is to use a ballistic Lambert-arc approximation, in which the acceleration needed for the transfer is compared to the maximum acceleration that the solar sail can achieve, multiplied by a penalty factor¹. However, a low-thrust trajectory differs from a ballistic Lambert arc and this difference increases with the time of flight. Furthermore, a solar sail performs best for trajectories with long flight times, due to the low but continuous acceleration. In order to obtain solutions that are more reliable from the sequence search and, therefore, decrease effort and time needed in the optimisation phase, the shape-based approach described in Section 3.1 has been used with the objective function $J = T_{0f}$. In fact, the timeline of the asteroid encounters is one of the fundamental output of the asteroid sequence search. The relative phasing between two consecutive encounters at the beginning of the transfer trajectory and the available transfer time are two essential characteristics of the sequence that can affect the feasibility of the overall multiple rendezvous mission. That is, it may be difficult to find a solar-sail solution for a sequence of asteroids and encounter dates found by means of the ballistic Lambert-arc approximation. On the other hand, the shape-based approach gives a better description of the trajectory. Therefore, the output of the asteroid sequence search (i.e. the sequence of asteroids and encounter epochs, which will be referred to as *timed sequence*) is more likely to describe a mission feasible by a solar sail if the shape-based approach is used. The drawback of the shape-based approach, with respect to the use of Lambert arcs, is the use of the genetic algorithm that increases the computational time needed to find preliminary sequences. Nevertheless, the increased complexity of the transformation of Lambert arcs into solar-sail trajectories and, therefore, the little reliability of such trajectory model, with respect to solar sailing, justifies the increased computational time needed by the shape-based approach. Other methods are used in the literature for guessing the

¹ Peloni, A. and Ceriotti, M., “Solar Sailing Multiple NEO Rendezvous Mission: Preliminary Results”, *First Stardust Global Virtual Workshop (SGVW-1) on Asteroids and Space Debris*, University of Strathclyde, Glasgow, Scotland, UK, 6-9 May 2014. Presentation available online at <https://www.youtube.com/watch?v=j-uxCvo09Hc> [retrieved 06 June 2017].

Δv needed for a low-thrust transfer which exploit, for instance, Edelbaum's formulation [220] or a parametrisation of the trajectory [59]. These would be faster than the shape-based approach if used within the sequence search. However, as for the case of the Lambert-arc approximation, these methods do not consider the dynamics of a solar sail, which is more constrained than that of a classical low thrust. Lastly, a low- Δv transfer is sought for classical low-thrust trajectories because of the limited amount of propellant onboard. For solar sailing, however, the amount of Δv is not a good indicator for the feasibility of a transfer trajectory.

4.4. Sequence Search Algorithm

Figure 4.6 shows the flowchart of the process of searching for sequences, which is detailed in Algorithm 4.1. First, the selected database (i.e. the PHA-NHATS or the PHA-LCDB database, in this case) is locally pruned (details in Section 4.2) by taking into account that the sequence starts at Earth at a fixed time t_0 . This pruning allows the algorithm to consider a list of encounters $L_{b,tmp}$ that contains fewer objects at a time, avoiding spending time on objects that would be difficult to reach. Approximated solar-sail trajectories are found by means of the shape-based approach, as discussed in Section 4.3. For all the trajectories found, the arrival NEAs are kept and considered as starting objects for the next iteration of the algorithm. This is carried out by updating the list L_{part} that contains all the partial timed sequences found so far. Next, once the objects in the current pruned list $L_{b,tmp}$ have been considered for the trajectory calculation, the same process is carried out in a tree-search algorithm, starting from the arrival body of each of the temporary timed sequences s_i found so far. When the total mission duration reaches the maximum allowed time (i.e. ten years, in the current scenario) or no feasible solar-sail trajectories are found, the current timed sequence is considered complete. Once all the temporary timed sequences are completed and the list of partial timed sequences is empty (i.e. $L_{part} = \emptyset$), the algorithm stops.

The computational time of the described sequence search increases as the number of feasible transfer trajectories increases due to the tree nature of the search itself (Fig. 4.3). Therefore, the possibility to reduce the number of partial

timed sequences considered at the beginning of each leg is added. Define N_{\max}^{seq} as the maximum number of partial timed sequences to be used in the following leg within the sequence search algorithm. Once all the potential transfer trajectories have been studied for the current leg, the set L_{tmp} of all the partial timed sequences found is rearranged so that these are sorted in ascending order with respect to the total mission time. This is done so that those timed sequences with fastest transfers have higher priority, since one of the goals of the sequence search is to find sequences with as many encounters as possible within a fixed mission time. Therefore, only the first N_{\max}^{seq} timed sequences that are part of L_{tmp} are used for the next leg of the tree search. The discarded timed sequences are stored so that they can be used or analysed after the algorithm has stopped.

Note that the only stochastic component of the sequence search algorithm is the GA used within the shape-based approach. Except this, the algorithm is fully deterministic.

The code has been implemented using mixed MATLAB/C code, speeding up the computations where bottlenecks have been found in the MATLAB code (Appendix B.1). Moreover, the algorithm is parallelised for different launch dates, since each run assesses one specific launch date (Algorithm 4.1, Line 1).

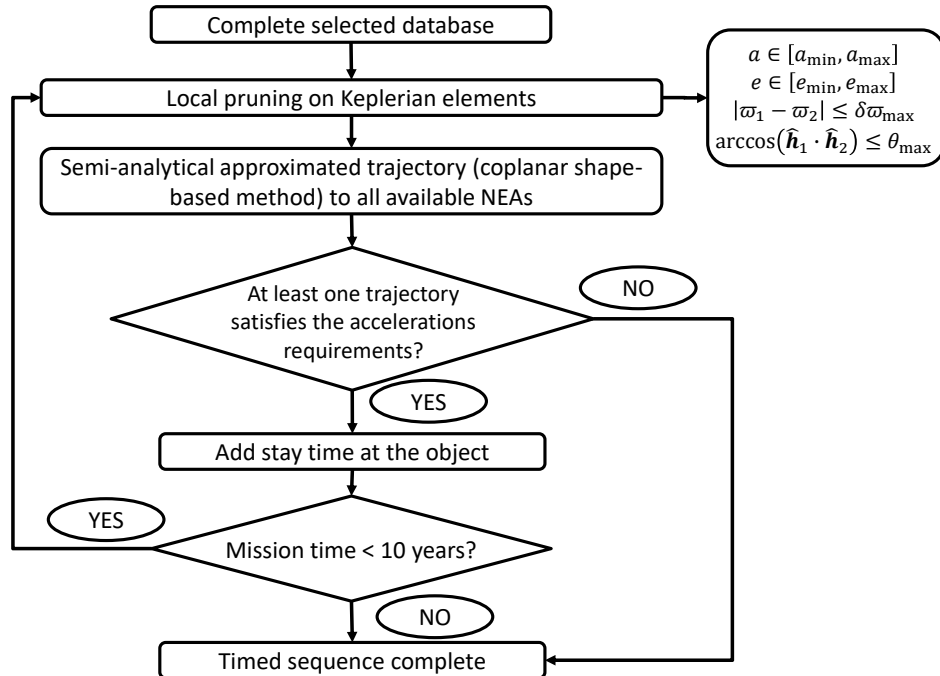


Fig. 4.6. Sequence search flowchart.

Algorithm 4.1. Sequence search algorithm.

```

1: Given  $\{t_0, b_0\}$ , initialise  $L_{part} = [t_0 \ b_0]^T$ 
2: Local pruning on  $L_b \rightarrow L_{b,tmp}$ 
3: For each object  $b_j \in L_{b,tmp}$ , Do
4:   Check the existence of a solar-sail trajectory  $\rightarrow T_{0f}$ 
5:   If a feasible trajectory exists, Then
6:     
$$L_{part} = L_{part} \cup \begin{bmatrix} t_0 + T_{0f} & t_0 + T_{0f} + t_{stay} \\ b_j & b_j \end{bmatrix}$$

7:   End If
8: End For
9:  $L_{compl} = \emptyset$ 
10: While  $L_{part} \neq \emptyset$ , Do
11:   For each partial timed sequence  $s_i$ , Do
12:     Retrieve the last time of the timed sequence:  $t = s_i(1, \text{end})$ 
13:     Retrieve the list of the bodies already encountered:  $L_{b,i} = s_i(2, \text{all})$ 
14:      $L_b = L_b \setminus L_{b,i}$ 
15:     Local pruning on  $L_b \rightarrow L_{b,tmp}$ 
16:     For each object  $b_j \in L_{b,tmp}$ , Do
17:       Check the existence of a solar-sail trajectory  $\rightarrow T_{0f}$ 
18:       If a feasible trajectory exists, Then
19:         
$$L_{tmp} = L_{part} \cup \begin{bmatrix} t + T_{0f} & t + T_{0f} + t_{stay} \\ b_j & b_j \end{bmatrix}$$

20:       End If
21:     End For
22:     If  $L_{tmp} = \emptyset$ , Then
23:        $L_{compl} = L_{compl} \cup s_i$ 
24:     End If
25:   End For
26:    $L_{part} = L_{tmp}; L_{tmp} = \emptyset$ 
27: End While

```

4.5. Application to Gossamer Mission

The reference work of Dachwald et al. [16] showed a three-NEA rendezvous mission through solar sailing, considering a sailcraft with a characteristic acceleration $a_c = 0.3 \text{ mm/s}^2$ and a maximum mission duration of ten years. The sequence of encounters, according to the DLR/ESA Gossamer roadmap [16], should be made of at least three NEAs with a stay time in the order of a few days. The mission lifetime should be at most ten years. Moreover, the mission should respect the following criteria:

- a) At least one object should be a PHA.
- b) At least one object should be a potential target for future human exploration (i.e. it should be part of the temporary NHATS database).
- c) The last NEA should be a small object (i.e. absolute magnitude ≥ 25.5).

Note that the reason for the last point was to demonstrate the feasibility of a solar sail as a gravity tractor [221, 222]. However, this point is not considered one of the main aims of such a mission but rather a secondary goal¹. Therefore, a sequence of NEAs that satisfies the first two criteria but is characterised by the last object being larger than 50 m in diameter is still considered a good sequence.

Because of the nature of the sequence search algorithm described in Section 4.4, these criteria can only be verified *a posteriori*. Although there is no guarantee for meeting the above requirements, a large number of sequences are discovered. Therefore, the candidate sequences are chosen such to best fit criteria a) - c) and that are made of the largest number of encounters.

Moreover, Dachwald et al. [16] proposed three further steps to be investigated in future works for improving the technical feasibility and for increasing the support of the scientific and planetary defence communities:

- i) Reduction of the total mission duration.
- ii) Reduction of the required characteristic acceleration.
- iii) Priority on PHAs within the target selection.

A reduction in the total mission duration has not been explicitly considered in the current work. Nevertheless, within the asteroid sequence search, the timed sequences are sorted for total mission duration and, if the maximum allowed number of temporary sequences is exceeded, those with the longest mission

¹ Prof Bernd Dachwald, 03 October 2014. Personal communication.

duration are discarded. Moreover, sequences with more than three encounters have been found for the same maximum mission duration, as it will be shown in Section 4.6.

A reduction of the required characteristic acceleration was addressed by considering a solar sail with a characteristic acceleration $a_c = \{0.1, 0.15, 0.2\} \text{ mm/s}^2$. Some results for the sequence search considering $a_c = 0.3 \text{ mm/s}^2$ will be shown as well for the sake of comparison. It is worth to underline that, in the ideal case of a perfectly-reflecting flat solar sail, the characteristic acceleration depends only on the area-to-mass ratio (AMR), as shown in Eq. (2.19). Therefore, a characteristic acceleration $a_c = 0.2 \text{ mm/s}^2$, instead of $a_c = 0.3 \text{ mm/s}^2$, leads to a reduction of the AMR from $33 \text{ m}^2/\text{kg}$ to $22 \text{ m}^2/\text{kg}$. That is, either more payload is allowed on the same sail or the use of a smaller sail or a heavier structure is considered, with the result of lowering the technological challenges and thus increasing the mission-specific TRL of the available technology. According to the DLR/ESA Gossamer technology [3], such a reduction in the characteristic acceleration leads to a reduction in the sail size from about $(54 \text{ m})^2 - (65 \text{ m})^2$ to about $(39 \text{ m})^2 - (48 \text{ m})^2$. The interval of sail dimensions depends on the sailcraft bus adopted, as discussed in [16].

Finally, the solutions with at least one PHA are preferred to the others in the final sequence selection.

4.6. Numerical Test Cases

The methodology proposed has been applied to the two reduced databases described in Section 0. In the following subsections, the results of the sequence search for both databases are shown and discussed.

4.6.1. PHA-NHATS Database

The PHA-NHATS database introduced in Section 4.1 is used for the first set of test cases. Therefore, the output sequences are very likely to fulfil the requirements from the DLR/ESA Gossamer roadmap, as discussed in Section 4.5.

Starting from the departure date of the reference mission (which is $t_0 = 28$ November 2019), a systematic search of sequences has been carried out on a set of launch dates spanning about ten years with a step size of 90 days ($t_0 \in [28 \text{ November 2019}, 06 \text{ October 2029}]$). This choice allows taking into account short- and long-term variations in the phasing between the asteroids. The four values of the sail characteristic acceleration discussed in Section 4.5 are considered to test different scenarios (namely, Test case 1 - 4, respectively). The characteristics of each test case are shown in Table 4.3. Moreover, the minimum allowed time of flight for each leg is the same in all test cases and is set to $T_{0f,\min} = 500$ days. The number of preliminary sequences found for each value of the characteristic acceleration can be an indicator of the performances needed by a solar sail for this kind of mission. In the following subsections, the four cases tested are discussed and the results are shown.

Table 4.3. PHA-NHATS database: test cases for the sequence search algorithm.

	a_c , mm/s ²	$T_{0f,\max}$, days	t_{stay} , days	N_{\max}^{seq}
Test case 1	0.20	1,000	100	∞
Test case 2	0.15	1,500	50	∞
Test case 3	0.10	1,500	50	∞
Test case 4	0.30	1,000	100	200

Test case 1. For this test case, the pruning on the maximum number of considered sequences is not limited and, therefore, it is $N_{\max}^{\text{seq}} = \infty$ in Table 4.3.

This search resulted in more than 4,800 unique sequences made of five encounters, of which at least one is a PHA. It is important to underline that all the sequences found within this study contain only NHATS asteroids and sometimes a PHA. Figure 4.7 shows the number of unique sequences found for each launch date. Here, the term unique sequence refers to the sequence of asteroids only, without considering the possible differences in time. Only those sequences with at least one PHA and at least four encounters are plotted. Note that more than 400 unique sequences with five encounters and at least one PHA have been found for a single launch date (which is $t_0 = 14$ April 2028). If sequences with more than

four encounters and at least one PHA are considered, more than 1,000 unique sequences have been found for a single launch date (which is $t_0 = 09$ January 2029).

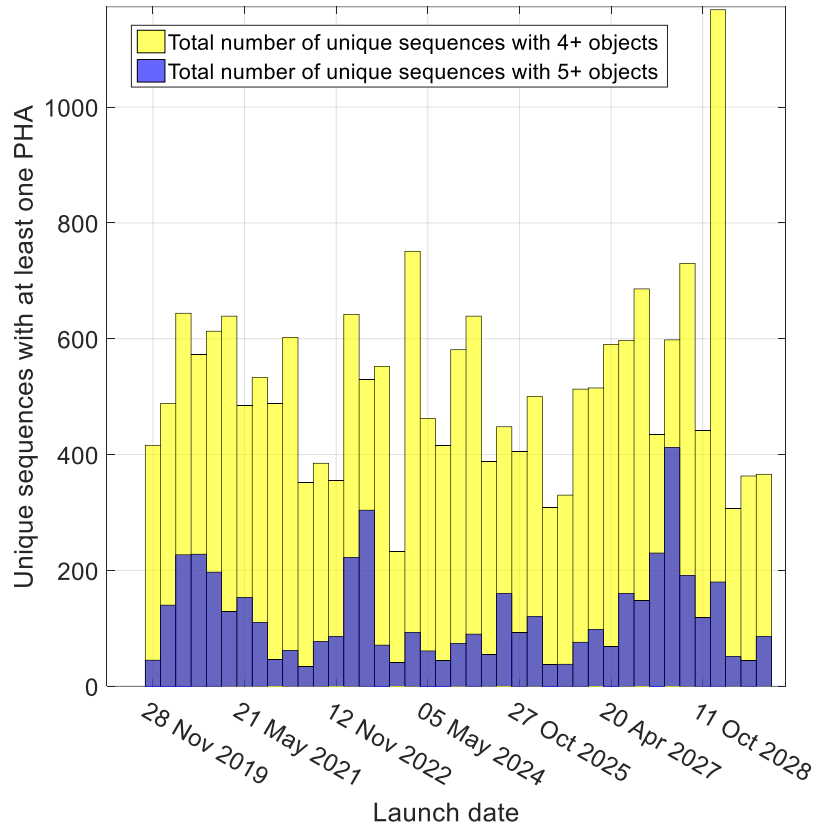


Fig. 4.7. Number of unique sequences with at least one PHA and four encounters as a function of the launch date. PHA-NHATS database with $a_c = 0.2 \text{ mm/s}^2$ (Test case 1).

Figure 4.8 shows an example of the first three legs of all the timed sequences with five encounters and at least a PHA found for the launch date $t_0 = 30$ April 2025. The graph shows the typical tree nature of the solution, as discussed in Section 0. Two different timed sequences are considered having a rendezvous with the same object when the arrival times differ by 40 days at most. For example, the object 2012 BB₄ appears three times in the second leg but the rendezvous times differ by more than 100 days. Therefore, these are considered as three separate branches of the solution tree. The sequence characterised by the dashed red path (that is, the sequence Earth - 2000 SG₃₄₄ - 2015 JD₃ - 2012 KB₄) is the first one of the fully-optimised sequences that will be shown in Section 5.4.3.

Figure 4.8 shows how several timed sequences are partly repeated. This allows the target asteroids to be easily changed, even after launch, if needed. Moreover,

because a solar sail does not need any propellant, such a change is theoretically easier with a solar sail than with an electric propulsion system.

Because of the tree nature of the sequence search and the need of a GA run to check the existence of each trajectory, the whole search has been carried out by running several parallel searches for the 41 launch dates over three different machines: a 3.4 GHz Core i7-3770, a 3.4 GHz Core i7-4770, and a 2.3 GHz Core AMD Opteron 6376. The first two machines have 16 GB of RAM and run Windows 7. The third one is part of the University of Glasgow Computer Cluster Facility¹, has up to 8 GB of RAM per core and runs CentOS 6. Considering only those simulations carried out on the latter, which is the slowest machine, the average computational time for each sequence search run is about 41.3 days, where each successful run of the shape-based approach took about 60 seconds on average.

¹ Data available online at <http://www.gla.ac.uk/services/it/hpcc/> [retrieved 24 August 2015].

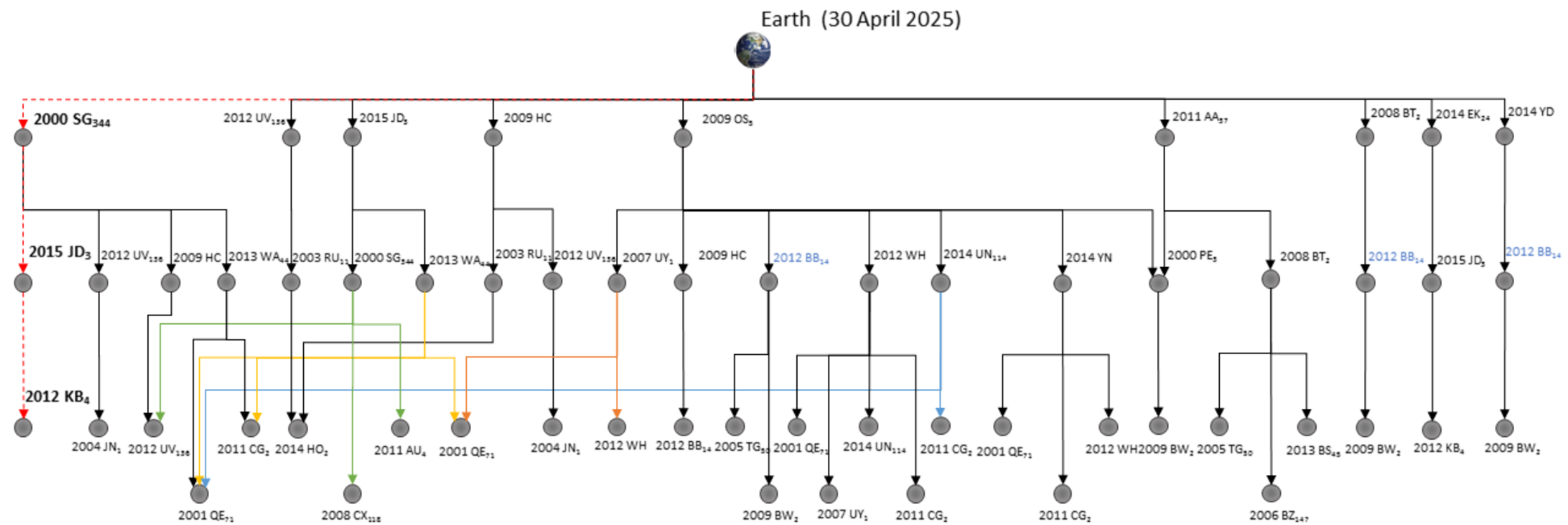


Fig. 4.8. Tree graph of first three legs of all timed sequences with five encounters found for launch date $t_0 = 30$ April 2025 (Test case 1).

Test case 2. For this test case, a maximum allowed time of flight $T_{0f,max} = 1,500$ days has been considered within the trajectory model to account for the lower performances of the sailcraft. Such increased upper boundary on the allowed flight time potentially reduces the number of objects that can be visited by the chosen sailcraft within the maximum mission duration limit of ten years. In fact, if the stay time at each object (Algorithm 4.1) used in the previous test case is considered and the duration of each transfer leg is set to $T_{0f,max}$, only two objects can be visited in ten years, as follows:

$$T_{0f,max} + t_{stay} + T_{0f,max} + t_{stay} = 3,200 \text{ days} > 10 \text{ years} - T_{0f,min} \quad (4.17)$$

However, if the stay time at each object is reduced to $t_{stay} = 50$ days, the possibility to visit a third object with a shorter time of flight is added, as follows:

$$T_{0f,max} + t_{stay} + T_{0f,max} + t_{stay} + T_{0f,min} = 3,600 \text{ days} \quad (4.18)$$

This is the reason for considering a stay time $t_{stay} = 50$ days for this test case, as shown in Table 4.3. Nonetheless, the results are expected to show sequences made of fewer objects with respect to the previous Test case 1. In fact, Fig. 4.9 shows that no sequences with five encounters are found. Nevertheless, this search resulted in more than 1,200 unique sequences made of four encounters, of which one is a PHA. If sequences with more than three encounters and at least one PHA are considered, more than 3,200 unique sequences have been found over the ten-year time span considered. That is, these results show that a large number of three-NEA rendezvous missions still exists if a sailcraft with a characteristic acceleration that is half of the one in the reference paper [16] is considered. In fact, more than 40 unique three-NEA sequences exist for each launch date considered.

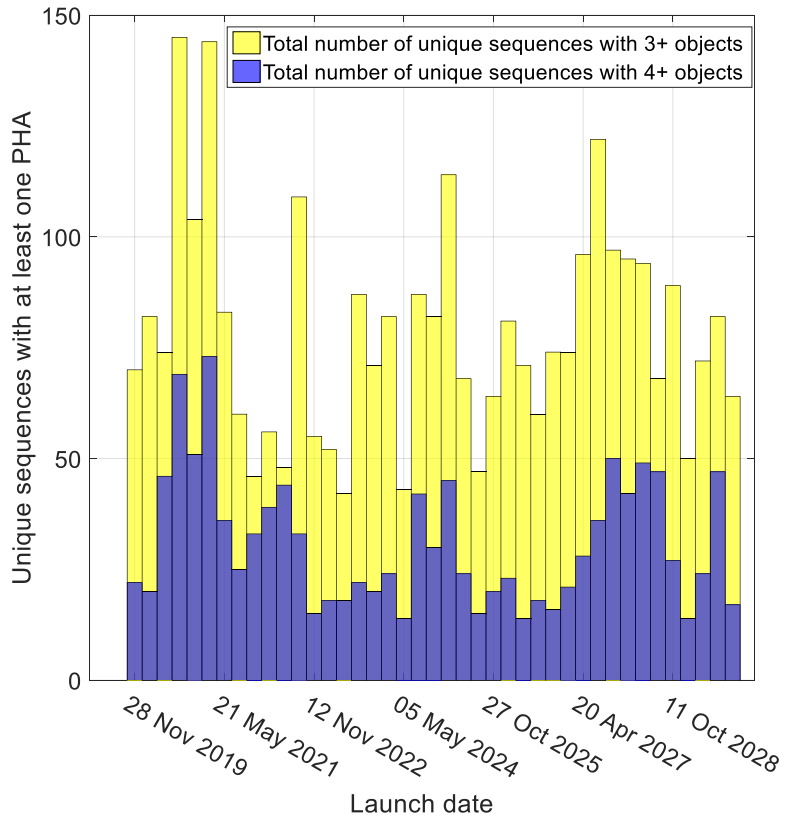


Fig. 4.9. Number of unique sequences with at least one PHA and three encounters as a function of the launch date. PHA-NHATS database with $a_c = 0.15 \text{ mm/s}^2$ (Test case 2).

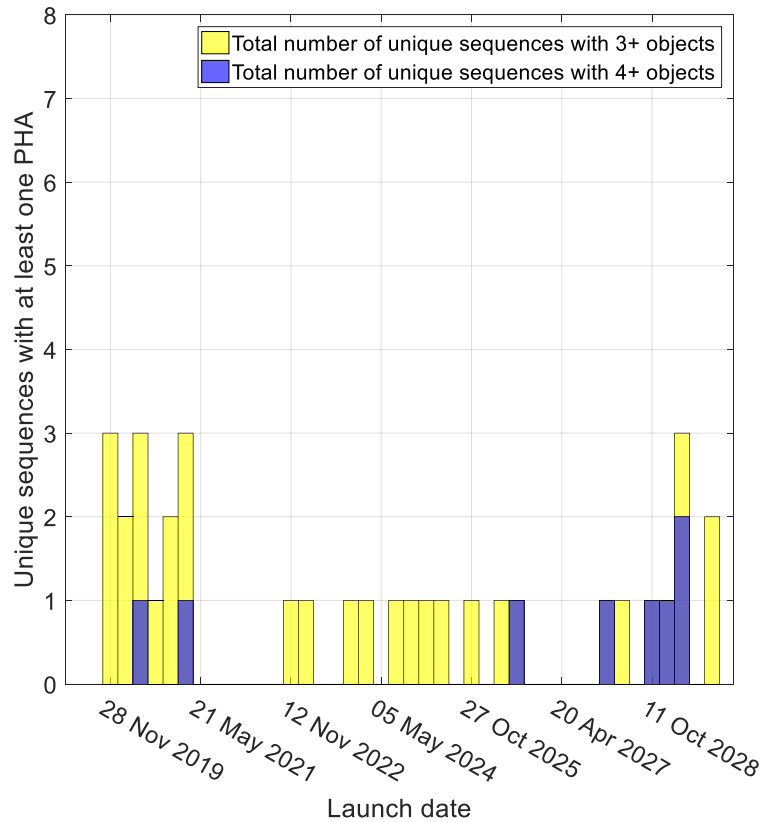


Fig. 4.10. Number of unique sequences with at least one PHA and three encounters as a function of the launch date. PHA-NHATS database with $a_c = 0.1 \text{ mm/s}^2$ (Test case 3).

Test case 3. For this test case, the values of the maximum allowed time of flight and the stay time are chosen for the same reasons explained in the previous subsection for Test case 2. Figure 4.10 shows the results for this test case. In this case, the sail characteristic acceleration is too low to guarantee a significant number of sequences made of at least two NEAs and a PHA for each launch date considered. In fact, there are no such sequences for certain launch dates.

Test case 4. This case has been studied to show the potential amount of sequences feasible if the characteristic acceleration of the DLR/ESA Gossamer roadmap is considered [16, 51, 52]. Moreover, because of the larger characteristic acceleration with respect to the previous test cases, a large amount of sequences is expected to be found. For these reasons, as well as to decrease the total computational time required, a reduced set of launch dates has been considered for Test case 4. Moreover, the algorithm for this test case has been set so that $N_{\max}^{\text{seq}} = 200$. That is, only the 200 timed sequences with the shortest time of flight are kept for the next leg. This significantly reduces the amount of sequences that will be found. Nevertheless, this search resulted in yet an extremely large number of feasible sequences. In fact, considering both the complete and the discarded (and thus incomplete) sequences, more than 20,000 unique sequences made of at least five encounters, of which one is a PHA, are found. Figure 4.11 shows the number of unique sequences found for each launch date. Only those sequences with one PHA and at least five encounters are plotted. Note that more than 600 unique sequences with at least five encounters and one PHA have been found for each launch date considered. Moreover, more than 1,000 sequences with six encounters in less than ten years have been found as well. In fact, Fig. 4.11 shows that there are up to 229 unique sequences made of six NEAs, of which one is a PHA, for a single launch date (which is $t_0 = 26 \text{ May } 2020$).

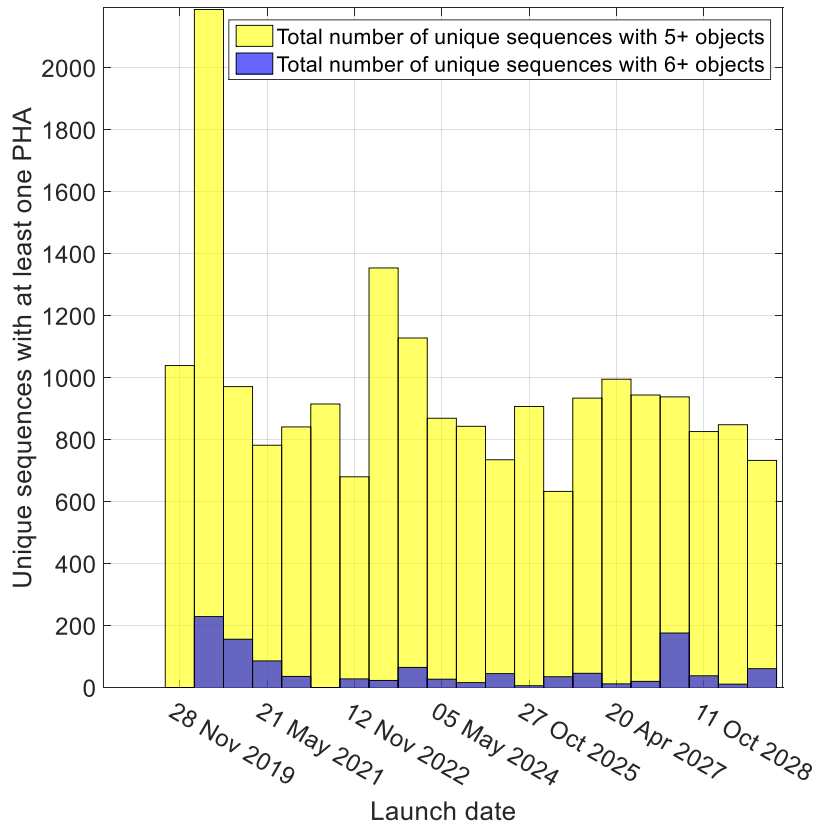


Fig. 4.11. Number of unique sequences with at least one PHA and five encounters as a function of the launch date. PHA-NHATS database with $a_c = 0.3 \text{ mm/s}^2$ (Test case 4).

Note the peak of sequences found for $t_0 = \tilde{t}_0 = 26 \text{ May 2020}$ (Fig. 4.11). An analysis of it might give an insight about the structure of the solution itself. Among the 2,188 sequences found for this launch date, 1,240 are characterised by the first two ordered encounters being 2011 CG₂ and 2014 UN₁₁₄. That is, more than half of the branches of the solution tree grow from the same bough. If the next depth of the tree is analysed, it can be seen that more than half of the solutions develop over three branches only. Figure 4.12 shows the first three depths of the solution tree for \tilde{t}_0 . Specifically, it is shown that 1,490 sequences share the same first encounter, whereas only 698 sequences are characterised by a different one. The results found for $t_0 = 11 \text{ May 2023}$, which is the launch date relative to the second peak shown in Fig. 4.11, are qualitatively similar. In fact, the two NEAs 2011 CG₂ and 2014 UN₁₁₄ are again the two most recurrent objects in all the sequences found for that very launch date. In particular, 2011 CG₂ is the second encounter after 2012 BB₁₄ for about 400 sequences. On the contrary, among all the 1,039 unique sequences found for the first launch date (Fig. 4.11), 2011 CG₂ appears only 108 times in total.

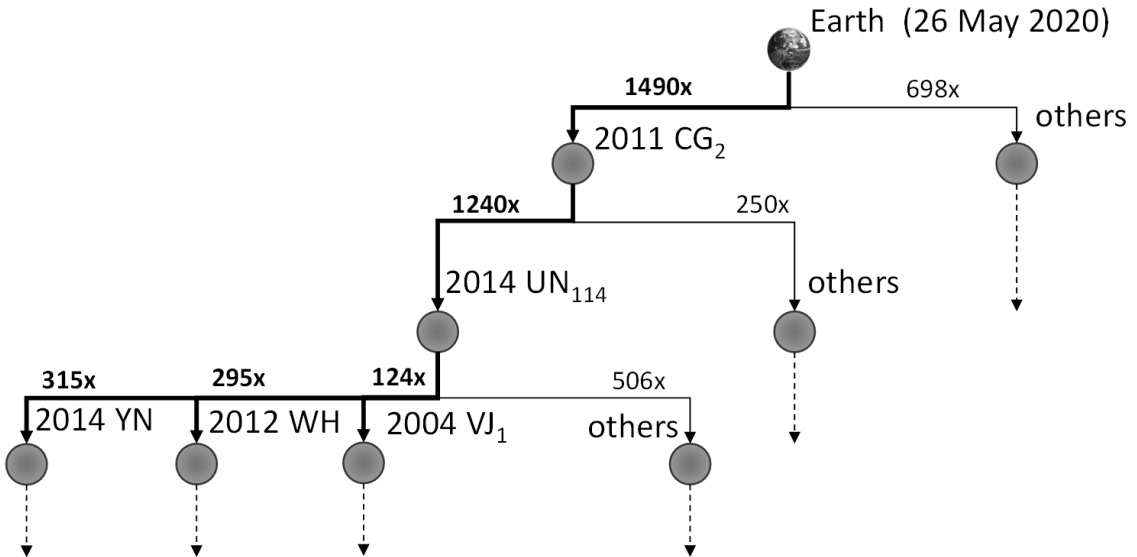


Fig. 4.12. Tree graph of the first three legs of all sequences with five encounters found for launch date $t_0 = 26$ May 2020 (Test case 4). The number of sequences that share the same branch is shown above each of them.

Further analysis is carried out on \tilde{t}_0 to study the repeatability of the solution. Specifically, two more runs of the sequence search are performed for $t_0 = \tilde{t}_0 \pm 2$ days. The run for $t_0 = \tilde{t}_0 - 2$ days resulted in 1,949 unique sequences found with at least five encounters, one of which is a PHA. This is compatible with what found for $t_0 = \tilde{t}_0$. On the other hand, only 817 unique sequences were found for $t_0 = \tilde{t}_0 + 2$ days which is a significantly smaller number. An analysis on the characteristics of the last run shows that there are no sequences for which the first two ordered encounters are 2011 CG₂ and 2014 UN₁₁₄. This explains the difference in the total number of sequences found. However, it is unlikely that a difference of two days in the launch date causes the loss of the phasing between the Earth and the two NEAs. Therefore, six runs of the sequence search are performed for the same launch date to investigate the repeatability of such solution. The results are shown in Fig. 4.13. It can be seen that five runs out of six resulted into a number of unique sequences comparable with that of $t_0 = \tilde{t}_0$ shown in Fig. 4.11. In fact, the result of the second run is the only one in which no sequences are characterised by the first two encountered being 2011 CG₂ and 2014 UN₁₁₄. A deeper analysis shows that the leg from the Earth to 2011 CG₂ for the second run takes 956 days. On the contrary, all the other runs, for which the leg from 2011 CG₂ to 2014 UN₁₁₄ is found, show a time of flight for the first leg of

about 537 days. This means that two minima exist in the OCP solved by GA. If GA finds the local minimum $T_{0f} \approx 956$ days, the phasing between 2011 CG₂ and 2014 UN₁₁₄ is lost and no solution exists. Note that this holds true for the problem formulation considered. It can be shown that a feasible solar-sail trajectory does indeed exist with $T_{0f}=1,200$ days between the two objects. It is worth reminding, however, that the maximum allowed time of flight has been chosen as $T_{0f,\max} = 1,000$ days in the current study (Table 4.3).

The discussion above highlighted an intrinsic characteristic of the tree search. That is, a whole set of solutions might not be shown in the results of the sequence search if no solutions are found for one branch or this is discarded by the BS algorithm. For instance, it has been shown that several local minima (within the chosen problem formulation) exist for one single leg. By using the genetic algorithm, there is a statistical confidence that the global minimum is found but there are rare cases in which this does not happen. In these cases, all the branches that grow from those legs will be affected. Nonetheless, the results of the sequence search showed that more than 600 unique sequences are found for each launch date. Therefore, there is a guarantee that at least the preliminary sequences shown exist.

Lastly, from the results shown for this test case, it can be seen that the choice of sorting the partial sequences in ascending order with respect to the total mission duration produced good results, in terms of number of sequences with at least one PHA. Therefore, there is no need to add an explicit rule that analyses the objects in each partial sequence. If, however, one wants to weight more those sequences that already contain one or more objects of interest (e.g. PHAs), a different rule can be considered for ordering the sequences to keep for the next leg. A Pareto optimality rule, for instance, could be used to sort the partial sequences so that preference is given to those sequences with the shortest mission time and the largest number of PHAs.

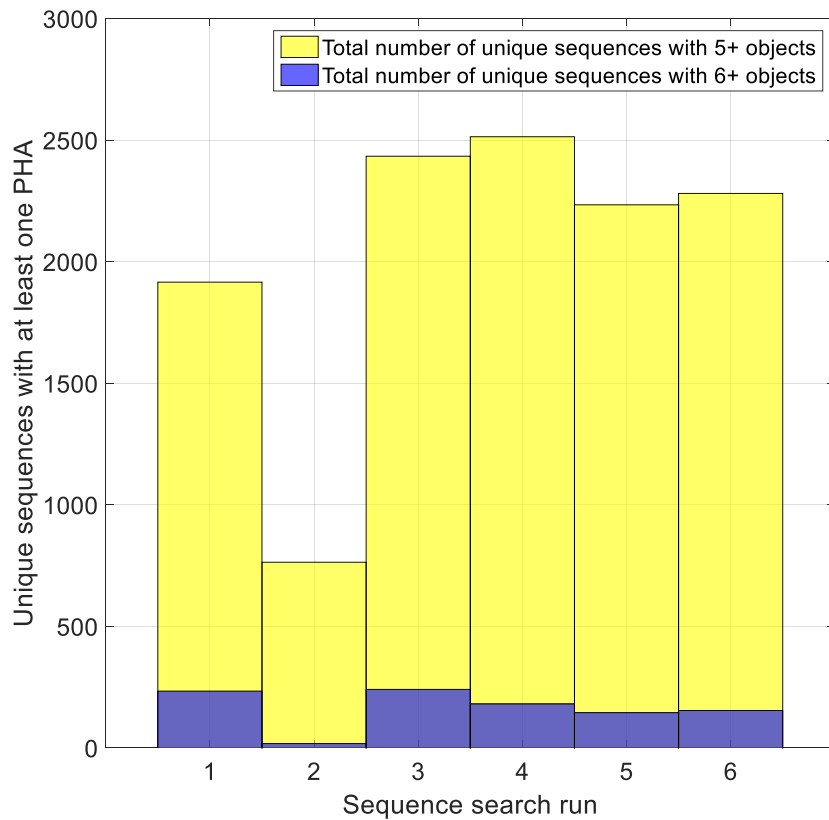


Fig. 4.13. Number of unique sequences with at least one PHA and five encounters for six runs on the sequence search for launch date $t_0 = 28$ May 2020 (Test case 4).

4.6.2. PHA-LCDB Database

The PHA-LCDB database introduced in Section 4.1 has been chosen to test the reliability of the proposed approach on a more challenging mission scenario than transfers between NHATS asteroids. Because of this, the number of sequences found by the sequence search algorithm is expected to be significantly smaller than what found considering the PHA-NHATS database.

For this test case, only one value of the characteristic acceleration is considered. That is, $a_c = 0.2 \text{ mm/s}^2$. The same set of departure dates considered in the case of the PHA-NHATS database and discussed in Section 4.6.1 is used in this case. A stay time of 50 days has been considered between two consecutive legs within the sequence search algorithm. A maximum time of flight of 1,000 days for each leg was allowed in the sequence search with the PHA-NHATS database, whereas a maximum one-leg time of flight of 1,500 days was chosen for this study. This choice has been driven by the fact that the single transfers are more challenging in the case of the PHA-LCDB database.

This search resulted in 589 unique sequences made of three encounters, of which at least one is a PHA. Figure 4.14 shows the number of unique sequences found for each departure date. Only those sequences with at least one PHA and at least three encounters are plotted.

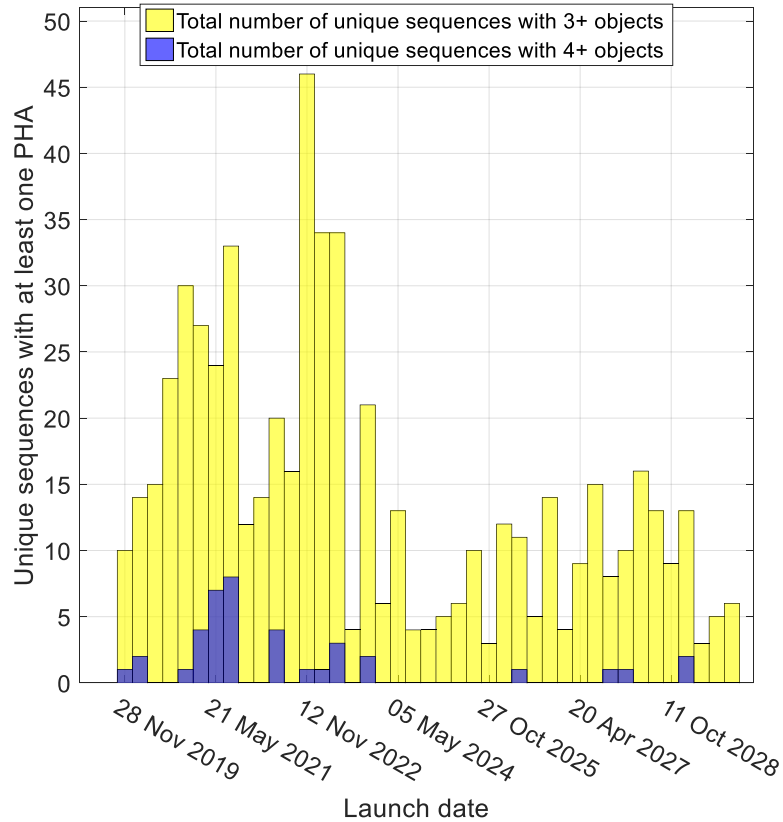


Fig. 4.14. Number of unique sequences with at least one PHA and three encounters as a function of the launch date. PHA-LCDB database with $a_c = 0.2 \text{ mm/s}^2$.

4.7. Discussion

In this chapter, a methodology to find sequences of encounters for multiple NEA rendezvous missions through solar sailing was presented and discussed. The sequence search algorithm is characterised by: (a) the use of the shape-based approach, presented in CHAPTER 3, to find approximated solar-sail trajectories, (b) a local pruning to reduce the computational effort needed, and (c) the use of two reduced databases of objects. Moreover, the proposed sequence search algorithm returns sequences of NEAs with preliminary epochs for the asteroid encounters, i.e. timed sequences. This provides a guideline for the next phase of

the mission design, which is the trajectory-optimisation phase, as it will be discussed in CHAPTER 5.

The use of the PHA-NHATS database resulted in more than 4,800 unique sequences made of at least five asteroids (at least four NHATS asteroids and at least one PHA) within less than ten years of total mission duration. This is true if a solar sail with lower performances than the one considered in a previous reference study is taken into account. If, instead, the characteristic acceleration of the reference work is used, it has been shown that an extremely large number of feasible sequences of at least five NEAs, of which one is a PHA, does exist. However, a reduction of the characteristic acceleration was one of the future steps to be addressed in the DLR/ESA Gossamer roadmap, as a lower characteristic acceleration involves a smaller or heavier sail for the same spacecraft bus. Therefore, this study showed that the mission-related TRL for the available solar-sail technology is larger than it was previously thought and that such a mission can be performed with current or at least near-term solar sail technology¹. Moreover, it was shown that, at least for the PHA-NHATS database, a 5-NEA-rendezvous mission is always possible within ten years by means of a solar sail.

The PHA-LCDB database was used to test the proposed asteroid sequence search on a different scenario. In fact, this second study was characterised by transfers that are more challenging than those of the previous study, which considered NHATS objects that, by definition, are targets easy to reach from the Earth.

An additional advantage of the proposed sequence search algorithm is the generation of a set of several feasible timed sequences, rather than a single optimal one. This is of great help to the mission analysts or the decision makers in the choice of the best mission. In fact, a solution is defined optimal on the basis of the mathematical model and mission parameters (e.g. launch window, current objects of interest, etc.) considered. If there is a change in one of these parameters within a later phase of the mission design, the single “optimal” solution, which has been found in a preliminary mission design phase, can be worthless.

¹ Note that a sail characteristic acceleration $a_c = 0.2 \text{ mm/s}^2$ is within the capability of current and near-term Gossamer sailcraft technology, according to [16, 31, 223]. Moreover, the technology developed at DLR for a controlled deployment of a Gossamer spacecraft is currently on TRL four approaching level five, according to [50].

Finally, this study showed that, for each launch date, hundreds of accessible NEA target sequences exist even within the restricted database of targets. Therefore, it can be concluded that there are little to no constraints on the launch window for a multiple-NEA rendezvous mission, if a solar sail is involved. Moreover, solar sailing has the advantage of flexibility on the target asteroids. The targets do not have to be selected before launch and they can be changed en route if, for instance, scientific or commercial interest changes over the years of the mission or when a new target of particular interest appears.

CHAPTER 5.

SEQUENCE OPTIMISATION

Once complete sequences of encounters for a multiple NEA rendezvous mission through solar sailing have been found, an optimisation problem must be solved to find 3D solar-sail trajectories. This chapter describes two optimisation approaches developed for finding multiple NEA rendezvous trajectories feasible by a solar sail. Both approaches employ the general-purpose optimal control software GPOPS-II, which uses a variable-order adaptive Radau collocation method, together with sparse nonlinear programming, as discussed in Section 2.2.2.

Several numerical test cases are shown and discussed to: (a) test the reliability of the proposed algorithms, (b) test such algorithms in an environment characterised by minimal inputs from the user, and (c) demonstrate the capabilities and the versatility of the solar-sail propulsion system.

The content of this chapter was published and/or presented in [31, 197-200, 214-216].

5.1. Problem Formulation

Because of the nature of the problem we are dealing with, an optimisation algorithm able to solve both single- and multi-phase problems is needed. For what concerns the optimisation of solar-sail trajectories described in this chapter, a single-phase problem is defined as a transfer between a departure and a target object (celestial bodies); instead, a multi-phase problem is characterised by several consecutive transfer legs, starting and ending at an object. The transfer legs are connected through coasting arcs during which the spacecraft stays in proximity of the target object, and follows the same ballistic trajectory, as schematically shown in Fig. 5.1. Since the spacecraft is considered in a state of rendezvous with the object between two consecutive transfer legs, the coasting arc is not explicitly modelled. The multi-phase problem is formulated such that the state of the sailcraft at the times corresponding to the beginning and end of each phase matches with the state of the target object within a user-defined tolerance.

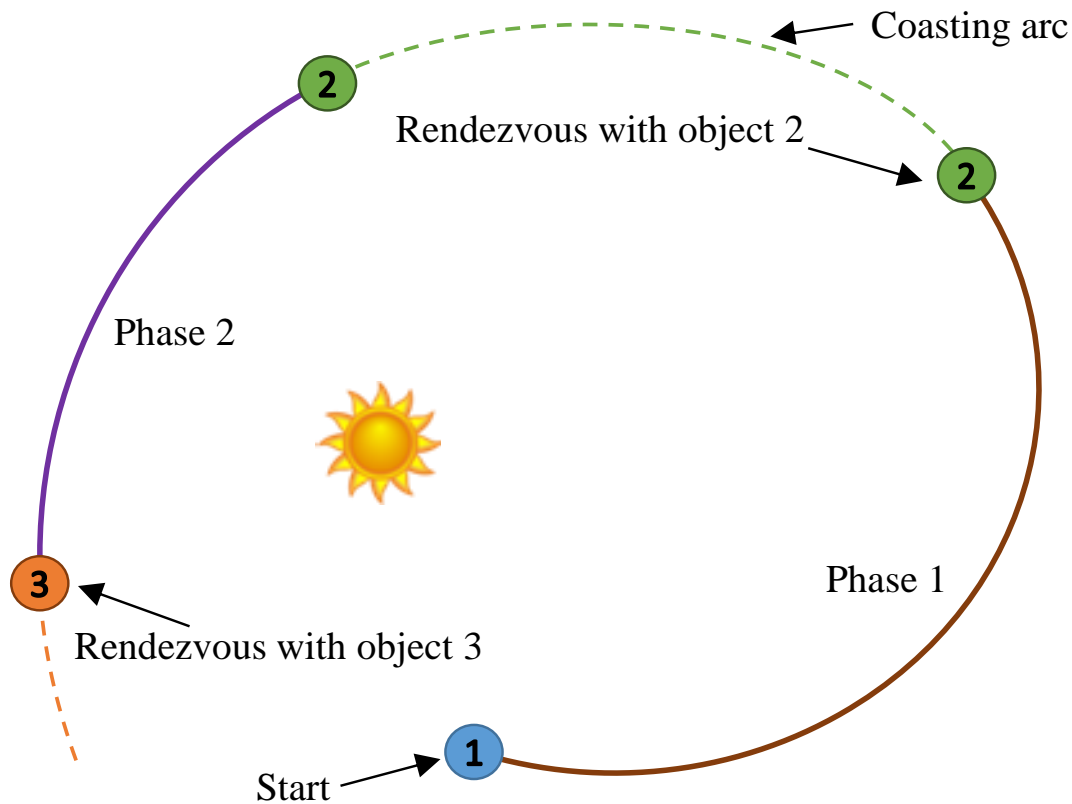


Fig. 5.1. Schematic of the multi-phase problem under consideration.

The dynamics within each phase is defined, in modified equinoctial elements, as [7]

$$\dot{\mathbf{x}} = \mathbf{A}(\mathbf{x})\mathbf{a} + \mathbf{b}(\mathbf{x}) \quad (5.1)$$

in which \mathbf{a} is the propulsive acceleration given by Eq. (2.18). The terms $\mathbf{A}(\mathbf{x})$ and $\mathbf{b}(\mathbf{x})$ that appear in Eq. (5.1) are, respectively, the matrix and vector of the dynamics expressed, in the orbital reference frame $\{\hat{r}, \hat{\theta}, \hat{h}\}$, as follows [7]:

$$\mathbf{A}(\mathbf{x}) = \begin{bmatrix} 0 & \frac{2p}{q} \sqrt{\frac{p}{\mu}} & 0 \\ \sqrt{\frac{p}{\mu}} \sin L & \sqrt{\frac{p}{\mu}} \frac{1}{q} \{(q+1)\cos L + f\} & -\sqrt{\frac{p}{\mu}} \frac{g}{q} \{h\sin L - k\cos L\} \\ -\sqrt{\frac{p}{\mu}} \cos L & \sqrt{\frac{p}{\mu}} \frac{1}{q} \{(q+1)\sin L + g\} & \sqrt{\frac{p}{\mu}} \frac{f}{q} \{h\sin L - k\cos L\} \\ 0 & 0 & \sqrt{\frac{p}{\mu}} \frac{s^2 \cos L}{2q} \\ 0 & 0 & \sqrt{\frac{p}{\mu}} \frac{s^2 \sin L}{2q} \\ 0 & 0 & \sqrt{\frac{p}{\mu}} \frac{1}{q} \{h\sin L - k\cos L\} \end{bmatrix} \quad (5.2)$$

$$\mathbf{b}(\mathbf{x}) = \left[0 \ 0 \ 0 \ 0 \ 0 \ \sqrt{\mu p} \left(\frac{q}{p} \right)^2 \right]^T \quad (5.3)$$

The terms q and s^2 are the auxiliary variables defined in Eq. (3.3). Note that both the state \mathbf{x} and the acceleration \mathbf{a} in Eqs. (5.1) - (5.3) are functions of the time but their explicit dependency on the time has been omitted for the sake of readability.

The problem of finding the optimal control vector $\mathbf{u}^* = [N_r^* \ N_g^* \ N_h^*]^T$ such that the total mission duration is minimised while fulfilling the dynamics constraints of Eq. (5.1) at any time, is solved via a direct collocation method [88]. This has been chosen against indirect methods because:

1. It is easier to deal with multi-phase problems. Furthermore, if the number of phases is not fixed, the problem should be reformulated each time the number of phases varies, if an indirect approach is used.
2. Its convergence to an optimal solution is usually easier than with an indirect method, although the solution is less accurate. Nevertheless, very accurate solutions are not required at this stage of the mission design.
3. Finding first guesses for the costates needed in the indirect method is usually difficult, since the costates do not have any physical meaning. On the other hand, an initial guess for the trajectory and the control history is usually easier to find.

The control vector \mathbf{u} should be bounded so that $\{N_g, N_h\} \in [-1, 1]$, whereas $N_r \in [0, 1]$ because of the inability of the solar sail to thrust towards the Sun. Moreover, a path constraint should be considered which enforces the control vector to be a unit vector. However, it has been noted that the NLP solvers can sometimes have difficulties in solving an OCP for which the optimal control lies exactly on the bounds. This is more likely to happen if a path constraint is set which enforces the magnitude of the control vector to be within certain limits¹. Therefore, the bounds on each component of the control vector are set to be larger than one and no path constraint on the magnitude of the control vector is enforced. Nevertheless, the actual thrust unit vector considered within the dynamics is the normalised control vector, such as

$$\hat{\mathbf{N}} = \frac{\mathbf{u}}{\|\mathbf{u}\|} \quad (5.4)$$

In this way, there is one less constraint to be satisfied and the problem is numerically easier to solve. Note that the components of the normal unit vector are preferred to the sail clock and cone angles as a control vector. Because of their periodicity, in fact, the sail control angles can lead to numerical issues within direct optimisation methods. Additionally, a set of endpoint constraints must be satisfied in each phase j , such as

¹ Dr Anil V. Rao, February 2016. Personal communication.

$$\begin{cases} \|\delta r(\{t_0^j, t_f^j\})\| \leq \delta r_{\max} \\ \|\delta v(\{t_0^j, t_f^j\})\| \leq \delta v_{\max} \end{cases} \quad (5.5)$$

in which δr and δv are, respectively, the position and velocity error of the spacecraft with respect to the target.

Lastly, and again to help the numerical convergence of the optimiser, the problem is scaled so that $r_{\oplus} = 1$ and $\mu = 1$. Because all the considered target orbits are near the Earth, this scaling guarantees that the norm of the position vector is always $\|r\| = \mathcal{O}(1)$; a characteristic acceleration $a_c = 0.2 \text{ mm/s}^2$ is scaled to $a_c = 0.0337$ in normalised units. Note that $a_c/\|r\| = \mathcal{O}(10^{-15})$ if the SI units are used, whereas the scaled problem is so that $a_c/\|r\| = \mathcal{O}(10^{-2})$, which is more suitable for numerical optimisation.

5.2. STO: Sequential Trajectory Optimiser

The sequential trajectory optimiser (STO) is the first optimisation approach developed to find solutions to the multiple NEA rendezvous mission problem. The trajectory found through the coplanar shape-based approach described in Section 3.1 is used as an initial-guess solution for the optimiser, which transforms it into a 3D trajectory. The general-purpose optimal control software GPOPS-II, together with the NLP solver SNOPT [72], is used within STO. Note that the interface for WORHP within GPOPS-II was not yet implemented at the time STO was developed and this is the reason for which WORHP has not been used within STO.

An algorithm has been developed in MATLAB to find the optimal trajectory in terms of total mission duration, as shown in Fig. 5.2. Given the selected timed sequence (i.e. list of target objects and encounter epochs), the algorithm performs as follows.

- 1) The algorithm automatically computes the initial guess for each leg separately by means of the shape-based approach with the objective function of Eq. (3.25), as described in Section 3.1.6. To avoid possible numerical problems in the optimisation phase that can affect the convergence of the optimiser, several initial-guess solutions are generated

for each leg. That is, the trajectory is propagated by considering both a constant control law between two points of the shaped function and a cubic spline interpolation of the control law. Moreover, two different stopping criteria are considered in the GA, so that four different initial-guess solutions are generated for each leg.

- 2) The algorithm optimises the 3D trajectory leg by leg. Each initial guess is optimised both without considering any further scaling method and by further scaling the problem through the *automatic-guessUpdate* choice provided by GPOPS-II [89]. Moreover, if no feasible or optimal solutions are found for the current leg, the default *hp* adaptive mesh refinement is changed so that the one developed by Liu et al. [92] is used for the whole optimisation. Within this optimisation phase, the solution of each leg is constrained to start at least two days after the arrival of the previous leg. In this way, the optimiser is forced to find a solution that guarantees a minimum time in the vicinity of the object for close-up observations. Moreover, a multi-phase optimisation, which would only be used to reduce the total mission duration, is not necessary.
- 3) Finally, if at least one feasible solution is found in all the legs individually, the whole multi-phase trajectory is built by patching together all the single-phase solutions found. This can be used as an initial guess for a subsequent multi-phase optimisation, if the total mission duration needs to be further reduced.

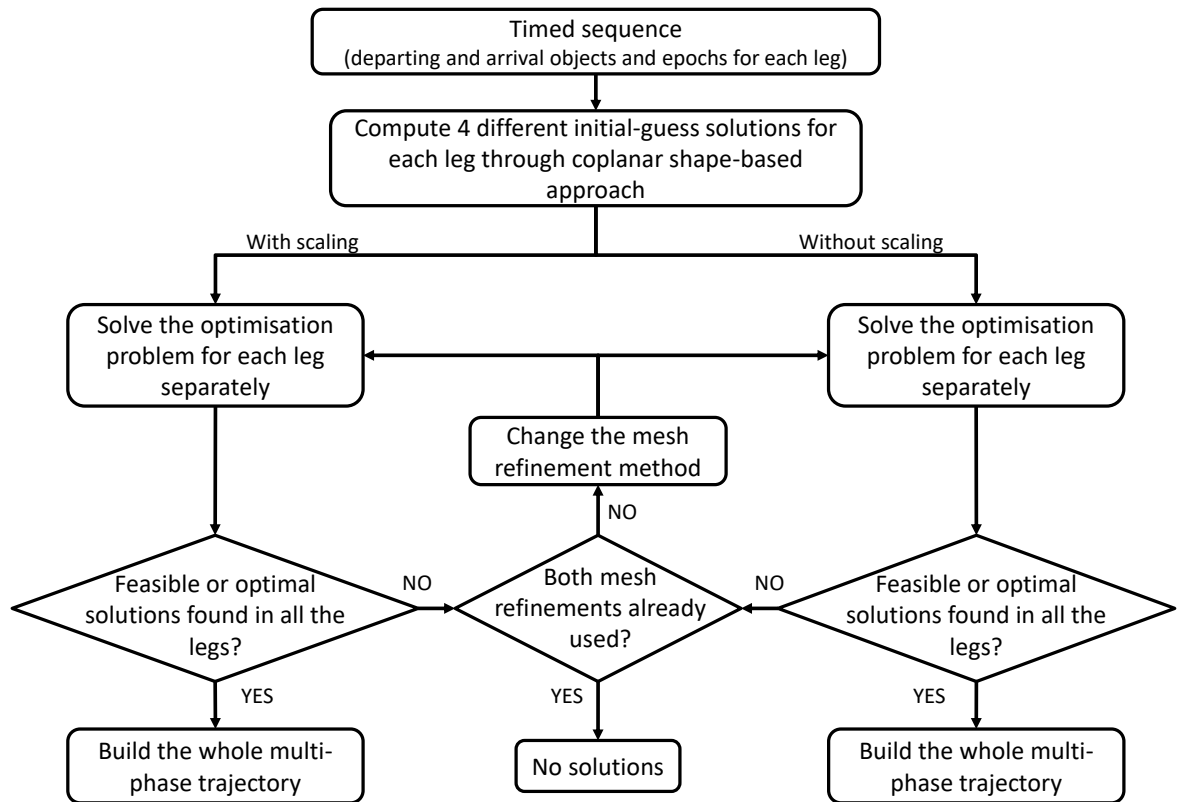


Fig. 5.2. Sequential trajectory optimiser algorithm.

5.3. ATOSS: Automated Trajectory Optimiser for Solar Sailing

The Automated Trajectory Optimiser for Solar Sailing (ATOSS) has been developed to find optimal solar-sail trajectories automatically and reliably. It has been developed as an upgrade of the sequential trajectory optimiser described in Section 5.2. ATOSS combines an initial-guess generator, which uses the shape-based approach described in Section 3.1, with an optimisation strategy based on a two-stage approach. Such approach, described in detail in Section 5.3.2, first finds a solution to the OCP and then improves it by modifying the description of the problem. Moreover, ATOSS can find solutions of single-phase as well as multi-phase problems. The general-purpose optimal control solver GPOPS-II is used to find the optimal solution to the solar-sail trajectory problem. Any of the NLP solvers implemented within GPOPS-II can be used. However, only SNOPT and WORHP [73] will be used in the test cases shown in Section 5.4, since those are

the two NLP solvers that perform better for the mission scenario under consideration (see Section 3.1.7). The *hp* adaptive mesh refinement developed by Liu et al. [92] is used in this work. Nevertheless, the mesh refinement method, as well as most of the GPOPS-II settings, can be easily chosen by the user through the ATOSS interface.

ATOSS can function in two modes, depending on the availability of a timed sequence. This allows ATOSS to be easily interfaced with the sequence-search algorithm described in CHAPTER 4 and thus to have a standalone toolbox able to both look for preliminary sequences and optimise their trajectories, but also to work independently of it. In fact, the output of the sequence-search algorithm is L_{compl} , which is a list of timed sequences (Algorithm 4.1). In those cases for which only a sequence of objects is provided (i.e. a non-timed sequence), ATOSS will self-generate the preliminary timeline. This is generated considering the locally-optimal control laws to maximise the rate of change of the orbital parameters, as described in [2]. In particular, the laws to change individually semimajor axis, eccentricity and inclination are implemented within ATOSS. For each transfer between two consecutive objects, the preliminary timeline considers the time of flight needed to achieve the desired change in one or more orbital elements. In this work, the allowed time of flight for each transfer leg is bounded between 500 and 1,500 days. Moreover, a set stay time is added between two consecutive transfers (100 days, in this work). It is worth noting that Graham and Rao [97] showed that “the solutions to the minimum-time low-thrust optimal control problem [...] have essentially the same number of revolutions as that of the initial guess”. Therefore, to improve ATOSS’ robustness in case of a non-timed sequence, the possibility to add an extra full revolution to the self-generated time of flight is considered.

A description of both the initial-guess generator and the optimisation strategy implemented within ATOSS is given in the next subsections.

5.3.1. Initial-Guess Generator

Three different methods can be used to generate an initial-guess solution for the optimiser, as follows.

- 1) Shape-based approach: propagated trajectory.
- 2) Shape-based approach: shaped trajectory.
- 3) Transversal-thrust law.

Note that the first two methods are two different variants of the shape-based approach, as discussed in Section 3.1.6. Because there is no reliable indicator on which one is best to serve as an initial guess for the subsequent numerical optimisation, both can be used to generate an initial-guess solution for the optimiser. Moreover, as discussed in Section 3.1.7, the performances of the two variants are comparable when they are used to generate an initial-guess solution for the solar-sail OCP. Lastly, the transversal-thrust law has been added to the initial-guess generator only to be used as a benchmark for the shape-based approach, as discussed in Section 3.1.7.

If an initial-guess solution to the problem at hand is already available, ATOSS can use it to initialise the optimiser. For instance, the homotopy-continuation approach for solar sailing, described in Section 3.2, can be used to generate initial-guess solutions for ATOSS. An example of this is shown in Section 5.4.5.

5.3.2. Optimisation Strategy

The optimisation strategy implemented within ATOSS consists of two sequential stages. Within the first stage, an initial solution for the multi-phase OCP is sought. In the second stage, a better solution, in terms of total mission duration, is computed by starting with the one found in the previous stage.

The general idea of the first stage is to find a solution to the OCP by starting with simpler dynamics and eventually solve the problem with the full dynamics. That is, starting from the chosen initial guess, the OCP is solved in three sequential steps to help the convergence of the numerical optimiser. The solution of each step is used as a first guess for the following step. Here and in the remainder of this thesis, the term *first guess* is referred to as the solution used to initialise GPOPS-II. For instance, the optimal solution found for the coplanar solar-sail dynamics is used as the first-guess solution within GPOPS-II for solving the

following OCP that considers 3D dynamics, as shown in Fig. 5.3. The description of the first stage is given, for a single-phase problem, as follows (Fig. 5.3).

- 1) Solve the single-phase OCP within a coplanar (2D) approximation, i.e. the plane of the orbit of the final target object is projected onto the one of the departing object, as shown in Eq. (3.21). The pseudo solar-sail model shown in Eq. (3.26) is considered for the description of the acceleration.
- 2) Solve the single-phase optimisation problem by considering the solar-sail acceleration [Eq. (2.18)] within a coplanar approximation.
- 3) Solve the single-phase optimisation problem by considering the 3D dynamics with the solar-sail acceleration of Eq. (2.18).

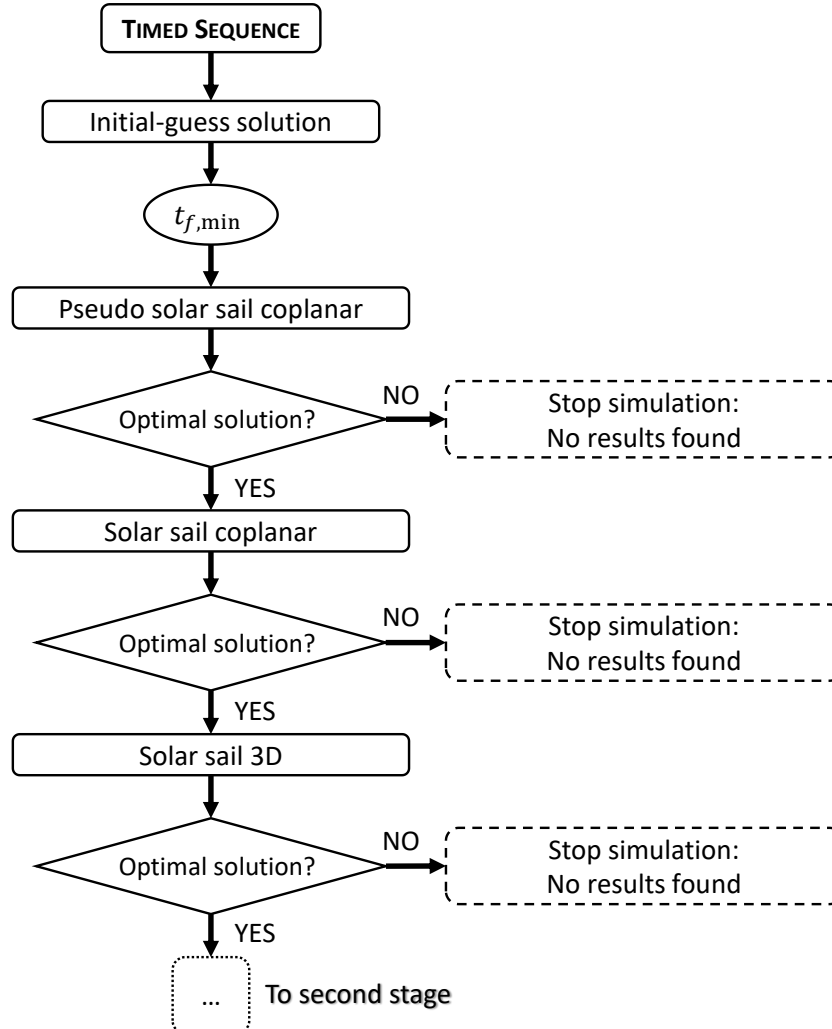


Fig. 5.3. Flowchart of single-phase ATOSS' optimisation strategy for the first stage.

The boundaries on the initial and final time considered in the numerical formulation of each OCP shown in Fig. 5.3 depend on the first-guess solution. This is implemented so that it is possible to consider an upper limit to the time of flight of a single-phase problem. For what concerns a multi-phase problem, this implementation allows setting the boundaries on initial and final times of two consecutive phases so that the latter phase is not allowed to start before the end of the former. Nevertheless, it has been noted that very often the time of flight of the optimal solution found is the minimum allowed by the problem formulation. A reduction in the lower boundary on the final time by about 50-100 days often resulted in unsuccessful runs of the numerical optimiser. Therefore, once an optimal solution has been found for the 3D dynamics, the second stage of the optimisation strategy is used.

In the second stage, ATOSS performs a discrete continuation on the lower boundary of the final time, using the previous solution as a first guess for GPOPS-II (Fig. 5.4). A user-defined value Δt_f is used to decrease the lower boundary on the final time ($\Delta t_f = 20$ days, in this work), whereas the boundaries on the initial time are related to the initial time of the first-guess solution. Such continuation is repeated until an unsuccessful run occurs. When an unsuccessful run occurs for the first time, the value Δt_f is halved to try a smaller continuation step. If a solution is found with the new value of the step size, the continuation loop proceeds with this new value until another unsuccessful run occurs. Once the loop has stopped, the solution of the entire optimisation is the last optimal solution found. The loop can stop also when an optimal solution has been found if the time of flight is larger than the minimum one allowed.

Note that, by using this continuation approach, more OCP problems are solved than using a substantially reduced lower boundary on the time of flight. Nevertheless, this approach significantly helps the convergence of the numerical optimiser. Moreover, the computational time needed for each successful run of the optimiser is usually small (varying between seconds and minutes).

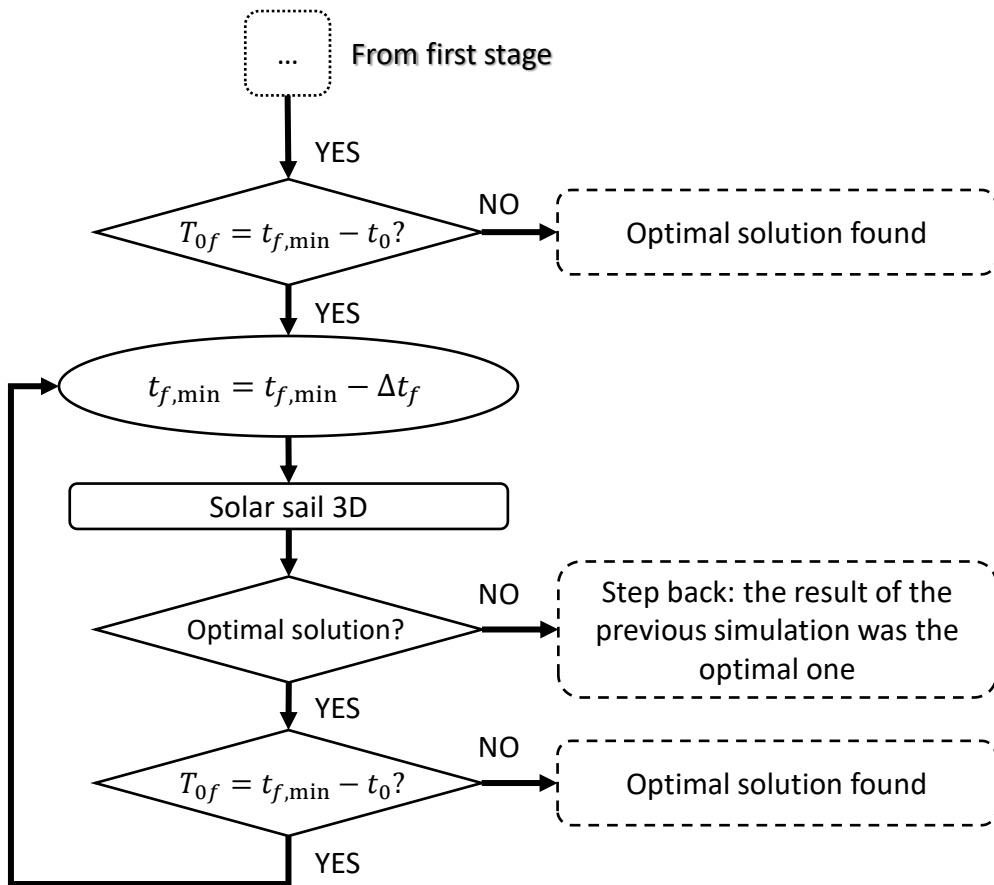


Fig. 5.4. Flowchart of both single- and multi-phase ATOSS' optimisation strategy for the second stage.

The strategy used for a multi-phase problem is similar to the one described for the single-phase problem. The algorithm begins by optimising the first phase starting from the selected initial-guess solution and following steps 1) - 3) described above. Once a 3D solar-sail solution has been found for the first phase, instead of performing the continuation on the lower boundary on the final time, the second phase is added to the problem (Fig. 5.5). Subsequently, each phase is sequentially added to the previous multi-phase solution (with j phases) so that the updated multi-phase solution (with $(j+1)$ phases) is computed. The first guess for this new problem is given by patching the solution of the previous optimisation with the initial guess of the new phase. The updated multi-phase OCP is therefore solved so that the dynamics considered for the first j phases are the 3D solar-sail ones, whereas the three-step approach shown in Fig. 5.3 is considered for the last phase only. This approach is different respect to the sequential trajectory optimiser described in Section 5.2, in which each phase of the problem is optimised separately and, subsequently, all the single-phase optimal solutions are

patched together to build the multi-phase solution. That is, even if the solutions of all phases are optimal, there is no guarantee that the overall multi-phase solution is also optimal. On the contrary, the approach used within ATOSS guarantees the optimality of the entire multi-phase solution. This is in agreement with the Bellman's principle of optimality, which states that "an optimal policy has the property that whatever the initial state and initial decision are, the remaining decisions must constitute an optimal policy with regard to the state resulting from the first decision" [224]. Once a solution for the complete multi-phase problem has been found, the continuation on the lower boundaries on the final time is performed, as shown in Fig. 5.4. That is, the lower boundary on the final time of each phase is decreased by the selected value Δt_f .

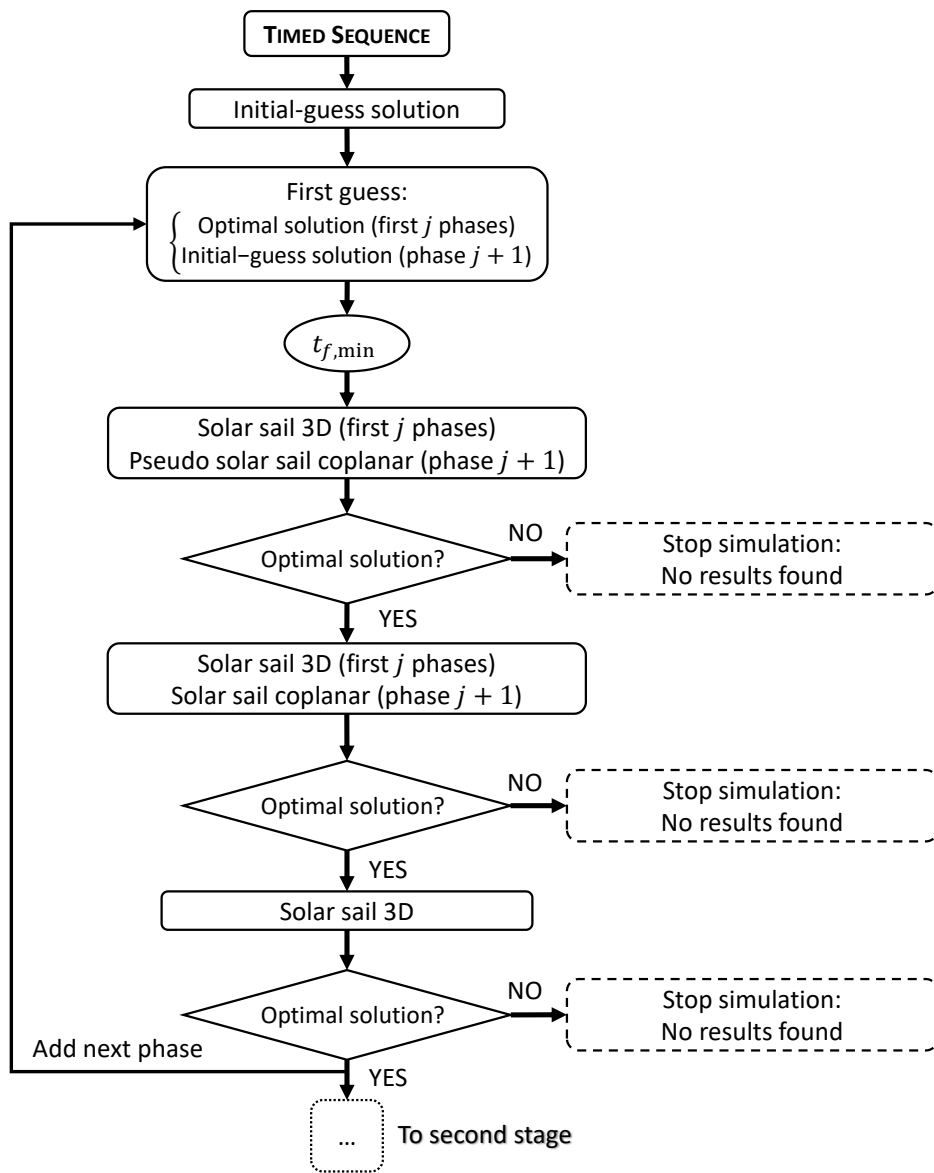


Fig. 5.5. Flowchart of multi-phase ATOSS' optimisation strategy for the first stage.

5.4. Numerical Test Cases

Several numerical test cases are used to prove the ability of the two optimisers in finding 3D trajectories for multiple NEA rendezvous mission. Moreover, in Section 5.4.6, the performances of both optimisers are tested in an automatic optimisation campaign. All the simulations presented in this section were carried out on a 3.40 GHz Core i7-3770 with 16 GB of RAM and running Windows 7. Both NLP solvers SNOPT and WORHP are used and the results found with the one that performs better are shown. Moreover, STO has been developed before the interface for WORHP was implemented within GPOPS-II, thus the use of SNOPT in those test cases solved with STO. Note that, despite it will be shown that ATOSS statistically performs better than STO, there are cases in which the latter finds a better solution than the former. These are the cases for which STO has been chosen for the optimisation.

Different scenarios for multiple NEA rendezvous missions, other than those discussed in this work, were published in [197, 198, 200, 214-216].

5.4.1. Circular-to-Circular Orbit Transfers: A Comparison with the Literature

Quarta and Mengali [225] presented two planar circular-to-circular orbit transfers considering an ideal sail with a characteristic acceleration $a_c = 0.03 \text{ mm/s}^2$. With such a small value of the characteristic acceleration, several complete revolutions are needed for the Earth-Mars and Earth-Venus transfers. This increases the possibility of failure of the numerical optimiser, since a larger number of revolutions might affect the numerical accuracy of the solver. As such, these are interesting test cases to validate ATOSS. The shaped-trajectory variant of the shape-based approach (No. 2) in Section 5.3.1) was used to generate the initial-guess solution and SNOPT was used as NLP solver. The boundaries on L_f for the GA were set as follows. A minimum-time transfer between two circular coplanar orbits is achieved by maximising the absolute value of the rate of change of the semimajor axis da/dL , which can be expressed, by means of the Lagrange variational equations, as [2]

$$\frac{da}{dL} = \frac{2a_c r_{\oplus}^2 a}{\mu} \cos^2 \alpha^* \sin \alpha^* \quad (5.6)$$

in which $\alpha^* = \arctan(\sqrt{1/2})$ is the cone angle that maximises the transversal acceleration [2]. Note that Eq. (5.6) has been derived in the approximation of circular osculating orbits during the transfer. This is an acceptable approximation because the transfer is between two circular orbits and the characteristic acceleration is very small. The lower boundary on L_f is set as the value of true longitude \hat{L}_f for which the change in semimajor axis Δa is the desired one, such as

$$\Delta a = \int_{L_0}^{\hat{L}_f} \frac{da}{dL} dL \quad (5.7)$$

The upper boundary on L_f is set so that $L_f \in [\hat{L}_f, \hat{L}_f + 2\pi]$.

ATOSS found a solution for both Earth-Mars and Earth-Venus orbit transfers which are equivalent to those shown in [225]. Specifically, the time of flight for the Earth-Venus transfer found by ATOSS is 3,837 days, which is similar to the 3,844 days of the reference paper. The time of flight for the Earth-Mars transfer found by ATOSS is 8,773 days, which is again equivalent to the 8,800 days of the reference paper. The Earth-Venus and Earth-Mars optimal trajectories are shown in Fig. 5.6.

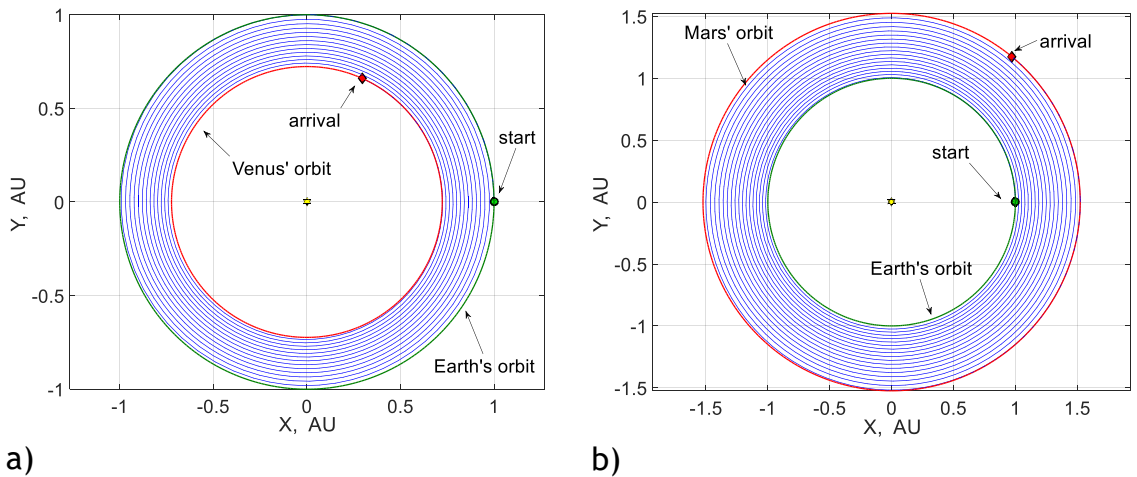


Fig. 5.6. Optimal orbit transfers in the heliocentric ecliptic reference frame. (a) Earth-Venus. (b) Earth-Mars.

5.4.2. Three-NEA Rendezvous Mission: A Comparison with the Literature

Dachwald et al. [16] presented a 3-NEA rendezvous mission, considering a sail with a characteristic acceleration $a_c = 0.3 \text{ mm/s}^2$. The total mission duration, from launch until arrival to the final target body, is 9.16 years (which is 3,345 days). In that work, the sail is injected directly into an interplanetary trajectory at Earth, with zero hyperbolic excess energy. Table 5.1 shows the properties of all the encountered bodies. Here and in the following test cases, the estimated sizes of the objects are calculated from the Minor Planet Center table of conversion from absolute magnitude to diameter, considering an albedo in the range 0.05 to 0.25¹.

Table 5.1. Properties of all the encounters of the sequence presented in [16]².

Object	2004 GU ₉	2001 QJ ₁₄₂	2006 QQ ₅₆
Orbital type	Apollo	Apollo	Aten
Semimajor axis, AU	1.001	1.062	0.985
Eccentricity	0.136	0.086	0.046
Inclination, deg	13.650	3.103	2.796
Absolute magnitude	21.2	23.7	25.9
Estimated size, m	170-380	50-120	10-40
EMOID, AU	0.0006	0.0094	0.0152
PHA	Yes	No	No
NHATS	No	Yes	No

ATOSS has been used to find a solar-sail trajectory for the same list of encounter bodies to validate the proposed optimiser. ATOSS has been used considering both a timed and a non-timed sequence as an input. In the first case, the mission parameters of the reference work were used to produce the timed sequence needed by ATOSS. This has been done to check whether ATOSS can

¹ Data available online at <http://www.minorplanetcenter.net/iau/lists/Sizes.html> [retrieved 08 August 2015].

² Data available online at <https://cneos.jpl.nasa.gov/orbits/elements.html> [retrieved 08 August 2015].

reproduce and refine the trajectory of the reference work by starting from the same timed sequence. In the second case, instead, only the list of objects and the departing date from the reference work have been given as an input to ATOSS. This has been done to check whether ATOSS can find a similar solution to that shown in [16] without any external input. Since the objects in the non-timed sequence are NEAs, it has been chosen to consider only the time of flight given by the law to maximise the rate of change of the inclination to generate the preliminary timeline within ATOSS. In fact, Table 5.1 shows that the differences in semimajor axis and eccentricity are small for the objects under consideration, whereas there are significant differences in inclination. For both cases, the shaped-trajectory variant of the shape-based approach was used to generate the initial-guess solution and SNOPT was used as NLP solver.

The features of the mission are described in Table 5.2 for the case of the timed sequence used as an input for ATOSS. Figure 5.7a shows the trajectory of the first leg from Ref. [16], whereas the corresponding trajectory found by ATOSS is shown in Fig. 5.7b. ATOSS found a solution for which the total mission duration is 8.46 years (i.e. 3,090 days), which is almost a year less than that proposed in [16]. However, the time spent at the first object, which is also classified as a PHA, is the minimum allowed by the optimiser (i.e. two days). Even though this value of the stay time is in line with the mission requirements (see Section 4.5), more time might be needed at the object. If this is the case, a slower mission was found in the same optimisation run which is one of the intermediate results of the optimisation strategy shown in Fig. 5.4. The characteristics of this mission are shown in Table 5.3. In this case, the total mission duration is 8.82 years (i.e. 3,220 days), spending 50 days at 2004 GU₉. Such a mission is still approximately 120 days shorter than the reference one. Note that ATOSS gives the possibility to set the minimum allowed stay time at each object. Therefore, if a longer stay time at the object is needed, this can be set and a new optimisation run.

Table 5.2. Mission parameters for the optimal 3-NEA rendezvous (values in brackets are those presented in [16] and used as timed sequence for ATOSS).

Object	Stay time, days		Start	End	Time of flight, days
Earth	---		16 May 2020	13 May 2023	1093
2004 GU ₉	2	⟳	(28 Nov 2019)	(13 Dec 2022)	(1111)
	(113)	⟳	15 May 2023	28 Jan 2027	1354
2001 QJ ₁₄₂	133	⟳	(05 Apr 2023)	(30 Jan 2027)	(1396)
	(90)	⟳	10 Jun 2027	31 Oct 2028	509
2006 QQ ₅₆	---	⟳	(30 Apr 2027)	(24 Jan 2029)	(635)

Table 5.3. Mission parameters for the optimal 3-NEA rendezvous, longer mission (values in brackets are those presented in [16] and used as timed sequence for ATOSS).

Object	Stay time, days		Start	End	Time of flight, days
Earth	---		27 Mar 2020	12 Feb 2023	1053
2004 GU ₉	50	⟳	(28 Nov 2019)	(13 Dec 2022)	(1111)
	(113)	⟳	03 Apr 2023	30 Jan 2027	1398
2001 QJ ₁₄₂	106	⟳	(05 Apr 2023)	(30 Jan 2027)	(1396)
	(90)	⟳	16 May 2027	19 Jan 2029	614
2006 QQ ₅₆	---	⟳	(30 Apr 2027)	(24 Jan 2029)	(635)

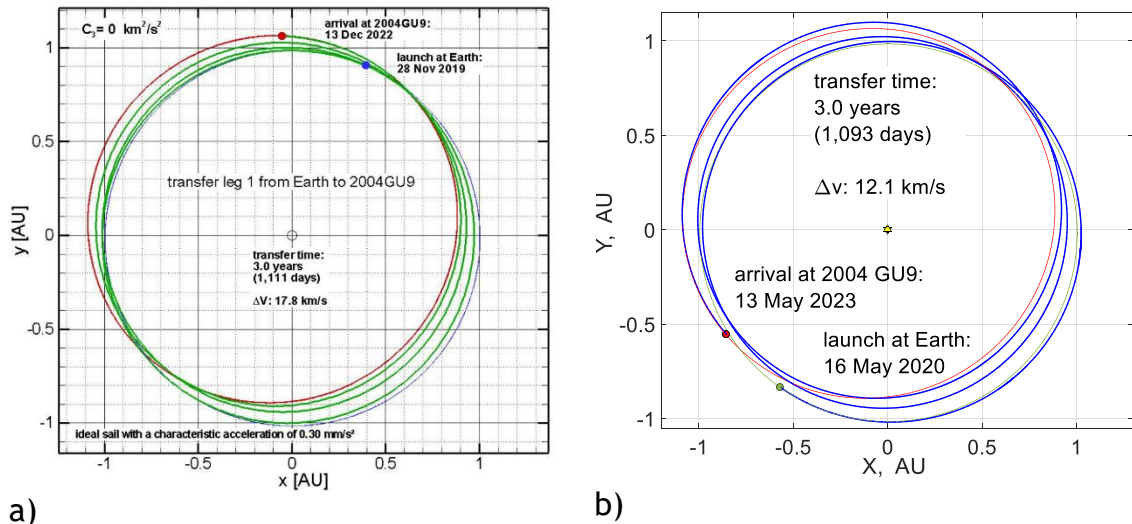


Fig. 5.7. Trajectory of the first leg from Earth to 2004 GU₉. Heliocentric ecliptic reference frame. (a) Ref. [16] (Reproduced with permission of Springer). (b) ATOSS with timed sequence as an input.

In the second case, in which a non-timed sequence was used as an input, ATOSS found a solution by self-generating the preliminary timeline for the encounters. The total mission duration found by ATOSS is 8.83 years (i.e. 3,223 days), which is about 120 days less than that shown in [16]. Table 5.4 shows the characteristics of this mission together with the preliminary timeline self-generated by ATOSS. Note that the sailcraft spends more than 90 days at each object, which is a stay time equivalent to that shown in the reference paper.

Table 5.4. Mission parameters for the optimal 3-NEA rendezvous in the case of a non-timed sequence as an input (values in brackets are those self-generated by ATOSS).

Object	Stay time, days		Start	End	Time of flight, days
Earth	---		04 Mar 2020	24 Dec 2022	1026
2004 GU ₉	99		(28 Nov 2019)	(19 Dec 2022)	(1117)
	(100)		02 Apr 2023	23 Oct 2026	1300
2001 QJ ₁₄₂	111		(29 Mar 2023)	(12 Sep 2026)	(1263)
	(100)		11 Feb 2027	30 Dec 2028	688
2006 QQ ₅₆	---		(21 Dec 2026)	(04 May 2028)	(500)

5.4.3. Multiple NEA Rendezvous Missions

The test cases studied in this subsection aim to show some fully-optimised trajectories for a multiple NEA rendezvous mission. Because of the Gossamer requirements discussed in Section 4.5, a solar sail with a characteristic acceleration $a_c = 0.2\text{mm/s}^2$ is considered throughout this subsection. Therefore, from the results of the sequence search shown in Section 4.6 with $a_c = 0.2\text{mm/s}^2$, two sequences have been selected as samples and fully optimised. The first sequence has been selected among all the sequences found with five encounters, of which one is a PHA and the last object is small, as from the mission requirements a) - c) in Section 4.5. This sequence is one of those found for the PHA-NHATS database. On the other hand, the second sequence has been chosen among the results of the PHA-LCDB database. This sequence has been chosen because it is characterised by the presence of two PHAs and all the target orbits are significantly more eccentric than the one of the Earth, despite it has only three encounters.

Sequence 1. The first sequence presented here contains five objects. All the objects in the selected sequence are part of the NHATS database used and the fourth, 2008 EV₅, is also classified as a PHA. Table 5.5 shows the encountered bodies in the sequence. Note that, in Table 5.5, the change in inclination between two consecutive objects is always less than 5 deg, which is the threshold used for the coplanar approximation [Eq. (4.16)]. However, Table 5.5 shows that the inclination of the encounter's orbits increases by moving from an object to the following, eventually reaching an inclination of about 10 deg for the last encounter. This result is significantly different respect to what could be found by following the sequence search method described in [197], in which a threshold of 5 deg on the maximum inclination was considered within the pruning of the whole database. Therefore, this sequence could not have been found because the last three asteroids have an inclination larger than the 5 deg threshold.

Table 5.5. Properties of the encounters of sequence 1¹.

Object	2000 SG ₃₄₄	2015 JD ₃	2012 KB ₄	2008 EV ₅	2014 MP
Orbital type	Aten	Amor	Amor	Aten	Amor
Semimajor axis, AU	0.977	1.058	1.093	0.958	1.050
Eccentricity	0.067	0.009	0.061	0.083	0.029
Inclination, deg	0.111	2.730	6.328	7.437	9.563
Absolute magnitude	24.7	25.6	25.3	20	26
Estimated size, m	35-75	20-50	20-50	260-590	17-37
EMOID, AU	0.0008	0.054	0.073	0.014	0.020
PHA	No	No	No	Yes	No
NHATS	Yes	Yes	Yes	Yes	Yes

By following the optimisation steps described in Section 5.3, a multi-phase solution was found. ATOSS has been used with the NLP solver WORHP and the shaped-trajectory variant of the shape-based approach as the initial-guess solution. The parameters of the optimised mission are briefly described in Table 5.6. The values in brackets are the results of the sequence search algorithm, which have been used as the timed sequence needed by ATOSS. Note that the stay time

¹ Data available online at <https://cneos.jpl.nasa.gov/orbits/elements.html> [retrieved 08 August 2015].

in brackets is always equal to 100 days, since it is a fixed value, as specified in Section 4.6.1. The sail is injected directly into an interplanetary trajectory at Earth, with zero hyperbolic excess energy. The mission is completed in about 8.6 years after departing from Earth on 05 December 2025. As shown in Table 5.6, the sail spends at least three months in the proximity of each object, giving sufficient time for close-up NEA observations.

It is worth noting that the arrival at 2014 MP after 3,133 days is not necessarily the end of the mission. As long as the sailcraft remains flightworthy, the visit at 2015 MP may well be followed by further legs to other NEAs. In fact, the duration of the mission is not constrained by the amount of propellant on board, as it usually happens when an electrical or chemical propulsion system is used. It only depends on the ageing of the systems aboard and the will to pay the flight operators a while longer for their effort. For instance, Pioneer 6 was designed to last about 6 months, after its launch on 16 December 1965. The last successful contact with it was made on 08 December 2000 - 35 years later. In 1997, three of its instruments still worked well¹.

Table 5.6. Mission parameters for optimised sequence 1 (values in brackets are those found through the sequence search algorithm and used as a first guess for ATOSS).

Object	Stay time, days		Start	End	Time of flight, days
Earth	---		05 Dec 2025 (30 Apr 2025)	18 Mar 2027 (11 Mar 2027)	468 (680)
2000 SG ₃₄₄	93 (100)	↻	19 Jun 2027 (19 Jun 2027)	03 Nov 2028 (31 Oct 2028)	503 (500)
2015 JD ₃	104 (100)	↻	16 Feb 2029 (08 Feb 2029)	22 Nov 2030 (14 Nov 2030)	644 (644)
2012 KB ₄	94 (100)	↻	23 Feb 2031 (22 Feb 2031)	22 Nov 2032 (30 Nov 2032)	637 (647)
2008 EV ₅	95 (100)	↻	25 Feb 2033 (10 Mar 2033)	04 Jul 2034 (25 Nov 2034)	493 (625)
2014 MP	---	↻			

¹ Data available online at <https://www.nasa.gov/centers/ames/missions/archive/pioneer.html> [retrieved 15 June 2017].

The complete trajectory of the optimised sequence 1 is shown in Fig. 5.8. The stay times at the objects are highlighted against the interplanetary legs. The orbit of the Earth is also plotted. Plots of the control histories on each leg are in Fig. 5.9. The three components of the acceleration vector in the orbital reference frame over time are shown, together with the magnitude of the acceleration over time.

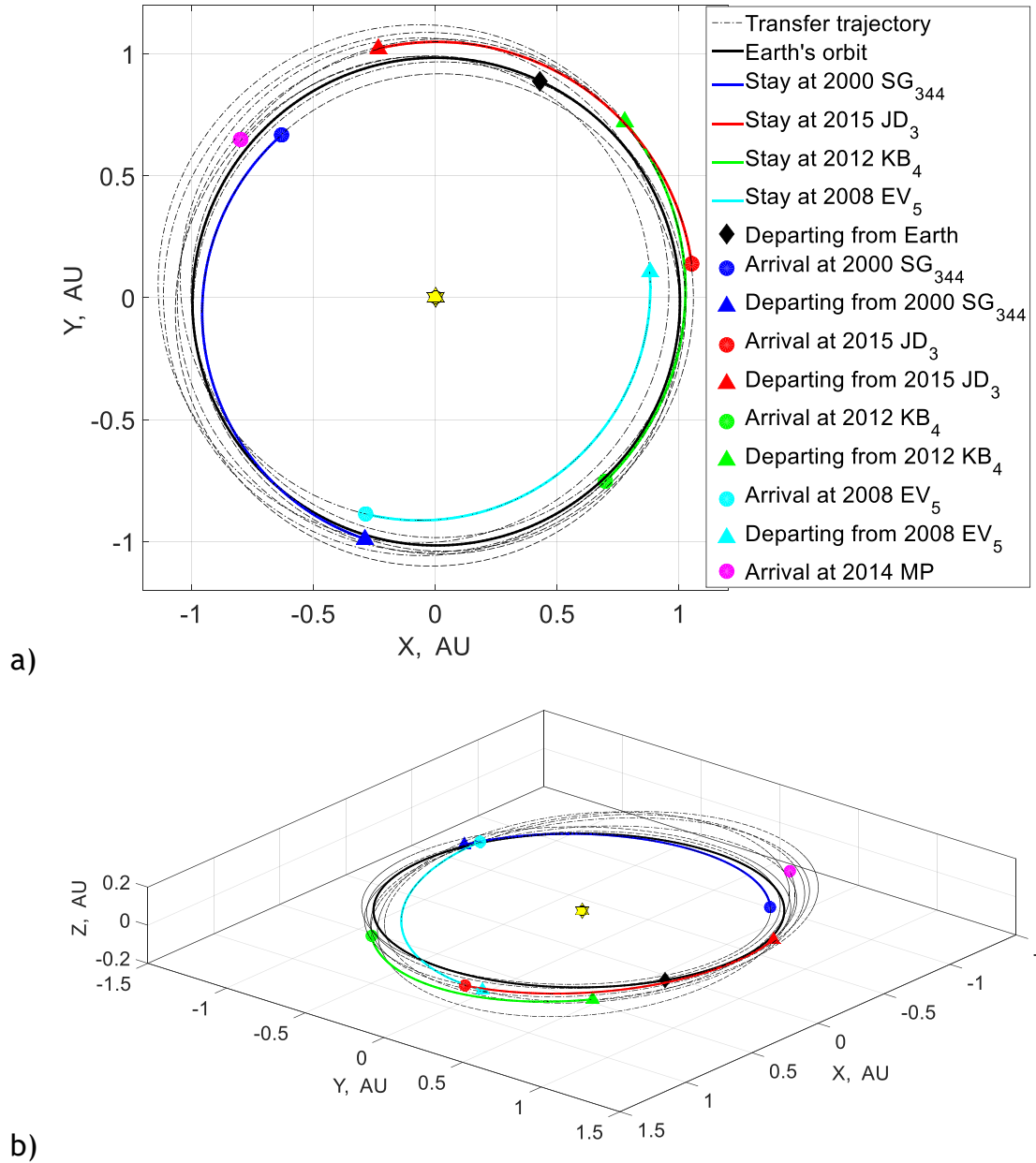


Fig. 5.8. Heliocentric view of the 3D trajectory of optimised sequence 1: (a) ecliptic plane view; (b) 3D view.

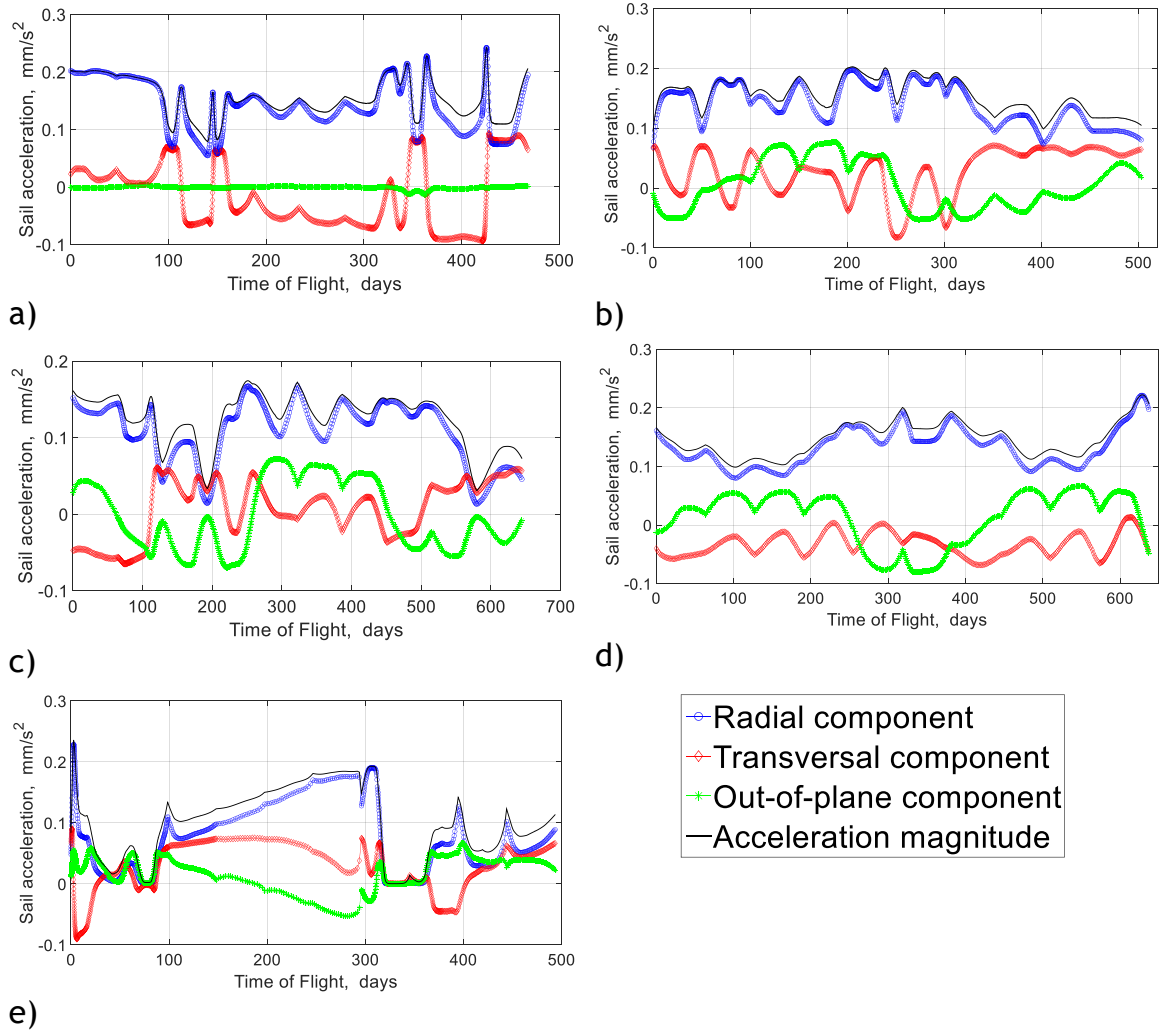


Fig. 5.9. Acceleration components history on each transfer leg of optimised sequence 1.

It is worth noting that, despite the few spikes in the control history shown in the plots in Fig. 5.9, the results are feasible by a solar sail with currently-available technology. This can be demonstrated by studying both slew rate and angular acceleration of the sail required to follow the control histories shown in Fig. 5.9. Denoting the angle ζ as the angle between two consecutive attitudes [i.e. $\zeta \triangleq \arccos(\hat{\mathbf{N}}(t_i) \cdot \hat{\mathbf{N}}(t_{i+1}))$], the sail slew rate $\dot{\zeta}$ is defined as the rate of change of the sail attitude. Figure 5.10a shows the sail slew rate for the last leg of the current five-NEA sequence. This leg has been chosen because it is the one with the highest value of slew rate. Figure 5.10a shows that the sail slew rate is always $\dot{\zeta} < 3 \times 10^{-4}$ deg/s. Studies on solar-sail attitude control in the literature show that a solar sail with a characteristic acceleration of $a_c = 0.1$ mm/s² is able to perform a 35 deg manoeuvre in less than 3 hours [48, 226], thus with an average sail slew rate of $\dot{\zeta} \approx 5 \times 10^{-3}$ deg/s. Moreover, Wie and Murphy [226] show that

the spike in the slew rate for a 35 deg yaw manoeuvre is $\dot{\zeta}_{\max} \approx 0.03 \text{ deg/s}$, which is higher than the maximum slew rate required during the whole mission described here.

The angular acceleration needed to follow the control found through ATOSS shall also be investigated to verify the feasibility of such a mission from the attitude-control point of view. Figure 5.10b shows the angular acceleration for the last transfer leg of the first optimised sequence, obtained by time differentiation of the sail slew rate shown in Fig. 5.10a. It is possible to see a spike in the angular acceleration, related to the first pick in the slew rate, of $\ddot{\zeta} \approx 2 \times 10^{-9} \text{ deg/s}^2$. For comparison, note that the maximum torque allowed for a Mars rendezvous mission in [227] (pp. 69-86) is set to $\tau_{\max} = 10^{-3} \text{ Nm}$. Because a solar sail with an area $A = (160 \text{ m})^2$ and a total mass $m_0 = 450 \text{ kg}$ is considered in the aforementioned work, the equivalent maximum allowed angular acceleration is $\dot{\zeta}_{\max} \approx 6 \times 10^{-8} \text{ deg/s}^2$, considering a perfect square sail rotating around one of the principal axes of inertia on the sail plane. Such value is larger than the maximum sail angular acceleration needed to achieve the proposed transfers (Fig. 5.10b).

Because no explicit constraints have been set on either the sail slew rate or the angular acceleration within ATOSS, further optimisation may be needed if stricter constraints are required.

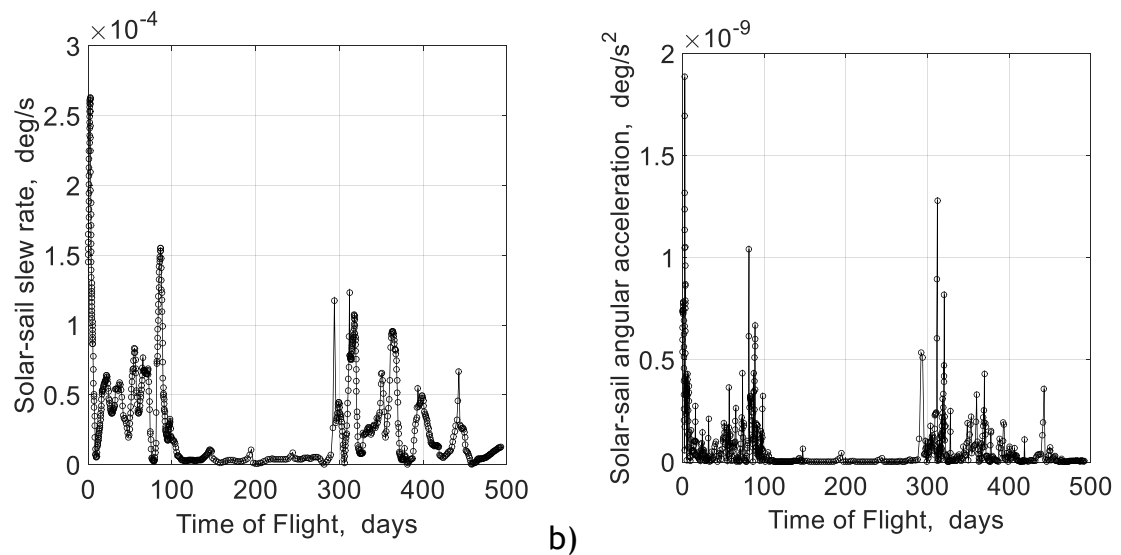


Fig. 5.10. Sail slew rate (a) and sail angular acceleration (b) over time on the last leg of optimised sequence 1.

From a trajectory optimisation point of view, it is interesting to study the evolution of the total mission duration during the second stage of the optimisation strategy implemented within ATOSS. As detailed in Section 5.3.2, once the entire multi-phase 3D trajectory has been found, a discrete continuation on the lower boundary on the final time is carried out to find a solution with a lower total mission duration. Figure 5.11 shows the evolution of the total mission duration within ATOSS. The total cumulative computational time needed to find a solution is shown along the horizontal axis. Each point in the figure corresponds to a solution found by ATOSS in each intermediate step. The first point is related to the mission duration of the entire trajectory obtained by patching together the initial-guess trajectories for each transfer leg. Note that the significantly longer time related to the second point is due to ATOSS finding a 3D multi-phase trajectory starting from the solutions of the shape-based approach, which is the first stage of the optimisation strategy described in Section 5.3.2 and shown in Fig. 5.5. In conclusion, Fig. 5.11 demonstrates the importance of the continuation stage implemented within ATOSS, which decreases the total mission duration by 10% respect to the value of the initial guess. In fact, a gain of 6% of total mission duration is achieved during the second stage of the optimisation strategy developed within ATOSS (i.e. between the last and the second point shown in Fig. 5.11).

Lastly, the end-to-end optimisation phase, as described in Section 5.3, needed about four hours of computational time. It is important to note, however, that this is the overall time required by ATOSS and it includes the time spent within the optimiser when the convergence was not achieved, other than the generation of the initial guesses. If the time spent by the optimiser to find the shown trajectory is considered alone, a total time of about half an hour is needed for the end-to-end optimisation of the entire multi-leg trajectory, as shown in Fig. 5.11.

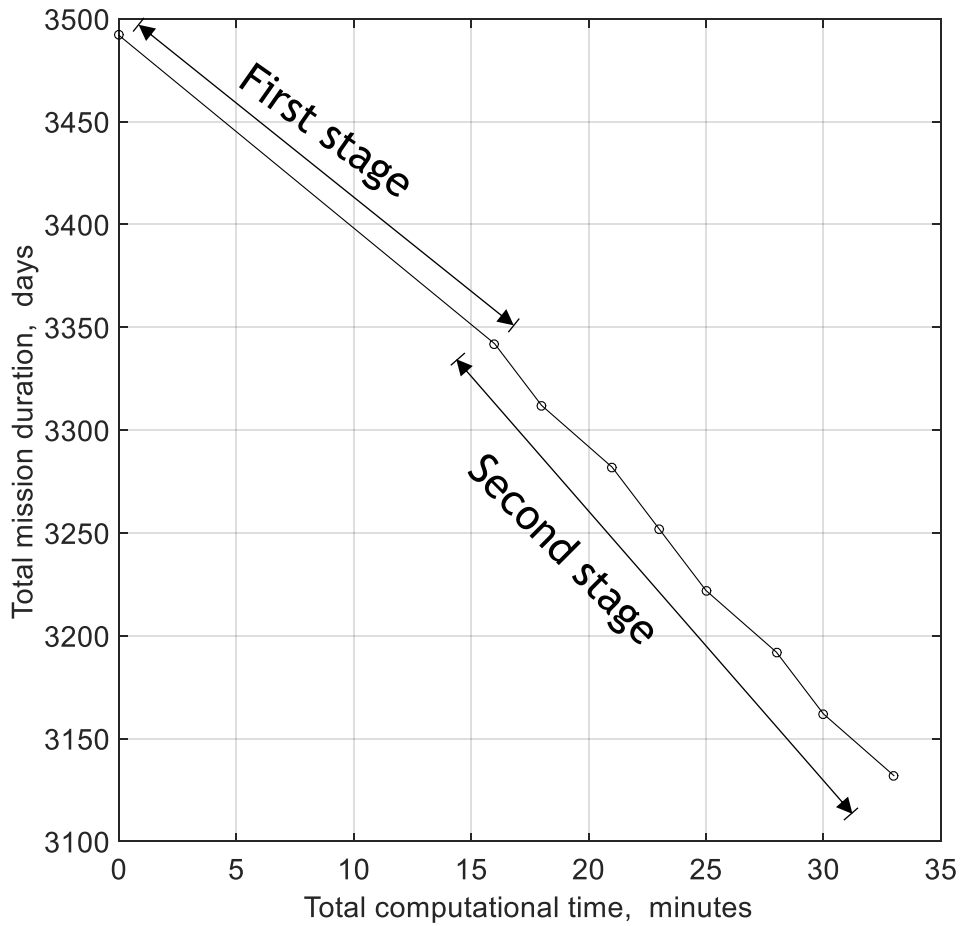


Fig. 5.11. Evolution of the total mission duration within ATOSS for optimised sequence 1.

Sequence 2. The second sequence contains three objects. This sequence has been chosen among the others because it is characterised by the presence of two PHAs, 1989 UQ and 2002 RW₂₅. The first object of the sequence, 2003 WT₁₅₃, is part of the LCDB database with $U \leq 2$ –. All the objects are Aten asteroids. That is, their semimajor axes are all less than one astronomical unit. Moreover, the orbits of all the encounters in the sequence are significantly more eccentric than the one of the Earth, as shown in Table 5.7.

Table 5.7. Properties of the encounters of sequence 2¹.

Object	2003 WT ₁₅₃	1989 UQ	2002 RW ₂₅
Orbital type	Aten	Aten	Aten
Semimajor axis, AU	0.894	0.915	0.825
Eccentricity	0.178	0.265	0.287
Inclination, deg	0.371	1.299	1.327
Absolute magnitude	28	19.4	18.8
Estimated size, m	7-15	330-740	420-940
EMOID, AU	0.002	0.014	0.016
PHA	No	Yes	Yes

A multi-phase trajectory for the selected solar sail has been found by following the optimisation steps described in Section 5.2 and the mission is summarised in Table 5.8. The sailcraft needs 3,541 days (i.e. 9.7 years) to reach all asteroids in this sequence, after spending more than three months in the proximity of each.

Figure 5.12 shows the two-dimensional projection of the complete 3D trajectory of the chosen sequence. Plots of single-leg trajectories and controls over time are not shown for the sake of brevity.

Table 5.8. Mission parameters for optimised sequence 2 (values in brackets are the ones found through the sequence search algorithm and used as an initial guess for STO).

Object	Stay time, days		Start	End	Time of flight, days
Earth	---		24 Apr 2028	18 Jul 2031	1181
2003 WT ₁₅₃	134 (50)	↻	(14 Apr 2028)	(01 Oct 2031)	(1265)
1989 UQ	110 (50)	↻	30 Nov 2031 (20 Nov 2031)	29 Jun 2034 (19 Aug 2034)	943 (1003)
2002 RW ₂₅	---	↻	18 Oct 2034 (08 Oct 2034)	02 Jan 2038 (19 Mar 2038)	1173 (1258)

¹ Data available online at <https://cneos.jpl.nasa.gov/orbits/elements.html> [retrieved 08 August 2015].

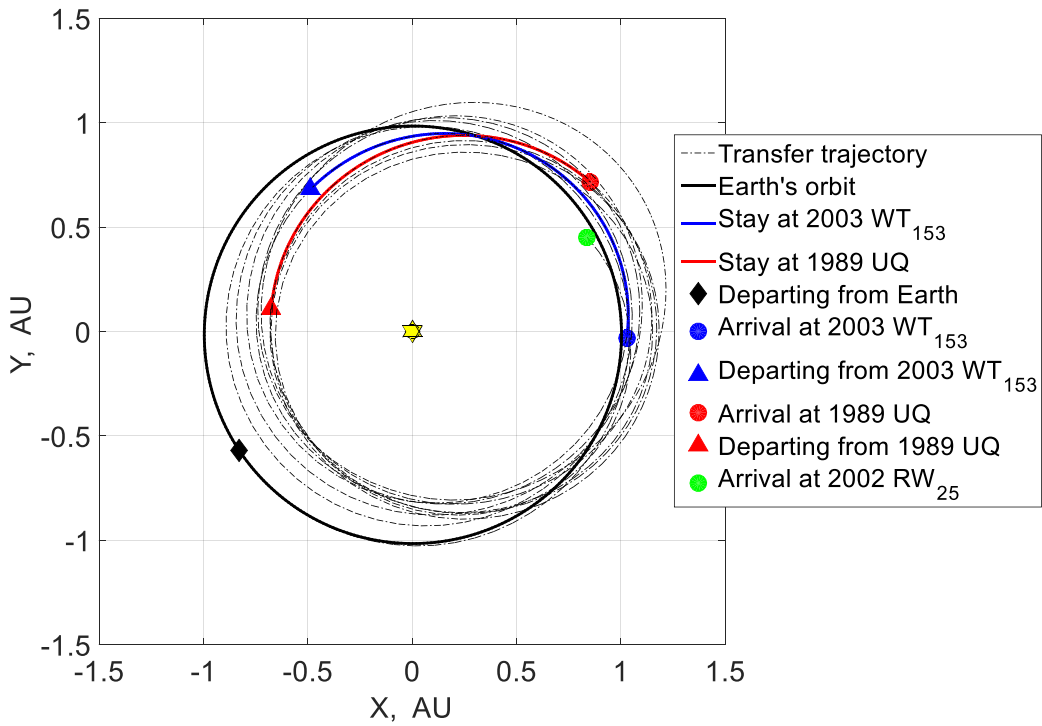


Fig. 5.12. Heliocentric view of the complete three-dimensional trajectory of optimised sequence 2 (ecliptic plane view).

The total Δv needed for this mission is $\Delta v = 52.1 \text{ km/s}$, which has been calculated as the integral of the acceleration over time. Despite such a high Δv is the result of a control law optimised for solar sailing, it is interesting to compare with an electric propulsion system. As such, consider the spacecraft used in the 8th Global Trajectory Optimisation Competition (GTOC8) [175, 228]. This spacecraft is characterised by a total mass $m_0 = 4,000 \text{ kg}$, a dry mass $m_{dry} = 1,890 \text{ kg}$ and a low-thrust engine with a specific impulse $I_{sp} = 5,000 \text{ s}$. It is worth noting that both the specific impulse and the mass ratio $m_{dry}/m_0 = 0.47$ considered are very high performing and no spacecraft, to the best of the author's knowledge, has similar performances to date. Recall the Tsiolkovsky rocket equation as [229]

$$\Delta v = I_{sp} g_0 \ln\left(\frac{m_0}{m_f}\right) \quad (5.8)$$

in which, in this case, the final mass m_f is considered as the spacecraft dry mass m_{dry} . By using Eq. (5.8), the maximum Δv available with such low-thrust system

is $\Delta v = 37$ km/s. On the other hand, to reach a Δv as high as 52 km/s, a spacecraft with the electric propulsion system considered in the GTOC8 should be characterised by a mass ratio as low as $m_{dry}/m_0 = 0.35$, which is very low for the near-term electric-propulsion technology. For the above reasons, a multiple NEA rendezvous mission with a total $\Delta v = 52$ km/s is not feasible by an electric propelled spacecraft, even if a high-performing propulsion system is considered. A solar sail, on the other hand, enables high- Δv trajectories such as the one shown.

5.4.4. Multiple NEA Sample Return Mission

The optimised sequence 1 described in Section 5.4.3 has been considered to study the potential for a multiple NEA sample return mission. To do so, the last leg to 2014 MP has been removed and substituted with a return leg to the Earth. STO was used to compute the return leg to the Earth. The total mission duration is now 3,821 days (which is about 10.5 years), which is still compatible with the ten-year mission requirements described in Section 4.5. The return leg to the Earth is shown in Fig. 5.13, whereas Table 5.9 shows the updated mission parameters.

It is worth noting that the sequence still contains 2008 EV₅, which is classified as a PHA and was selected as one of the candidate targets for the Asteroid Redirect Robotic Mission (ARRM) by NASA [230]. Moreover, the stay time at 2008 EV₅ is above 100 days, which is the longest of this sequence of asteroids.

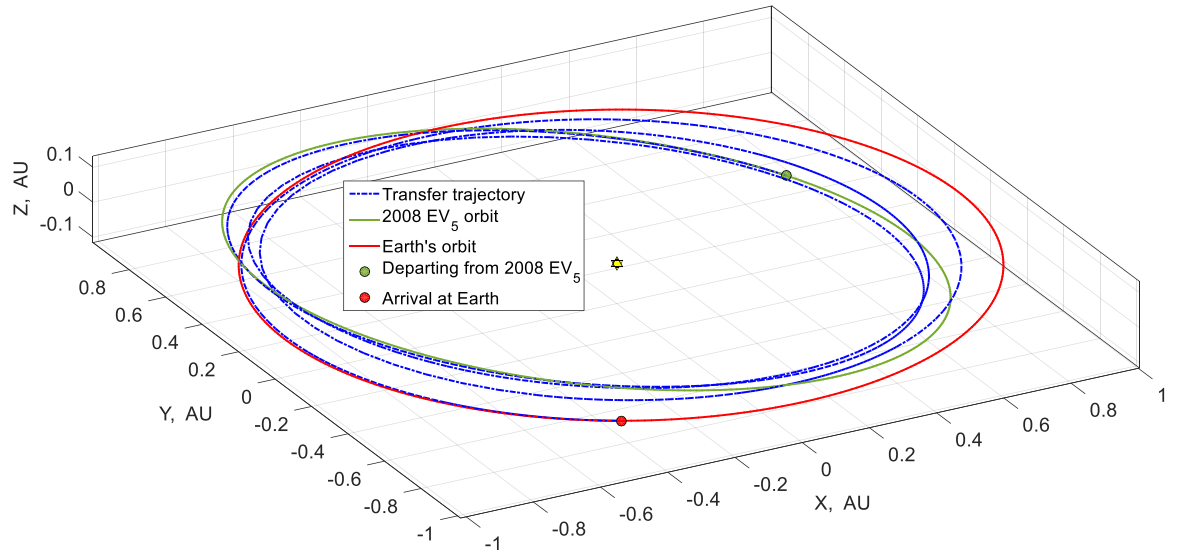


Fig. 5.13. Heliocentric view of the 3D return leg to the Earth.

Table 5.9. Mission parameters for the optimised sequence 1 with the last leg to the Earth.

Object	Stay time, days	Start	End	Time of flight, days
Earth	---		05 Dec 2025	18 Mar 2027
2000 SG ₃₄₄	93		19 Jun 2027	03 Nov 2028
2015 JD ₃	104		16 Feb 2029	22 Nov 2030
2012 KB ₄	94		23 Feb 2031	22 Nov 2032
2008 EV ₅	116		18 Mar 2033	22 May 2036
<i>Earth</i>	∞			1161

5.4.5. Online Change of the Mission: Two Test Cases for the Planetary Defence

Two test cases have been studied as possible mission scenarios in response to the mission exercises proposed by the planetary defence community. In both test cases, the sailcraft is considered already flying to its planned mission to several NEAs, when a PHA appears to gain interest over the worldwide community. Therefore, the mission control decides to reroute the sailcraft to rendezvous or flyby with such object. This will also demonstrate the target flexibility unique to solar sailing. In the following subsections, the two test cases are discussed in detail.

Test Case 1: 2011 AG₅. During the 3rd International Academy of Astronautics (IAA) Planetary Defense Conference (PDC) held in Flagstaff, AZ, USA in 2013, the asteroid 2011 AG₅ was considered as one of the reference scenarios to conduct an exercise to respond to a hypothetical asteroid threat¹. At the time of the conference, the asteroid had a probability of impact with the Earth of 1 in 500 (i.e. 2×10^{-3}) on 05 February 2040 [231], and the value of the object on the Palermo scale [232] was $\mathcal{P} = -1$, which indicates that the PHA merits careful

¹ Data available online at <http://pdc.iaaweb.org/?q=content/2013-flagstaff> [retrieved 15 June 2017].

monitoring. In fact, only two objects among all the ones studied in [232] had a value $\mathcal{P} > -1$.

The first multiple NEA rendezvous mission discussed in Section 5.4.3 has been considered as the baseline for the current scenario. That is, in the hypothesis that the mission is flying as scheduled, the last leg to 2014 MP shown in Table 5.6 is replaced to a leg to the potentially-hazardous asteroid 2011 AG₅. Note that, according to Chodas et al. [231], a deflection that will take place after 03 February 2023 is about 50 times harder than before such date. Nevertheless, the rerouted sailcraft will inevitably reach the PHA after that date, since the entire baseline mission starts on 2025 (Table 5.6). The solar sail can easily change its route and reach 2011 AG₅ before the potential predicted impact with the Earth, thus providing detailed updates on the asteroid and its course. Moreover, this will be performed at the only cost of the last asteroid not being visited as scheduled. However, if 2011 AG₅ will not collide with the Earth and destroy the mission control centre, the sailcraft could be, in principle, still rerouted to its original mission. Table 5.10 shows the properties of 2011 AG₅.

Table 5.10. Properties of 2011 AG₅¹.

Object	2011 AG ₅
Orbital type	Apollo
Semimajor axis, AU	1.431
Eccentricity	0.390
Inclination, deg	3.681
Absolute magnitude	21.8
Estimated size, m	110-240
EMOID, AU	0.0002
PHA	Yes
NHATS	No

To find the transfer leg to the new target, the homotopic approach to solar sailing, described in Section 3.2, has been used at first. Firstly, a constant-mass low-thrust transfer between 2008 EV₅ and 2011 AG₅ has been computed by means

¹ Data available online at <https://cneos.jpl.nasa.gov/orbits/elements.html> [retrieved 08 August 2015].

of the indirect optimisation approach. The time of flight and the initial values of the costates have been determined through the PSO algorithm described in Appendix B.2. For this scenario, the orbits of both objects are considered coplanar. That is, the orbital plane of 2011 AG₅ has been rotated and projected onto the one of 2008 EV₅, as described in Eq. (3.21). Moreover, the maximum acceleration given by the propulsion system has been set to $a_{\max} = 1 \text{ mm/s}^2$. Starting from the low-thrust solution, the homotopy-continuation approach has been used to find a coplanar solar-sail transfer with $a_c = 0.2 \text{ mm/s}^2$. Then, ATOSS has been used to find the final three-dimensional trajectory by first changing the orientation of the orbital plane and then changing its inclination.

The total mission duration is now 4,398 days (i.e. about 12 years) and the sailcraft arrives at the final target object on 25 May 2037, about 3 years before the potential impact. Figure 5.14 shows the last transfer leg between 2008 EV₅ and 2011 AG₅, whereas Table 5.11 shows the updated mission parameters. Note that the value of the stay time related to 2011 AG₅ is the time interval between the rendezvous and the expected impact with the Earth.

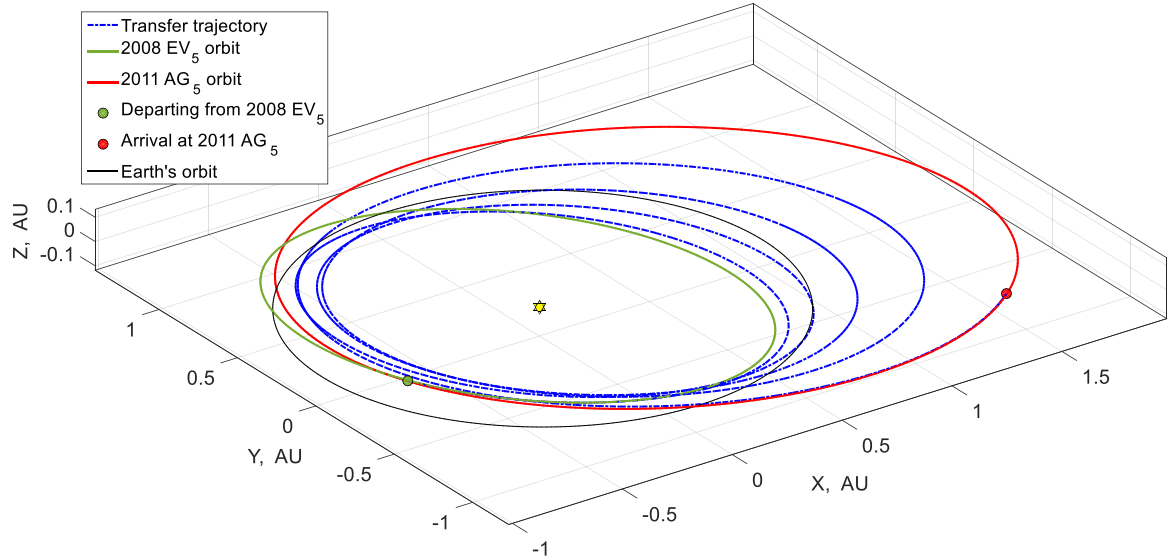


Fig. 5.14. Heliocentric view of the 3D transfer leg between 2008 EV₅ and 2011 AG₅.

Table 5.11. Mission parameters for optimised sequence 1 with the last leg to 2011 AG₅.

Object	Stay time, days	Start	End	Time of flight, days	
Earth	---		10 May 2025	26 Feb 2027	657
2000 SG ₃₄₄	123		29 Jun 2027	06 Sep 2028	436
2015 JD ₃	164		18 Feb 2029	24 Sep 2030	584
2012 KB ₄	160		04 Mar 2031	29 Sep 2032	576
2008 EV ₅	7.5		07 Oct 2032	25 May 2037	1691
2011 AG ₅	987				

Test Case 2: 2017 PDC. A second test case is considered in this subsection which targets the fictitious PHA 2017 PDC. This has been introduced at the 5th IAA Planetary Defense Conference held in Tokyo, Japan on 2017¹. The full description of the 2017 PDC hypothetical asteroid impact scenario can be retrieved at the JPL/NASA Center for Near Earth Object Studies (CNEOS) website². According to this scenario, the asteroid 2017 PDC is discovered on 06 March 2017 and, on the following day, a potential impact of this fictitious object with the Earth is expected to be on 21 July 2027. Two months after its discovery, the asteroid has a probability of impact with the Earth of 1 in 100 and, therefore, its value on the Palermo scale is $\mathcal{P} = 0.22$ ³, which corresponds to “a situation more threatening than the background hazard” [232]. Table 5.12 shows the properties of the fictitious asteroid 2017 PDC.

¹ Data available online at <http://pdc.iaaweb.org/?q=content/2017-tokyo> [retrieved 16 June 2017].

² Data available online at <https://cneos.jpl.nasa.gov/pd/cs/pdc17/> [retrieved 16 June 2017].

³ Value obtained according to [232], considering the properties of a standard NEA.

Table 5.12. Properties of 2017 PDC¹.

Object	2017 PDC
Orbital type	Apollo
Semimajor axis, AU	2.24
Eccentricity	0.607
Inclination, deg	6.297
Absolute magnitude	21.9
Estimated size, m	110-240
EMOID, AU	0.0008
PHA	Yes
NHATS	No

Note that, because of the expected date of impact, the first multiple NEA rendezvous mission discussed in Section 5.4.3 is not a good candidate as a baseline mission. Therefore, from the results of the same sequence search performed on the PHA-NHATS database and discussed in Section 4.6.1, a different sequence has been optimised and considered as a baseline mission for a leg to 2017 PDC. Table 5.13 shows the mission parameters for this optimised sequence.

Table 5.13. Mission parameters for the baseline mission for the 2017 PDC test case.

Object	Stay time, days	Start	End	Time of flight, days
Earth	---		13 Aug 2020	26 Apr 2022
2005 TG ₅₀	128		02 Sep 2022	13 Jan 2024
2015 JF ₁₁	104		25 Apr 2024	10 Jun 2026
2012 BB ₁₄	139		28 Oct 2026	02 Aug 2028
2014 YN	---			644

¹ Data available online at https://ssd.jpl.nasa.gov/horizons.cgi?find_body=1&body_group=all&sstr=2017+PDC [retrieved 06 March 2017].

As for the previous test case, in the hypothesis that the mission is flying as scheduled, the sailcraft is rerouted, after the second transfer leg, to go towards 2017 PDC. The same methodology applied to the previous test case has been used, starting from a low-thrust solution with $a_{\max} = 2 \text{ mm/s}^2$. Nevertheless, the orbit of 2017 PDC is significantly different from the one of the departing object because of the high eccentricity and the large semimajor axis. Moreover, the time constraint on the mission¹ and the low characteristic acceleration of the sailcraft make this scenario very difficult to solve and no feasible transfer trajectories have been found to rendezvous 2017 PDC. In fact, a solar-sail transfer leg with $a_c = 0.73 \text{ mm/s}^2$ has been found which needs more than 2,000 days to be performed, considering the orbit of 2017 PDC coplanar with the one of 2011 JF₁₁. That is, a sailcraft with a considerably larger characteristic acceleration than the one considered in this study would arrive at the target object on 21 August 2030, which is about three years after the predicted impact with the Earth. Figure 5.15 shows the transfer leg together with the non-dimensional acceleration vector.

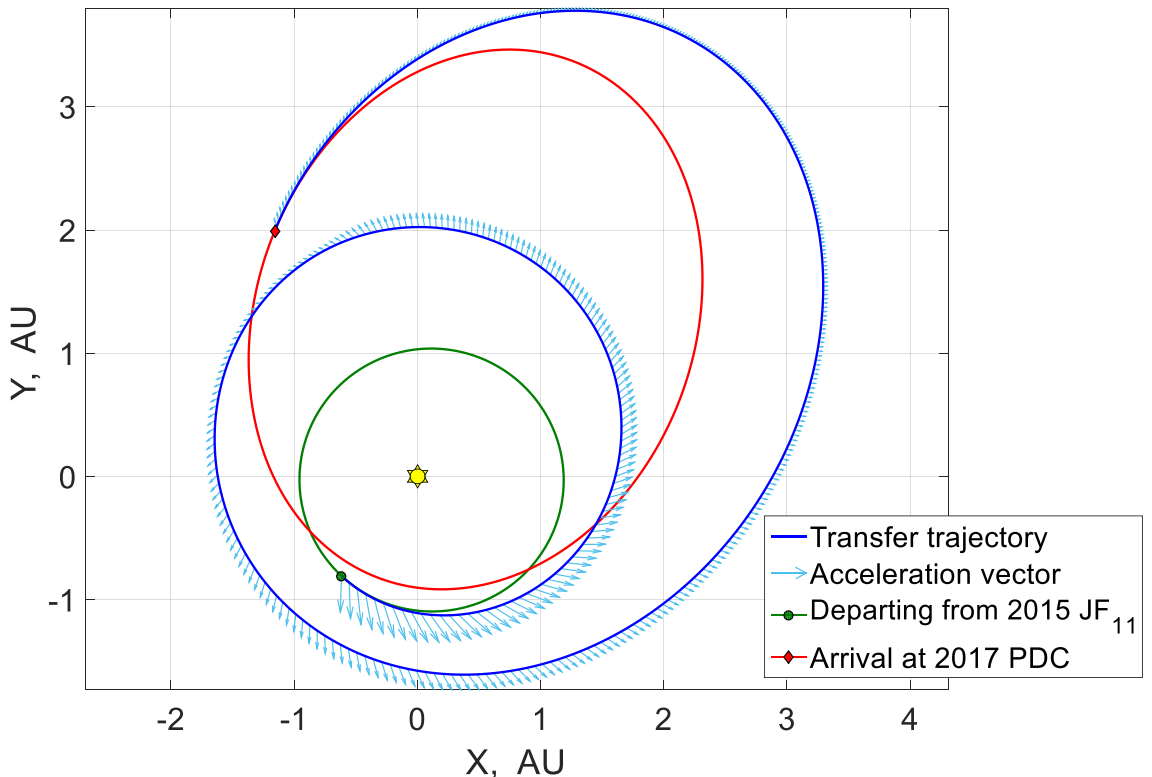


Fig. 5.15. Heliocentric view of the coplanar transfer between 2015 JF₁₁ and 2017 PDC ($a_c = 0.73 \text{ mm/s}^2$).

¹ After the second leg of the baseline mission, there are only three years left to reach 2017 PDC before the impact with the Earth, if any.

Even though the sailcraft rerouting has been proven inefficient for a rendezvous with 2017 PDC, the same (already flying) sailcraft can still be used to target 2017 PDC for a fast flyby. Such a mission gives an extra (free) opportunity to monitor the asteroid's path before the expected impact, even after a potential deflection mission takes place. In fact, if a deflection mission was successful, the orbit of 2017 PDC would only be slightly different from the unperturbed one¹. Therefore, the unperturbed orbit of the asteroid can be safely considered for the trajectory design.

The initial-guess solution for ATOSS has been computed by means of the homotopy-continuation approach, starting from a low-thrust transfer with $a_{\max} = 0.2 \text{ mm/s}^2$. In this case, the final spacecraft velocity is left free, since a flyby is considered. The optimised 3D trajectory found by ATOSS is shown in Fig. 5.16, whereas Table 5.14 shows the mission parameters of the updated sequence with the addition of the flyby to 2017 PDC. After a three-year journey, the sailcraft reaches 2017 PDC on 07 April 2027, which is about three months before the expected impact. Note that no stay time at 2017 PDC is considered, since the sailcraft reaches the asteroid for a fast flyby.

Table 5.14. Mission parameters for the baseline mission for the 2017 PDC test case with the last leg to 2017 PDC.

Object	Stay time, days	Start	End	Time of flight, days
Earth	---		13 Aug 2020	26 Apr 2022
2005 TG ₅₀	128		02 Sep 2022	13 Jan 2024
2015 JF ₁₁	91		13 Apr 2024	07 Apr 2027
2017 PDC	---			1089

¹ At the end of the PDC 2017 exercise, it was shown that the orbit of 2017 PDC after the successful deflection mission was such that the asteroid would miss the Earth by about 1,000 km.

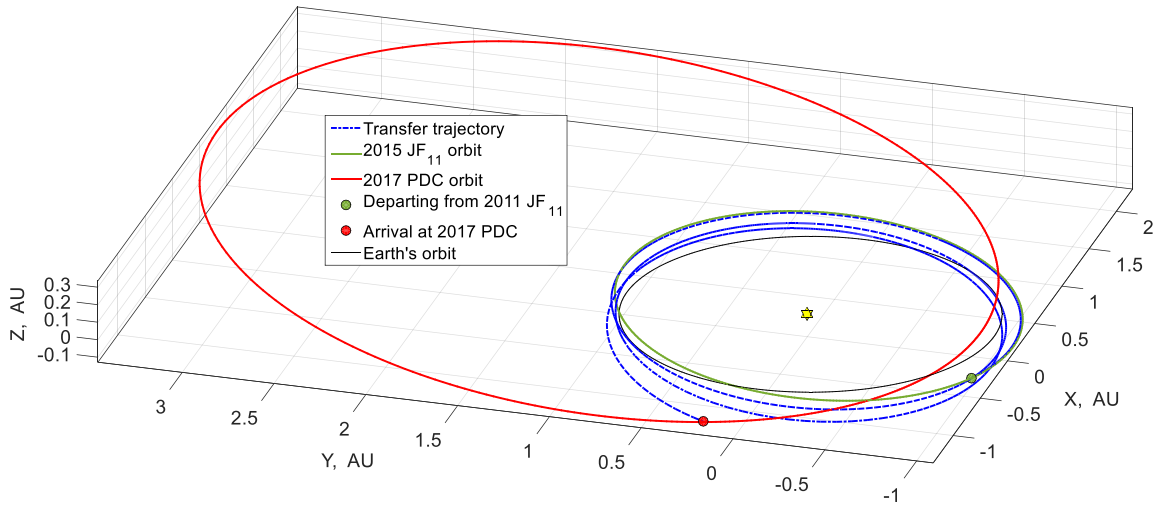


Fig. 5.16. Heliocentric view of the 3D transfer trajectory to flyby 2017 PDC.

5.4.6. Automated Optimisation Campaign

The last set of test cases aims to assess the performances of both STO and ATOSS as automated optimisers. To do so, all the 589 preliminary sequences with at least three encounters and at least one PHA found for the PHA-LCDB database shown in Section 4.6.2 are optimised by means of the two optimisers developed. Moreover, the performances of ATOSS are compared to those of the sequential trajectory optimiser. The number of optimal solutions found and the computational time needed for the entire automated optimisation campaign are the two parameters used for the performance test. For the entire optimisation campaign, the NLP solver SNOPT, together with the propagated-trajectory variant of the shape-based approach, is used within ATOSS.

Once the initial settings are defined at the beginning of the optimisation campaign, all the simulations are carried out with the same settings and with no user intervention. Of course, it is likely that some of the results found can be improved by choosing *ad hoc* settings for each test case so that the optimisers are tuned for that specific scenario (see, for instance, the “no free lunch theorems for optimisation” [233]). Nevertheless, this is beyond the scope of this work, which aims to test the capability of the developed optimisers to find as many optimal solutions as possible automatically. Once solutions for all the test cases have been found, the user can choose the most interesting ones to be further optimised.

The results of the automated optimisation campaign are schematically shown in Table 5.15. STO found a solution for 343 sequences, which is 58% of the total number of sequences tested. On the other hand, ATOSS found fully-optimised solar-sail trajectories for 390 sequences, which is 66% of the total number of sequences tested. The sequences optimised through ATOSS are characterised by 84 unique NEAs. Among them, there are 58 PHAs, 11 asteroids which are part of the NHATS database and 28 NEAs which are part of the LCDB with $U \leq 2 -$.

STO took less than a month looking for solutions to all the 589 sequences found, performing more than 20 optimisations per day on average. On the other hand, when ATOSS was used on the same machine, the entire automated optimisation campaign took less than six days of computational time.

These results demonstrate the reliability of both STO and ATOSS as automated optimisers. Moreover, such results also demonstrate the reliability of the sequence search algorithm described in CHAPTER 4, since more than 50% of the preliminary sequences found are shown to be feasible. It is interesting to compare the quality of the solutions found by the two optimisers. An estimate of the quality of the solutions can be obtained by analysing the total mission durations found by the two optimisers. This is done only on those sequences (292) for which both optimisers found a solution. Two solutions are considered equivalent if the difference in their mission durations is within twenty days. An analysis of the numerical results showed that in 285 test cases (~98%) the solutions found by ATOSS are shorter than those found by STO. On the other hand, STO found a shorter solution than ATOSS in only one test case; the two optimisers found equivalent solutions in the remaining six test cases (~2%). From the comparison of the results found by means of the two optimisers developed, it can be seen that ATOSS outperforms the sequential trajectory optimiser in success rate, computational speed and quality of the solutions found. The better performances of ATOSS in terms of success rate and computational speed are likely due to the first stage of the optimisation strategy, which has been developed in purpose to help the numerical convergence of the NLP solver. The second stage of the optimisation strategy developed within ATOSS is the reason for the better solutions, in terms of quality, found by ATOSS in comparison with those found by STO.

Table 5.15. Automated optimisation campaign results.

Optimiser	Number of solutions found	Success rate	Computational time
STO	343	58%	< 30 days
ATOSS	390	66%	< 6 days

5.5. Discussion

In this chapter, two optimisation tools have been presented which are developed to find solutions to the solar-sailing multiple NEA rendezvous OCP. Both optimisers have been developed with the main goal of being mostly automatic, thus requiring minimal input from the user. This is because, at this stage of the mission design, it is more important to have many candidate mission scenarios rather than finding very accurate solutions.

A number of test cases demonstrated the capabilities of the two optimisers presented. A five-NEA rendezvous mission is shown to be feasible in less than ten years with a near-term solar sail, allowing at least three months in the vicinity of each encounter for close-up observations. A second test case showed a mission to rendezvous three objects on eccentric orbits. It was shown that such very mission would not be feasible with a near-term electric propulsion system because of the limited amount of propellant available. Furthermore, three more test cases showed the versatility of the solar-sail propulsion system, which allows changing the mission even after has started. The capability to change targets en-route allows a mission already in flight to respond to either extreme events such as a potential Earth impactor being discovered or changes in the commercial/scientific interest. Lastly, an automated optimisation campaign demonstrated the reliability of both optimisers to perform without any input from the user. This is a key feature of the developed optimisers, since very often the numerical optimisation is sensitive to the optimisation parameters. Nevertheless, ATOSS showed better performances, in terms of success rate, computational time needed and quality of the solutions found, than its counterpart does. This is understandable, being ATOSS an upgrade of the sequential trajectory optimiser. Lastly, ATOSS allows setting a minimum desired stay time at each target object. This feature can be

fundamental in the mission design of a multiple NEA rendezvous, for which a minimum time for close-up observation might be needed by the onboard instruments.

All the numerical test cases discussed in this section not only demonstrated the capabilities of the two optimisers developed but also revealed the potential of solar sailing to achieve goals unattainable by a classical electric propulsion system.

CHAPTER 6.

CONCLUSIONS

This thesis presented several techniques and methodologies for preliminary trajectory design of multiple near-Earth asteroid (NEA) rendezvous missions through solar sailing. This final chapter summarises the work carried out, the tools developed, and the main findings of this thesis. Known limitations are also discussed and directions for a possible future research are drawn.

6.1. Summary of the Work

In this thesis, the problem of preliminary mission design for solar-sail multiple NEA rendezvous is tackled. A NEA rendezvous with close-up observations is important to improve our knowledge about these objects. A multiple rendezvous is even a more attractive mission because of the large population of asteroids and the many uncertainties that still characterise them. This, however, introduces several difficulties in the mission design, such as the potentially-high Δv needed. Furthermore, the rate of NEAs' discovery and the dynamic change in the objects of interest make the en-route change of the target objects an appealing perspective. As it was shown for the case of the Hayabusa-2 extended mission, however, this is usually complicated by the amount of propellant available on board. For this reason, solar sailing is an attractive propulsion system since its thrust is entirely generated by reflecting sunlight and thus no onboard propellant is needed. As such, it is well suited for a multiple rendezvous mission.

The principal objective of this thesis was to develop a tool for the preliminary trajectory design of multiple NEA rendezvous missions through solar sailing. In fact, not a single tool was built but several techniques, algorithms and tools were

developed. These can work independently or can be easily interfaced between themselves and thus be used as a larger standalone toolbox able to perform the required multiple-NEA rendezvous mission design from the selection of the sequence of asteroids to the full trajectory optimisation.

The first step towards the achievement of this objective was the development of a mathematical model for the fast representation of a solar-sail trajectory. This is the cornerstone of the entire work as a fast and reliable trajectory model is needed for generating preliminary sequences of encounters as well as having an initial approximated trajectory. The shape-based approach was considered for the description of the trajectory because it is a semi-analytical approach and no complex and time-consuming optimal control problem (OCP) needs to be solved. In fact, this approach consists in designing the desired shape of the trajectory by means of a set of chosen equations. Thus, the acceleration that the spacecraft shall provide to follow the planned trajectory is analytically retrieved *a posteriori*. Because of the intrinsic differences between the thrust that can be produced by a classical low-thrust system and a solar sail, a new set of shaping functions was proposed for solar sailing. This was proven to give a reliable approximation of the solar-sail trajectory on a number of NEA-to-NEA transfers. A second method was developed which generates solar-sail trajectories starting from classical low-thrust ones. A homotopy-continuation technique is the core of the method, which solves several OCPs by slightly changing the acceleration model. The advantages and drawbacks of both methods were discussed. It appeared that the shape-based approach is better suited for finding a large number of trajectories in an automated way, whereas the second method is more suited for complex trajectories (such as the fast flyby of the fictitious potentially hazardous asteroid 2017 PDC).

The second step towards the completion of this thesis' goal was to develop an algorithm to look for possible sequences of NEAs to be visited in a multiple rendezvous mission. In fact, it was noted that all the solar-sailing multiple asteroid rendezvous missions studied in the literature lack an actual search for sequences and the NEAs to visit are mostly handpicked. Therefore, an algorithm was developed which exploits the tree-like search space given by all the possible sequences of objects. The reason behind this choice is that this is a preliminary mission design study and one of the expected outcomes is to provide a set of feasible mission scenarios for the stakeholders. A tree search provides the user

with a large number of possible mission scenarios that can be chosen on the basis of the current cost function (e.g. available launch date, some objects are currently more interesting than others, etc.). Nevertheless, a complete tree search over the whole database of known NEAs is computationally unmanageable. For this reason, a reduced database made of asteroids interesting for the planetary defence and for the human spaceflight was considered. This allowed a reduction of the search-space dimensionality by more than three orders of magnitude. Moreover, a local pruning of those branches of the tree that are more likely to be unfeasible by means of the chosen sailcraft was performed at the beginning of each transfer leg. This was carried out based on astrodynamics considerations, such as the maximum change of a selected orbital element that is feasible by the given propulsion system in the maximum allowed time. This enabled a significant reduction of the number of objects to be considered. Some heuristics (such as the minimum/maximum allowed transfer time) gives the user the possibility to shape the search for sequences to suit their requirements in terms, for instance, of computational effort or number of sequences returned. In fact, stricter pruning criteria involve a reduced branching of the tree of feasible sequences of NEA encounters. Lastly, the shape-based approach for solar sailing was used to provide the trajectory within the search for sequences without the need of solving an OCP for each transfer leg to be tested. Despite other models are available in the literature which are faster than the shape-based approach (e.g. ballistic Lambert arc), the trajectories generated with the shape-based approach are more reliable. That is, there is a high probability that the preliminary sequences found by means of the sequence search are feasible if optimised with a refined trajectory model.

The third and last step towards the achievement of this thesis' goal was to develop a strategy to optimise the chosen sequences of NEAs with a refined trajectory model. Since a shaped solar-sail trajectory was already available from the sequence search, it was chosen to use it as an initial-guess solution for a direct-transcription optimisation technique. Moreover, multi-phase problems are usually easy to be dealt with if a direct optimisation method is used. Two optimisation strategies were developed; namely the Sequential Trajectory Optimiser (STO) and the Automated Trajectory Optimiser for Solar Sailing (ATOSS). These focused on the automation of the optimisation itself. In fact, both strategies require minimal input from the user and, therefore, are well suited to solve a

large number of OCPs in an automated way. This is a valuable feature for a tool for preliminary mission analysis, since a large number of possible trajectories are usually evaluated in the preliminary phases of the mission design. Moreover, ATOSS allows setting a minimum desired stay time at each target asteroid. This feature can be fundamental in the mission design of a multiple NEA rendezvous, for which a minimum time for close-up observation might be needed by the onboard instruments. Several numerical test cases were carried out considering both single and multiple rendezvous with NEAs. Specifically, the three-NEA rendezvous presented by Dachwald et al. was reproduced, thus validating the proposed optimisation strategies. Moreover, an automated optimisation campaign was carried out which demonstrated the ability of the developed optimisers to work autonomously. In fact, more than 500 solar-sail multiple-NEA rendezvous OCPs were solved without any interaction with the user. This test case also assessed the validity of the preliminary sequences returned by the asteroid sequence search.

In the following subsection, the major findings of this thesis are highlighted and briefly discussed.

6.2. Summary of the Findings

Solar sailing is a very attractive propulsion system, as it was highlighted in Section 2.1. Nonetheless, this technology is not ready yet to be used as a conventional spacecraft propulsion system. Many researchers are currently studying solar sailing to increase its technology readiness level (TRL). For this reason, all the solar-sailing missions that have already flown (e.g. IKAROS and NanoSail-D) were mainly technological demonstrators. On the other hand, one of the aims of this thesis was to look at the TRL-related problem from a different perspective. That is, scenarios with high mission-related TRL were sought for solar-sailing multiple NEA rendezvous. In fact, a sailcraft with lower performances than the one considered by Dachwald et al. in their reference mission was used throughout this thesis. In this case, lower performances are expressed in terms of a lower characteristic acceleration. As it was shown in Section 2.1, the characteristic acceleration is proportional to the sail area-to-mass ratio (AMR). Achieving a high AMR is one of the technological challenges that many of the

researchers on solar sailing are currently working on. This thesis showed that a large number of interesting mission scenarios exists for a solar sail with performances within the capabilities of current and near-term DLR/ESA Gossamer sailcraft technology. That is, the mission-related TRL for multiple NEA rendezvous through solar sailing was demonstrated to be larger than it was previously thought.

The results from the sequence search algorithm showed that several sequences of target NEAs are possible for a wide window of launch dates. For instance, more than 200 different four-NEA mission scenarios were found for each launch date tested within a ten-year window. It is worth reminding that all the numerical test cases shown were computed by considering a maximum mission flight time of ten years. Such large variety of potential mission scenarios demonstrates that there are little to no constraints on the launch window for a multiple NEA rendezvous mission if a solar sail is considered.

Lastly, the unique characteristic of solar sailing of being propellantless was exploited in two mission scenarios related to the planetary defence. In both cases, it was assumed that the sailcraft was flying its planned multiple rendezvous mission when a potential hazardous asteroid gained importance among the worldwide community because of its increasing threat. Therefore, it was considered to deviate the sailcraft route from its original path towards the new target. Obviously, such a new modified mission would not be able to substitute a mitigation mission but it would provide the planetary-defence community with additional useful information about the asteroid. These test cases (which currently constitute only academic exercises) demonstrated the versatility of the solar-sail propulsion system, which can accommodate a change in the mission even after the launch. This would be potentially very difficult for a spacecraft that uses a classical low-thrust propulsion system because of the limited amount of propellant on board.

6.3. Current Limitations and Future Research

Despite the positive results shown in this thesis, the proposed research has also some known limitations. These might constitute a basis for a future study. In the following subsections, the current limitations are examined and proposed directions for a future research are outlined.

6.3.1. Current Limitations

The research presented in this thesis was aimed to address the problem of preliminary mission design. As such, some approximations were considered which allowed the development of the described tools and thus provided a full picture of the solar-sailing potential for this kind of mission. The current known limitations of this work can be divided into two main groups and are as follows.

Dynamics. The sailcraft was considered as a mass point subject only to the gravitational pull of the Sun and the solar radiation pressure. The asteroids were treated as massless points on Keplerian orbits around the Sun. As such, the sailcraft was assumed rendezvousing a NEA when its state matched with the one of the target and the gravitational interaction between the two bodies was not modelled. As purely two-body dynamics were considered, no planetary gravity assists were taken into account. Moreover, the sailcraft was considered injected directly into interplanetary orbit at Earth, whereas a whole new set of solutions arises if the possibility of having a nonzero hyperbolic excess energy at Earth is introduced.

Solar-sail model. The work of Dachwald et al. was used as a reference for a near-term multiple-NEA rendezvous mission feasible by a solar sail. As such, the same model for the acceleration generated by the sailcraft was used. A different and more detailed acceleration model might be used in a future research to refine the baseline tools developed here. Moreover, the attitude control of the spacecraft was not modelled and the solar sail was considered able to perform the required orbital manoeuvres instantaneously. Despite this is not realistic, it was shown that the trajectories found after the optimisation phase require an attitude control effort below the allowed values found in the literature.

6.3.2. Proposed Future Research

Considering the current limitations of this work discussed in Section 6.3.1, directions for further studies can be followed. Therefore, lines for a future research are proposed here. These would further improve the tools developed for mission design of multiple-NEA rendezvous through solar sailing, as well as give the possibility to widen our knowledge about near-Earth asteroids and increase the worldwide interest on solar sailing.

Proximity operations at the asteroids. A phase can be added between two consecutive transfer legs in which proximity operations at the encounter are investigated. This would need a model for the gravitational field of the asteroid as well so that both the close approach and the interaction between spacecraft and asteroid are analysed. Some studies have already been carried out for sailcraft hovering about large asteroids [234, 235] or deploying landers for in-situ characterisation [31, 223]. These might be considered as a good inception for the proposed work.

Hyperbolic excess energy at Earth and gravity assist of the main bodies. The possibility to consider a hyperbolic excess energy at Earth within the asteroid sequence search adds three degrees of freedom to the entire search space (namely, the three components of the spacecraft velocity vector when leaving Earth). Other than increasing the computational effort needed to find interesting sequences of NEAs, this potentially widens the typology of feasible missions, allowing trajectories to more eccentric orbits. A parametric study on solar-sail orbit transfers with the inclusion of hyperbolic excess velocity at Earth showed an interesting relation between the optimal direction of the hyperbolic excess velocity vector and the Lagrange multipliers [144]. This might be used as a reference for the proposed research direction. Furthermore, also the possibility to use one or more gravity assists of the main bodies (e.g. Earth, Moon and Mars, in this case) increases the amount and typology of potential solar-sail missions for multiple NEA rendezvous. A study in this direction can start by looking at the broad literature available on multiple gravity assist trajectory planning.

Trajectory refinement. A third proposed direction for future study involves a refinement of the trajectory by considering, for instance, a different solar-sail force model or the interaction between attitude and orbital dynamics. A study in this direction was carried out by Borggräfe within the framework of the low-thrust trajectory optimisation software InTrance [227]. Furthermore, N-body dynamics can be considered for the transfer trajectories, using models such as the circular restricted three-body problem (CR3BP). As such, the gravitational influence of major bodies like the Earth can be examined. A potential approach to this problem is the use of a homotopy-continuation method, such as the one described in Section 3.2. A homotopic transformation can be defined to link the dynamics of the sailcraft in the two-body problem to the solar-sail dynamics in the CR3BP.

Solar-sail trajectory indicator. Indicators to compute equivalent Δv for low-thrust cases, such as Edelbaum's formulation for near-circular orbits [236], are used extensively in pruning the search space for the target selection of multiple-target mission [220]. However, as discussed in Section 4.3, the amount of Δv needed for a transfer does not provide a good indication about the feasibility of such a trajectory by means of the sailcraft under consideration. Therefore, a solar-sail trajectory indicator can be investigated which would be the reciprocal of the equivalent Δv for low thrust. As such, this can be used in addition to the pruning criteria already developed within the sequence search, thus further reducing the computational effort needed to compute the shaped trajectories.

APPENDIX A.

METAHEURISTIC OPTIMISATION

METHODS: A CLOSER LOOK

This appendix presents a brief description of two of the most studied metaheuristic optimisation methods, which are the genetic algorithm and the particle swarm optimisation. In fact, these are the two metaheuristic optimisation methods used to find some of the results shown within this thesis. Lastly, InTrance is briefly presented. Although it has not been used in this work, InTrance is a promising algorithm for low-thrust trajectory optimisation. Therefore, the author considers worthwhile giving a brief review of it.

A.1. Genetic Algorithm

GA simulates the natural selection within the biological evolution of species, as described by Darwin's theory. This is based on the "survival of the fittest" concept [101] (thus the term fitness function often used instead of cost or objective function). GA is a population-based algorithm in which each individual (the so-called chromosome) contains all the information about the optimisation variables. First, an initial population is randomly generated. To find the optimum of the desired function, an evolution process is applied on the current population (Fig. A.1). Such evolution process consists of the following steps [101]:

- Evaluation: the cost function associated with each chromosome is evaluated.
- Selection: some of the chromosomes are randomly (yet with a probability depending on their cost function) selected for reproduction.
- Crossover: the selected chromosomes (parents) cross over to form new offspring (children).
- Mutation: the new offspring mutate with a set probability.

After the reproduction (i.e. crossover and mutation) is completed for all the parents, the new population is formed and is ready to be evaluated again for a new iteration of the evolution process. The genetic algorithm stops when some stopping criteria are triggered (e.g. the cost function over the entire population is almost the same, the value of the cost function did not change over the last iterations, the maximum number of iterations is reached, etc.).

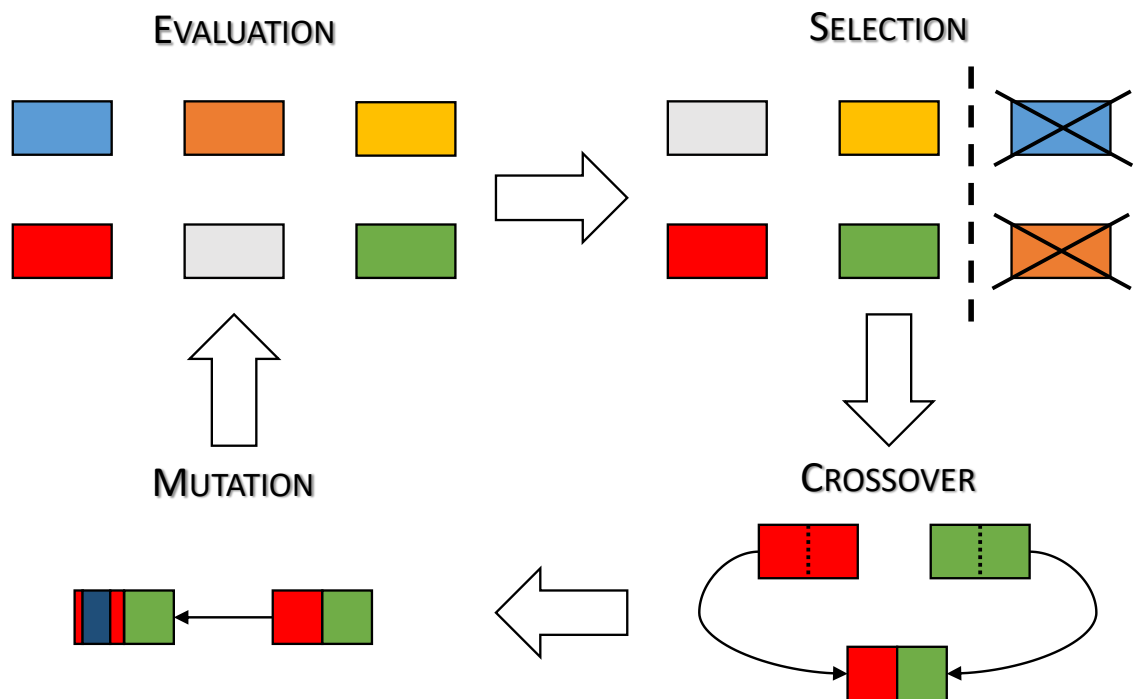


Fig. A.1. Schematic of the GA's evolution process.

A.2. Particle Swarm Optimisation

PSO is a population-based optimisation method in which each individual (the so-called particle) is characterised by a position \mathbf{r} and a velocity \mathbf{v} in the space whose coordinates are the optimisation variables. The whole algorithm mimics a flock of birds looking for food. Each individual knows the place in which it found more food (which is the so-called cognitive factor) and the place in which the largest amount of food has been found so far by the entire flock (which is the so-called social factor). Therefore, the next place in which the bird will look for food depends on its current position and velocity (which is the so-called inertial factor), as well as both the cognitive and the social factors, properly weighted. Figure A.2 shows a schematic of the state (position and velocity) evolution implemented within PSO. If the time evolution is seen as a succession of steps $k = 1, \dots, K_{\max}$, the state history of each particle $i = 1, \dots, N$ is described by the position $\mathbf{r}^{(k)}(i)$ and velocity $\mathbf{v}^{(k)}(i)$ of each particle i at each step k [102]. At each step, the current historical best position of each particle $\mathbf{p}_{best}^{(k)}(i)$ is evaluated as

$$\mathbf{p}_{best}^{(k)}(i) = \operatorname{argmin} J^{(k)}(i) \quad (\text{A.1})$$

Likewise, the current historical best position of the entire swarm $\mathbf{g}_{best}^{(k)}$ is evaluated as

$$\mathbf{g}_{best}^{(k)} = \operatorname{argmin} J^{(k)} \quad (\text{A.2})$$

The velocity vector is then updated for the next step $k + 1$ as

$$\mathbf{v}^{(k+1)}(i) = c_i \mathbf{v}^{(k)}(i) + c_c (\mathbf{p}_{best}^{(k)}(i) - \mathbf{r}^{(k)}(i)) + c_s (\mathbf{g}_{best}^{(k)} - \mathbf{r}^{(k)}(i)) \quad (\text{A.3})$$

in which the terms c_i , c_c and c_s are the inertial, cognitive and social weights, respectively. These are defined as [102]

$$\begin{cases} c_i \triangleq 0.5 + 0.5r_1(0,1) \\ c_c \triangleq 1.49445r_2(0,1) \\ c_s \triangleq 1.49445r_3(0,1) \end{cases} \quad (\text{A.4})$$

in which $r_1(0,1)$, $r_2(0,1)$, and $r_3(0,1)$ are three independent random numbers between 0 and 1. Note that different values of such weights can lead to different convergence rates of the optimiser and can even make the difference between a successful and an unsuccessful run of the PSO. Lastly, the position vector related to the next step $k+1$ is updated as

$$\mathbf{r}^{(k+1)}(i) = \mathbf{r}^{(k)}(i) + \mathbf{v}^{(k+1)}(i) \quad (\text{A.5})$$

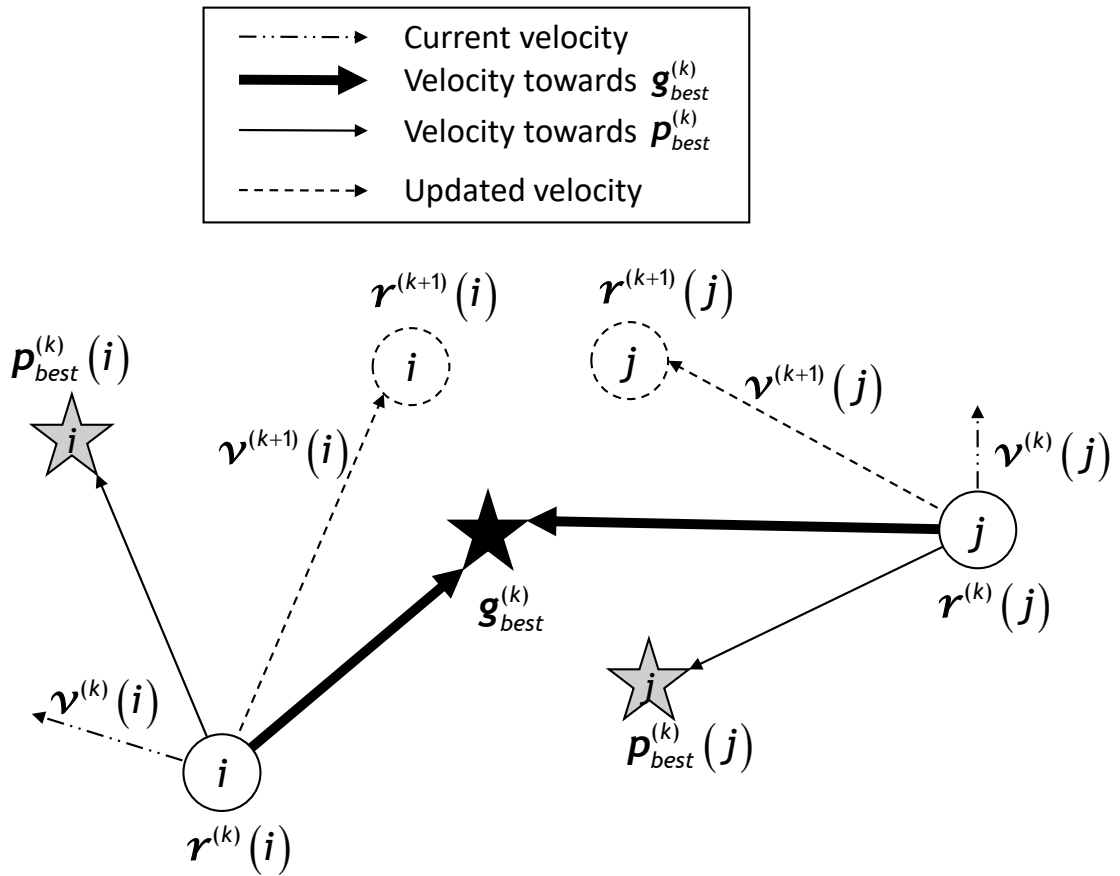


Fig. A.2. Schematic of position and velocity evolution implemented within PSO. The next position of each particle is influenced by the current velocity, the location of its current personal best solution p_{best} , and the location of the current best solution of the swarm g_{best} [237].

A.3. InTrance

InTrance (Intelligent Trajectory optimization using neurocontroller evolution) is implemented as the fusion between ANNs and metaheuristic optimisation methods, the so-called evolutionary neurocontroller (NC). ANNs are based on the way the information is processed within the animal nervous systems. This process is “massively parallel, analog, fault tolerant and adaptive” [117] and is a good approach to solve general learning problems. ANNs need to be trained on a training set of known exemplary input-output pairs. However, the optimisation of low-thrust trajectories is a so-called delayed reinforcement-learning problem, because the result of the output is visible only at the end of the integration. For this kind of problems, usually no training sets are available and ANNs generally fail to find a solution. For this reason, a metaheuristic optimisation algorithm is used to test the solutions found by ANN. In particular, a GA is implemented within InTrance but any other metaheuristic optimisation method can be, in principle, used. GA is employed to tune the set of parameters π (the so-called neurons) used by the NC. The evolution of the (random) initial parameters is ruled by the fitness function that weights the input parameters on the basis of the final trajectory, deciding which set of neurons are more promising for the optimal solution. A schematic of the method implemented within InTrance for solving a trajectory optimisation OCP is shown in Fig. A.3. For a more exhaustive explanation of the evolutionary neurocontroller method, the interested reader is referred to [117, 227].

InTrance is designed to automatically find low-thrust trajectories, exploiting the learning behaviour of ANNs and the evolutionary characteristics of GA. Therefore, it is a powerful tool to find preliminary solutions to missions challenging from a design point of view, such as the solar-sail mission designed to maximise the kinetic impact with the asteroid 2004 WR [238]. Nevertheless, one of the main drawbacks of InTrance is the computational effort needed to find a solution. In fact, the double loop formed by the GA and the propagation of the equations of motion shown in Fig. A.3 is intrinsically computationally expensive. This is not a big issue if few trajectories need to be evaluated. On the other hand, if a large number of trajectories are needed, the computational effort needed by InTrance to find all the solutions becomes unmanageable.

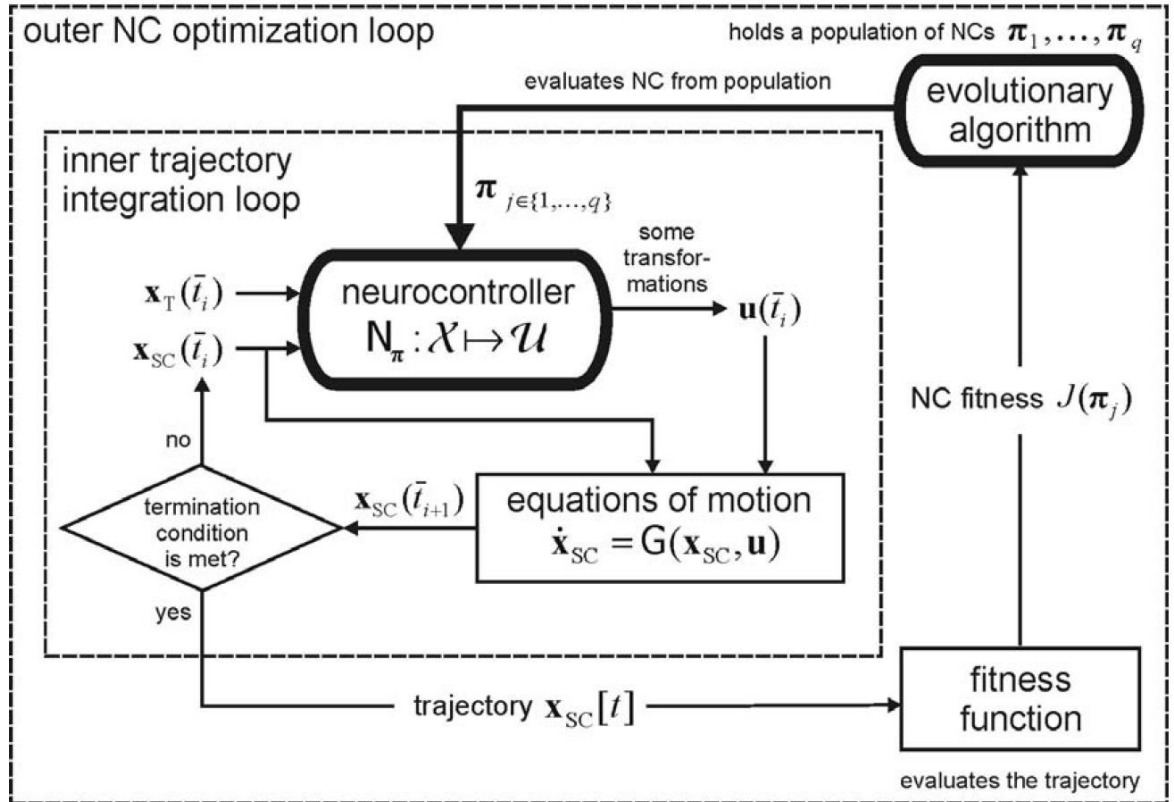


Fig. A.3. Schematic of trajectory optimisation using the evolutionary neurocontroller implemented within InTrance [117].

APPENDIX B.

IMPLEMENTATION DETAILS

B.1. MATLAB and C: A Performances Study

The asteroid sequence search described in CHAPTER 4 is mostly coded in MATLAB. The analytical ephemerides are coded in C and interfaced with MATLAB through MEX functions, as described in [170]. Because of the significant number of times the ephemerides are needed within the asteroid sequence search, this choice was straightforward for a first speedup of the entire sequence search. However, a further action was needed in the code implementation for an additional decrease in the computational effort needed. Therefore, a study was carried out to locate the bottlenecks within the algorithm implementation. That is, a test run of the asteroid sequence search, as described in Algorithm 4.1, was carried out by setting the maximum depth of the BS to one (i.e. only the first leg of the multiple rendezvous mission was sought). The MATLAB built-in function *profile* was used to profile the execution time of all the functions called. The entire run took about 3.5 hours, the majority of which spent to compute the shaping functions. Specifically, the function that computes the Cartesian acceleration [Eq. (3.23)] was called almost 500,000 times for an overall time of more than 6,600 s. That is, more than 50% of the overall runtime was spent in computing \ddot{r} . Therefore, the function related to Eq. (3.23), as well as the one that computes the velocity vector [Eq. (3.5)], was implemented in C and a new test run was carried out. This time, the entire run took about 96 minutes, which is less than 50% of the previous test. The MATLAB *profile* highlighted the function that computes the boundary conditions [Eq. (3.18)] as the one that took the longest computational time. In fact, being called within a Newton loop (i.e. the

MATLAB built-in function *fsolve*) inside a GA, this function was called almost 17,000,000 times for a total time of about 1,350 s (which is the 23% of the overall runtime). A third test run was carried out with the C implementation of the boundary-condition function. This took about 71 minutes, the 61% of which spent inside the *fsolve* function. Therefore, the modified version of the Levenberg-Marquardt algorithm implemented within the MINPACK C subroutine *lmdif*¹ was used instead of the MATLAB counterpart *fsolve*. That is, the entire function that computes the nonlinear constraints for GA is now coded in C and interfaced with MATLAB through a MEX function. A last test run was carried out which took 13 minutes in total. The combined MATLAB/C implementation was able to reduce by 94% the computational effort needed by the original MATLAB code. A graphical view of the computational times for the four aforementioned test runs is shown in Fig. B.1.

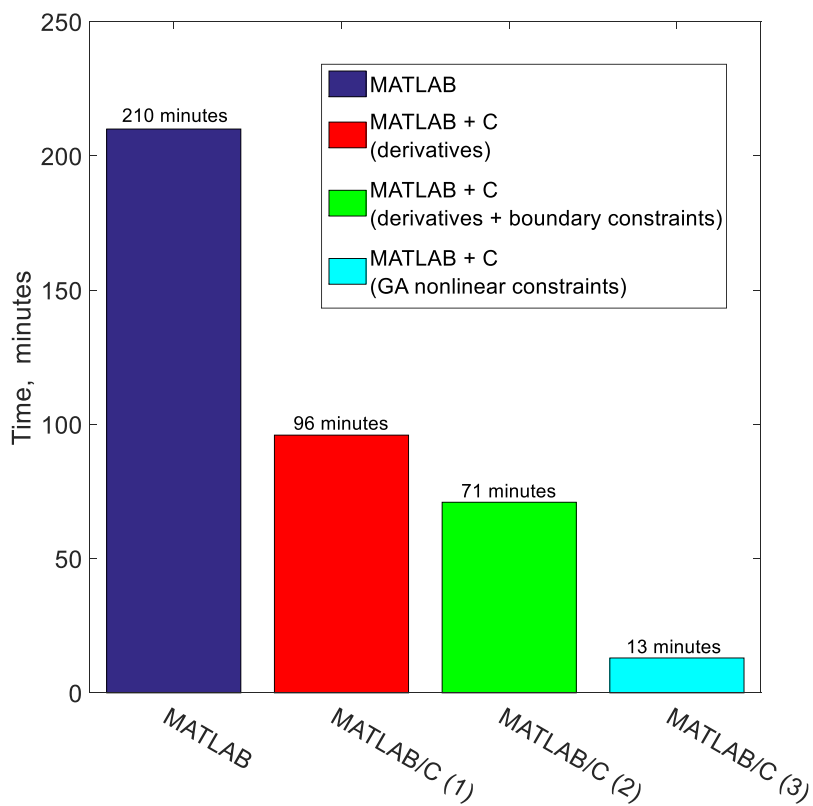


Fig. B.1. Computational times needed for the computation of the first leg of the asteroid sequence search considering four different implementations of the shape-based approach.

¹ Data available online at <http://www.netlib.no/netlib/minpack/lmdif.f> [retrieved 23 November 2014].

B.2. PPSO: Peloni Particle Swarm Optimiser

Following the PSO algorithm presented by Pontani and Conway [102], PPSO has been implemented in MATLAB. It is freely available online at <https://uk.mathworks.com/matlabcentral/fileexchange/58895-ppso> under the BSD 2-Clause License. PPSO has been implemented to have a custom alternative to the MATLAB built-in functions for GA and PSO, which are *ga* and *particleswarm*, respectively. Therefore, no extra effort has been put to optimise the implementation and the algorithm itself. Moreover, at the time PPSO was firstly implemented, there was no MATLAB built-in function for the particle swarm optimisation.

A number of numerical cases have been tested to assess the reliability of the PPSO implementation. PPSO does not explicitly handle nonlinear constraints and thus the test cases are chosen accordingly. Moreover, both a parallelised and a vectorised version of the algorithm are implemented within PPSO to have the possibility to reduce the total runtime needed. For the test cases presented here, the standard sequential non-vectorised version of the code is used. In the following subsections, the test cases are briefly described and the results shown.

A.1.1. Test Case 1: Rastrigin's Function

Test case 1 is the Rastrigin's function, which is the example used in the MATLAB User's Guide [204] to show how to minimise a function with the GA. Two independent variables x_1 and x_2 are used for this test case. Thus, the objective function is

$$J(x_1, x_2) = 20 + x_1^2 + x_2^2 - 10(\cos(2\pi x_1) + \cos(2\pi x_2)) \quad (\text{B.1})$$

and the known global minimum is $J(x_1^*, x_2^*) = J(0,0) = 0$. The performances of PPSO are compared with those of the MATLAB built-in functions *ga* and *particleswarm*. Table B.1 shows the non-default settings considered. Because of the statistical convergence of the metaheuristic optimisation algorithms, each optimiser is run 100 times. The number of times the optimiser finds the optimum (which is, the success rate), within the set tolerance δ_{opt} , is the measure of the performances used for this test case.

Table B.1. PPSO Test Case 1: Non-default settings.

<i>Setting</i>	<i>Value</i>
Optimiser's function tolerance	10^{-8}
Maximum number of iterations K_{max}	500
Population size	25 (PPSO and <i>particleswarm</i>), 100 (<i>ga</i>)
δ_{opt}	10^{-3}

The results of Test case 1 are shown in Table B.2. The average number of function evaluations among the successful runs only is used as an estimate of the optimisers' speed. This is done to avoid external factors that might affect the results. However, it has been noted that the rankings based on the average number of function evaluations mirror those based on the cpu time. For what concerns the success rate, it can be seen that PPSO is the most reliable optimiser among those tested. Regarding the speed, PPSO rates second in the ranking.

Table B.2. PPSO Test Case 1: Results.

<i>Optimiser</i>	<i>Success Rate</i>	<i>Average Function Evaluations</i>
PPSO	100%	7014
<i>ga</i>	78%	9427
<i>particleswarm</i>	95%	3068

A.1.2. Test Case 2: Simple Function of Two Variables

Test case 2 is the example used in the MATLAB User's Guide [204] to show how to minimise a function with the built-in function *particleswarm*. Two independent variables x_1 and x_2 are used for this test case. Thus, the objective function is

$$J(x_1, x_2) = x_1 \exp(-x_1^2 - x_2^2) \quad (\text{B.2})$$

and the known global minimum is $J(x_1^*, x_2^*) = J(-\sqrt{2}/2, 0) = -0.4289$. The performances of PPSO are compared with those of the MATLAB built-in functions *ga* and *particleswarm*. Table B.3 shows the non-default settings considered. As in the previous case, each optimiser is run 100 times.

Table B.3. PPSO Test Case 2: Non-default settings.

<i>Setting</i>	<i>Value</i>
Optimiser's function tolerance	10^{-8}
Maximum number of iterations K_{max}	500
Population size	30 (PPSO and <i>particleswarm</i>), 100 (<i>ga</i>)
δ_{opt}	10^{-3}

The results of Test case 2 are shown in Table B.4. For what concerns the success rate, it can be seen that PPSO is the most reliable optimiser among those tested. Regarding the speed, PPSO rates second in the ranking.

Table B.4. PPSO Test Case 2: Results.

<i>Optimiser</i>	<i>Success Rate</i>	<i>Average Function Evaluations</i>
PPSO	77%	4446
<i>ga</i>	74%	7759
<i>particleswarm</i>	10%	1607

A.1.3. Test Case 3: CEC 2005

Test case 3 aims to test the performances of PPSO against some of the test functions considered for the Congress on Evolutionary Computation (CEC) 2005 [239]. The functions 1 - 6 and 8 - 14 are tested, considering the problem dimension $D = 10$. The interested reader is referred to [239] for a detailed description of the single functions. Each function is tested 25 times and the success rate is used as a performance index. Also in this case, PPSO is compared to *ga* and *particleswarm*. Moreover, the two versions of PSO that competed in CEC 2005 are used as a further comparison. These are: 519-PSO [240] and 620-PSO [241] (the names are those given by the congress organisers as unique identifiers).

Table B.5 shows the results of Test case 3. Note that, on average, PPSO performs better than the two MATLAB built-in optimisers and in line with the results of the two PSO that took part in the competition. In fact, PPSO is able to find more solutions than 519-PSO and 620-PSO for more than one test function. Moreover, PPSO was coded using a standard implementation of the particle swarm theory, whereas both 519-PSO and 620-PSO were implemented with the purpose to improve the standard implementation of PSO.

Table B.5. PPSO Test Case 3: Results.

<i>Function</i>	PPSO	<i>particleswarm</i>	<i>ga</i>	519-PSO	620-PSO
1	96%	100%	100%	100%	100%
2	100%	100%	96%	100%	100%
3	0%	0%	0%	0%	100%
4	92%	0%	0%	100%	0%
5	100%	100%	0%	100%	80%
6	4%	12%	0%	0%	100%
8	0%	0%	0%	0%	100%
9	0%	0%	8%	0%	0%
10	0%	0%	0%	0%	0%
11	0%	0%	0%	0%	76%
12	16%	8%	0%	0%	0%
13	0%	0%	0%	0%	0%
14	0%	0%	0%	0%	88%

A.1.4. Test Case 4: Optimal Two-Impulsive Transfer between Two Circular Orbits

Test case 4 aims to test PPSO on a simple space-trajectory problem. This test case, which is the second example in [102], describes a two-impulsive transfer between two circular orbits. The goal is to find the impulsive thrust, in terms of magnitude and direction, such that the total Δv is minimised. In this case, the optimal known solution is given by the Hohmann transfer. Therefore, a run is considered successful if the difference between the total Δv found by the optimiser and the known optimal one is less than a set tolerance δ_{opt} . Defining β as the ratio between arrival and departing radius, ten scenarios are considered with $\beta = 2, \dots, 11$, as in the reference paper. For each scenario, both PPSO and *ga* are used and run 100 times. Table B.6 shows the non-default settings used for the two optimisers, whereas Table B.7 shows the results in terms of success rate and average function evaluations.

Table B.6. PPSO Test Case 4: Non-default settings.

<i>Setting</i>	<i>Value</i>
Optimiser's function tolerance	10^{-10}
Maximum number of iterations K_{max}	500
Population size	30 (PPSO), 100 (<i>ga</i>)
δ_{opt}	10^{-10}

Table B.7. PPSO Test Case 4: Results.

β	PPSO		<i>ga</i>	
	Success Rate	Average Function Evaluations	Success Rate	Average Function Evaluations
2	100%	8,124	0%	---
3	100%	8,179	0%	---
4	100%	8,315	0%	---
5	100%	8,536	3%	5,332
6	100%	8,324	6%	5,329
7	100%	8,719	7%	5,326
8	100%	8,658	9%	5,325
9	100%	9,018	9%	5,327
10	100%	8,974	11%	5,335
11	100%	8,883	13%	5,324

A.1.5. Test Case 5: Bi-Impulsive Earth-Apophis Transfer

In the last test case, the bi-impulsive Earth-Apophis transfer described in [110] is considered. Three values for the population size are considered for both PPSO and *ga*, as done in the reference paper. In this case, each optimiser is run 200 times and a solution is considered optimal if the value of the objective function differs from the known optimum by at most δ_{opt} . A maximum number of function evaluations is allowed for each test, as shown in Table B.8. Table B.9 shows the results, in terms of success rate, compared with the three versions of PSO described in [110], namely PSOn05, PSOn07 and PSOn09 with $n = \{5, 10, 20\}$ depending on the population size considered. Note that, if a population of 10 particles is considered, PPSO performances are inferior to the others. For the case

of a population of 20 particles, the performances of PPSO are in line with the other optimisers. Lastly, the success rate of PPSO with a population size of 40 particles is the best one.

Table B.8. PPSO Test Case 5: Non-default settings.

<i>Setting</i>	<i>Value</i>
Maximum number of function evaluations	10,000
Population size	10, 20, 40 (PPSO), 100, 200, 400 (<i>ga</i>)
δ_{opt}	10^{-3}

Table B.9. PPSO Test Case 5: Results.

<i>Optimiser</i>	<i>Population Size</i>	<i>Success Rate</i>
PPSO	10	25.5%
PPSO	20	36%
PPSO	40	62%
<i>ga</i>	100	22%
<i>ga</i>	200	44%
<i>ga</i>	400	53%
PSO505	10	35.5%
PSO1005	20	34.5%
PSO2005	40	41%
PSO507	10	39.5%
PSO1007	20	42.5%
PSO2007	40	41%
PSO509	10	43.5%
PSO1009	20	38.5%
PSO2009	40	42%

REFERENCES

- [1] Jahn, R. G. and Choueiri, E. Y., “Electric Propulsion”, *Encyclopedia of Physical Science and Technology (Third Edition)*, edited by R.A. Meyers, Academic Press, New York, NY, USA, 2003, pp. 125-141.
- [2] McInnes, C. R., *Solar Sailing: Technology, Dynamics and Mission Applications*, Springer Praxis Publishing, Chichester, UK, 1999, pp. 2,32-55,112-120,129-148,171.
- [3] Geppert, U., Biering, B., Lura, F., Block, J., Straubel, M. and Reinhard, R., “The 3-step DLR-ESA Gossamer road to solar sailing”, *Advances in Space Research*, Vol. 48, No. 11, 2011, pp. 1695-1701. DOI: 10.1016/j.asr.2010.09.016.
- [4] Conway, B. A., *Spacecraft Trajectory Optimization*, Cambridge Aerospace Series, Cambridge University Press, New York, NY, USA, 2010, pp. 1-7,16-36.
- [5] Conway, B. A., “A brief survey of methods available for numerical optimization of spacecraft trajectories”, *61st International Astronautical Congress*, International Astronautical Federation Paper IAC-10-C1.2.1, Prague, Czech Republic, 2010.
- [6] Betts, J. T., “Survey of Numerical Methods for Trajectory Optimization”, *Journal of Guidance, Control, and Dynamics*, Vol. 21, No. 2, 1998, pp. 193-207. DOI: 10.2514/2.4231.
- [7] Betts, J. T., *Practical Methods for Optimal Control and Estimation Using Nonlinear Programming (Second Edition)*, Soc. for Industrial and Applied Mathematics, Philadelphia, PA, USA, 2010, pp. 45,91,123-126,132-165,266.
- [8] Petropoulos, A. E. and Longuski, J. M., “Shape-Based Algorithm for the Automated Design of Low-Thrust, Gravity Assist Trajectories”, *Journal of Spacecraft and Rockets*, Vol. 41, No. 5, 2004, pp. 787-796. DOI: 10.2514/1.13095.
- [9] De Pascale, P. and Vasile, M., “Preliminary Design of Low-Thrust Multiple Gravity-Assist Trajectories”, *Journal of Spacecraft and Rockets*, Vol. 43, No. 5, 2006, pp. 1065-1076. DOI: 10.2514/1.19646.
- [10] Colasurdo, G. and Casalino, L., “Optimal Control Law for Interplanetary Trajectories with Nonideal Solar Sail”, *Journal of Spacecraft and Rockets*, Vol. 40, No. 2, 2003, pp. 260-265. DOI: 10.2514/2.3941.
- [11] Mengali, G. and Quarta, A. A., “Solar sail trajectories with piecewise-constant steering laws”, *Aerospace Science and Technology*, Vol. 13, No. 8, 2009, pp. 431-441. DOI: 10.1016/j.ast.2009.06.007.
- [12] Mengali, G. and Quarta, A. A., “Rapid Solar Sail Rendezvous Missions to Asteroid 99942 Apophis”, *Journal of Spacecraft and Rockets*, Vol. 46, No. 1, 2009, pp. 134-140. DOI: 10.2514/1.37141.

- [13] Li, S., Zhu, Y. and Wang, Y., "Rapid design and optimization of low-thrust rendezvous/interception trajectory for asteroid deflection missions", *Advances in Space Research*, Vol. 53, No. 4, 2014, pp. 696-707. DOI: 10.1016/j.asr.2013.12.012.
- [14] Taheri, E. and Abdelkhalik, O., "Shape Based Approximation of Constrained Low-Thrust Space Trajectories using Fourier Series", *Journal of Spacecraft and Rockets*, Vol. 49, No. 3, 2012, pp. 535-546. DOI: 10.2514/1.58789.
- [15] Dachwald, B. and Seboldt, W., "Multiple near-Earth asteroid rendezvous and sample return using first generation solar sailcraft", *Acta Astronautica*, Vol. 57, No. 11, 2005, pp. 864-875. DOI: 10.1016/j.actaastro.2005.04.012.
- [16] Dachwald, B., Boehnhardt, H., Broj, U., Geppert, U., Grundmann, J. T., Seboldt, W., et al., "Gossamer Roadmap Technology Reference Study for a Multiple NEO Rendezvous Mission", *Advances in Solar Sailing*, edited by M. Macdonald, Springer Praxis Books, Springer-Verlag, Berlin, Germany, 2014, pp. 211-226.
- [17] Johnson, L., Young, R., Montgomery, E. and Alhorn, D., "Status of solar sail technology within NASA", *Advances in Space Research*, Vol. 48, No. 11, 2011, pp. 1687-1694. DOI: 10.1016/j.asr.2010.12.011.
- [18] Macdonald, M. and McInnes, C., "Solar sail science mission applications and advancement", *Advances in Space Research*, Vol. 48, No. 11, 2011, pp. 1702-1716. DOI: 10.1016/j.asr.2011.03.018.
- [19] Giannone, P., *Elementi di Astronomia*, Pitagora Editrice, Bologna, Italy, 2004, pp. 48-50, 56, 163-164, 468-472 (Italian).
- [20] Kutner, M. L., *Astronomy: A Physical Perspective (Second Edition)*, Cambridge University Press, Cambridge, UK, 2003, pp. 9-21, 101-119.
- [21] Grossman, J., "Solar Sailing: The Next Space Craze?", *Engineering and Science*, Vol. 63, No. 4, 2000, pp. 18-29. ISSN: 0013-7812.
- [22] Janhunen, P., "Electric Sail for Spacecraft Propulsion", *Journal of Propulsion and Power*, Vol. 20, No. 4, 2004, pp. 763-764. DOI: 10.2514/1.8580.
- [23] Zubrin, R., "The Use of Magnetic Sails to Escape from Low Earth Orbit", *27th Joint Propulsion Conference*, AIAA Paper 91-3352, Sacramento, CA, USA, 1991.
- [24] Mengali, G., Quarta, A. A. and Janhunen, P., "Electric Sail Performance Analysis", *Journal of Spacecraft and Rockets*, Vol. 45, No. 1, 2008, pp. 122-129. DOI: 10.2514/1.31769.
- [25] Griffiths, D. J., *Introduction to Quantum Mechanics*, Prentice Hall, Upper Saddle River, NJ, USA, 1995, pp. 2, 143, 216.
- [26] Mencuccini, C. and Silvestrini, V., *FISICA II: Elettromagnetismo - Ottica*, Liguori Editore, Naples, Italy, 1998, pp. 490-498 (Italian).
- [27] Stratton, J. A., *Electromagnetic Theory*, International Series in Physics, McGraw-Hill, New York, NY, USA, 1941, pp. 128, 131-135.
- [28] Maxwell, J. C., *A Treatise on Electricity and Magnetism. Vol. II*, Clarendon Press, Oxford, UK, 1881, pp. 402-403.

- [29] Mengali, G., Quarta, A. A., Circi, C. and Dachwald, B., “Refined Solar Sail Force Model with Mission Application”, *Journal of Guidance, Control, and Dynamics*, Vol. 30, No. 2, 2007, pp. 512-520. DOI: 10.2514/1.24779.
- [30] Heiligers, J., Diedrich, B., Derbes, W. and McInnes, C., “Sunjammer: Preliminary End-to-End Mission Design”, *AIAA/AAS Astrodynamics Specialist Conference*, AIAA Paper 2014-4127, San Diego, CA, USA, 2014.
- [31] Grundmann, J. T., Boden, R. C., Ceriotti, M., Dachwald, B., Dumont, E., Grimm, C. D., et al., “Soil to Sail - Asteroid Landers on Near-Term Sailcraft as an Evolution of the GOSSAMER Small Spacecraft Solar Sail Concept for In-Situ Characterization”, *5th IAA Planetary Defense Conference - PDC 2017*, International Academy of Astronautics Paper IAA-PDC-17-05-19, Tokyo, Japan, 2017.
- [32] Conway, B. A., “The Problem of Spacecraft Trajectory Optimization”, *Spacecraft Trajectory Optimization*, edited by B.A. Conway, Cambridge Aerospace Series, Cambridge University Press, Cambridge, UK, 2010, pp. 1-15.
- [33] Tsuda, Y., Mori, O., Funase, R., Sawada, H., Yamamoto, T., Saiki, T., et al., “Flight status of IKAROS deep space solar sail demonstrator”, *Acta Astronautica*, Vol. 69, No. 9-10, 2011, pp. 833-840. DOI: 10.1016/j.actaastro.2011.06.005.
- [34] Tsuda, Y., Mori, O., Funase, R., Sawada, H., Yamamoto, T., Saiki, T., et al., “Achievement of IKAROS - Japanese deep space solar sail demonstration mission”, *Acta Astronautica*, Vol. 82, No. 2, 2013, pp. 183-188. DOI: 10.1016/j.actaastro.2012.03.032.
- [35] Heaton, A. F., Faller, B. F. and Katan, C. K., “NanoSail-D Orbital and Attitude Dynamics”, *Advances in Solar Sailing*, edited by M. Macdonald, Springer Praxis Books, Springer-Verlag, Berlin, Germany, 2014, pp. 95-113.
- [36] Johnson, L., Whorton, M., Heaton, A., Pinson, R., Laue, G. and Adams, C., “NanoSail-D: A solar sail demonstration mission”, *Acta Astronautica*, Vol. 68, 2011, pp. 571-575. DOI: 10.1016/j.actaastro.2010.02.008.
- [37] Betts, B., Nye, B., Vaughn, J., Greeson, E., Chute, R., Spencer, D. A., et al., “LightSail 1 Mission Results and Public Outreach Strategies”, *The Fourth International Symposium on Solar Sailing 2017*, Paper 17093, Kyoto, Japan, 2017.
- [38] McNutt, L., Johnson, L., Clardy, D., Castillo-Rogez, J., Frick, A. and Jones, L., “Near-Earth Asteroid Scout”, *AIAA SPACE 2014 Conference and Exposition*, AIAA Paper 2014-4435, San Diego, CA, USA, 2014.
- [39] Bach, V., Becker, C., Dervan, J., Diedrich, B. L., Few, A., Heaton, A. F., et al., “Near Earth Asteroid (NEA) Scout Solar Sail Implementation”, *Annual AIAA/USU Conference on Small Satellites*, AIAA, Logan, UT, USA, 2016.
- [40] Johnson, L., “Solar Sails for Spacecraft Propulsion”, University of Tennessee, Knoxville, TN, USA, 04 April 2016, <https://ntrs.nasa.gov/archive/nasa/casi.ntrs.nasa.gov/20160005683.pdf> [retrieved 11 July 2017].
- [41] Ceriotti, M. and McInnes, C. R., “Generation of Optimal Trajectories for Earth Hybrid Pole Sitters”, *Journal of Guidance, Control, and Dynamics*, Vol. 34, No. 3, 2011, pp. 847-859. DOI: 10.2514/1.50935.

- [42] McKay, R., Macdonald, M., Biggs, J. and McInnes, C., "Survey of Highly Non-Keplerian Orbits with Low-Thrust Propulsion", *Journal of Guidance, Control, and Dynamics*, Vol. 34, No. 3, 2011, pp. 645-666. DOI: 10.2514/1.52133.
- [43] Forward, R. L., "Statite - A Spacecraft That Does Not Orbit", *Journal of Spacecraft and Rockets*, Vol. 28, No. 5, 1991, pp. 606-611. DOI: 10.2514/3.26287.
- [44] Circi, C., "Simple Strategy for Geostationary Stationkeeping Maneuvers Using Solar Sail", *Journal of Guidance, Control, and Dynamics*, Vol. 28, No. 2, 2005, pp. 249-253. DOI: 10.2514/1.6797.
- [45] Sarli, B. V. and Tsuda, Y., "Hayabusa 2 extension plan: Asteroid selection and trajectory design", *Acta Astronautica*, Vol. 138, 2017, pp. 225-232. DOI: 10.1016/j.actaastro.2017.05.016.
- [46] Farrés, A., "Transfer orbits to L4 with a solar sail in the Earth-Sun system", *Acta Astronautica*, Vol. 137, 2017, pp. 78-90. DOI: 10.1016/j.actaastro.2017.04.010.
- [47] Ceriotti, M., Diedrich, B. L. and McInnes, C. R., "Novel mission concepts for polar coverage: An overview of recent developments and possible future applications", *Acta Astronautica*, Vol. 80, No. 0, 2012, pp. 89-104. DOI: 10.1016/j.actaastro.2012.04.043.
- [48] Peloni, A., Barbera, D., Laurenzi, S. and Circi, C., "Dynamic and Structural Performances of a New Sailcraft Concept for Interplanetary Missions", *The Scientific World Journal*, Vol. 2015, 2015. DOI: 10.1155/2015/714371.
- [49] Grundmann, J. T., Bauer, W., Biele, J., Cordero, F., Dachwald, B., Koch, A. D., et al., "From Sail to Soil - Getting Sailcraft Out of the Harbour on a Visit to One of Earth's Nearest Neighbours", *4th IAA Planetary Defense Conference - PDC 2015*, International Academy of Astronautics Paper IAA-PDC-15-04-17, Frascati, Italy, 2015.
- [50] Seefeldt, P., Spietz, P., Sproewitz, T., Grundmann, J. T., Hillebrandt, M., Hobbie, C., et al., "Gossamer-1: Mission concept and technology for a controlled deployment of gossamer spacecraft", *Advances in Space Research*, Vol. 59, No. 1, 2017, pp. 434-456. DOI: 10.1016/j.asr.2016.09.022.
- [51] McInnes, C. R., Bothmer, V., Dachwald, B., Geppert, U., Heiligers, J., Hilgers, A., et al., "Gossamer Roadmap Technology Reference Study for a Sub-L1 Space Weather Mission", *Advances in Solar Sailing*, edited by M. Macdonald, Springer Praxis Books, Springer-Verlag, Berlin, Germany, 2014, pp. 227-242.
- [52] Macdonald, M., McGrath, C., Appourchaux, T., Dachwald, B., Finsterle, W., Gizon, L., et al., "Gossamer Roadmap Technology Reference Study for a Solar Polar Mission", *Advances in Solar Sailing*, edited by M. Macdonald, Springer Praxis Books, Springer-Verlag, Berlin, Germany, 2014, pp. 243-257.
- [53] Goldstine, H. H., *A History of the Calculus of Variations from the 17th through the 19th Century*, Studies in the History of Mathematics and Physical Sciences, Springer-Verlag, New York, NY, USA, 1980, pp. 373-383.
- [54] Hull, D. G., *Optimal Control Theory for Applications*, Mechanical Engineering Series, Springer-Verlag, New York, NY, USA, 2003, pp. 11-12,45-47.

- [55] Conway, B. A., "A Survey of Methods Available for the Numerical Optimization of Continuous Dynamic Systems", *Journal of Optimization Theory and Applications*, Vol. 152, No. 2, 2012, pp. 271-306. DOI: 10.1007/s10957-011-9918-z.
- [56] Rao, A. V., "Survey of Numerical Methods for Optimal Control", *2009 AAS/AIAA Astrodynamics Specialist Conference*, AAS Paper 09-334, Pittsburgh, PA, USA, 2009.
- [57] Alemany, K. and Braun, R. D., "Survey of Global Optimization Methods for Low-Thrust, Multiple Asteroid Tour Missions", *17th AAS/AIAA Space Flight Mechanics Meeting*, AAS Paper 07-211, Sedona, AZ, USA, 2007.
- [58] Gao, Y., "Near-Optimal Very Low-Thrust Earth-Orbit Transfers and Guidance Schemes", *Journal of Guidance Control and Dynamics*, Vol. 30, No. 2, 2007. DOI: 10.2514/1.24836.
- [59] Kluever, C. A., "Efficient Computation of Optimal Interplanetary Trajectories Using Solar Electric Propulsion", *Journal of Guidance, Control, and Dynamics*, Vol. 38, No. 5, 2014, pp. 821-830. DOI: 10.2514/1.g000144.
- [60] Casalino, L., "Approximate Optimization of Low-Thrust Transfers Between Low-Eccentricity Close Orbits", *Journal of Guidance, Control, and Dynamics*, Vol. 37, No. 3, 2014, pp. 1003-1008. DOI: 10.2514/1.62046.
- [61] Gatto, G. and Casalino, L., "Fast Evaluation and Optimization of Low-Thrust Transfers to Multiple Targets", *Journal of Guidance, Control, and Dynamics*, Vol. 38, No. 8, 2015, pp. 1525-1530. DOI: 10.2514/1.g001116.
- [62] Zuiani, F., Vasile, M., Palmas, A. and Avanzini, G., "Direct transcription of low-thrust trajectories with finite trajectory elements", *Acta Astronautica*, Vol. 72, 2012, pp. 108-120. DOI: 10.1016/j.actaastro.2011.09.011.
- [63] Pontryagin, L. S., Boltyanskii, V. G., Gamkrelidze, R. V. and Mishchenko, E. F., *The Mathematical Theory of Optimal Processes*, John Wiley & Sons, New York, NY, USA, 1962, pp. 9-114.
- [64] Whitehead, G. W., *Elements of Homotopy Theory*, Graduate Texts in Mathematics, Springer-Verlag, New York, NY, USA, 1978, pp. 3-8.
- [65] Allgower, E. L. and Georg, K., *Introduction to Numerical Continuation Methods*, Classics in Applied Mathematics, Soc. for Industrial and Applied Mathematics, Philadelphia, PA, USA, 2003, pp. 1-6.
- [66] Sullo, N., Peloni, A. and Ceriotti, M., "Low-Thrust to Solar-Sail Trajectories: A Homotopic Approach", *Journal of Guidance, Control, and Dynamics*, Vol. 40, No. 11, 2017, pp. 2796-2806. DOI: 10.2514/1.G002552.
- [67] Pan, B., Lu, P., Pan, X. and Ma, Y., "Double-Homotopy Method for Solving Optimal Control Problems", *Journal of Guidance, Control, and Dynamics*, Vol. 39, No. 8, 2016, pp. 1706-1720. DOI: 10.2514/1.G001553.
- [68] Polsgrove, T., Kos, L., Hopkins, R. and Crane, T., "Comparison of Performance Predictions for New Low-Thrust Trajectory Tools", *AIAA/AAS Astrodynamics Specialist Conference and Exhibit*, AIAA Paper 2006-6742, Keystone, CO, USA, 2006.

- [69] Boyd, S. and Vandenberghe, L., *Convex Optimization*, Cambridge University Press, Cambridge, UK, 2004, pp. 241-249.
- [70] Büskens, C., Knauer, M., Geffken, S., Kuhlmann, R., Hasse, J. N. and Jacobse, M., “User’s Guide to WORHP 1.10”, Steinbeis-Forschungszentrum Optimierung, Steuerung und Regelung, 2017, 11 May 2017, <http://worhp.de> [retrieved 17 May 2017].
- [71] Wächter, A. and Biegler, L. T., “On the implementation of an interior-point filter line-search algorithm for large-scale nonlinear programming”, *Mathematical Programming*, Vol. 106, No. 1, 2006, pp. 25-57. DOI: 10.1007/s10107-004-0559-y.
- [72] Gill, P., Murray, W. and Saunders, M., “SNOPT: An SQP Algorithm for Large-Scale Constrained Optimization”, *SIAM Review*, Vol. 47, No. 1, 2005, pp. 99-131. DOI: 10.1137/S0036144504446096.
- [73] Büskens, C. and Wassel, D., “The ESA NLP Solver WORHP”, *Modeling and Optimization in Space Engineering*, edited by G. Fasano and J.D. Pinter, Springer Optimization and Its Applications, Springer-Verlag, New York, NY, USA, 2012, pp. 85-110.
- [74] Sims, J. A. and Flanagan, S. N., “Preliminary Design of Low-Thrust Interplanetary Missions”, *AAS/AIAA Astrodynamics Specialist Conference*, AAS Paper 99-0328, Girdwood, AK, USA, 1999.
- [75] Sims, J. A., Finlayson, P. A., Rinderle, E. A., Vavrina, M. A. and Kowalkowski, T. D., “Implementation of a Low-Thrust Trajectory Optimization Algorithm for Preliminary Design”, *AIAA/AAS Astrodynamics Specialist Conference and Exhibit*, AIAA Paper 2006-6746, Keystone, CO, USA, 2006.
- [76] Yam, C. H., Izzo, D. and Biscani, F., “Towards a High Fidelity Direct Transcription Method for Optimisation of Low-Thrust Trajectories”, *4th International Conference on Astrodynamics Tools and Techniques - ICATT*, ESA, Madrid, Spain, 2010.
- [77] Battin, R. H., *An Introduction to the Mathematics and Methods of Astrodynamics, Revised Edition*, AIAA Education Series, AIAA, Reston, VA, USA, 1999, pp. 174-175, 295-342, 392-393, 492-493.
- [78] Jorba, À. and Zou, M., “A Software Package for the Numerical Integration of ODEs by Means of High-Order Taylor Methods”, *Experimental Mathematics*, Vol. 14, No. 1, 2005, pp. 99-117. DOI: 10.1080/10586458.2005.10128904.
- [79] Garg, D., Patterson, M. A., Francolin, C., Darby, C. L., Huntington, G. T., Hager, W. W., et al., “Direct trajectory optimization and costate estimation of finite-horizon and infinite-horizon optimal control problems using a Radau pseudospectral method”, *Computational Optimization and Applications*, Vol. 49, No. 2, 2011, pp. 335-358. DOI: 10.1007/s10589-009-9291-0.
- [80] Garg, D., Patterson, M., Hager, W. W., Rao, A. V., Benson, D. A. and Huntington, G. T., “A unified framework for the numerical solution of optimal control problems using pseudospectral methods”, *Automatica*, Vol. 46, No. 11, 2010, pp. 1843-1851. DOI: 10.1016/j.automatica.2010.06.048.
- [81] Yong, E., “Trajectory Optimization of Lifting-type Reentry Vehicle Via Gauss Pseudospectral Method”, *62nd International Astronautical Congress*, International Astronautical Federation Paper IAC-11-C1.2.5, Cape Town, South Africa, 2011.

- [82] Huntington, G. T., "Advancement and Analysis of a Gauss Pseudospectral Transcription for Optimal Control Problems", PhD Thesis, Department of Aeronautics and Astronautics, Massachusetts Institute of Technology, Cambridge, MA, USA, 2007.
- [83] Huntington, G. T. and Rao, A. V., "Comparison of Global and Local Collocation Methods for Optimal Control", *Journal of Guidance, Control, and Dynamics*, Vol. 31, No. 2, 2008, pp. 432-436. DOI: 10.2514/1.30915.
- [84] Garg, D., Hager, W. W. and Rao, A. V., "Pseudospectral methods for solving infinite-horizon optimal control problems", *Automatica*, Vol. 47, No. 4, 2011, pp. 829-837. DOI: 10.1016/j.automatica.2011.01.085.
- [85] Patterson, M. A., Hager, W. W. and Rao, A. V., "A ph Mesh Refinement Method for Optimal Control", *Optimal Control Applications and Methods*, Vol. 36, No. 4, 2014, pp. 398-421. DOI: 10.1002/oca.2114.
- [86] Canuto, C., Hussaini, M. Y., Quarteroni, A. and Zang, T. A. J., *Spectral Methods - Fundamentals in Single Domains*, Scientific Computation, Springer-Verlag, Berlin, Germany, 2006, pp. 76.
- [87] Rao, A. V., Benson, D. A., Darby, C. L., Patterson, M. A., Francolin, C., Sanders, I., et al., "Algorithm 902: GPOPS, A MATLAB Software for Solving Multiple-Phase Optimal Control Problems Using the Gauss Pseudospectral Method", *ACM Transactions on Mathematical Software*, Vol. 37, No. 2, 2010. DOI: 10.1145/1731022.1731032.
- [88] Patterson, M. A. and Rao, A. V., "GPOPS – II: A MATLAB Software for Solving Multiple-Phase Optimal Control Problems Using hp-Adaptive Gaussian Quadrature Collocation Methods and Sparse Nonlinear Programming", *ACM Transactions on Mathematical Software*, Vol. 41, No. 1, 2014, Article 1. DOI: 10.1145/2558904.
- [89] Patterson, M. A. and Rao, A. V., "GPOPS-II: A General-Purpose MATLAB Software for Solving Multiple-Phase Optimal Control Problems (Version 2.3)", University of Florida, Gainesville, FL, USA, December 2016, www.gpops2.com [retrieved 28 June 2017].
- [90] Darby, C. L., Hager, W. W. and Rao, A. V., "An hp-adaptive pseudospectral method for solving optimal control problems", *Optimal Control Applications and Methods*, Vol. 32, No. 4, 2011, pp. 476-502. DOI: 10.1002/oca.957.
- [91] Darby, C. L., Hager, W. W. and Rao, A. V., "Direct Trajectory Optimization Using a Variable Low-Order Adaptive Pseudospectral Method", *Journal of Spacecraft and Rockets*, Vol. 48, No. 3, 2011, pp. 433-445. DOI: 10.2514/1.52136.
- [92] Liu, F., Hager, W. W. and Rao, A. V., "Adaptive mesh refinement method for optimal control using nonsmoothness detection and mesh size reduction", *Journal of the Franklin Institute*, Vol. 352, No. 10, 2015, pp. 4081-4106. DOI: 10.1016/j.jfranklin.2015.05.028.
- [93] Patterson, M. A. and Rao, A., "Exploiting Sparsity in Direct Collocation Pseudospectral Methods for Solving Optimal Control Problems", *Journal of Spacecraft and Rockets*, Vol. 49, No. 2, 2012, pp. 354-377. DOI: 10.2514/1.a32071.
- [94] Porsa, S., Lin, Y.-C. and Pandy, M. G., "Direct Methods for Predicting Movement Biomechanics Based Upon Optimal Control Theory with Implementation in

- OpenSim”, *Annals of Biomedical Engineering*, Vol. 44, No. 8, 2016, pp. 2542-2557. DOI: 10.1007/s10439-015-1538-6.
- [95] Van den Bogert, A. J., Blana, D. and Heinrich, D., “Implicit methods for efficient musculoskeletal simulation and optimal control”, *Procedia IUTAM*, Vol. 2, 2011, pp. 297-316. DOI: 10.1016/j.piutam.2011.04.027.
- [96] De Groot, F., Kinney, A. L., Rao, A. V. and Fregly, B. J., “Evaluation of Direct Collocation Optimal Control Problem Formulations for Solving the Muscle Redundancy Problem”, *Annals of Biomedical Engineering*, Vol. 44, No. 10, 2016, pp. 2922-2936. DOI: 10.1007/s10439-016-1591-9.
- [97] Graham, K. F. and Rao, A. V., “Minimum-Time Trajectory Optimization of Multiple Revolution Low-Thrust Earth-Orbit Transfers”, *Journal of Spacecraft and Rockets*, Vol. 52, No. 3, 2015, pp. 711-727. DOI: 10.2514/1.a33187.
- [98] Weinstein, M. J. and Rao, A. V., “A Source Transformation via Operator Overloading Method for the Automatic Differentiation of Mathematical Functions in MATLAB”, *ACM Transactions on Mathematical Software*, Vol. 42, No. 2, 2016, pp. 1-44. DOI: 10.1145/2699456.
- [99] Glover, F. W. and Laguna, M., *Tabu Search*, Springer, New York, NY, USA, 1997, pp. 17-23.
- [100] Elbeltagi, E., Hegazy, T. and Grierson, D., “Comparison among five evolutionary-based optimization algorithms”, *Advanced Engineering Informatics*, Vol. 19, No. 1, 2005, pp. 43-53. DOI: 10.1016/j.aei.2005.01.004.
- [101] Sivanandam, S. N. and Deepa, S. N., *Introduction to Genetic Algorithms*, Springer-Verlag, Berlin, Germany, 2008, pp. 15-37.
- [102] Pontani, M. and Conway, B. A., “Particle Swarm Optimization Applied to Space Trajectories”, *Journal of Guidance, Control, and Dynamics*, Vol. 33, No. 5, 2010, pp. 1429-1441. DOI: 10.2514/1.48475.
- [103] Pontani, M. and Conway, B. A., “Optimal Low-Thrust Orbital Maneuvers via Indirect Swarming Method”, *Journal of Optimal Theory and Applications*, Vol. 162, No. 1, 2014, pp. 272-292. DOI: 10.1007/s10957-013-0471-9.
- [104] Dorigo, M. and Gambardella, L. M., “Ant colony system: a cooperative learning approach to the traveling salesman problem”, *IEEE Transactions on Evolutionary Computation*, Vol. 1, No. 1, 1997, pp. 53-66. DOI: 10.1109/4235.585892.
- [105] Ceriotti, M. and Vasile, M., “Automated Multigravity Assist Trajectory Planning with a Modified Ant Colony Algorithm”, *Journal of Aerospace Computing, Information, and Communication*, Vol. 7, No. 9, 2010, pp. 261-293. DOI: 10.2514/1.48448.
- [106] Ceriotti, M. and Vasile, M., “MGA trajectory planning with an ACO-inspired algorithm”, *Acta Astronautica*, Vol. 67, No. 9-10, 2010, pp. 1202-1217. DOI: 10.1016/j.actaastro.2010.07.001.
- [107] Storn, R. and Price, K., “Differential Evolution - A Simple and Efficient Heuristic for Global Optimization over Continuous Spaces”, *Journal of Global Optimization*, Vol. 11, No. 4, 1997, pp. 341-359. DOI: 10.1023/a:1008202821328.

- [108] Kirkpatrick, S., Gelatt, C. D. J. and Vecchi, M. P., "Optimization by Simulated Annealing", *Science*, Vol. 220, No. 4598, 1983, pp. 671-680. DOI: 10.1126/science.220.4598.671.
- [109] Vasile, M., Martin, J. M. R., Masi, L., Minisci, E., Epenoy, R., Martinot, V., et al., "Incremental planning of multi-gravity assist trajectories", *Acta Astronautica*, Vol. 115, 2015, pp. 407-421. DOI: 10.1016/j.actaastro.2015.05.033.
- [110] Vasile, M., Minisci, E. and Locatelli, M., "On Testing Global Optimization Algorithms for Space Trajectory Design", *AIAA/AAS Astrodynamics Specialist Conference and Exhibit*, AIAA Paper 2008-6277, Honolulu, HI, USA, 2008.
- [111] Rosa Sentinella, M. and Casalino, L., "Cooperative evolutionary algorithm for space trajectory optimization", *Celestial Mechanics and Dynamical Astronomy*, Vol. 105, No. 1-3, 2009, pp. 211-227. DOI: 10.1007/s10569-009-9223-4.
- [112] Pontani, M., "Particle swarm optimization of ascent trajectories of multistage launch vehicles", *Acta Astronautica*, Vol. 94, No. 2, 2014, pp. 852-864. DOI: 10.1016/j.actaastro.2013.09.013.
- [113] Sullo, N., Sousa-Silva, P. A., O. Terra, M. and Ceriotti, M., "Optimisation of Low-Thrust and Hybrid Earth-Moon Transfers", *67th International Astronautical Congress*, International Astronautical Federation Paper IAC-16-C1.4.5, Guadalajara, Mexico, 2016.
- [114] Englander, J. A., Vavrina, M. A. and Hinckley, D., "Global Optimization of Low-Thrust Interplanetary Trajectories Subject to Operational Constraints", *26th AAS/AIAA Space Flight Mechanics Meeting*, AAS Paper 16-239, Napa, CA, USA, 2016.
- [115] Vavrina, M. A., Englander, J. A. and Ellison, D. H., "Global Optimization of N-Maneuver, High-Thrust Trajectories Using Direct Multiple Shooting", *26th AAS/AIAA Space Flight Mechanics Meeting*, AAS Paper 16-272, Napa, CA, USA, 2016.
- [116] Izzo, D., "PyGMO and PyKEP: Open Source Tools for Massively Parallel Optimization in Astrodynamics (the case of interplanetary trajectory optimization)", *5th International Conference on Astrodynamics Tools and Techniques - ICATT*, ESA, Noordwijk, The Netherlands, 2012.
- [117] Dachwald, B., "Low-Thrust Trajectory Optimization and Interplanetary Mission Analysis Using Evolutionary Neurocontrol", PhD Thesis, Institut für Raumfahrttechnik, Universität der Bundeswehr München, Munich, Germany, 2004.
- [118] Dachwald, B., "Optimization of very-low-thrust trajectories using evolutionary neurocontrol", *Acta Astronautica*, Vol. 57, 2005, pp. 175-185. DOI: 10.1016/j.actaastro.2005.03.004.
- [119] Rosa Sentinella, M. and Casalino, L., "Hybrid Evolutionary Algorithm for the Optimization of Interplanetary Trajectories", *Journal of Spacecraft and Rockets*, Vol. 46, No. 2, 2009, pp. 365-372. DOI: 10.2514/1.38440.
- [120] Dachwald, B. and Ohndorf, A., "1st ACT global trajectory optimisation competition: Results found at DLR", *Acta Astronautica*, Vol. 61, No. 9, 2007, pp. 742-752. DOI: 10.1016/j.actaastro.2007.03.011.

- [121] Walker, M. J. H., Ireland, B. and Owens, J., "A set of modified equinoctial orbit elements", *Celestial Mechanics*, Vol. 36, No. 4, 1985, pp. 409-419. DOI: 10.1007/bf01227493.
- [122] Walker, M. J. H., "A set of modified equinoctial orbit elements" (Errata), *Celestial Mechanics*, Vol. 38, No. 4, 1986, pp. 391-392. DOI: 10.1007/bf01238929.
- [123] Wall, B. J. and Conway, B. A., "Shape-Based Approach to Low-Thrust Rendezvous Trajectory Design", *Journal of Guidance, Control, and Dynamics*, Vol. 32, No. 1, 2009, pp. 95-102. DOI: 10.2514/1.36848.
- [124] Izzo, D., "Lambert's Problem for Exponential Sinusoids", *Journal of Guidance Control and Dynamics*, Vol. 29, No. 5, 2006, pp. 1242-1245. DOI: 10.2514/1.21796.
- [125] Vasile, M., De Pascale, P. and Casotto, S., "On the optimality of a shape-based approach based on pseudo-equinoctial elements", *Acta Astronautica*, Vol. 61, No. 1-6, 2007, pp. 286-297. DOI: 10.1016/j.actaastro.2007.01.017.
- [126] Wall, B. J., "Shape-Based Approximation Method for Low-Thrust Trajectory Optimization", *AIAA/AAS Astrodynamics Specialist Conference and Exhibit*, AIAA Paper 2008-6616, Honolulu, HI, USA, 2008.
- [127] Wall, B. J. and Conway, B. A., "Genetic algorithms applied to the solution of hybrid optimal control problems in astrodynamics", *Journal of Global Optimization*, Vol. 44, No. 4, 2009, pp. 493-508. DOI: 10.1007/s10898-008-9352-4.
- [128] Wang, D., Zhang, G. and Cao, X., "Modified inverse-polynomial shaping approach with thrust and radius constraints", *Proceedings of the Institution of Mechanical Engineers, Part G: Journal of Aerospace Engineering*, Vol. 229, No. 13, 2015, pp. 2506-2518. DOI: 10.1177/0954410015579473.
- [129] Novak, D. M. and Vasile, M., "Improved Shaping Approach to the Preliminary Design of Low-Thrust Trajectories", *Journal of Guidance, Control, and Dynamics*, Vol. 34, No. 1, 2011, pp. 128-147. DOI: 10.2514/1.50434.
- [130] Wall, B. J. and Novak, D., "A 3D shape-based approximation method for low-thrust trajectory design", *AAS/AIAA Astrodynamics Specialist Conference*, AAS Paper 11-479, Girdwood, AK, USA, 2011.
- [131] Novak, D. M., "Methods and Tools for Preliminary Low Thrust Mission Analysis", PhD Thesis, School of Engineering, University of Glasgow, Glasgow, Scotland, UK, 2012.
- [132] Taheri, E. and Abdelkhalik, O., "Fast Initial Trajectory Design for Low-Thrust Restricted-Three-Body Problems", *Journal of Guidance, Control, and Dynamics*, Vol. 38, No. 11, 2015, pp. 2146-2160. DOI: 10.2514/1.G000878.
- [133] Taheri, E. and Abdelkhalik, O., "Initial three-dimensional low-thrust trajectory design", *Advances in Space Research*, Vol. 57, No. 3, 2016, pp. 889-903. DOI: 10.1016/j.asr.2015.11.034.
- [134] Gondelach, D. J. and Noomen, R., "Hodographic-Shaping Method for Low-Thrust Interplanetary Trajectory Design", *Journal of Spacecraft and Rockets*, Vol. 52, No. 3, 2015, pp. 728-738. DOI: 10.2514/1.A32991.

- [135] Taheri, E., Kolmanovsky, I. and Atkins, E., "Shaping Velocity Coordinates for Generating Low-Thrust Trajectories", *27th AAS/AIAA Space Flight Mechanics Meeting*, AAS Paper 17-440, San Antonio, TX, USA, 2017.
- [136] Xie, C., Zhang, G. and Zhang, Y., "Simple Shaping Approximation for Low-Thrust Trajectories Between Coplanar Elliptical Orbits", *Journal of Guidance, Control, and Dynamics*, 2015, pp. 2448-2455. DOI: 10.2514/1.G001209.
- [137] Fang, Q., Wang, X., Sun, C. and Yuan, J., "A Shape-Based Method for Continuous Low-Thrust Trajectory Design between Circular Coplanar Orbits", *International Journal of Aerospace Engineering*, Vol. 2017, 2017. DOI: 10.1155/2017/9234905.
- [138] Roa, J., Peláez, J. and Senent, J., "New Analytic Solution with Continuous Thrust: Generalized Logarithmic Spirals", *Journal of Guidance, Control, and Dynamics*, Vol. 39, No. 10, 2016, pp. 2336-2351. DOI: 10.2514/1.G000341.
- [139] Roa, J., Peláez, J. and Senent, J., "Spiral Lambert's Problem", *Journal of Guidance, Control, and Dynamics*, Vol. 39, No. 10, 2016, pp. 2250-2263. DOI: 10.2514/1.G000342.
- [140] Sauer, C. G. J., "Optimum Solar-Sail Interplanetary Trajectories", *AIAA/AAS Astrodynamics Conference*, AIAA Paper 76-792, San Diego, CA, USA, 1976.
- [141] Powers, R. B., Coverstone-Carroll, V. and Prussing, J. E., "Solar sail optimal orbit transfers to synchronous orbits", *Astrodynamic 1999, Pts 1-3*, edited by K.C. Howell et al., Advances in the Astronautical Sciences, Univelt Inc, San Diego, CA, USA, 2000, pp. 523-537.
- [142] Circi, C., "Mars and Mercury Missions Using Solar Sails and Solar Sails and Solar Electric Propulsion", *Journal of Guidance, Control, and Dynamics*, Vol. 27, No. 3, 2004, pp. 496-498. DOI: 10.2514/1.5425.
- [143] Mengali, G. and Quarta, A. A., "Optimal Three-Dimensional Interplanetary Rendezvous Using Non-Ideal Solar Sail", *Journal of Guidance, Control, and Dynamics*, Vol. 28, No. 1, 2005, pp. 173-177. DOI: 10.2514/1.8325.
- [144] Zeng, X., Gong, S. and Li, J., "Fast solar sail rendezvous mission to near Earth asteroids", *Acta Astronautica*, Vol. 105, No. 1, 2014, pp. 40-56. DOI: 10.1016/j.actaastro.2014.08.023.
- [145] Otten, M. and McInnes, C. R., "Near Minimum-Time Trajectories for Solar Sails", *Journal of Guidance, Control, and Dynamics*, Vol. 24, No. 3, 2001, pp. 632-634. DOI: 10.2514/2.4758.
- [146] Stolbunov, V., Ceriotti, M., Colombo, C. and McInnes, C., "Optimal Law for Inclination Change in an Atmosphere Through Solar Sailing", *Journal of Guidance, Control and Dynamics*, Vol. 36, No. 5, 2013, pp. 1310-1323. DOI: 10.2514/1.59931.
- [147] Macdonald, M. and McInnes, C., "Analytical Control Laws for Planet-Centered Solar Sailing", *Journal of Guidance, Control, and Dynamics*, Vol. 28, No. 5, 2005, pp. 1038-1048. DOI: 10.2514/1.11400.
- [148] Tsu, T. C., "Interplanetary Travel by Solar Sail", *ARS Journal*, Vol. 29, No. 6, 1959, pp. 422-427. DOI: 10.2514/8.4791.

- [149] Heiligers, J., McInnes, C. R., Biggs, J. D. and Ceriotti, M., “Displaced geostationary orbits using hybrid low-thrust propulsion”, *Acta Astronautica*, Vol. 71, 2012, pp. 51-67. DOI: 10.1016/j.actaastro.2011.08.012.
- [150] Wawrzyniak, G. G. and Howell, K. C., “Numerical techniques for generating and refining solar sail trajectories”, *Advances in Space Research*, Vol. 48, No. 11, 2011, pp. 1848-1857. DOI: 10.1016/j.asr.2011.04.012.
- [151] Uchiyama, K. and McInnes, C. R., “Analytical Control Laws for Interplanetary Solar Sail Trajectories with Constraints”, *59th International Astronautical Congress*, International Astronautical Federation Paper IAC-08-C1.5.4, Glasgow, Scotland, UK, 2008.
- [152] Liu, Y., Cheng, Z., Huang, X., Zhou, L. and Wang, L., “Propellantless sail-craft design for the Main Belt Asteroid Exploration Mission”, *The Fourth International Symposium on Solar Sailing 2017*, Paper 17033, Kyoto, Japan, 2017.
- [153] Bando, M. and Yamakawa, H., “Near-Earth Asteroid Flyby Survey Mission Using Solar Sailing Technology”, *The Journal of the Astronautical Sciences*, Vol. 58, No. 4, 2011, pp. 569-581. DOI: 10.1007/bf03321532.
- [154] McInnes, C. R., “Inverse Solar Sail Trajectory Problem”, *Journal of Guidance, Control, and Dynamics*, Vol. 26, No. 2, 2003, pp. 369-371. DOI: 10.2514/2.5057.
- [155] von Stryk, O. and Glocker, M., “Numerical Mixed-Integer Optimal Control and Motorized Traveling Salesmen Problems”, *Journal Européen des Systèmes Automatisés*, Vol. 35, No. 4, 2001, pp. 519-533.
- [156] Stuart, J., Howell, K. and Wilson, R., “Application of Multi-Agent Coordination Methods to the Design of Space Debris Mitigation Tours”, *Advances in Space Research*, Vol. 57, 2016, pp. 1680-1697. DOI: 10.1016/j.asr.2015.05.002.
- [157] Wagner, S. and Wie, B., “Hybrid Algorithm for Multiple Gravity-Assist and Impulsive Delta-V Maneuvers”, *Journal of Guidance, Control, and Dynamics*, Vol. 38, No. 11, 2015, pp. 2096-2107. DOI: 10.2514/1.G000874.
- [158] Stuart, J. R., Howell, K. C. and Wilson, R. S., “Design of End-to-End Trojan Asteroid Rendezvous Tours Incorporating Scientific Value”, *Journal of Spacecraft and Rockets*, Vol. 53, No. 2, 2016, pp. 278-288. DOI: 10.2514/1.A33396.
- [159] Boden, R. C., Hein, A. M. and Kawaguchi, J., “Target selection and mass estimation for manned NEO exploration using a baseline mission design”, *Acta Astronautica*, Vol. 111, 2015, pp. 198-221. DOI: 10.1016/j.actaastro.2015.02.018.
- [160] Olympio, J. T., “Optimal Control Problem for Low-Thrust Multiple Asteroid Tour Missions”, *Journal of Guidance, Control, and Dynamics*, Vol. 34, No. 6, 2011, pp. 1709-1720. DOI: 10.2514/1.53339.
- [161] Englander, J. A., Conway, B. A. and Williams, T., “Automated Mission Planning via Evolutionary Algorithms”, *Journal of Guidance, Control, and Dynamics*, Vol. 35, No. 6, 2012, pp. 1878-1887. DOI: 10.2514/1.54101.
- [162] Izzo, D., “1st ACT global trajectory optimisation competition: Problem description and summary of the results”, *Acta Astronautica*, Vol. 61, No. 9, 2007, pp. 731-734. DOI: 10.1016/j.actaastro.2007.03.003.

- [163] Bertrand, R., Epenoy, R. and Meyssignac, B., “Problem Description for the 4th Global Trajectory Optimisation Competition”, Centre National d’Etudes Spatiales (CNES), 2009, http://www.esa.int/gsp/ACT/doc/MAD/ACT-RPT-MAD-GTOC4-problem_stmt.pdf [retrieved 24 August 2017].
- [164] Bertrand, R., Epenoy, R. and Meyssignac, B., “Final Results of the 4th Global Trajectory Optimisation Competition”, Centre National d’Etudes Spatiales (CNES), 2009, http://mech.math.msu.su/~iliagri/gtoc4/gtoc4_final_results.pdf [retrieved 24 August 2017].
- [165] Chilan, C. M. and Conway, B. A., “Automated Design of Multiphase Space Missions Using Hybrid Optimal Control”, *Journal of Guidance, Control, and Dynamics*, Vol. 36, No. 5, 2013, pp. 1410-1424. DOI: 10.2514/1.58766.
- [166] Di Carlo, M., Romero Martin, J. M. and Vasile, M., “CAMELOT - Computational-Analytic Multi-fidelity Low-thrust Optimisation Toolbox”, *6th International Conference on Astrodynamics Tools and Techniques - ICATT*, Darmstadt, Germany, 2016.
- [167] Di Carlo, M., Romero Martin, J. M. and Vasile, M., “Automatic Trajectory Planning for Low-Thrust Active Removal Mission in Low-Earth Orbit”, *Advances in Space Research*, Vol. 59, No. 5, 2017, pp. 1234-1258. DOI: 10.1016/j.asr.2016.11.033.
- [168] Di Carlo, M., Romero Martin, J. M., Gomez, N. O. and Vasile, M., “Optimised Low-Thrust Mission to the Atira Asteroids”, *Advances in Space Research*, Vol. 59, No. 7, 2017, pp. 1724-1739. DOI: 10.1016/j.asr.2017.01.009.
- [169] Perozzi, E., Rossi, A. and Valsecchi, G. B., “Basic targeting strategies for rendezvous and flyby missions to the near-Earth asteroids”, *Planetary and Space Science*, Vol. 49, No. 1, 2001, pp. 3-22. DOI: 10.1016/S0032-0633(00)00124-0.
- [170] Ceriotti, M., “Global Optimisation of Multiple Gravity Assist Trajectories”, PhD Thesis, School of Engineering, University of Glasgow, Glasgow, Scotland, UK, 2010.
- [171] Izzo, D., Hennes, D., Simões, L. F. and Märtens, M., “Designing Complex Interplanetary Trajectories for the Global Trajectory Optimization Competitions”, *Space Engineering: Modeling and Optimization with Case Studies*, edited by G. Fasano and J.D. Pintér, Springer Optimization and Its Applications, Springer International Publishing, Cham, Switzerland, 2016, pp. 151-176.
- [172] Casalino, L. and Pastrone, D., “Mission Design and Disposal Method Comparison for the Removal of Multiple Debris”, *26th AAS/AIAA Space Flight Mechanics Meeting*, AAS Paper 16-278, Napa, CA, USA, 2016.
- [173] Yi, L., Jisheng, L., Hengnian, L., Zheng, C., Pu, H., Jun Feng, L., et al., “Fast Design of Low-Thrust Transfer Orbit for Manned Asteroids Exploration”, *65th International Astronautical Congress*, International Astronautical Federation Paper IAC-14-C1.9.10, Toronto, Canada, 2014.
- [174] Petropoulos, A. E., Bonfiglio, E. P., Grebow, D. J., Lam, T., Parker, J. S., Arrieta, J., et al., “GTOC5: Results from the Jet Propulsion Laboratory”, *Acta Futura*, Vol. 8, 2014, pp. 21-27. DOI: 10.2420/AF08.2014.21.
- [175] Peloni, A., Wolz, D., Ceriotti, M. and Althöfer, I., “Construction and Verification of a Solution of the 8th Global Trajectory Optimization Competition Problem. Team 13: GlasgowJena+”, *26th AAS/AIAA Space Flight Mechanics Meeting*, AAS Paper 16-425, Napa, CA, USA, 2016.

- [176] Stuart, J. R., Howell, K. C. and Wilson, R. S., "Automated Design of Propellant-Optimal, Low-Thrust Trajectories for Trojan Asteroid Tours", *Journal of Spacecraft and Rockets*, Vol. 51, No. 5, 2014, pp. 1631-1647. DOI: 10.2514/1.A32748.
- [177] Barbee, B. W., Davis, G. W. and Hur-Diaz, S., "Spacecraft Trajectory Design for Tours of Multiple Small Bodies", *2009 AAS/AIAA Astrodynamics Specialist Conference*, AAS Paper 09-433, Pittsburgh, PA, USA, 2009.
- [178] Vasile, M. and Locatelli, M., "A hybrid multiagent approach for global trajectory optimization", *Journal of Global Optimization*, Vol. 44, No. 4, 2009, pp. 461-479. DOI: 10.1007/s10898-008-9329-3.
- [179] Sanchez, P., Colombo, C., Vasile, M. and Radice, G., "Multicriteria Comparison Among Several Mitigation Strategies for Dangerous Near-Earth Objects", *Journal of Guidance, Control, and Dynamics*, Vol. 32, No. 1, 2009, pp. 121-142. DOI: 10.2514/1.36774.
- [180] Sugimoto, Y., Radice, G. and Sanchez, J. P., "Effects of NEO composition on deflection methodologies", *Acta Astronautica*, Vol. 90, No. 1, 2013, pp. 14-21. DOI: 10.1016/j.actaastro.2012.08.030.
- [181] Miller, P. L., Barbee, B. W. and Morrison, D., "Asteroid-Characterization Priorities for Planetary Defense", *4th IAA Planetary Defense Conference - PDC 2015*, International Academy of Astronautics Paper IAA-PDC-15-03-01, Frascati, Italy, 2015.
- [182] Mainzer, A., Grav, T., Masiero, J., Bauer, J., McMillan, R. S., Giorgini, J., et al., "Characterizing Subpopulations within the near-Earth Objects with NEOWISE: Preliminary Results", *The Astrophysical Journal*, Vol. 752, No. 2, 2012, pp. 110-125. DOI: 10.1088/0004-637X/752/2/110.
- [183] Harris, A. W., Barucci, M. A., Cano, J. L., Fitzsimmons, A., Fulchignoni, M., Green, S. F., et al., "The European Union funded NEOShield project: A global approach to near-Earth object impact threat mitigation", *Acta Astronautica*, Vol. 90, No. 1, 2013, pp. 80-84. DOI: 10.1016/j.actaastro.2012.08.026.
- [184] Koschny, D. and Drolshagen, G., "Activities in Europe related to the mitigation of the threat from near-Earth objects", *Advances in Space Research*, Vol. 56, No. 3, 2015, pp. 549-556. DOI: 10.1016/j.asr.2015.03.027.
- [185] Cheng, A. F., Santo, A. G., Heeres, K. J., Landshof, J. A., Farquhar, R. W., Gold, R. E., et al., "Near-Earth Asteroid Rendezvous: Mission overview", *Journal of Geophysical Research*, Vol. 102, No. E10, 1997, pp. 23695 - 23708. DOI: 10.1029/96JE03364.
- [186] Blume, W. H., "Deep Impact Mission Design", *Space Science Reviews*, Vol. 117, No. 1, 2005, pp. 23-42. DOI: 10.1007/s11214-005-3386-4.
- [187] Fujiwara, A., Kawaguchi, J. and Uesugi, K. T., "Role of sample return mission MUSES-C in asteroid study", *Advances in Space Research*, Vol. 34, No. 11, 2004, pp. 2267-2269. DOI: 10.1016/j.asr.2003.07.065.
- [188] Fujiwara, A., Kawaguchi, J., Yeomans, D. K., Abe, M., Mukai, T., Okada, T., et al., "The Rubble-Pile Asteroid Itokawa as Observed by Hayabusa", *Science*, Vol. 312, No. 5778, 2006, pp. 1330-1334. DOI: 10.1126/science.1125841.

- [189] Glassmeier, K. H., Boehnhardt, H., Koschny, D., Kührt, E. and Richter, I., "The Rosetta Mission: Flying Towards the Origin of the Solar System", *Space Science Reviews*, Vol. 128, No. 1, 2007, pp. 1-21. DOI: 10.1007/s11214-006-9140-8.
- [190] Pätzold, M., Andert, T. P., Asmar, S. W., Anderson, J. D., Barriot, J. P., Bird, M. K., et al., "Asteroid 21 Lutetia: Low Mass, High Density", *Science*, Vol. 334, No. 6055, 2011, pp. 491-492. DOI: 10.1126/science.1209389.
- [191] Berry, K., Sutter, B., May, A., Williams, K., Barbee, B. W., Beckman, M., et al., "OSIRIS-REx Touch-And-Go (TAG) Mission Design and Analysis", *36th AAS Guidance and Control Conference*, AAS Paper 13-095, Breckenridge, CO, USA, 2013.
- [192] Tsuda, Y., Nakazawa, S., Kushiki, K., Yoshikawa, M., Kuninaka, H. and Watanabe, S., "Flight status of robotic asteroid sample return mission Hayabusa2", *Acta Astronautica*, Vol. 127, 2016, pp. 702-709. DOI: 10.1016/j.actaastro.2016.01.027.
- [193] Cheng, A. F., Atchison, J., Kantsiper, B., Rivkin, A. S., Stickle, A., Reed, C., et al., "Asteroid Impact and Deflection Assessment mission", *Acta Astronautica*, Vol. 115, 2015, pp. 262-269. DOI: 10.1016/j.actaastro.2015.05.021.
- [194] Gates, M., Stich, S., McDonald, M., Muirhead, B., Mazanek, D., Abell, P., et al., "The Asteroid Redirect Mission and sustainable human exploration", *Acta Astronautica*, Vol. 111, 2015, pp. 29-36. DOI: 10.1016/j.actaastro.2015.01.025.
- [195] Bonin, G., Foulds, C., Armitage, S. and Faber, D., "Prospector-1: The First Commercial Small Spacecraft Mission to an Asteroid", *AIAA/USU Conference on Small Satellites*, AIAA Paper SSC16-VI-2, Logan, UT, USA, 2016.
- [196] Grundmann, J. T., Bauer, W., Biele, J., Boden, R. C., Ceriotti, M., Cordero, F., et al., "Small Spacecraft Solar Sailing for Small Solar System Body Multiple Rendezvous and Landing", *2018 IEEE Aerospace Conference*, IEEE Paper 2360, Big Sky, MT, USA, 2018.
- [197] Peloni, A., Ceriotti, M. and Dachwald, B., "Preliminary Trajectory Design of a Multiple NEO Rendezvous Mission Through Solar Sailing", *65th International Astronautical Congress*, International Astronautical Federation Paper IAC-14-C1.9.7, Toronto, Canada, 2014.
- [198] Peloni, A., Ceriotti, M. and Dachwald, B., "Solar-Sail Trajectory Design for a Multiple Near-Earth-Asteroid Rendezvous Mission", *Journal of Guidance, Control, and Dynamics*, Vol. 39, No. 12, 2016, pp. 2712-2724. DOI: 10.2514/1.G000470.
- [199] Peloni, A., Rao, A. V. and Ceriotti, M., "ATOSS: Automated Trajectory Optimiser for Solar Sailing", *Fourth European Optimisation in Space Engineering (OSE) Workshop*, Bremen, Germany, 2017.
- [200] Peloni, A., Rao, A. V. and Ceriotti, M., "Automated Trajectory Optimizer for Solar Sailing (ATOSS)", *Aerospace Science and Technology*, Vol. 72, 2018, pp. 465-475. DOI: 10.1016/j.ast.2017.11.025.
- [201] Sullo, N., Peloni, A. and Ceriotti, M., "From Low Thrust to Solar Sailing: A Homotopic Approach", *26th AAS/AIAA Space Flight Mechanics Meeting*, AAS Paper 16-426, Napa, CA, USA, 2016.
- [202] Efroimsky, M., "Gauge Freedom in Astrodynamics", *Modern Astrodynamics*, edited by P. Gurfil, Butterworth-Heinemann, London, UK, 2006, pp. 23-52.

- [203] Vallado, D. A. and McClain, W. D., *Fundamentals of Astrodynamics and Applications*, Space Technology Series, McGraw-Hill, New York, NY, USA, 1997, pp. 31-37, 546.
- [204] MATLAB User's Guide, Ver. R2014b, MathWorks, Natick, MA, USA, 2014.
- [205] González, Á. F., "A shape-based approach to solar sail trajectory optimization in 3D", BSc Thesis, School of Engineering, University of Glasgow, Glasgow, Scotland, UK, 2015.
- [206] Barbee, B. W., Esposito, T., Pinon, E., Hur-Diaz, S., Mink, R. G. and Adamo, D. R., "A Comprehensive Ongoing Survey of the Near-Earth Asteroid Population for Human Mission Accessibility", *AIAA Guidance, Navigation and Control Conference*, AIAA Paper 2010-8368, Toronto, Canada, 2010.
- [207] Mengali, G. and Quarta, A. A., "Optimal nodal flyby with near-Earth asteroids using electric sail", *Acta Astronautica*, Vol. 104, No. 2, 2014, pp. 450-457. DOI: 10.1016/j.actaastro.2014.02.012.
- [208] Jiang, F., Baoyin, H. and Li, J., "Practical Techniques for Low-Thrust Trajectory Optimization with Homotopic Approach", *Journal of Guidance, Control, and Dynamics*, Vol. 35, No. 1, 2012, pp. 245-258. DOI: 10.2514/1.52476.
- [209] Geffroy, S. and Epenoy, R., "Optimal low-thrust transfers with constraints---generalization of averaging techniques", *Acta Astronautica*, Vol. 41, No. 3, 1997, pp. 133-149. DOI: 10.1016/S0094-5765(97)00208-7.
- [210] Sullo, N. and Ceriotti, M., "A Homotopy-Based Method for Optimization of Hybrid High-Low Thrust Trajectories", *65th International Astronautical Congress*, International Astronautical Federation Paper IAC-14-C1.8.6, Toronto, Canada, 2014.
- [211] Gong, S., Li, J. and Jiang, F., "Interplanetary trajectory design for a hybrid propulsion system", *Aerospace Science and Technology*, Vol. 45, 2015, pp. 104-113. DOI: 10.1016/j.ast.2015.04.020.
- [212] Press, W. H., Teukolsky, S. A., Vetterling, W. T. and Flannery, B. P., *Numerical Recipes in C: The Art of Scientific Computing, Second Edition*, Cambridge University Press, New York, NY, USA, 1992, pp. 724-732.
- [213] Moré, J. J., "The Levenberg-Marquardt algorithm: Implementation and theory", *Numerical Analysis*, edited by G.A. Watson, Lecture Notes in Mathematics, Springer-Verlag, Berlin, Germany, 1978, pp. 105-116.
- [214] Peloni, A., Ceriotti, M. and Dachwald, B., "Solar-Sailing Trajectory Design for Close-up NEA Observations Mission", *4th IAA Planetary Defense Conference - PDC 2015*, International Academy of Astronautics Paper IAA-PDC-15-P-19, Frascati, Italy, 2015.
- [215] Peloni, A., Dachwald, B. and Ceriotti, M., "Multiple NEA Rendezvous Mission: Solar Sailing Options", *The Fourth International Symposium on Solar Sailing 2017*, Paper 17017, Kyoto, Japan, 2017.
- [216] Peloni, A., Dachwald, B. and Ceriotti, M., "Multiple Near-Earth Asteroid Rendezvous Mission: Solar-Sailing Options", *Advances in Space Research*, (in press). DOI: 10.1016/j.asr.2017.10.017.

- [217] Warner, B. D., Harris, A. W. and Pravec, P., “The asteroid lightcurve database”, *Icarus*, Vol. 202, No. 1, 2009, pp. 134-146. DOI: 10.1016/j.icarus.2009.02.003.
- [218] Carusi, A., Kresák, L. and Valsecchi, G. B., “Conservation of the Tisserand Parameter at Close Encounters of Interplanetary Objects with Jupiter”, *Earth, Moon, and Planets*, Vol. 68, No. 1-3, 1995, pp. 71-94. DOI: 10.1007/BF00671499.
- [219] Shen, H. and Tsiortras, P., “Using Battin's method to obtain multiple-revolution Lambert's solutions”, *AAS/AIAA Astrodynamics Specialist Conference*, AAS Paper 03-568, Big Sky, Montana, USA, 2003.
- [220] Shen, H.-X., Zhang, T.-J., Huang, A.-Y. and Li, Z., “GTOC9: Results from the Xi'an Satellite Control Center (team XSCC)”, *Acta Futura*, Vol. 11, 2018, pp. 49-55. DOI: 10.5281/zenodo.1139240.
- [221] Lu, E. T. and Love, S. G., “Gravitational tractor for towing asteroids”, *Nature*, Vol. 438, No. 7065, 2005, pp. 177-178. DOI: 10.1038/438177a.
- [222] Wie, B., “Dynamics and Control of Gravity Tractor Spacecraft for Asteroid Deflection”, *Journal of Guidance, Control, and Dynamics*, Vol. 31, No. 5, 2008, pp. 1413-1423. DOI: 10.2514/1.32735.
- [223] Grundmann, J. T., Biele, J., Dachwald, B., Grimm, C. D., Lange, C., Ulamec, S., et al., “Small Landers and Separable Sub-Spacecraft for Near-term Solar Sails”, *The Fourth International Symposium on Solar Sailing 2017*, Paper 17094, Kyoto, Japan, 2017.
- [224] Bellman, R., *Dynamic Programming*, Princeton University Press, Princeton, NJ, USA, 1957, pp. 83.
- [225] Quarta, A. A. and Mengali, G., “Semi-Analytical Method for the Analysis of Solar Sail Heliocentric Orbit Raising”, *Journal of Guidance, Control, and Dynamics*, Vol. 35, No. 1, 2012, pp. 330-335. DOI: 10.2514/1.55101.
- [226] Wie, B. and Murphy, D., “Solar-Sail Attitude Control Design for a Sail Flight Validation Mission”, *Journal of Spacecraft and Rockets*, Vol. 44, No. 4, 2007, pp. 809-821. DOI: 10.2514/1.22996.
- [227] Borggräfe, A., “Analysis of Interplanetary Solar Sail Trajectories with Attitude Dynamics”, Diploma Thesis, Institute of Flight System Dynamics, RWTH Aachen, Aachen, Germany, 2011.
- [228] Petropoulos, A. E., “GTOC8: Problem Description and Summary of the Results”, *26th AAS/AIAA Space Flight Mechanics Meeting*, AAS Paper 16-501, Napa, CA, USA, 2016.
- [229] Wertz, J. R. and Larson, W. J., *Space Mission Analysis and Design, Third Edition*, Space Technology Library, Microcosm Press and Springer, New York, NY, USA, 2010, pp. 688-691.
- [230] Reeves, D. M., Mazanek, D. D., Cichy, B. D., Broschart, S. B. and Deweese, K. D., “Asteroid Redirect Mission Proximity Operations for Reference Target Asteroid 2008 EV5”, *39th Annual AAS Guidance and Control Conference*, AAS Paper 16-105, Breckenridge, CO, USA, 2016.

- [231] Chodas, P. W., Chesley, S. R. and Yeomans, D. K., “Impact Hazard Assessment for 2011 AG5”, *3rd IAA Planetary Defense Conference*, International Academy of Astronautics Paper IAA-PDC13-03-11, Flagstaff, AZ, USA, 2013.
- [232] Chesley, S. R., Chodas, P. W., Milani, A., Valsecchi, G. B. and Yeomans, D. K., “Quantifying the Risk Posed by Potential Earth Impacts”, *Icarus*, Vol. 159, No. 2, 2002, pp. 423-432. DOI: 10.1006/icar.2002.6910.
- [233] Wolpert, D. H. and Macready, W. G., “No Free Lunch Theorems for Optimization”, *IEEE Transactions on Evolutionary Computation*, Vol. 1, No. 1, 1997, pp. 67-82. DOI: 10.1109/4235.585893.
- [234] Farrés, A., Jorba, À. and Mondelo, J.-M., “Orbital Dynamics and Control for a Non-Perfectly Reflecting Solar Sail Close to an Asteroid”, *2nd IAA Conference on Dynamics and Control of Space Systems*, International Academy of Astronautics Paper IAA-AAS-DyCoSS1-11-09, Rome, Italy, 2014.
- [235] Morrow, E., Scheeres, D. J. and Lubin, D., “Solar Sail Orbit Operations at Asteroids”, *Journal of Spacecraft and Rockets*, Vol. 38, No. 2, 2001, pp. 279-286. DOI: 10.2514/2.3682.
- [236] Edelbaum, T. N., “Propulsion Requirements for Controllable Satellites”, *ARS Journal*, Vol. 31, No. 8, 1961, pp. 1079-1089. DOI: 10.2514/8.5723.
- [237] Wang, X., Wan, W., Zhang, X. and Yu, X., “Annealed particle filter based on particle swarm optimization for articulated three-dimensional human motion tracking”, *Optical Engineering*, Vol. 49, No. 1, 2010, pp. 017204: 1-11. DOI: 10.1117/1.3281669.
- [238] Dachwald, B. and Wie, B., “Solar Sail Trajectory Optimization for Intercepting, Impacting, and Deflecting Near-Earth Asteroids”, *AIAA Guidance, Navigation, and Control Conference and Exhibit*, AIAA Paper 2005-6176, San Francisco, CA, USA, 2005.
- [239] Suganthan, P. N., Hansen, N., Liang, J. J., Deb, K., Chen, Y.-P., Auger, A., et al., “Problem Definitions and Evaluation Criteria for the CEC 2005 Special Session on Real-Parameter Optimization”, Nanyang Technological University, KanGAL Report Number 2005005, Singapore, 2005, May 2005, <http://web.mysites.ntu.edu.sg/epnsugan/PublicSite/Shared%20Documents/Forms/AllItems.aspx?RootFolder=%2fepnsugan%2fPublicSite%2fShared%20Documents%2fCEC2005&FolderCTID=&View=%7bDAF31868-97D8-4779-AE49-9CEC4DC3F310%7d> [retrieved 30 August 2017].
- [240] Fatih Tasgetiren, M., Liang, Y. C., Gencyilmaz, G. and Eker, I., “Global Optimization of Continuous Functions Using Particle Swarm Optimization”, *IEEE Congress on Evolutionary Computation (Special Session on Real-Parameter Optimization)*, IEEE Paper 519, Edinburgh, Scotland, UK, 2005.
- [241] Liang, J. J. and Suganthan, P. N., “Dynamic Multi-Swarm Particle Swarm Optimizer with Local Search”, *IEEE Congress on Evolutionary Computation (Special Session on Real-Parameter Optimization)*, IEEE Paper 620, Edinburgh, Scotland, UK, 2005.